
**JOINT ANALYSIS OF THREE FLAVOUR NEUTRINO OSCILLATIONS
COMBINING THE ν_e APPEARANCE AND ν_μ DISAPPEARANCE CHANNELS
IN THE T2K EXPERIMENT**

Lorena Escudero Sánchez

Doctorado en Física
Universidad de Valencia

Director:

Anselmo Cervera Villanueva
Instituto de Física Corpuscular -
CSIC y Universidad Valencia

Co-director:

Konstantinos Andreopoulos
Rutherford Appleton Laboratory -
Oxford



VNIVERSITAT DE VALÈNCIA

The work described in this thesis has been developed at the Instituto de Física Corpuscular (IFIC) in Valencia, affiliated with Consejo Superior de Investigaciones Científicas (CSIC) and Universitat de València, and it has been possible thanks to the University Faculty Training (FPU) program of PhD Scholarships awarded by the Spanish Ministry of Education and Science.

©Lorena Escudero Sánchez, 2014. All rights reserved.

Abstract

The T2K (Tokai-to-Kamioka) experiment, located in Japan, is the first long-baseline neutrino oscillation experiment using an off-axis configuration. It consists of a very pure ν_μ beam generated at the J-PARC accelerator complex in Tokai, characterized by a set of near detectors placed 280 m from the target, and directed towards the Super-Kamiokande (SK) water Čerenkov detector, situated 295 km away in the Kamioka mine. T2K is optimized to perform two kind of oscillation analyses: ν_μ disappearance analysis, which provides measurements of the atmospheric mixing angle θ_{23} and mass-squared splitting Δm_{32}^2 ; and ν_e appearance analysis, which is sensitive to the angle θ_{13} and the CP-violating phase δ_{CP} .

In this thesis, the first T2K joint 3-flavour oscillation analysis, combining the ν_μ disappearance and the ν_e appearance channels, and performed using a frequentist approach, is presented. This analysis consists in a simultaneous fit to the energy spectra of both the ν_μ and ν_e event candidates from the T2K beam at SK, in which the four oscillation parameters Δm_{32}^2 (or Δm_{13}^2), $\sin^2 \theta_{23}$, $\sin^2 \theta_{13}$ and δ_{CP} are jointly determined. The best-fit values obtained for the T2K Run 1+2+3+4 dataset, with 6.57×10^{20} POT, assuming normal (inverted) mass hierarchy with their 1σ errors are:

$$\begin{aligned}
 \Delta m_{32}^2 (\Delta m_{13}^2) &= 2.51_{-0.12}^{+0.11} (2.49_{-0.12}^{+0.12}) \times 10^{-3} eV^2/c^4, \\
 \sin^2 \theta_{23} &= 0.524_{-0.059}^{+0.057} (0.523_{-0.065}^{+0.055}), \\
 \sin^2 \theta_{13} &= 0.042_{-0.021}^{+0.013} (0.049_{-0.021}^{+0.015}) \\
 \delta_{CP} &= 1.91_{-5.05}^{+1.23} (1.01_{-4.15}^{+2.14})
 \end{aligned} \tag{1}$$

Separately, precise measurements of the angle θ_{13} have been obtained by experiments using electron antineutrinos from nuclear reactors, being the average value from the 2013 results $\sin^2 \theta_{13} = 0.095 \pm 0.01$. By constraining $\sin^2 \theta_{13}$ to the reactor value, the T2K joint 3-flavour oscillation analysis led to a first measurement of the δ_{CP} phase: its best-fit value is consistent with $-\pi/2$ and the following values are excluded at the 90% CL

$$\begin{aligned}
 [0.146, 0.825] \pi &\text{ for normal hierarchy} \\
 [-0.080, 1.091] \pi &\text{ for inverted hierarchy}
 \end{aligned}$$

No sabré quién soy,
no reconoceré en mí la misma naturaleza,
cuando termine estas líneas;
quizá no haya tenido suficiente interacción,
ni siquiera con mis propias palabras,
pero es ligero el razonamiento,
y una larga distancia separa la idea original
de la que ahora concluye.

Contributions

During the first two years of my PhD, I have worked on the high level calibration of the Time Projection Chambers (TPCs) of the ND280 near detector. This initial work was focused on two tasks: the measurement and correction of spatial distortions created by the electromagnetic field (briefly explained in Chapter 3), and the calculation of the TPC momentum resolution and the associated systematic error (mentioned in Chapter 4.4). In addition, I was TPC Data Quality expert for a year, analyzing the TPC data and reporting on its performance in a weekly basis. For the completion of this task, I worked on the development of the TPC software tools.

Afterwards, I focused my work on neutrino oscillation physics, collaborating with one of the T2K oscillation analysis groups, based at RAL, Oxford, and Lancaster, who had previously performed the T2K muon neutrino disappearance analyses. I contributed extending their analysis in order to perform a joint three flavour neutrino oscillation analysis which combines the muon neutrino disappearance and the electron neutrino appearance channels. This joint three flavour neutrino oscillation analysis is the main topic of this thesis, described in Chapter 5.

Acknowledgements

The history of neutrinos started for me in 2008, when I was at CERN as a summer student and got fascinated by neutrino physics during some lectures: thanks to Juan José Gómez-Cadenas, for the continuous sharing of his passion and for the literary coffees. The first exciting result was the possibility to work with Anselmo Cervera, to whom I will always be grateful for this chance, for helping, supporting and trusting me during these five years. I have been lucky to work and learn about neutrino oscillations with Costas Andreopoulos, who I want to specially acknowledge for his warm welcome and invaluable guidance. I want to thank Nick Grant and Michel Sorel for their helpful comments and ideas, and Pilar Hernández for the fruitful theoretical discussions. I also want to express my gratitude to Tsuyoshi Nakaya, Atsuko Ichikawa, Alfons Weber and the T2K oscillation analysis group, for the motivation and support I have found working with them.

During these years I had a tiny social cross section, as Paola knows pretty well; however, I had the chance to experience interactions with mainly three different nuclei, namely:

- **Valencia:** Valencia means some people that I know they will always stay in my life. Laura Monfregola, with whom I have shared chocolates and illustrations, a true friend I definitely miss. Panos Stamoulis, my old brother to talk about life, the Universe and everything. Raphaël Schroeter, whose advices are indispensable, as well as the procrastination bites with him. Justo Martín-Albo, an inspiring example of "Homo sum, humani nihil a me alienum puto". Paola Ferrario, bravissima, together we spacca tutto! Miguel Villaplana, my sports coach in the many times I went with him to the gym. Andrew Laing, sic a rebel completing oor fowk. To all the ones who have enjoyed the mythical vibration of our office, thanks for the good moments we have shared (specially the market ones): Luis Serra, David Lorca, Miquel Nebot, Joan Català. To Sasha Izmaylov, for the fun moments there and in Japan; to Igor Liubarsky for his recommendations about Oxford and the ROH and to Tapasi Ghosh, with whom I hope to enjoy yoga again soon.

-
- **Oxford:** You must know that this thesis is the result of the work of a team, the VaLOR group, guided by Costas Andreopoulos and initially integrated by me, Tom Dealtry and Nick Grant, to whom I am very thankful for the nice work environment created. I owe them a chocolate con churros!
 - **Tokai:** Any place can be home if you fill it with the appropriate people, like Melody Ravonel, Flor de María Blaszczyk, Eike Frank, Javi Caravaca, Raquel Castillo, Leïla Haegel, Jiae Kim, Enrico Scantamburlo and Mark Rayner, I will remember you guys anytime life brings me into a karaoke. The shifts, even those terrifying ones in which you are an *expert*, can be fun with Sujeewa Kamaratunga (Fuku wa uchi!) or a discovery with Mark Rayner, always honorificabilitudinitatibus! And breakfast can turn on your brain if you can share it with Kendall's energy.

And, of course, the oscillations. Accomplishing a PhD can drive you to extremes you have never experienced before. And in those moments it is essential to have a wonderful family and friends to help you climbing up from any possible oscillation dip. Así que termino agradeciendo a mis queridas amigas María Hernández y Cristina Sardón que siempre estén tan cerca, sin importar la distancia que nos separe. A Sergio Rico, por estar siempre a mi lado durante estos años, por todo lo que me ha aportado y por no dejar nunca que me rindiera. Y finalmente a mis padres y a mi hermana Rocío, por su apoyo y ayuda incondicionales.

Lorena Escudero
Boston, 21 de noviembre de 2014

Contents

Abstract	ii
Contributions	i
Acknowledgements	iii
Contents	vii
Resumen	1
1 Introduction	6
2 Three Active Neutrino Paradigm	11
2.1 Mysterious Neutrinos	11
2.2 The Standard Model Neutrino	14
2.3 Massive Neutrinos	17
2.3.1 Dirac and Majorana Masses	18
2.3.2 The Origin of Neutrino Mass	20
2.4 Neutrino Mixing and Oscillations	21
2.4.1 Neutrino Mixing	21
2.4.2 Three-flavour Neutrino Oscillations	22
2.4.3 Matter Effects	26
2.5 The Flavour Puzzle	28
2.6 Open Questions and Future Perspectives	32
3 The T2K Experiment	35
3.1 T2K Physics Goals	36
3.2 T2K Neutrino Beam	37
3.2.1 J-PARC Accelerator	38
3.2.2 T2K Neutrino Beamline	39

3.2.3	Muon Monitor	41
3.2.4	Off-Axis Configuration	41
3.3	Near Detectors	44
3.3.1	INGRID On-Axis Detector	45
3.3.2	ND280 Off-Axis Detector	47
3.4	Far Detector: Super-Kamiokande	57
3.4.1	SK Reconstruction Techniques	59
4	T2K Predictions and Measurements for the Joint Oscillation Analysis	65
4.1	T2K Beam Data Taking Summary	65
4.2	T2K Neutrino Flux Prediction	67
4.2.1	Monitor Measurements	67
4.2.2	Flux Simulation	70
4.2.3	Flux Uncertainties	74
4.3	T2K Neutrino Interaction Models	77
4.3.1	Interaction Models in NEUT	77
4.3.2	Cross Section Uncertainties	81
4.3.3	Final State, Secondary and Photo-Nuclear Interaction Uncertainties	86
4.4	Near Detector Fit to Constrain Flux and Cross Section Uncertainties	88
4.4.1	ND280 Data	88
4.4.2	ND280 Data Fit and Detector Uncertainties	91
4.4.3	Constraint on Flux and Correlated Cross Section Uncertainties	98
4.5	Far Detector Event Selection and Efficiencies	101
4.5.1	SK Neutrino Event Selection	101
4.5.2	SK Detector Uncertainties	109
5	T2K Joint Oscillation Analysis	113
5.1	Motivation	113
5.2	Oscillation Analysis Overview	116
5.3	Oscillation Probability Calculation and Choice of Oscillation Parameters	117
5.4	Predictions of Single μ -like and e-like Ring Event Reconstructed Energy Spectra in SK	120
5.4.1	Methodology	120
5.4.2	Construction of SK Monte Carlo Templates	121
5.4.3	Predictions of Nominal and Tuned-MC Single μ -like Ring and Single e-like Ring Spectra	125

5.5	Systematic Effects in the Prediction of the Single μ -like Ring and Single e-like Ring Event Reconstructed Energy Spectra in SK . . .	131
5.5.1	Evaluation of Effects of the Systematic Parameters	143
5.6	Neutrino Oscillation Fitting Method	143
5.6.1	Treatment of solar (12-sector) oscillation parameters	146
5.6.2	Adding Reactor Constraint	146
5.6.3	Validation	146
5.6.4	Construction of Confidence Regions	150
5.7	Results of the Joint Oscillation Analysis on the Run 1+2+3+4 (6.570×10^{20} POT) dataset	152
5.7.1	Results with T2K Data Only for Normal and Inverted Hierarchy	152
5.7.2	Results Including the Reactor Constraint	161
5.7.3	Comparisons of Confidence Regions	171
5.8	Future Improvements for the T2K Joint Oscillation Analysis . . .	176
6	T2K Sensitivity Studies and Prospects	178
6.1	T2K Sensitivity Studies	178
6.2	Beyond T2K: Hyper-Kamiokande	182
7	Conclusion	185
Appendices		198
A	T2K Latest Results of Stand-alone Analyses	199
A.1	T2K Latest Results on ν_e Appearance	199
A.2	T2K Latest Results of ν_μ Disappearance	203
B	Effect of the Solar Oscillation Parameters on the Run 1+2+3+4 Joint Oscillation Analysis	208
C	Validation of the Run1+2+3+4 Joint 3-flavour Oscillation Analysis: Fitter Performance	210
C.1	Residuals and pulls of oscillation parameters	210
C.2	Residuals and pulls of systematic parameters	218
D	Validation of the Run1+2+3+4 Joint 3-flavour Oscillation Analysis: Toy Dataset Fits	227

E Difference Between $\sin^2\theta_{23}$ Values for Maximal Mixing and Maximal Disappearance	234
List of Figures	243
List of Tables	246

Contents

Resumen

La física de partículas es la rama de la física dedicada al estudio de los componentes fundamentales de la materia y de las leyes que rigen sus interacciones. Entre ellos destacan los neutrinos, partículas neutras de espín 1/2 que participan únicamente en interacciones débiles, ya que su extraordinaria naturaleza ha contribuido a ampliar los conocimientos sobre partículas elementales y a actualizar las teorías que las describen.

La existencia del neutrino tuvo que ser postulada por Wolfgang Pauli en 1930 para explicar los procesos de desintegración β , en los cuales la distribución energética del electrón emitido sugería la presencia de otra partícula de carga eléctrica neutra no detectada. Algunos años después, Hans Bethe y Rudolf Peierls demostraron que la probabilidad de interacción del neutrino con un núcleo era ínfima. De este modo, los neutrinos se consideraron indetectables durante un cuarto de siglo, hasta que Frederick Reines y Clyde Cowan consiguieron observarlos, más concretamente antineutrinos, mediante un experimento de desintegración beta inversa con antineutrinos producidos en reactores nucleares.

Desde entonces se han desarrollado diversos experimentos para estudiar esta partícula, obteniendo en algunos casos resultados inesperados. El Sol y la atmósfera son dos importantes fuentes naturales de neutrinos y diferentes experimentos han proporcionado medidas de su flujo, observando en ambos casos un déficit respecto a la predicción de los modelos teóricos. Estas discrepancias se conocen como las anomalías solares y atmosféricas que, tras varios años de controversia y confirmaciones experimentales, solo pudieron ser explicadas a través del fenómeno denominado oscilaciones de neutrinos, el cual describe el cambio que experimentan los neutrinos tras haber recorrido una cierta distancia.

Las oscilaciones de neutrinos son consecuencia de la existencia de mezcla de sabor en los neutrinos, cuyos autoestados de sabor o interacción no corresponden exactamente a los autoestados de masa o propagación, sino a una combinación lineal de ellos por medio de una matriz unitaria de mezcla. En el modelo de tres neutrinos activos, una parametrización estándar de esta matriz incluye tres ángulos de mezcla (θ_{12} , θ_{13} , θ_{23}) y una fase δ_{CP} asociada a la violación de la simetría CP (más otras dos fases extra si los neutrinos son partículas de Majorana). Además, este fenómeno implica que las masas de los neutrinos no pueden ser nulas, re-

quiriendo por tanto una modificación o extensión del Modelo Estándar, en el cual los neutrinos eran considerados partículas sin masa. Los experimentos de oscilaciones de neutrinos pueden medir las diferencias cuadráticas de masas Δm_{21}^2 y Δm_{32}^2 (donde $\Delta m_{ij}^2 = m_i^2 - m_j^2$), pero no las masas directamente, accesibles tan solo mediante medidas cosmológicas y experimentos de desintegración β y doble β sin neutrinos. A pesar de la certeza de que el neutrino es una partícula masiva, el origen de dicha masa es aún desconocido, como lo es la propia mezcla (el valor exacto de los parámetros de mezcla) e incluso el número de especies de neutrinos. Nociones de física de neutrinos y el marco teórico para el modelo de tres neutrinos activos se presentan en el Capítulo 2.

Las oscilaciones de neutrinos han sido confirmadas por los resultados de multitud de experimentos durante las pasadas décadas, los cuales han proporcionado medidas de los valores de los parámetros de oscilación mediante el estudio de neutrinos atmosféricos, solares y procedentes de reactores y aceleradores. Entre ellos, los experimentos de aceleradores a larga distancia que tienen acceso a oscilaciones de neutrinos en los tres sabores, son especialmente importantes, ya que pueden proporcionar medidas de los parámetros de oscilación atmosféricos θ_{23} y Δm_{32}^2 , así como estimar el ángulo de mezcla θ_{13} . Además, tras la reciente confirmación de que $\theta_{13} \neq 0$ por los experimentos con antineutrinos producidos en reactores nucleares, es posible investigar la violación de CP en el sector leptónico midiendo la fase δ_{CP} en los experimentos de oscilaciones de larga distancia, entre los cuales el experimento T2K ocupa una posición destacada.

El experimento T2K (Tokai-to-Kamioka) en Japón es un experimento de oscilaciones de neutrinos de larga distancia y el primero de esta clase en usar una configuración *fuera del eje* (off-axis), en la cual la dirección del haz de neutrinos forma un ángulo de 2.5° con respecto a la dirección hacia el detector lejano. T2K utiliza un haz de neutrinos muónicos de gran pureza, producido mediante la desintegración de las partículas secundarias (esencialmente piones y kaones) originadas en las interacciones con el blanco de grafito del haz de protones de 30 GeV generado en el Japan Proton Accelerator Research Complex (J-PARC) en Tokai. Mediante su configuración *fuera del eje*, la energía del haz de neutrinos se ajusta al máximo de la probabilidad de oscilación ($\sim 600\text{MeV}$ para la distancia de T2K), realzando de este modo el canal de interacción de corriente cargada cuasielástico (CCQE) y reduciendo los canales que contribuyen al ruido de fondo.

El detector lejano del experimento T2K es Super-Kamiokande (SK), un detector Čerenkov de 50 kilotoneladas de agua situado a 1 km de profundidad en la mina Kamioka, capaz de detectar los eventos candidatos a interacciones de neutrinos procedentes de su haz y de distinguir con gran eficiencia los eventos producidos por ν_μ y ν_e . Comparando estos eventos con la composición inicial del haz se puede determinar la fracción de neutrinos que han oscilado tras atravesar los 295 km de corteza terrestre que separan la fuente de neutrinos y el detector

lejano. Para ello es necesario caracterizar con precisión el haz de neutrinos antes de oscilar, estudio que se realiza mediante un complejo de detectores cercanos, situados a 280 m del blanco, que se divide en un detector sobre el eje, INGRID, el cual monitoriza la dirección e intensidad del haz de neutrinos diariamente; y un detector situado fuera del eje (en la dirección hacia SK), ND280, que proporciona medidas de la probabilidad de los diferentes modos de interacción y mide el espectro energético y la composición en sabor del haz de neutrinos, y cuyos datos sirven para reducir algunos de los errores sistemáticos en los análisis de oscilaciones. La descripción del experimento T2K y sus detectores se encuentra en el Capítulo 3.

El experimento T2K realiza dos tipos de análisis de oscilaciones: análisis de desaparición de neutrinos muónicos, mediante el cual se miden los parámetros de oscilación atmosféricos θ_{23} y Δm_{32}^2 ; y análisis de aparición de neutrinos electrónicos, que proporciona medidas del ángulo θ_{13} y de la fase δ_{CP} . T2K comenzó a tomar datos en enero de 2010 y desde entonces se han acumulado 6.57×10^{20} protones en el blanco (POT) y se han observado en SK 120 eventos candidatos a interacciones de ν_μ y 28 de ν_e . Con estos datos, que suponen tan solo un $\sim 8\%$ de la estadística final esperada, T2K ha obtenido la medida más precisa del ángulo θ_{23} y la más sólida evidencia de aparición de ν_e 's en un haz de ν_μ 's hasta la fecha.

Para llevar a cabo estos análisis es necesario simular detalladamente el flujo de neutrinos y las interacciones de estos en los diferentes detectores, usando datos externos para ajustar los modelos y reducir las incertidumbres iniciales. Aplicando el análisis de los datos del detector cercano, se reducen de manera significativa las incertidumbres estimadas relacionadas con el flujo en el detector lejano y algunas secciones eficaces que son comunes para los detectores cercano y lejano. Por otro lado, los errores sistemáticos debidos a las eficiencias en la selección de eventos en SK son estudiados mediante muestras de control de neutrinos atmosféricos, muones procedentes de rayos cósmicos y electrones asociados a su desintegración. Estas predicciones y medidas necesarias para realizar los análisis de oscilación se describen en el Capítulo 4.

Por lo general, los experimentos de oscilaciones de neutrinos realizan análisis independientes de desaparición de ν_μ 's y de aparición de ν_e 's, en los cuales se fijan los valores de los parámetros de oscilación que no se miden directamente en cada caso. Sin embargo, se ha demostrado que un cambio en los valores de estos parámetros fijos puede afectar de forma significativa los resultados obtenidos para los parámetros de oscilación medidos. Por lo tanto, es necesario desarrollar un nuevo tipo de análisis de oscilaciones que incluya correctamente todas las interdependencias entre los parámetros de oscilación: un análisis *conjunto* de oscilaciones de los tres sabores de neutrinos, combinando los canales de desaparición de ν_μ 's y de aparición de ν_e 's.

En esta tesis se presenta el primer análisis *conjunto* de oscilaciones de los tres sabores de neutrinos llevado a cabo por el experimento T2K, basado en técnicas

estadísticas frequentistas¹. Este análisis determina de forma simultánea los parámetros de oscilación Δm_{32}^2 , $\sin^2 \theta_{23}$, $\sin^2 \theta_{13}$ y δ_{CP} ² empleando un modelo de oscilaciones de tres neutrinos en materia (asumiendo densidad de materia constante).

Este análisis se describe a lo largo del Capítulo 5, comenzando con una visión general del proceso seguido para realizar los análisis de oscilación en la Sección 5.2. El modelo de oscilaciones de tres neutrinos en materia empleado se describe en la Sección 5.3, y en las Secciones 5.4 y 5.5 se explican respectivamente el cálculo de la predicción en SK y los errores sistemáticos considerados. Detalles sobre los métodos utilizados para hallar los valores de los parámetros de oscilación que producen el mejor ajuste a los datos y para construir los contornos en los diferentes espacios de parámetros se incluyen en la Sección 5.6.

En la Sección 5.7.1 se presentan los resultados de este primer análisis de oscilación *conjunto* realizado por el experimento T2K, ajustando los datos correspondientes a un total de 6.57×10^{20} POT. Los valores de los parámetros de oscilación para los cuales se obtiene el mejor ajuste a los datos son los siguientes, asumiendo jerarquía de masas normal (invertida):

$$\begin{aligned}\Delta m_{32}^2 (\Delta m_{13}^2) &= 2.51_{-0.12}^{+0.11} (2.49_{-0.12}^{+0.12}) \times 10^{-3} eV^2/c^4, \\ \sin^2 \theta_{23} &= 0.524_{-0.059}^{+0.057} (0.523_{-0.065}^{+0.055}), \\ \sin^2 \theta_{13} &= 0.042_{-0.021}^{+0.013} (0.049_{-0.021}^{+0.015}) \\ \delta_{CP} &= 1.91_{-5.05}^{+1.23} (1.01_{-4.15}^{+2.14})\end{aligned}\tag{2}$$

Recientemente, experimentos con antineutrinos electrónicos producidos en reactores nucleares han obtenido una medida muy precisa del ángulo θ_{13} . El ajuste a los datos de T2K se ha llevado a cabo también en combinación con la medida de $\sin^2 \theta_{13}$ proporcionada por estos experimentos, y los resultados obtenidos se presentan en la Sección 5.7.2. Cabe destacar que, aplicando la restricción para el ángulo θ_{13} obtenida por los experimentos con reactores, T2K ha obtenido la primera estimación del valor de la fase δ_{CP} , siendo el valor que mejor ajusta los datos de T2K consistente con $-\pi/2$, y las regiones excluidas al 90% CL:

$$\begin{aligned}[0.146, 0.825] \pi &\text{ para jerarquía de masas normal} \\ [-0.080, 1.091] \pi &\text{ para jerarquía de masas invertida}\end{aligned}$$

¹En paralelo se ha llevado a cabo también un análisis bayesiano dentro del experimento T2K.

²Tras comprobar que el efecto en los resultados al introducir los parámetros de oscilación solares θ_{12} y Δm_{21}^2 en el ajuste a los datos es despreciable, sus valores se han mantenido fijos a lo largo del análisis.

Al final del Capítulo 5 se incluye una pequeña introducción a futuras mejoras de este análisis, mientras que el Capítulo 6 describe los estudios de sensibilidad del experimento T2K, por ejemplo a establecer que $\sin \delta_{CP} \neq 0$, la cual puede mejorar notablemente en combinación con otros experimentos futuros. Finalmente, las conclusiones se presentan en el Capítulo 7.

Además se han incluido una serie de apéndices al final de este documento. En primer lugar, en el Apéndice A se presentan los últimos resultados de los análisis de oscilación independientes realizados con los datos más recientes del experimento T2K. Después, en el Apéndice B se resumen los estudios realizados para investigar el efecto producido por los parámetros de oscilación solares cuando estos son incluidos en el análisis. Los Apéndices C y D detallan los estudios de validación realizados para el análisis de oscilación *conjunto* presentado en esta tesis. Y finalmente el Apéndice E muestra la diferencia entre los valores de $\sin^2 \theta_{23}$ correspondientes a mezcla máxima y máxima desaparición de ν_μ .

Chapter 1

Introduction

Particle physics is the branch of physics that seeks to understand the laws organizing the fundamental constituents of matter. Among them, neutrinos, neutral weakly-interacting fundamental particles of spin 1/2, are continuously forcing to revisit the existing knowledge on elementary particles due to their extraordinary nature.

The existence of the neutrino had to be postulated in 1930 by Wolfgang Pauli in order to explain β -decay processes, in which the energy spectrum of the emitted electron suggested the presence of another undetected neutral particle. Some years later, Hans Bethe and Rudolf Peierls showed that the probability of the neutrino to interact with a nucleus was tiny. Thus, neutrinos were long believed undetectable, until Frederick Reines and Clyde Cowan observed them in 1956 through inverse β -decay in an experiment detecting antineutrinos produced in nuclear reactors.

Since then, different experiments have studied this particle, with some of them obtaining unexpected results. The Sun and the atmosphere are abundant natural sources of neutrinos, and experiments were devoted to measure their fluxes, observing in both cases a deficit with respect to the prediction from theoretical models. This was known as the solar and atmospheric neutrino anomalies, which needed decades of experimental research to finally be explained in terms of a new process called neutrino oscillations, which describes the change of flavour occurring to neutrinos after travelling some distance.

Neutrino oscillations are a consequence of the existence of neutrino flavour mixing, since the neutrino flavour or interaction eigenstates do not correspond to the mass or propagation eigenstates, but to a linear combination of them described by a unitary mixing matrix. In the three active neutrino paradigm, a standard parameterization of this mixing matrix is expressed in terms of three mixing angles (θ_{12} , θ_{13} , θ_{23}) and the Dirac CP-violating phase δ_{CP} (plus two more phases if neutrinos are Majorana particles). This phenomenon implies that neutrino masses must be non-zero, requiring an extension or modification of the Standard Model

of particle physics, in which neutrinos were assumed to be massless. Neutrino oscillations are sensitive to the mass-squared splittings Δm_{21}^2 y Δm_{32}^2 (where $\Delta m_{ij}^2 = m_i^2 - m_j^2$), but not directly to the masses, only accessible through cosmological measurements, β decays and neutrinoless double β decays. Despite the certainty that neutrinos are massive particles, the origin of their masses is still unknown, as it is their mixing (the exact values of the oscillation parameters) and even the number of neutrino species. Some notions about neutrino physics and the theoretical framework for the three active neutrino paradigm are presented in Chapter 2.

A multitude of experiments have obtained compelling evidence of neutrino oscillations in the past decades, and have constrained the values of the oscillation parameters through the study of atmospheric, solar, reactor and accelerator neutrinos. Among them, long-baseline neutrino experiments which have access to 3-flavour neutrino oscillations are specially important, as they can provide measurements of the atmospheric oscillation parameters θ_{23} and Δm_{32}^2 , and estimate the mixing angle θ_{13} as well. Furthermore, after experiments using antineutrinos from nuclear reactors have recently confirmed that $\theta_{13} \neq 0$ and have provided precise measurements of this angle, the search for CP violation in the lepton sector is now attainable by measuring the δ_{CP} phase in long-baseline neutrino experiments like T2K, which occupies a leading position within this context.

The T2K (Tokai-to-Kamioka) experiment, located in Japan, is the first long-baseline neutrino oscillation experiment using an off-axis configuration, with the neutrino beam directed at an angle of 2.5° away from the direction towards the far detector. T2K uses a very pure ν_μ beam produced via the decay of the secondary particles (essentially pions and kaons) originated in the interactions with a graphite target of the 30 GeV proton beam generated at the Japan Proton Accelerator Research Complex (J-PARC) in Tokai. With the off-axis configuration, the energy of the neutrino beam is tuned to the maximum of the $P(\nu_\mu \rightarrow \nu_e)$ oscillation probability at ~ 600 MeV, enhancing the charged current quasi-elastic (CCQE) interaction channel and reducing its backgrounds.

The Super-Kamiokande (SK) water Čerenkov detector, a cylindrical tank filled with 50 ktons of water situated 1 km underground in the Kamioka mine, acts as far detector for the T2K experiment, observing the event candidates from its neutrino beam and efficiently distinguishing the ν_μ and ν_e event candidates. Comparing the number of events observed at SK with the initial composition of the neutrino beam, the fraction of neutrinos that have oscillated after travelling the 295 km separating the target and the far detector can be determined. To achieve this, it is necessary to precisely characterize the neutrino beam before oscillations with a complex of near detectors located 280 m from the target, consisting of an on-axis detector, INGRID, that monitors the neutrino beam direction and intensity; and an off-axis detector, ND280, which measures the energy spectrum and flavour composition

of the neutrino beam, as well as cross sections for several interaction channels, and whose data is used to reduce the systematic errors in the oscillation analyses. A description of the T2K experiment configuration and detectors is presented in Chapter 3.

The T2K experiment is optimized to perform two kind of oscillation analyses: ν_μ disappearance analysis, which provides measurements of the mixing angle θ_{23} and the mass-squared splitting Δm_{32}^2 ; and ν_e appearance analysis, which is sensitive to the angle θ_{13} and the CP-violating phase δ_{CP} . T2K started taking data in January 2010, and since then a total dataset corresponding to 6.57×10^{20} protons on target (POT) have been accumulated, and 120 ν_μ and 28 ν_e event candidates have been observed at SK. With this dataset, corresponding to only $\sim 8\%$ of its goal POT, the world's most accurate value of the angle θ_{23} and the first observation of ν_e appearance from a ν_μ beam have been obtained by the T2K experiment.

In order to perform these oscillation analyses, the neutrino flux and the interactions taking place in the different detectors are simulated in detail, using fits to external datasets to tune their initial models and uncertainties. Some of the estimated errors, the ones accounting for the uncertainties on the far detector flux and some of the cross sections which are common between the near and far detector, are significantly reduced by a fit performed to the near detector data. In addition, systematic uncertainties related to the efficiencies of the SK neutrino event selection and reconstructed energy scale are studied using control samples of atmospheric neutrinos, cosmic-ray muons and their decay electrons. These T2K predictions and measurements, which constitute the necessary inputs for the oscillation analyses, are described in Chapter 4.

In general, neutrino oscillation experiments perform stand-alone ν_μ disappearance and ν_e appearance analyses, fixing the oscillation parameters not directly measured. However, it has been proved that a change in their prior values could affect significantly the results of the oscillation parameters measured. Thus, it is necessary to develop a new kind of analysis that takes into account the interdependencies between the oscillation parameters: a joint 3-flavour oscillation analysis combining the ν_μ disappearance and ν_e appearance channels.

In this thesis, the first T2K frequentist joint 3-flavour oscillation analysis is presented. It consists in a simultaneous fit, in a 3 flavour framework including matter effects (assuming constant density matter), to the reconstructed energy spectra of the ν_μ and ν_e event candidates from the T2K beam at SK, in which the atmospheric squared-mass splitting Δm_{32}^2 (or Δm_{13}^2), the mixing parameters $\sin^2 \theta_{23}$, $\sin^2 \theta_{13}$ and the CP-invariance violating phase δ_{CP} ¹ are simultaneously determined. This analysis finds the best-fit values of the four oscillation parameters by

¹The effect of including the solar parameters Δm_{21}^2 and $\sin^2 \theta_{12}$ in the fit has been studied and it was found to be negligible; therefore, those parameters are fixed to the values $\sin^2 \theta_{12}=0.306$ and $\Delta m_{21}^2 = 7.5 \times 10^{-5}$ eV²/c⁴ from [178] in the analyses.

minimizing the negative log-likelihood ratio computed with the predicted and observed reconstructed energy spectra of both the ν_μ and ν_e event candidates in SK.

This joint 3-flavour oscillation analysis is presented along Chapter 5. Firstly, an overview of the analysis is given in Section 5.2, and the 3-flavour framework including matter effects being used is described in Section 5.3. The key element for this analysis is the construction of the prediction at SK, which is calculated as explained in Section 5.4. Section 5.5 describes the systematic parameters considered in this analysis, related to the efficiency, energy scale, flux, neutrino cross sections, final state and secondary interactions is to be taken into account in the analysis. Then, details about the methods used to find the best-fit estimates of the oscillation parameters and to build confidence regions are presented in Section 5.6.

The results of the first joint 3-flavour oscillation analysis performed with T2K data, specifically on the combined Run 1+2+3+4 dataset, corresponding to an integrated exposure of 6.57×10^{20} POT, are presented in Section 5.7.1 of this thesis. Thereupon, the results of the T2K joint oscillation analysis combined with the measurements of θ_{13} by experiments using electron antineutrinos from nuclear reactors are presented in Section 5.7.2. It is specially remarkable the fact that this combination led to the first hint towards $\delta_{CP} \approx -\pi/2$ and the first constraint on the values of this parameter. A brief introduction to future improvements of this analysis closes Chapter 5.

Then, Chapter 6 summarizes T2K prospects and future sensitivity studies. And finally, the conclusions of this thesis are presented in Chapter 7.

Different appendixes are also added at the end of this document. Firstly, Appendix A presents the latest results of the T2K stand-alone analyses. In Appendix B, the studies performed to investigate the effect of including the solar parameters in the joint oscillation analysis are presented. Appendixes C and D summarize the validation accomplished for the fitter used in the joint oscillation analysis, based on the study of pulls and fake dataset fits respectively. And in Appendix E the difference between the values of $\sin^2 \theta_{23}$ corresponding to maximal mixing and maximal disappearance is explained.

Chapter 2

Three Active Neutrino Paradigm

Neutrinos are one of the most abundant particles in the Universe (a hundred billion neutrinos are crossing a finger nail per second [7]) produced in a wide range of artificial and natural reactions on Earth and beyond, such as β -decays of fission fragments in reactors or nuclear fusion reactions taking place in the Sun. In addition, they are also the most elusive particles: with a tiny mass, no electric charge and interacting only via the weak force. Thus, they were long believed undetectable; but far from that, they were observed and since then their extraordinary nature has forced physicists to revisit the existing knowledge on elementary particles.

2.1 Mysterious Neutrinos

Neutrinos had to be postulated in order to explain β -decay processes. When at the end of the 19th century radioactivity was discovered by Henri Bequerel [8], β -decays were observed as a process by which certain elements transform into different ones producing a flux of β radiation. The charge and mass of this radiation was established by Pierre and Marie Curie and Walter Kaufmann respectively, and the β particles were discovered to be high energetic electrons or positrons. Thus, the process was described with a single particle emitted which should have a fixed energy corresponding to the difference between two nuclear energy levels. But experimental results obtained by James Chadwick in 1914 [9] showed that the energy spectrum of the emitted electrons was continuous rather than discrete, what entailed a violation of the law of conservation of energy. Several theories emerged trying to explain this anomaly, and finally it was necessary to postulate an undetected particle also involved in the process, first called *neutron* by Wolfgang Pauli in his famous letter to the ("Dear radioactive ladies and gentlemen") participants in a conference on radioactivity in 1930. Two years later Chadwick discovered a new massive neutral particle that he also named neutron [10]; although some first con-

fusion appeared, it was clear that the two particles could not be the same. The term *neutrino* (small neutron in Italian) was coined by Enrico Fermi in 1933 in his theory of β -decay [11], which successfully reconciled the proton-neutron model by Werner Heisenberg [12] and Dmitri Iwanenko [13] with Pauli's hypothesis. This theory described the β -decay as a transition of the form (notice that a generic ν is introduced although nowadays it is known that should be $\bar{\nu}_e$):

$$n \rightarrow p + e^- + \nu \quad (2.1)$$

and was able to successfully explain, along with its generalization by George Gamow and Edward Teller [14], all the available beta decay data. In 1934 Hans Bethe and Rudolf Peierls showed that the cross section for the neutrino to interact with a nucleus was of the order of 10^{-44} cm^2 at 2 MeV neutrino energy [15]. Their conclusion was that the neutrino could never be detected.

However, twenty years later, the first direct observation of the neutrino was made by Frederick Reines and Clyde Cowan [16]. They performed an experiment to detect antineutrinos via inverse β -decay:

$$\bar{\nu} + p \rightarrow n + e^+ \quad (2.2)$$

using neutrinos from the nuclear reactors at the Savannah River Site in South Carolina, and a detector consisting of water tanks with dissolved cadmium chloride (CdCl_2) and sandwiched with liquid scintillator layers containing photomultiplier tubes (PMTs). The water in the tanks was acting as target, so that the antineutrinos were interacting with protons, and the neutrons created were detected with the Cadmium, which is a highly effective neutron absorber. To complete the signal, the positrons produced were detected in the scintillator material through the pair of gamma rays that appear when they annihilate with electrons. They accumulated data on about three neutrinos per hour in their detector, and demonstrated that the events observed were actually coming from the nuclear reactors by switching them off and observing the decrease in the rate of events.

About the same time Raymond Davis was trying to detect antineutrinos from a nuclear reactor in Brookhaven [17] through the process:

$$\bar{\nu} + Cl^{37} \rightarrow Ar^{37} + e^- \quad (2.3)$$

Since no evidence of this process was found, his work indicated that neutrinos and antineutrinos were different particles.

That there were more than one neutrino flavour was found shortly afterwards, in 1962, in an experiment performed by Leon Lederman, Melvin Schwartz and Jack Steinberger at the Brookhaven accelerator facility [19]. Protons accelerated to 15 GeV impacted a Beryllium target producing pions that decayed in flight

into muons and neutrinos. A steel shield was placed to absorb all particles except neutrinos. If the neutrinos produced in this process (associated to a muon) were identical to the neutrinos studied in β -decays, then a number of electrons of approximately half of the interactions observed in the spark chamber would be expected. However, only muons were detected in this experiment, demonstrating that two different kind of neutrinos exist. A third neutrino generation, associated to the tau lepton, was discovered much later, in 2001, by the DONUT experiment at Fermilab [20].

Neutrinos, those particles that had to be postulated to solve a problem, had been finally observed, and soon unexpected results started to appear. In the late 1960s Raymond Davis and John Bahcall headed the Homestake experiment [21], the first one to measure the flux of solar neutrinos. Nuclear fusion reactions occurring in the Sun, with four protons fusing into Helium, is an intense source of neutrinos. These reactions are modeled with a very detailed simulation of the Sun, the so-called Standard Solar Model (SSM), which resulted in the prediction of the solar neutrino flux by J. Bahcall [22]. Surprisingly, the flux measured through inverse β -decay in Chlorine in the Homestake experiment presented a deficit with respect to this prediction: only a third of the expected neutrinos were measured. This deficit was confirmed at different energy ranges by other radiochemical and water Čerenkov detectors such as GALLEX [23] or Kamiokande [24], and it was called the solar neutrino problem. It was the first evidence of neutrino flavour transitions, controversial until 2001, when the Sudbury Neutrino Observatory (SNO) experiment [25], a heavy water Čerenkov detector able to detect not only the ν_e charged current interactions but also the neutral interactions of any neutrino flavour, measured the total solar neutrino flux and observed that this flux, originally consisting of only ν_e , contained ν_μ and ν_τ as well.

Already in 1958 Bruno Pontecorvo suggested that neutrinos could be massive and that oscillations between neutrinos and antineutrinos could take place [26], in analogy with the neutral kaon system. Neutrino oscillations were found to be the explanation for another puzzle: the atmospheric neutrino anomaly. Atmospheric neutrinos are produced in the atmosphere by cosmic rays that interact with air molecules producing mainly showers of pions that subsequently decay to muon neutrinos and muons. The later can decay in flight and produce more muon neutrinos along with electron neutrinos. Thus, muon and electron neutrinos are produced in approximately a ratio 2:1. In 1998 the Super-Kamiokande (SK) water Čerenkov detector (able to distinguish muon and electron events and measure the direction of the outgoing lepton), found that the number of electron neutrino (ν_e) events was in good agreement with predictions, while a deficit in the number of muon neutrino (ν_μ) events was observed depending on the zenith angle [27]. This deficit could not be understood in terms of interactions with Earth, since then a similar asymmetry would have appeared for electron neutrinos and no deficit or excess was

observed. Therefore, the only explanation was that muon neutrinos had oscillated into a different neutrino type.

In order to be explained, the anomalies found in different neutrino experiments required neutrino flavour oscillations, and this phenomenon requires in turn that neutrinos must be massive, implying physics beyond the Standard Model, the most successful model conceived to describe elementary particles in which, however, neutrinos are assumed to be massless particles.

2.2 The Standard Model Neutrino

The construction and validation of the Standard Model (SM) of particle physics [28, 29, 30], theory encompassing the electroweak with the quantum chromodynamics theories, is undoubtedly one of the greatest achievements in twentieth-century science. This theory is based on the gauge group

$$G_{SM} = SU(3)_C \times SU(2)_L \times U(1)_Y \quad (2.4)$$

(where $SU(3)$ belongs to the color group of quantum chromodynamics, $SU(2)$ to the weak isospin and $U(1)$ to the hypercharge), which is spontaneously broken to the subgroup $SU(3)_C \times U(1)_{EM}$ by the vacuum expectation value (VEV) of a Higgs doublet field [31, 32, 33].

The SM describes the electromagnetic, weak and strong interactions within the exchange of spin-1 gauge fields: massless gauge fields in the electromagnetic (photon) and strong (8 gluons) interactions, and three massive gauge bosons in the weak interaction (W^\pm, Z^0).

The matter content in the SM is organized in three families:

$$\begin{bmatrix} \nu_l & q_u \\ l^- & q_d \end{bmatrix} \quad (2.5)$$

which are equivalent in terms of gauge interaction as they only differ in mass and flavour:

$$\begin{bmatrix} \nu_e & u \\ e^- & d' \end{bmatrix} \begin{bmatrix} \nu_\mu & c \\ \mu^- & s' \end{bmatrix} \begin{bmatrix} \nu_\tau & t \\ \tau^- & b' \end{bmatrix} \quad (2.6)$$

Each generation consists of five different representations of the gauge group:

$$(1, 2, -\frac{1}{2}), (3, 2, -\frac{1}{6}), (1, 1, -1), (3, 1, \frac{2}{3}), (3, 1, -\frac{1}{3})$$

where the numbers indicate the corresponding charges under the gauge group in Eq. 2.4, so that for instance leptons are colorless ($C = 1$), whereas three types of color charge are associated to quarks ($C = 3$). Table 2.1 presents a summary of the fermions of the SM and their quantum numbers.

$L_L(1, 2, -\frac{1}{2})$	$Q_L(3, 2, \frac{1}{6})$	$E_R(1, 1, -1)$	$U_R(3, 1, \frac{2}{3})$	$D_R(3, 1, -\frac{1}{3})$
$\begin{pmatrix} \nu_e \\ e \\ \nu_\mu \\ \mu \\ \nu_\tau \\ \tau \end{pmatrix}_L$	$\begin{pmatrix} u \\ d \\ c \\ s \\ t \\ b \end{pmatrix}_L$	e_R	u_R	d_R
		μ_R	c_R	s_R
		τ_R	t_R	b_R

Table 2.1: Standard Model fermions and their quantum numbers indicating the corresponding charges under the gauge group in Eq. 2.4.

As shown in Tab. 2.1, the elementary particles are arranged in the SM in doublets for left-handed fields (first two columns on the left) and singlets for right-handed fields (rest of columns). In addition, only left-handed fields carry the $SU(2)_L$ charge. Here, left-handed denotes the negative chirality component (eigenstate of the chiral projector P_L , indicated by the subscript L) and right-handed the positive chirality (eigenstate of the chiral projector P_R , indicated by the subscript R) of the fermion field [33]:

$$\psi = \psi_R + \psi_L = P_R \psi + P_L \psi = \left(\frac{1 + \gamma_5}{2} \right) \psi + \left(\frac{1 - \gamma_5}{2} \right) \psi \quad (2.7)$$

Neutrinos introduced in Tab. 2.1, appearing in the lepton doublets with charges $(1, 2, -\frac{1}{2})$, are called *active neutrinos*. These are fermions electrically neutral and colorless, as they are singlets of $SU(3)_C \times U(1)_{EM}$, and therefore they do not interact neither electromagnetically nor strongly. Thus, neutrinos can only interact via weak interaction. Two types of weak interaction exist:

- **Charged-current (CC) interactions**, mediated by charged W^\pm bosons that couple neutrinos and charged leptons, for instance:

$$\begin{aligned} \nu_l + d &\rightarrow l^- + u \\ \bar{\nu}_l + u &\rightarrow l^+ + d \end{aligned} \quad (2.8)$$

- **Neutral-current (NC) interactions**, mediated by the neutral Z^0 boson that couples neutrinos to themselves:

$$\begin{aligned} \nu_l + q &\rightarrow \nu_l + q \\ \nu_l + l' &\rightarrow \nu_l + l' \end{aligned} \quad (2.9)$$

The number of left-handed neutrinos can be calculated through the $Z^0 \rightarrow \nu_a \bar{\nu}_a$ decay, whose width has been very precisely measured at the LEP experiments, discarding any other number of *active* neutrino families but three [34]: $N_\nu = 2.984 \pm 0.008$. If more neutrinos exist, they must not have any gauge interaction within the SM, being therefore singlets of the complete SM gauge group with charges (1,1,0). Whether such neutrinos, known as *sterile* neutrinos, exist or not is one of the open questions in neutrino physics.

Concerning the mass, neutrinos are massless in the SM theory. A mass term for fermions of the form

$$-L_m = m \bar{\psi} \psi = m(\bar{\psi}_L \psi_R + \bar{\psi}_R \psi_L) \quad (2.10)$$

is forbidden since it is not gauge invariant as it breaks $SU(2) \times U(1)$. For the charged leptons and quarks, Dirac masses are provided by the Higgs mechanism, coupling right-handed singlets and left-handed doublets via the Yukawa couplings:

$$\begin{aligned} -L_{Yukawa} &= Y_{ij} \bar{\psi}_{Li} \phi \psi_{Rj} + h.c. \\ &= Y_{ij}^d \bar{Q}_{Li} \phi d_{Rj} + Y_{ij}^u \bar{Q}_{Li} \tilde{\phi} u_{Rj} + Y_{ij}^l \bar{L}_{Li} \phi l_{Rj} + h.c. \end{aligned} \quad (2.11)$$

where ψ is the fermion field, ϕ is the scalar Higgs doublet, $\tilde{\phi} = i\tau_2 \phi^*$, Y is a complex 3×3 matrix of Yukawa couplings and L_L , Q_L , l_R etc are the leptonic and quark doublets and singlets.

After spontaneous symmetry breaking, the Yukawa coupling leads to a mass term of the form:

$$m_l \bar{l}_L l_R + m_q \bar{q}_L \bar{q}_R \quad (2.12)$$

where the fermion mass is given by:

$$m_{ij}^f = Y_{ij}^f \frac{v}{\sqrt{2}} \quad (2.13)$$

with v the vacuum expectation value of the Higgs field. For charged leptons, the masses take the form $m_\alpha = \frac{Y_\alpha^L v}{\sqrt{2}}$ with unknown coefficients Y_α^L , so that their masses are not predicted by the SM theory and are to be determined by experimental measurements.

Since the right-handed singlets for neutrinos are absent in the SM, a mass term from the Yukawa interactions can not be introduced for them within this theory. Neutrino masses arising from loop corrections are also forbidden because of total lepton number conservation (global symmetry of the model) [32]. Therefore, there is no way to construct a renormalizable mass term for neutrinos in the SM.

In addition, since in the SM only left-handed fields carry charge and neutrinos are assumed to be massless, they are postulated to be Weyl fermions. As described

by Hermann Weyl's theory [35], neutrinos are left-handed particles and their anti-particles, the antineutrinos, are right-handed. Thus, neutrinos and antineutrinos are distinct in this model.

Therefore, neutrinos in the Standard Model are purely left-handed and massless particles, antineutrinos are distinct from neutrinos and they are right-handed, and only three different neutrino flavours exist along with the three families of charged leptons. Conversely, experimental results are in clear discrepancy with the massless nature of neutrinos: even though experiments have given only an upper limit of neutrino masses so far and no direct measurements exist yet, the observation of the phenomenon of neutrino oscillations, evidenced by different experiments, is an indirect proof that neutrinos must have non-zero masses. Hence, the minimal SM is to be extended or abandoned, in order to accommodate neutrino masses.

2.3 Massive Neutrinos

The compelling experimental evidence for neutrino oscillations imply that neutrinos are massive. However, neutrino oscillation experiments can not probe the absolute values of the neutrino masses, since they are only sensitive to mass-squared splittings $\Delta m_{ij}^2 = m_i^2 - m_j^2$. In addition, the ordering of the masses is still unknown, with two possible representations still viable according to data, which are called normal and inverted mass hierarchies and are illustrated in Fig. 2.1.

The absolute value of the lightest neutrino mass is accessible via beta decay experiments, neutrinoless double beta decay searches and cosmological observations¹. Neutrinoless double beta decay ($0\nu\beta\beta$) searches can shed light on the nature of the neutrino, as experimental evidence of this process would establish that neutrinos are Majorana particles, i.e. their own antiparticles [18], and provide information on the absolute neutrino mass scale. Beta decay experiments can probe the absolute neutrino mass by using the shape of the endpoint of the beta decay spectra, which is independent of the Dirac or Majorana nature of the neutrino and the nuclear matrix element calculations. The most stringent bounds to date are provided by the measurement of tritium beta decay (${}^3\text{H} \rightarrow {}^3\text{He}^+ e^- \bar{\nu}_e$), providing a limit of the effective mass $m_\beta = \sqrt{\sum_i |U_{ei}|^2 m_i^2}$ which is, at the 95% CL, $m_\beta < 2.0\text{eV}$ [36, 37, 38]. This limit will be updated with future data from experiments like KATRIN [37, 39]. In addition, limits on the sum of the neutrino masses $\sum m_\nu = m_1 + m_2 + m_3$ can be found with cosmological observables like the rate of expansion of the Universe or cosmological perturbations [40]. For

¹Cosmological observations can probe the sum of the neutrino masses, from which the mass of the lightest neutrino mass can be obtained in combination with the measurements of the mass-squared splittings Δm_{21}^2 and Δm_{32}^2 .

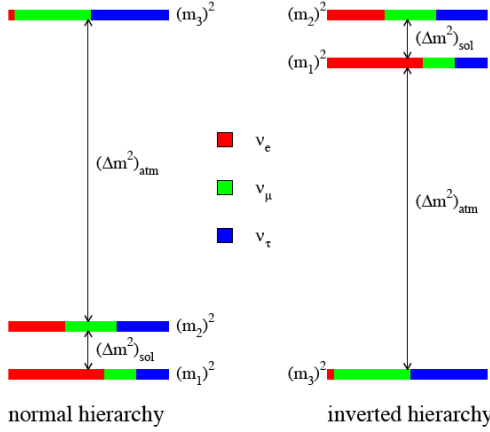


Figure 2.1: Drawing of the normal and inverted neutrino mass hierarchies, showing the fractions of flavour eigenstates in each mass eigenstate, indicated by colours, that nearly fit the current neutrino data with fixed values of the oscillation parameters. Figure from [64].

instance, measurements of cosmic microwave background (CMB) anisotropies are particularly noticeable, with the highest precision observations made by the Planck satellite [41, 42], which obtained a limit based on CMB temperature and lensing-potential power spectra measurements, and the WMAP satellites, whose data included temperature and polarization measurements of the CMB [43, 44]. The combination of the latest CMB datasets with baryon acoustic oscillation (BAO) surveys results in a limit of about 0.2 eV for the sum of the neutrino masses [45].

Although neutrinos are demonstrated to be massive, their mass is tiny compared to the mass of other fermions in the SM, at least six orders of magnitude smaller than the electron mass. The reason for this different neutrino mass scale is still unknown. Furthermore, the fact that they are massive and the consequent extension of the SM to accommodate their masses opens the question whether neutrinos are Dirac or Majorana fermions.

2.3.1 Dirac and Majorana Masses

Massive fermions can be either Dirac or Majorana fermions: only Dirac if they carry electric charge, both possibilities for electrically neutral neutrinos.

The SM can be enlarged in order to build neutrino masses by adding a set of three right-handed neutrino states which should be singlets under the SM gauge group G_{SM} in Eq. 2.4, known as *sterile* neutrinos since they do not participate

in the fundamental interactions (except gravity). Then, masses would be obtained through the vacuum expectation value of the Higgs field (v) as described previously for the rest of fermions, building the analogous Lagrangian (usually referred as *Dirac mass term*):

$$-L_m^D = Y_{ij}^\nu \bar{\nu}_{Li} \phi \nu_{Rj} + h.c. = m_{Di} \bar{\nu}_i \nu_i \quad (2.14)$$

where $\nu = \nu_L + \nu_R$ and $m_{Di} = Y_i^\nu \frac{v}{\sqrt{2}}$. As a consequence of the tiny mass of the neutrino (six orders of magnitude smaller than the electron mass) the Yukawa coupling constants are so small that do not seem plausible, weakening the explanation of neutrino mass with just a Dirac mass term.

Ettore Majorana postulated that for neutral particles, the right-handed state could be identified with the antiparticle of the left-handed state:

$$\nu_R \rightarrow (\nu_L)^c = C \bar{\nu}_L^T = C \gamma_0 \nu_L^*$$

where C is the charge conjugation operator in spinor space. Neutrinos are possible candidates to be Majorana particles since this possibility is compatible with charge conservation. Thus, a Majorana mass term could be written for neutrinos with a structure similar to the Dirac one, building it with neutrino fields with negative chirality:

$$-L_m^{M,L} = \frac{m_L}{2} \overline{(\nu_L)^c} \nu_L + h.c. \quad (2.15)$$

However, this Majorana mass term is forbidden as it violates weak isospin by one unit and requires the existence of a Higgs triplet, and therefore is not allowed by the symmetries of the SM (it could still be possible if generated by New Physics). Nevertheless, if neutrino fields with positive chirality exist independently of the ones with negative chirality, another Majorana mass term can be written:

$$-L_m^{M,R} = \frac{m_R}{2} \overline{(\nu_R)^c} \nu_R + h.c. \quad (2.16)$$

In this case, m_R can be arbitrarily large as it is not connected to a Higgs VEV.

A full mass term can be constructed in matrix form combining the Dirac and Majorana mass terms:

$$-L_m = \frac{1}{2} \left(\begin{array}{cc} \overline{(\nu_L)^c} & \nu_R \end{array} \right) M_\nu \left(\begin{array}{c} \nu_L \\ (\nu_R)^c \end{array} \right) + h.c. \quad (2.17)$$

where

$$M_\nu = \left(\begin{array}{cc} 0 & m_D \\ m_D & m_R \end{array} \right) + h.c. \quad (2.18)$$

Dirac masses obtained are of the form $m_\nu = \lambda_\nu v$, while Majorana masses take the form $m_\nu = \alpha_\nu \frac{v^2}{M}$. If neutrinos are massive Majorana particles, they are their own antiparticles, and the SM total lepton number $L = L_e + L_\mu + L_\tau$ is violated by two units; in addition, a new physics scale M must exist. It is very important to establish whether neutrinos are Majorana particles or not, and to achieve it the rare process of neutrinoless double beta decay ($2\beta0\nu$), which can only occur if neutrinos are Majorana, must be searched for.

2.3.2 The Origin of Neutrino Mass

Different models have appeared trying to understand the mechanism allowing neutrinos to be massive, extending the SM. They can be classified according to whether additional neutral heavy states are introduced or not, or according to the mass scale introduced.

The most popular mechanism is the one known as **seesaw**, based on the exchange of heavy states and divided into different types.

The chiral fields ν_L and ν_R do not have a definite mass due to the off-diagonal Dirac mass elements in the matrix M_ν in Eq. 2.18. However, a unitary matrix V can be used to diagonalize M_ν such that:

$$V^T M_\nu V = \begin{pmatrix} m_1 & 0 \\ 0 & m_2 \end{pmatrix} \quad (2.19)$$

so that the full mass term can be rewritten as:

$$-L_m = \frac{1}{2}(m_1 \overline{(\nu_L)^c} \nu_L + m_2 \overline{(N_L)^c} N_L) + h.c. \quad (2.20)$$

with $N_L = \begin{pmatrix} \nu_L \\ (\nu_R)^c \end{pmatrix}$. Both mass eigenfields ν_L and N_L fulfill the Majorana condition as they coincide with their CP-conjugate fields, so the final Lagrangian is described by Majorana particles.

In the limit when $m_R \gg m_D$ the masses are [46]: $m_1 \approx \frac{m_D^2}{m_R}$ and $m_2 \approx m_R$; thus, there is one heavy state since it is proportional to m_R , and the other one very light as its mass is suppressed by the same value. This is the so-called *seesaw* mechanism that implies that one of the masses tends to be very small, while the other grows, postulating therefore a very heavy neutrino state and a very light one. The three basic *seesaw* models (at tree level) explain the small neutrino masses by the exchange of heavy G_{SM} singlet *right-handed* neutrino (called *seesaw Type-I*), heavy G_{SM} scalar triplet (called *seesaw Type-II*) or fermion triplet (called *seesaw Type-III*) [59].

The seesaw mechanism presented can be easily generalized from one to three neutrino species, yielding the three light *active* neutrinos ν_i and three heavy *sterile* neutrinos N_i [46]. In addition, other types of seesaw are possible (double, inverse...) since many realizations are allowed by this mechanism.

There are other models in which neutrino masses are induced by calculable **radiative corrections**, for instance arising at the two-loop level [47, 48]. Another interesting alternative are the models where **low energy supersymmetry** is the origin of the neutrino mass [49], taking place in a hybrid scenario, with one scale generated at tree level by the mixing of neutrinos and neutralinos and the other by calculable radiative corrections [50].

2.4 Neutrino Mixing and Oscillations

The observation of neutrino oscillations by different experiments, from the early days [25, 27] to present time [5, 6], is the evidence for neutrino masses and mixing, which implies that the mass eigenstates (ν_1, ν_2, ν_3) in which the neutrinos propagate are a combination of the flavour eigenstates $(\nu_e, \nu_\mu, \nu_\tau)$ that participate in the weak interactions.

2.4.1 Neutrino Mixing

The work by Bruno Pontecorvo, Ziro Maki, Masami Nakagawa and Shoichi Sakata stated the neutrino mixing [26, 51], which is described in terms of a mixing matrix, usually called PMNS in their honour.

A unitary matrix U of $n \times n$ dimension (where n is the number of flavour and mass eigenstates) can be built to describe neutrino mixing. In general, such matrix can be parametrized by $n(n-1)/2$ Euler angles and $n(n+1)/2$ phases, but the number of observable parameters must be computed removing from the independent elements of the Yukawa matrices the ones that can be absorbed in field redefinitions [33]. If neutrinos are Dirac particles, only $(n-1)(n-2)/2$ phases are physical parameters, whereas for Majorana neutrinos $n(n-1)/2$ physical phases remain. For three families ($n=3$) only one Dirac phase exists and there are three phases in the Majorana case.

Assuming the following basis for 3 neutrino flavours:

$$\begin{pmatrix} \nu_e \\ \nu_\mu \\ \nu_\tau \end{pmatrix} = \overset{(+) }{U}_{PMNS} \begin{pmatrix} \nu_1 \\ \nu_2 \\ \nu_3 \end{pmatrix} \quad (2.21)$$

a standard parameterization is given by the following PMNS matrix (which takes the form of U for Dirac neutrinos and \bar{U} for Majorana neutrinos):

$$U_{PMNS} = \begin{pmatrix} 1 & 0 & 0 \\ 0 & c_{23} & s_{23} \\ 0 & -s_{23} & c_{23} \end{pmatrix} \begin{pmatrix} c_{13} & 0 & s_{13}e^{-i\delta} \\ 0 & 1 & 0 \\ -s_{13}e^{i\delta} & 0 & c_{13} \end{pmatrix} \begin{pmatrix} c_{12} & s_{12} & 0 \\ -s_{12} & c_{12} & 0 \\ 0 & 0 & 1 \end{pmatrix} \quad (2.22)$$

$$\bar{U}_{PMNS} = U_{PMNS} \begin{pmatrix} 1 & 0 & 0 \\ 0 & e^{i\alpha_1} & 0 \\ 0 & 0 & e^{i\alpha_2} \end{pmatrix} \quad (2.23)$$

where $s_{ij} = \sin(\theta_{ij})$, $c_{ij} = \cos(\theta_{ij})$, representing θ_{ij} a rotation among $|\nu_i\rangle$ and $|\nu_j\rangle$, and $\delta = \delta_{CP}$ is the Dirac CP-violating phase; in the case of Majorana neutrinos, there are three phases: δ_{CP} and the extra phases α_1 and α_2 .

2.4.2 Three-flavour Neutrino Oscillations

Since a flavour eigenstate is described as a linear combination of mass eigenstates, and each mass eigenstate propagates differently in vacuum or matter due to its own phase, the mixing changes while the neutrino propagates, causing that the flavour of the neutrino detected after it has travelled some distance can change with respect to the initial one. This flavour changing process is called neutrino oscillations.

Neutrinos are produced in a defined flavour eigenstate (ν_α), since these are the states that couple to the W^\pm and Z^0 bosons, which is a combination of the mass eigenstates (ν_i) in the form:

$$|\nu_\alpha\rangle = \sum_i U_{\alpha i} |\nu_i\rangle \quad (2.24)$$

This equation can be inverted expressing a mass eigenstate as combination of flavour eigenstates using the complex conjugate of the mixing matrix:

$$|\nu_i\rangle = \sum_\alpha U_{\alpha i}^* |\nu_\alpha\rangle \quad (2.25)$$

In the ν_i rest frame (with τ_i the time in this frame and m_i its rest mass) the state vector obeys the Schrödinger equation, whose solution is²:

$$|\nu_i(\tau_i)\rangle = e^{-im_i\tau_i} |\nu_i(0)\rangle \quad (2.26)$$

By Lorentz invariance, the phase $m_i\tau_i$ can be written in terms of the laboratory frame time t , position L , energy E_i and momentum p_i , such that the mass

²A rigorous treatment should describe neutrino states with wave packets or quantum field theory [52].

eigenstate evolves following (in natural units):

$$|\nu_i(t)\rangle = e^{-i(E_i t - p_i L)} |\nu_i(0)\rangle \quad (2.27)$$

Since neutrinos are highly relativistic and their masses are very small ($m_i \ll E$), the elapsed time can be approximated as the traversed distance ($t \approx L$) and the momentum $p_i = \sqrt{E^2 - m_i^2} \approx E - \frac{m_i^2}{2E}$, and therefore:

$$|\nu_i(t)\rangle = e^{-im_i^2 \frac{L}{2E}} |\nu_i(0)\rangle \quad (2.28)$$

The probability of observing a neutrino in a flavour eigenstate $|\nu_\beta\rangle$ at a certain time t starting from a flavour eigenstate $|\nu_\alpha\rangle$ at $t = 0$ is given by:

$$\begin{aligned} P(\nu_\alpha \rightarrow \nu_\beta) &= |\langle \nu_\alpha(0) | \nu_\beta(t) \rangle|^2 \\ &= \left| \sum_i \langle \nu_i(0) | U_{\alpha i}^* \sum_j U_{\beta j} e^{-im_j^2 \frac{L}{2E}} |\nu_j(0)\rangle \right|^2 \\ &= \left| \sum_i U_{\alpha i}^* e^{-im_i^2 \frac{L}{2E}} U_{\beta i} \right|^2 \end{aligned} \quad (2.29)$$

The Majorana phases are not included in the calculation of the oscillation probabilities, so the matrix U in the previous equation is simply the one in Eq. 2.22.

Using unitarity of the mixing matrix, a general expression for the oscillation probability can be given in terms of the elements of the PMNS matrix as:

$$\begin{aligned} P(\nu_\alpha \rightarrow \nu_\beta) &= \delta_{\alpha\beta} - 4 \sum_{i>j} \Re \left[U_{\alpha i}^* U_{\beta i} U_{\alpha j} U_{\beta j}^* \right] \sin^2 \left(\frac{\Delta m_{ij}^2 L}{4E} \right) \\ &\quad + 2 \sum_{i>j} \Im \left[U_{\alpha i}^* U_{\beta i} U_{\alpha j} U_{\beta j}^* \right] \sin \left(\frac{\Delta m_{ij}^2 L}{2E} \right) \end{aligned} \quad (2.30)$$

where the probability is expressed in terms of the mass-squared splitting parameters $\Delta m_{ij}^2 = m_i^2 - m_j^2$, depending on the difference between neutrino masses but not on individual masses themselves. The name of neutrino oscillations arises from the fact that this probability involves sinusoidal functions and follows a sinusoidal with the distance. For antineutrinos, the complex conjugate of the mixing matrix 2.22 must be used $U \rightarrow U^*$. Conservation of CP means that neutrinos and anti-neutrinos follow the same physical process and therefore requires that $U = U^*$, which is only possible if the matrix U in 2.22 is real (in other words, $\sin \delta = 0$). Thus, as expressed in 2.30, the oscillation probability can be divided into a term involving $\cos \delta$ (the second term), which it is the CP-conserving part, and a term involving $\sin \delta$ (the third term), which is the CP-violating part.

In the case of three neutrinos, the mixing matrix U takes the form:

$$U_{PMNS} = \begin{pmatrix} c_{12}c_{13} & c_{13}s_{12} & s_{13}e^{-i\delta} \\ -c_{23}s_{12} - s_{13}s_{23}c_{12}e^{i\delta} & c_{12}c_{23} - s_{12}s_{13}s_{23}e^{i\delta} & c_{13}s_{23} \\ s_{12}s_{23} - s_{13}c_{12}c_{23}e^{i\delta} & -s_{23}c_{12} - s_{12}c_{23}s_{13}e^{i\delta} & c_{13}c_{23} \end{pmatrix} \quad (2.31)$$

where $c_{ij} = \cos \theta_{ij}$ and $s_{ij} = \sin \theta_{ij}$.

The 3-flavour ν_μ -survival probability can be written as:

$$\begin{aligned} P(\nu_\mu \rightarrow \nu_\mu) &= 1 - 4|U_{\mu 2}|^2|U_{\mu 1}|^2 \sin^2 \left(\frac{\Delta m_{21}^2 L}{4E} \right) \\ &\quad - 4|U_{\mu 3}|^2|U_{\mu 1}|^2 \sin^2 \left(\frac{\Delta m_{31}^2 L}{4E} \right) \\ &\quad - 4|U_{\mu 3}|^2|U_{\mu 2}|^2 \sin^2 \left(\frac{\Delta m_{32}^2 L}{4E} \right) \end{aligned} \quad (2.32)$$

where from equation 2.31 the PMNS matrix elements are

$$\begin{aligned} |U_{\mu 1}|^2 &= s_{12}^2 c_{23}^2 + s_{13}^2 s_{23}^2 c_{12}^2 + 2s_{12}s_{13}s_{23}c_{12}c_{23}\cos(\delta) \\ |U_{\mu 2}|^2 &= c_{12}^2 c_{23}^2 + s_{13}^2 s_{23}^2 s_{12}^2 - 2s_{12}s_{13}s_{23}c_{12}c_{23}\cos(\delta) \\ |U_{\mu 3}|^2 &= s_{23}^2 c_{13}^2 \end{aligned} \quad (2.33)$$

The general expression is therefore found by substituting 2.33 in 2.32. A simplification can be made neglecting Δm_{21}^2 , and therefore setting $\Delta m_{32}^2 \approx \Delta m_{31}^2$, so that the third terms in $|U_{\mu 1}|^2$ and $|U_{\mu 2}|^2$ cancel each other:

$$\begin{aligned} P(\nu_\mu \rightarrow \nu_\mu) &\approx 1 - 4 \sin^2 \left(\frac{\Delta m_{32}^2 L}{4E} \right) c_{13}^2 s_{23}^2 [s_{12}^2 c_{23}^2 + c_{12}^2 s_{13}^2 s_{23}^2 + c_{12}^2 c_{23}^2 + s_{12}^2 s_{13}^2 s_{23}^2] \\ &\approx 1 - 4 \sin^2 \left(\frac{\Delta m_{32}^2 L}{4E} \right) c_{13}^2 s_{23}^2 (s_{12}^2 + c_{12}^2) [c_{23}^2 + s_{13}^2 s_{23}^2] \\ &\approx 1 - 4 \sin^2 \left(\frac{\Delta m_{32}^2 L}{4E} \right) c_{13}^2 s_{23}^2 [c_{23}^2 + s_{13}^2 s_{23}^2] \end{aligned} \quad (2.34)$$

This is a useful expression to identify the leading term of the ν_μ survival probability and its dependencies with the oscillation parameters. It can be further approximated, and it is usually written as just its leading term (assuming a small value of θ_{13}):

$$P(\nu_\mu \rightarrow \nu_\mu) \approx 1 - \sin^2 2\theta_{23} \sin^2 \left(\frac{\Delta m_{32}^2 L}{4E} \right) \quad (2.35)$$

Similarly, the approximated leading-order term of the oscillation probability $P(\nu_\mu \rightarrow \nu_e)$ can be written as:

$$P(\nu_\mu \rightarrow \nu_e) \approx \sin^2 2\theta_{13} \sin^2 \theta_{23} \sin^2 \left(\frac{\Delta m_{31}^2 L}{4E} \right) \quad (2.36)$$

As illustrated, the three-flavour neutrino oscillation probabilities are written in terms of six oscillation parameters: three angles θ_{12} , θ_{13} and θ_{23} ; two mass-squared splitting parameters Δm_{21}^2 and $|\Delta m_{32}^2|^3$; and the δ_{CP} phase.

There are three independent two-fold parameter degeneracies inherent to the three-flavour analyses performed in long-baseline neutrino experiments [54]. These degeneracies are produced when different sets of oscillation parameters give the same value of the oscillation probability, and can lead to an eight-fold degeneracy in the determination of the oscillation parameters with a single baseline and neutrino energy in an experiment. They are: the two parameters $(\delta_{CP}, \theta_{13})$, the sign of the atmospheric mass-squared splitting parameter $\text{sign}(\Delta m_{32}^2)$ and the octant for $(\theta_{23}, \pi/2 - \theta_{23})$ (in the most general mixing matrix in Eq. 2.31 the angles are restricted to the first quadrant $0 \leq \theta_{ij} \leq \pi/2$ and any value $0 \leq \delta_{CP} < 2\pi$ is allowed for the phase). The $(\delta_{CP}, \theta_{13})$ ambiguity can be directly observed in the usual confidence regions for this parameter space, like in Fig. 5.3, where clearly different sets of values of the two oscillation parameters give the same oscillation probability and therefore the same result [54]. Another convention is often found in literature [55], where the $(\delta_{CP}, \theta_{13})$ ambiguity refers to the degeneracy remaining when the confidence regions for neutrinos and antineutrinos are combined, since due to the sinusoidal shape of both $P(\nu_\mu \rightarrow \nu_e)$ and $P(\bar{\nu}_\mu \rightarrow \bar{\nu}_e)$, two different values of $(\delta_{CP}, \theta_{13})$ can be a solution when combining both results. Additionally, the sign of Δm_{32}^2 is another degeneracy [56], that leads to the same result for a pair of values $(\delta_{CP}, \theta_{13})$ with $\Delta m_{32}^2 > 0$ (NH) and $(\delta_{CP'}, \theta_{13'})$ with $\Delta m_{32}^2 < 0$ (IH), as can be also observed in the usual ν_e appearance results where best-fit values and confidence regions are presented in both mass hierarchy assumptions with almost no difference between them (see for instance Tab. 5.8). Furthermore, a solution in the first octant for θ_{23} appears together with a mirror solution in the second octant $\pi/2 - \theta_{23}$ [54]. Measurements at multiple baseline lengths and neutrino energies can help to discriminate the different degenerated solutions. Using the appropriate baseline length and neutrino energy and measurements of $P(\nu_\mu \rightarrow \nu_e)$ and $P(\bar{\nu}_\mu \rightarrow \bar{\nu}_e)$ can resolve the $(\delta_{CP}, \theta_{13})$ degeneracy, while a combination with other channels, such as $P(\nu_\mu \rightarrow \nu_\mu)$ or $P(\nu_\mu \rightarrow \nu_\tau)$, is necessary to resolve the θ_{23} octant degeneracy if exists (if θ_{23} deviates from $\pi/4$).

³Alternatively δm^2 and Δm^2 can be used to represent the solar and atmospheric mass-squared differences respectively, sometimes defined as $\Delta m^2 = \Delta m_{FL}^2 \left(m_3^2 - \frac{m_1^2 + m_2^2}{2} \right)$ in literature [53].

Finally, the degeneracy related to the mass hierarchy, due to the sign of Δm_{32}^2 , can be overcome in experiments with large matter effects.

2.4.3 Matter Effects

The previous expressions were built assuming the approximation that neutrinos are propagating in vacuum. However, a more realistic treatment including the effect of the interactions between neutrinos and the matter traversed during their propagation is to be adopted. In general, the matter density is a function of the position that can also depend on time, and this dependence can be significant for certain traversed media like for instance the Sun. Sometimes, however, the density of the traversed medium can be considered roughly piece-wise constant, as it is the case of the Earth mantle and the approximation that will be followed from now on in this work.

The interaction between neutrinos and the traversed matter, through neutral or charged current interactions with electrons, neutrons and protons, modifies the amplitude of their propagation [57] and can be interpreted in terms of effective potentials depending on the density matter. The neutral current interactions between neutrinos and matter have the same amplitude for all flavours, and therefore they produce no observable effect in the neutrino oscillation probabilities⁴, which are however varied due to charged current interactions of electron neutrinos with electrons [58]. The neutrino evolution in matter in terms of neutrino flavour eigenstates can be described by the Schrödinger equation:

$$i \frac{\partial}{\partial t} \begin{pmatrix} \nu_e \\ \nu_\mu \\ \nu_\tau \end{pmatrix} = H \begin{pmatrix} \nu_e \\ \nu_\mu \\ \nu_\tau \end{pmatrix} \quad (2.37)$$

where the Hamiltonian matrix H is given by [59]:

$$H = U \begin{pmatrix} \frac{m_1^2}{2E} & 0 & 0 \\ 0 & \frac{m_2^2}{2E} & 0 \\ 0 & 0 & \frac{m_3^2}{2E} \end{pmatrix} U^\dagger + \begin{pmatrix} V & 0 & 0 \\ 0 & 0 & 0 \\ 0 & 0 & 0 \end{pmatrix} \quad (2.38)$$

representing V the extra matter potential acquired by electron neutrinos in matter due to their coherent forward scattering with electrons. This potential is written, in unpolarized media, as:

$$V = \pm 2E\sqrt{2}G_F N_e \quad (2.39)$$

⁴The contributions from coherent forward neutrino scattering with electrons and protons cancel out assuming that the traversed matter is electrically neutral. The contribution from the scattering with neutrons remains; however, it affects all flavors equally, and is therefore irrelevant for oscillations.

where G_F is the Fermi coupling constant and N_e is the number density of electrons in the medium; the positive sign is used for neutrinos and the negative sign for antineutrinos (notice that the complex conjugate of $U M U^\dagger$ must be used for antineutrinos).

This Hamiltonian can be written, by re-phasing all neutrino flavours by $\exp[-im_1^2x/2E]$, as:

$$H = U \text{ diag} \left(0, \frac{\Delta m_{21}^2}{2E}, \frac{\Delta m_{31}^2}{2E} \right) U^\dagger + \text{ diag}(V, 0, 0) \quad (2.40)$$

and diagonalized by using the effective mixing matrix in matter \tilde{U} :

$$H = \tilde{U} \text{ diag} \left(0, \frac{\Delta \tilde{m}_{21}^2}{2E}, \frac{\Delta \tilde{m}_{31}^2}{2E} \right) \tilde{U}^\dagger \quad (2.41)$$

so that the same number of physical parameters remains and the same treatment as in vacuum can be used by incorporating effective mass-squared splittings and effective mixing angles.

For instance, the oscillation probability of muon neutrino to electron neutrino in vacuum takes the form [60]:

$$\begin{aligned} P(\nu_\mu \rightarrow \nu_e) &= |U_{\mu 1}^* e^{-\frac{i m_1^2 L}{2E}} U_{e 1} + U_{\mu 2}^* e^{-\frac{i m_2^2 L}{2E}} U_{e 2} + U_{\mu 3}^* e^{-\frac{i m_3^2 L}{2E}} U_{e 3}|^2 \\ &= |2U_{\mu 2}^* U_{e 2} \sin \phi_{21} + 2U_{\mu 3}^* U_{e 3} e^{-i \phi_{32}} \sin \phi_{31}|^2 \end{aligned} \quad (2.42)$$

where $\phi_{ij} = \frac{\Delta m_{ij}^2 L}{4E}$. This expression can be rewritten as:

$$\begin{aligned} P(\nu_\mu \rightarrow \nu_e) &\approx |\sin \theta_{23} \sin 2\theta_{13} \sin \phi_{31} e^{-i(\phi_{32} + \delta)} + \cos \theta_{23} \cos \theta_{13} \sin 2\theta_{12} \sin \phi_{21}|^2 \\ &= \sin^2 \theta_{23} \sin^2 2\theta_{13} \sin^2 \phi_{31} + \cos^2 \theta_{23} \cos^2 \theta_{13} \sin^2 2\theta_{12} \sin^2 \phi_{21} \\ &\quad + \sin 2\theta_{23} \sin 2\theta_{12} \sin 2\theta_{13} \cos \theta_{13} \sin \phi_{31} \sin \phi_{21} \cos(\phi_{32} + \delta_{CP}) \end{aligned} \quad (2.43)$$

The same oscillation probability would take the following form, at first order approximation in matter effects and assuming constant density matter:

$$\begin{aligned}
 P(\nu_\mu \rightarrow \nu_e) = & \\
 4c_{13}^2 s_{13}^2 s_{23}^2 \sin^2(\phi_{31}) & \\
 + 4c_{13}^2 s_{13}^2 s_{23}^2 \sin^2(\phi_{31}) \frac{2V}{\Delta m_{31}^2} (1 - 2s_{13}) & \\
 - 8c_{13}^2 s_{13}^2 s_{23}^2 (1 - 2s_{13}^2) \cos(\phi_{32}) \sin(\phi_{31}) \frac{VL}{4E_\nu} & \\
 + 8c_{13}^2 s_{12} s_{13} s_{23} (c_{12} c_{23} \cos(\delta_{cp}) - s_{12} s_{13} s_{23}) \cos(\phi_{23}) \sin(\phi_{31}) \sin(\phi_{21}) & \\
 - 8c_{13}^2 c_{12} c_{23} s_{12} s_{13} s_{23} \sin(\delta_{cp}) \sin(\phi_{32}) \sin(\phi_{31}) \sin(\phi_{21}) & \\
 + 4s_{12}^2 c_{13}^2 (c_{12}^2 c_{23}^2 + s_{12}^2 s_{23}^2 s_{13}^2 - 2c_{12} c_{23} s_{12} s_{23} s_{13} \cos(\delta_{cp})) \sin^2(\phi_{21}) & \\
 \end{aligned} \tag{2.44}$$

For antineutrinos, the change $\delta_{CP} \rightarrow -\delta_{CP}$ must be done, and therefore in Eq. 2.43 when the factor $\cos(\phi_{32} + \delta_{CP})$ is expanded it is clear that there is a part which is CP-conserving, proportional to $\cos \phi_{32} \cos \delta_{CP}$, and one that is CP-violating, proportional to $\sin \phi_{32} \sin \delta_{CP}$. The effect of matter, however, can induce a fake CP-violating effect even if $\sin \delta_{CP} = 0$, as the sign of V will change for antineutrinos producing a difference in the oscillation probability described in Eq. 2.44 for neutrinos and antineutrinos.

In addition, matter effects affect the mixing of neutrino flavour eigenstates such that a resonance enhancement can appear in the oscillation probability, phenomenon usually known as Mikheyev-Smirnov-Wolfenstein (MSW) effect [57, 61]. In the case of two flavour neutrino oscillations, where the effective angle and mass splitting have the simple expressions [33]:

$$\sin^2 2\tilde{\theta} = \frac{(\Delta m^2 \sin 2\theta)^2}{(\Delta m^2 \cos 2\theta \mp 2\sqrt{2}G_F E N_e)^2 + (\Delta m^2 \sin 2\theta)^2} \tag{2.45}$$

$$\Delta\tilde{m}^2 = \sqrt{(\Delta m^2 \cos 2\theta \mp 2\sqrt{2}G_F E N_e)^2 + (\Delta m^2 \sin 2\theta)^2} \tag{2.46}$$

it is very easy to extract that the resonance, leading to maximal probability, that appears when $\sin^2 2\tilde{\theta} = 1$ and $\Delta\tilde{m}^2 = \Delta m^2 \sin 2\theta$, is produced at the neutrino energy $E = \frac{\Delta m^2 \cos 2\theta}{2\sqrt{2}G_F N_e}$. This resonance appears depending on whether neutrinos or antineutrinos are being detected and depending on the sign of the mass-squared splitting. Thus, in order to study the mass hierarchy, experiments with significant matter effects are necessary, with no essential requirement for the resonance enhancement to appear.

2.5 The Flavour Puzzle

According to recent global fits combining results from different experiments [63], neutrino oscillations can be described in terms of three active neutrinos with the

following parameters (assuming normal hierarchy), and their 1σ uncertainty:

$$\begin{aligned}\Delta m_{21}^2 &= 7.54^{+0.26}_{-0.22} \times 10^{-5} \text{ eV}^2/\text{c}^4 & \sin^2 \theta_{12} &= 0.308^{+0.017}_{-0.017} \\ \Delta m_{32}^2 &= 2.43^{+0.06}_{-0.06} \times 10^{-3} \text{ eV}^2/\text{c}^4 & \sin^2 \theta_{23} &= 0.437^{+0.033}_{-0.023} \\ \delta_{CP}/\pi &= 1.39^{+0.38}_{-0.23} & \sin^2 \theta_{13} &= 0.0234^{+0.0020}_{-0.0019}\end{aligned}\quad (2.47)$$

With these values of the oscillation parameters, the absolute values of the mixing PMNS matrix can be calculated:

$$|U_{PMNS}| \approx \begin{pmatrix} 0.822 & 0.548 & 0.153 \\ 0.396 & 0.645 & 0.653 \\ 0.409 & 0.532 & 0.742 \end{pmatrix} \quad (2.48)$$

A similar mixing matrix exist for the quark sector, known as CKM (Cabibbo-Kobayashi-Maskawa) matrix, and it can be written as [178]:

$$|V_{CKM}| \approx \begin{pmatrix} 0.974 & 0.225 & 0.003 \\ 0.225 & 0.973 & 0.04 \\ 0.009 & 0.04 & 0.999 \end{pmatrix} \quad (2.49)$$

Clearly, the two matrices are very different: while the CKM matrix is almost proportional to the identity matrix plus small, hierarchical, off-diagonal matrices, in the PMNS matrix diagonal and off-diagonal elements are of the same order $O(1)$. Several different theoretical models exist attempting to find an organizing principle to explain the lepton mixing and to provide a pattern for neutrinos masses. Some of them try to identify a symmetry applied to either only the lepton sector or to both leptons and quarks, while others plead for anarchy.

Neutrino Mixing Anarchy

Among all the attempts in literature to identify the organizing principle behind U , the anarchic model is still alive and kicking [65]. Neutrino mixing anarchy is the hypothesis that the leptonic mixing matrix U_{PMNS} is completely random as no flavour symmetry is specified, and can be described as the result of a random draw from an unbiased distribution of unitary 3×3 matrices [66, 67]. The model initially proposed in [66] used a numerical Monte Carlo analysis to test how many of the sample matrices (Dirac, Majorana or see-saw) were passing the specific cuts imposed to match the available data: large solar and atmospheric mixings, small ν_e mixing and a large ratio $\Delta m_{23}^2/\Delta m_{12}^2$. This model was later refined [65] applying the Kolmogorov-Smirnov (KS) statistical test to make predictions, and its results seem to favour maximal $\sin^2 \theta_{23}$ and large values of $\sin^2 \theta_{13}$.

Lepton Flavour Symmetries

There are different possible symmetries inspired by the neutrino observations, formulated in the leptonic flavour basis for which the charged lepton mass matrix is diagonal, with the light left-handed neutrino mass matrix distinguishing them [68]. On the one hand, there are models in which the most general neutrino mass matrix exhibits a $\mu - \tau$ symmetry of the form:

$$M_\nu = \begin{pmatrix} a & b & b \\ b & c & d \\ b & d & c \end{pmatrix} \quad (2.50)$$

but soft symmetry breaking corrections are to be introduced in this model in both mass hierarchy assumptions to be experimentally viable.

On the other hand, there are models involving S_3 lepton flavour symmetry in which the most general matrix can be written in terms of only two independent parameters, allowing permutation of three flavours in both rows and columns:

$$M_\nu = \begin{pmatrix} a & b & b \\ b & a & b \\ b & b & a \end{pmatrix} \quad (2.51)$$

The most extended model with this symmetry is the *tribimaximal* mixing [69], which postulates a specific mixing matrix trying to encapsulate the trends of a broad range of experimental data with the form:

$$U = \begin{pmatrix} \sqrt{\frac{2}{3}} & \frac{1}{\sqrt{3}} & 0 \\ -\frac{1}{\sqrt{6}} & \frac{1}{\sqrt{3}} & \frac{1}{\sqrt{2}} \\ -\frac{1}{\sqrt{6}} & \frac{1}{\sqrt{3}} & -\frac{1}{\sqrt{2}} \end{pmatrix} \quad (2.52)$$

The values of the mixing angles and δ phase obtained from this *tribimaximal* mixing matrix are:

$$\begin{aligned} \delta_{CP} &= 0 \\ \sin \theta_{13} &= 0 \rightarrow \theta_{13} = 0 \\ \sin \theta_{12} &= \frac{1}{\sqrt{3}} \rightarrow \theta_{12} \approx 35.3^\circ \\ \sin \theta_{23} &= \frac{1}{\sqrt{2}} \rightarrow \theta_{23} = 45^\circ \end{aligned} \quad (2.53)$$

Thus, the predictions made with this model were close to the experimental measurements, and in principle only small corrections were required, until the last experiments with antineutrinos from reactors measured a large value of the angle θ_{13} that would require huge deviations from this model in order to obtain predictions accordingly.

Other models exist, for instance considering the permutation group S_4 as a discrete flavour symmetry, being the subgroup A_4 of special interest as it is also the smallest discrete subgroup of $SO(3)$ [70].

Grand Unified Models

An alternative and more ambitious approach is to impose a family unification symmetry for quarks and leptons, in which the mass and mixing results for the leptons are highly constrained by the inputs introduced for the quark sector, since the Yukawa couplings are applied to both quark and lepton Dirac mass matrices [68]. These models can be divided in different categories.

First of all there are grand unification models with a high scale $SU(5)$ symmetry where the SM fermions (quarks, leptons and left-handed neutrinos) are unified in 10 and $\bar{5}$ representations (multiplets), while right-handed neutrinos remain gauge singlets [72]. These models have been pursued in the literature and look easily compatible with neutrino data, but they do not give numerical predictions.

Another attractive grand unification symmetry is based on $SO(10)$, where right-handed neutrinos become massive after $SO(10)$ breaks down to the SM gauge group. Many models exist and they differ by the flavour symmetry imposed (if any) and their Higgs representation assignments (separating into Higgs in high rank [73] or low rank representations [74]). In the simplest $SO(10)$ models, the Higgs is entirely contained in the minimal 10 representation, but the predictions obtained are in qualitative contrast with the observed data. Alternatively, the Higgs can be assigned a doublet to non-minimal $SO(10)$ representations, and this model might reproduce the observed fermion masses and mixing, although it is not complete and it is necessary an additional Higgs field to be able to break $SO(10)$ to the SM gauge group.

There are other models based on the E_6 gauge group or $E_8 \otimes E_8$ grand unified models, formulated in five or six dimensions, which are pursued by authors although not firm numerical predictions for the neutrino mixing angles are obtained.

For models based on GUT symmetries, normal mass hierarchy appears naturally and inverted can be also obtained with a type-II see-saw, and large values of the mixing angle θ_{13} are generally predicted. The models based on leptonic symmetries can predict inverted hierarchy and small values of θ_{13} . Thus, in order to discard any of the different models available, precision measurements of the oscillation parameters are necessary, specially of the mixing angles θ_{12} and θ_{13} and the mass hierarchy, with the additional need to precisely measure the deviation of θ_{23} from $\pi/4$ specially if the angle θ_{13} is relatively large, since then models based on GUTs or lepton symmetries are not easily distinguished [68, 75].

2.6 Open Questions and Future Perspectives

Understanding the nature of neutrinos is still a work in progress: there are open questions, and more questions emerging with new measurements. A summary of the known unknowns is given in this section, mentioning only some of the current experiments or proposals, although many others exist. An extensive compilation of current neutrino experiments and proposals, categorized according to the physics questions they are designed to address, and their references can be found in [64].

- **Neutrino oscillation parameters.** Recent measurements obtained by solar, atmospheric, reactor and accelerator experiments are constraining the neutrino oscillation parameters: the solar angle and mass-squared splitting are precisely estimated with data from solar experiments like SNO combined with the KamLAND and Super-Kamiokande experiments; the atmospheric mass-squared splitting is being measured by different experiments like T2K, SK and MINOS; the most accurate values of θ_{23} and θ_{13} are obtained by the T2K experiment and the experiments with antineutrinos from nuclear reactors (Daya Bay, RENO and Double Chooz) respectively. However, still more precise measurements of the oscillation parameters, to be achieved with more data from the current experiments and the future ones, are necessary in order to completely understand the nature of neutrinos, discriminate between theoretical models and answer the remaining questions.
- **Cross section measurements.** One of the major systematic uncertainties in the measurements of the current experiments are the ones related to the neutrino cross sections. Presently, the neutrino interactions are modelled by different neutrino generators like NEUT, GENIE or NuWro, assuming approximations that can change significantly the values of the cross sections obtained with each simulation, therefore producing big uncertainties. Measurements from different experiments like NOMAD, MiniBooNE and MINERvA are currently used to tune the neutrino interaction models. Precise measurements of the neutrino cross sections in different materials such as carbon (main nucleus in scintillators) and water (essential for water Čerenkov detectors), like the ones that the T2K experiment is currently performing, are of huge importance to reduce these systematic uncertainties, and consequently the uncertainty on the neutrino oscillation parameters.
- **Neutrino masses.** Although the mass-squared splittings are measured by different experiments like T2K, Super-Kamiokande or MINOS, the final order of the three masses, whether they follow normal or inverted hierarchy, is still unknown. To determine the mass pattern it is possible to study neutrino oscillations with large matter effects in experiments sensitive to them, like

NO ν A and T2HK (Tokai-to-Hyper-Kamiokande) using matter effects in appearance, and PINGU, ORCA and Hyper-Kamiokande using matter effects in disappearance. The knowledge of the mass hierarchy is important to reduce the number of theoretical models explaining the structure of neutrino masses and mixing, not only acting as discriminator but also revealing information about the origin of neutrino masses. The absolute value of the lightest neutrino mass is also unknown, being its measurement accessible via beta decay experiments, neutrinoless double beta decay searches and cosmological observations. Measurements on the absolute neutrino mass are provided by beta decay experiments, since the shape of the endpoint of the beta decay spectra is the most model-independent observable sensitive to it, with the most stringent bounds provided by studies of tritium beta decay, to be updated with new data from experiments like KATRIN.

- **Dirac or Majorana nature.** Whether neutrinos are Dirac or Majorana fermions is still an open question. Neutrinoless double beta decay ($0\nu\beta\beta$) searches will not only provide information on the absolute neutrino mass scale, but will also shed light on the nature of the neutrino, as experimental evidence of this process would establish that neutrinos are Majorana particles. Several experiments like NEXT, SNO+ or GERDA will be devoted to the search of this process.
- **CP violation in the lepton sector.** Precise measurements of the angle θ_{13} have been recently obtained by experiments using antineutrinos from nuclear reactors and, by constraining θ_{13} with the value measured by them, it is now possible for long-baseline neutrino oscillation experiments to probe the CP-violating phase δ_{CP} . The value of $\sin^2 \theta_{13}$ used as constraint is the averaged result of the measurements provided by three experiments: Daya Bay (China), RENO (Korea) and Double Chooz (France) [76]. The three experiments have found evidence for reactor electron antineutrino disappearance using far detectors at a distance of $O(1km)$ and also near detectors in the case of Daya Bay and RENO, detecting the antineutrinos via the process $\bar{\nu}_e + p \rightarrow e^+ + n$, using detectors with Gd-doped liquid scintillators (LS) to maximize the neutron capture efficiency. The averaged value in [86] was computed with the results from the rate-only analyses performed by the experiments Daya Bay and RENO, in which the number of observed events at the far detector is compared with the $\bar{\nu}_e$ prediction based on the measurements at the near detectors assuming no oscillations; and the results from the Double Chooz experiment analyzing the rate and spectrum of prompt positrons and using inverse β -decay interactions with neutron capture on hydrogen (H-capture) as well. CP violation, which would mean $\sin \delta_{CP} \neq 0$, can be tested in experiments sensitive to the CP-violating term

in the $P(\nu_\mu \rightarrow \nu_e)$ oscillation probability in Eq. 2.44, or directly through measurements of neutrino and antineutrino oscillation probabilities. The T2K experiment results presented in Sec. 5, combined with reactor measurements, have shown the first hints indicating that δ_{CP} is consistent with $-\pi/2$. Although more T2K neutrino and antineutrino data is necessary to confirm this result, whose sensitivity could be enhanced in combination with results from other experiments like NO ν A and latests reactor measurements, this first hint opens exciting possibilities like an indication of *Leptogenesis* [77] as the origin of the baryon asymmetry of the Universe.

- **Sterile neutrinos.** Although a three-flavour paradigm has been presented in this chapter, the current neutrino data allow for very large deviations from it. Anomalies in the results of certain neutrino experiments suggest the existence of more neutrino flavours which are called *sterile* neutrinos, being the most significant example the one by the LSND experiment [78], where electron antineutrinos were observed in a pure muon antineutrino beam and could be interpreted as oscillations with a mass-squared splitting of $\Delta m^2 \approx 1\text{eV}^2$, what would imply the existence of a fourth neutrino. Some experiments are already studying this possibility, like T2K [79] and MINOS [80], and intense work is being developed by theorists and experimentalists pursuing new measurements to probe the existence of these sterile neutrino flavour states [81].
- **New Physics.** In addition to the New Physics that could emerge with the answer of the questions stated above, many more non-standard physics can be studied with neutrinos, like for instance neutrino non-standard interactions and Lorentz-violating neutrino oscillations.

Chapter 3

The T2K Experiment

The T2K (Tokai-to-Kamioka) experiment is a second generation long-baseline neutrino oscillation experiment located in Japan [82]. T2K uses a neutrino beam consisting of muon neutrinos with a high purity ($\sim 93\%$ expected [83]), produced via the decay of the secondary particles (essentially pions and kaons) originated in the interactions with a graphite target of a 30 GeV proton beam, which is generated at the Japan Proton Accelerator Research Complex (J-PARC) site in Tokai. A near detector complex located 280 m from the production target provides the measurements of the unoscillated neutrino event rates, and the Super-Kamiokande (SK) detector situated in the Kamioka mine, 295 km away, provides the measurements of the neutrino event rates after oscillations.

T2K is the first long-baseline neutrino oscillation experiment using an off-axis configuration (originally proposed in [84]), with the beam directed at an angle of 2.5° away from the direction towards the far detector (a range between 2° - 2.5° is allowed by the facility design). With this off-axis technique, the peak of the beam energy spectrum is tuned to the maximum of the $P(\nu_\mu \rightarrow \nu_e)$ oscillation probability, at ~ 600 MeV for the T2K baseline of 295 km, enhancing the CCQE interactions and reducing the background contributions from the high energy tail.

The schematic layout of the T2K experiment is presented in Fig. 3.1. The advantages of the off-axis configuration and the main parts and sub-detectors that constitute the T2K experiment will be described in this chapter. The T2K collaboration is formed by about 500 physicists from 59 institutions in 11 countries working together to achieve the results on the different T2K's physic goals.

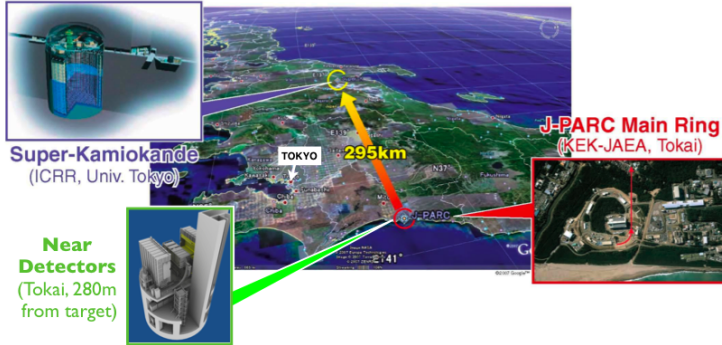


Figure 3.1: Layout of the T2K experiment, showing the position of the J-PARC accelerator complex where the ν_μ beam is produced, the near detectors located at 280 m from the target and the far detector Super-Kamiokande, situated 295 km away. Figure from [85].

3.1 T2K Physics Goals

The T2K experiment is the first long-baseline neutrino oscillation experiment proposed and approved to explicitly look for electron neutrino appearance in a muon neutrino beam. Thus, the main goal of T2K was in principle the measurement of the mixing angle θ_{13} via ν_e appearance analysis, as this parameter affects the leading term of the $P(\nu_\mu \rightarrow \nu_e)$ oscillation probability shown in Eq. 3.1, with a sensitivity to the value of $\sin^2 2\theta_{13}$ down to 0.006 [1, 2, 5].

$$P(\nu_\mu \rightarrow \nu_e) \approx \sin^2 2\theta_{13} \sin^2 \theta_{23} \sin^2 \left(1.267 \frac{\Delta m_{31}^2 L(km)}{E_\nu(GeV)} \right). \quad (3.1)$$

Recently, precise measurements of the mixing angle θ_{13} were obtained by experiments using antineutrinos from nuclear reactors, Daya Bay, RENO and Double Chooz [86], stating that $\theta_{13} \neq 0$. These experiments use a different channel to the one used by the T2K experiment to estimate the mixing angle θ_{13} , as they perform this measurement in antineutrino disappearance. Combining the observed event rates in the T2K experiment with the value of $\sin^2 \theta_{13}$ obtained by the reactor experiments allows to explore in more detail the 3-flavour neutrino paradigm, as probing the Dirac CP-violating phase δ_{CP} becomes accessible. Therefore, once its first physics goal of observing ν_e appearance in a ν_μ beam has been accomplished,

the T2K experiment has the possibility to search for CP violation in the lepton sector, and the first hint has been already obtained on the value of δ_{CP} , whose measurement is nowadays one important physics goal for T2K.

Furthermore, precise measurements of the atmospheric oscillation parameters $\sin^2\theta_{23}$ and Δm_{32}^2 can be achieved via ν_μ disappearance analysis [3, 4, 6] as their values determine the leading term of the survival oscillation probability of the muon neutrino shown in Eq. 3.2. T2K is expected to reach a precision of $\delta(\Delta m_{32}^2) \sim 10^{-4} eV^2/c^4$ and $\delta(\sin^2 2\theta_{23}) \sim 0.01$ with the approved exposure of 7.8×10^{21} POT.

$$P(\nu_\mu \rightarrow \nu_\mu) \approx 1 - \sin^2 2\theta_{23} \sin^2 \left(1.267 \frac{\Delta m_{32}^2 L(km)}{E_\nu(GeV)} \right). \quad (3.2)$$

T2K has published several ν_e appearance and ν_μ disappearance results, the latest ones will be presented in App. A.2 and A.1 respectively.

The T2K joint oscillation analysis, combining the ν_μ disappearance and ν_e appearance channels, and its results constrained by the measurement of the mixing angle θ_{13} by the reactor experiments, can provide information to answer important open questions in neutrino physics. First hints on the value of the δ_{CP} phase, which accounts for possible Charge-Parity (CP) violation in the lepton sector, were already obtained with the latest ν_e appearance analysis combined with the reactor results as it will be shown in Section A.1. This measurement can be improved with the joint oscillation analysis presented in this work as it will be discussed in Section 5.7.2.

In addition, cross section measurements have been performed in the different sub-detectors (ND280 FGDs, INGRID, etc.) of the T2K experiments, for different nuclei, being the first result published the inclusive muon neutrino charged current cross section on Carbon performed in the near detector [87].

Other studies are also being performed at the moment, such as studies on sterile neutrinos via electron neutrino disappearance in the ND280 tracker. Furthermore, with the joint oscillation analysis, T2K will have good sensitivity to the octant for the mixing angle θ_{23} and some sensitivity to the mass hierarchy determination, as it will be presented in Section 6. And, in June 2014, the T2K experiment had its first short run with antineutrino beam.

3.2 T2K Neutrino Beam

Neutrinos in the T2K beam are produced as the decay products of pions and kaons generated in the interaction with a graphite target of the 30 GeV proton beam from

Parameter	Design value	Current value (May 2013)
Beam energy	50 GeV	30 GeV
Beam power	0.75 MW	0.22 MW
Spill interval	3.3 s	2.48 s
Number of protons	3.3×10^{14} /spill	1.2×10^{14} /spill
Number of bunches	8 bunches/spill	8 bunches/spill
Bunch interval	581 ns	581 ns
Bunch width	58 ns	58 ns

Table 3.1: Summary table of design and current values of the T2K beam parameters.

the J-PARC (Japan Proton Accelerator Research Complex) main ring in Tokaimura, in the prefecture of Ibaraki, Japan.

3.2.1 J-PARC Accelerator

The J-PARC accelerator complex is a newly constructed system of three accelerators [88], commissioned in April 2009. It consists of a linear accelerator (LINAC), a rapid-cycling synchrotron (RCS) and the main ring (MR) synchrotron. Firstly, an H^- beam is accelerated up to 181 MeV (being the nominal design value 400 MeV) by the LINAC. Then, this H^- beam is converted to an H^+ beam by charge-stripping foils at the RCS injection, currently operating with a beam power of 300 kW although a beam power of more than 500 kW has been demonstrated in beam studies to be possible with sufficiently low beam loss [89], and this H^+ beam is accelerated up to 3 GeV with a 25 Hz cycle. About 5% of the bunches accelerated at the RCS are supplied to the MR (the rest of the bunches are supplied to other facilities at J-PARC). In the MR, with a circumference of 1567 m and a design beam power of 750 kW, the proton beam is accelerated up to 30 GeV. This beam is extracted from the MR to the T2K neutrino beamline with a fast extraction mode, using a set of five kicker magnets within a single turn, and is used to generate the T2K beam. Each proton beam spill currently consists of eight proton bunches (there were only six until June 2010). Table 3.1 presents a summary of the design and current values (in May 2013) of the T2K beam parameters. Upgrades have been recently performed in the LINAC by installing Annular-ring Coupled Structure (ACS) cavities in its drift tube to reach the design 400 MeV power. Furthermore, other upgrades are planned, including the replacement of the MR magnet power supplies, the improvement of the injection kicker power supplies and increasing the number of protons per bunch and the repetition rate.

3.2.2 T2K Neutrino Beamlne

The T2K neutrino beamline is composed of two sections called primary and secondary beamline, as illustrated in Fig. 3.2.

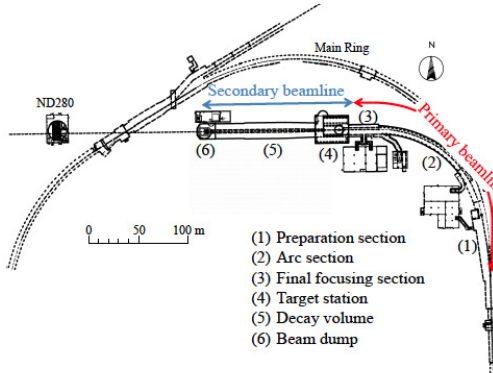


Figure 3.2: Overview of the T2K neutrino beamline: primary beamline on the right followed by the secondary beamline. Figure from [83].

Primary beamline

In the primary beamline, the proton beam extracted from the MR is bent to point toward the T2K far detector Super-Kamiokande. The primary beamline consists of three sections: the preparation section, the arc section and final focusing section. In the primary section, the proton beam is tuned by normal conducting magnets so that it can be accepted in the next section. In the arc section, the beam is bent toward SK direction using superconducting combined function magnets (SCFMs) (horizontal and vertical superconducting steering magnets are also used to correct the beam orbit). Finally, in the focusing section, normal conducting magnets are used again to guide and focus the beam onto the target [82].

In order to produce a stable neutrino beam it is essential that the proton beam is well-tuned and precisely monitored. The proton beam intensity is monitored by a set of five current transformers (CTs), which are toroidal coils around cylindrical ferromagnetic cores that measure the current produced by the toroidal magnetic field induced by the proton beam. Then the beam position monitor, composed by 21 electrostatic monitors (ESMs) surrounding the proton beam orbit, monitors the proton beam centre position by measuring top-bottom and left-right asymmetry of the current induced by the beam on the electrodes, and therefore without interacting with the beam. A set of 19 segmented secondary emission monitors (SSEM) are used during beam tuning (and removed during continuous beam operation since they cause beam loss) to monitor the beam profile by measuring the

currents induced by the interaction of protons with the titanium foil strips. Finally, 50 beam loss monitors (BLMs), which are proportional counters filled with a mixture gas Ar-CO₂, are installed at different places along the primary beamline to measure the beam loss.

Secondary beamline

In the secondary beamline, the proton beam is guided onto a graphite target where kaons and pions are produced, and these secondary products are focused by magnetic horns to finally decay into neutrinos. A schematic view of the secondary beamline is presented in Fig. 3.3.

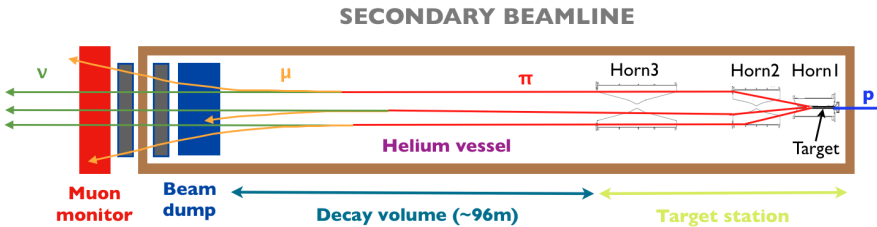


Figure 3.3: Schematic view of the T2K secondary beamline, divided in three sections: target station, decay volume and beam dump. The proton beam enters the target station and interacts with the graphite target. In neutrino beam mode, positive hadrons produced in the interaction are focused by the three horns and directed to the decay volume, where pions mainly decay into muons and muon neutrinos. At the end of the decay volume there is a beam dump made of graphite and iron plates.

The secondary beamline can be divided in three sections, all contained inside a helium vessel at 1 atm: the target station, the decay volume and the beam dump. The target station is separated from the primary beamline by a beam window, with a baffle, acting as a collimator to protect the horns, placed between the beam window and the Optical Transition Radiation monitor (OTR), which monitors the proton beam prior to the collision onto the target. The target core is a graphite rod with 91.4 cm long, with a diameter of 2.6 cm and a density of 1.8g/cm³. When the proton beam at the design beam power of 750 kW interacts with the target, it is expected that the temperature will reach 700°C at the target centre.

The T2K beamline uses three horns: each one consists of two coaxial conductors with a toroidal magnetic field in the closed volume encompassed between them. The first horn is used to collect the charged pions and kaons generated at the target, which is installed in its inner conductor. The other two horns are used

to focus positive pions and kaons and defocus negative particles¹.

The target station is connected to the decay volume, a ~ 96 m long steel tunnel, where the pions produced decay in flight mainly through $\pi^+ \rightarrow \mu^+ \nu_\mu$. The purpose of the helium filling the vessel is to reduce pion absorption and to suppress other products like tritium and NO_X .

There is a small contamination of electron neutrinos coming from the decay of muons and kaons, and of muon antineutrinos coming from the decay of muons, kaons and π^- . More details will be given in Chapter 4, where the T2K flux prediction will be explained together with its associated systematic errors.

At the end of the decay volume and closing the secondary beamline there is a beam dump with a core of 75 tons of graphite and iron plates (3.2 m of graphite and 2.4 m of iron) placed inside and outside the vessel. The purpose of this dump is to stop muons produced in the decay of pions and other secondary particles, so that only muons above ~ 5.0 GeV/c can traverse the dump along with the neutrinos, reaching the muon pit containing the muon monitor after the secondary beamline.

3.2.3 Muon Monitor

A muon monitor (MUMON) is located just after the beam dump to measure the distribution of muons in a bunch-by-bunch basis. Since muons are mainly produced along with neutrinos in the pion two-body decay described through $\pi^+ \rightarrow \mu^+ \nu_\mu$, the measurement of the muon profile centre (with a precision better than 3 cm) determines the neutrino beam direction (with a precision better than 0.25 mrad), which is calculated as the direction from the target to the centre of the muon profile. The muon monitor also monitors the neutrino beam intensity with a precision better than 3%. An emulsion tracker, composed of nuclear emulsion films, is installed downstream of the muon monitor and measures the absolute muon flux and the distribution of momenta of the muons by multiple Coulomb scattering.

3.2.4 Off-Axis Configuration

T2K is the first long-baseline neutrino oscillation experiment with an off-axis configuration. In the T2K beamline design, the neutrino beam direction does not coincide exactly with the direction to Super-Kamiokande, but forms an angle away from the direction towards the far detector. Such off-axis angle can be adjusted from a minimum of $\sim 2^\circ$ to a maximum (current) angle of $\sim 2.5^\circ$. The T2K baseline and off-axis angle were precisely measured by a GPS survey [82]: the measured distance from the graphite target to the centre of Super-Kamiokande

¹Contrarily, negative particles are focused in antineutrino beam mode, by inverting the polarity of the horns' currents.

is 295335.2 ± 0.7 m and the measured angle is $2.504 \pm 0.004^\circ$. With this off-axis technique, the neutrino energy spectrum at Super-Kamiokande presents a narrower band and its high energy tail is minimized as illustrated in Fig. 3.4, due to the reduction of the dependency of the neutrino energy with the energy of the parent pion as shown in Fig. 3.5, in which the distributions are calculated with 2-body decay kinematics for different angles. The off-axis angle is adjusted to tune the peak of the neutrino energy spectrum at Super-Kamiokande to the energy at which the oscillation probabilities $P(\nu_\mu \rightarrow \nu_e)$ and $P(\nu_\mu \rightarrow \nu_\mu)$ are maximum and minimum respectively. For the T2K baseline of 295 km and using $\Delta m_{32}^2 = 2.4 \times 10^{-3} \text{ eV}^2/c^4$, the maximum of the oscillation probability is found at ~ 600 MeV. Consequently, the off-axis angle improves the sensitivity to the oscillation parameters, since the effect of neutrino oscillations is maximized. Figure 3.4 shows, on the left side, the effect on the neutrino energy spectrum of an off-axis configuration for different off-axis angles: the neutrino energy spectrum becomes narrower for larger off-axis angles, although the absolute flux is reduced. The right side of Fig. 3.4 presents the superposition on the oscillation probability distributions of the energy band at ~ 600 MeV for an off-axis angle of $\sim 2.5^\circ$, which coincides with a maximum of the $P(\nu_\mu \rightarrow \nu_e)$ oscillation probability and a minimum of the $P(\nu_\mu \rightarrow \nu_\mu)$ oscillation probability.

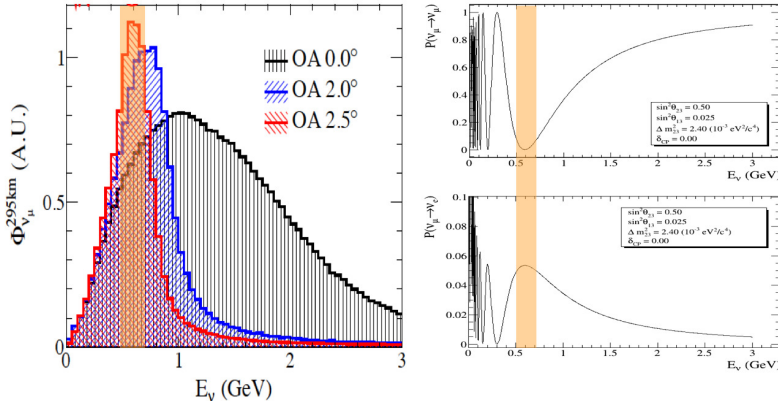


Figure 3.4: On the left, effect of an off-axis configuration on the neutrino energy spectrum for different off-axis angles: the neutrino energy spectrum is narrower for larger off-axis angles. On the right: superposition on the oscillation probability distributions of the energy band at ~ 600 MeV for an off-axis angle of $\sim 2.5^\circ$ (orange band), which coincides with a maximum of the $P(\nu_\mu \rightarrow \nu_e)$ oscillation probability and a minimum of the $P(\nu_\mu \rightarrow \nu_\mu)$ oscillation probability. Left figure from [83].

The charged current quasi elastic (CCQE) interaction channel described by $\nu_l + n \rightarrow l + p$ (where $l = e^-$ or μ^-), is used in Super-Kamiokande and ND280 to reconstruct the neutrino energy, since it is the channel allowing a full neutrino energy reconstruction through the formula (assuming that the target neutron is at rest):

$$E_\nu = \frac{(m_N - E_B)E_l - m_l^2/2 + m_N E_B - E_B^2/2 + (m_P^2 - m_N^2)/2}{m_N - E_B - E_l + p_l \cos \theta_l} \quad (3.3)$$

where m_N , m_P and m_l are respectively the masses of the neutron, proton and lepton created in the neutrino interaction, E_B is the binding energy and E_l , p_l and θ_l are the energy, momentum and angle of the lepton. As shown in Fig. 3.6, the energy band at ~ 600 MeV for T2K with an off-axis angle of $\sim 2.5^\circ$ enhances the CCQE channel and reduces the backgrounds induced by neutrinos in the high energy tail of the beam (charged current non quasi elastic and neutral current modes). On the other hand, some shape information is lost with the narrower beam as it can be observed in Fig. 3.4 by comparing the widths of the oscillation and flux peaks. However, the important shape information for the oscillation analyses, around the oscillation maximum and minimum, is retained in the narrower beam, and improved with the more accurate energy reconstruction using CCQE events.

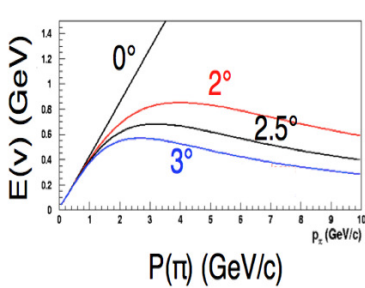


Figure 3.5: Neutrino energy vs parent pion momentum (2-body decay kinematics) for different off-axis angles, showing that the dependency of the neutrino energy with the parent pion energy is reduced using an off-axis angle. Figure from [90].

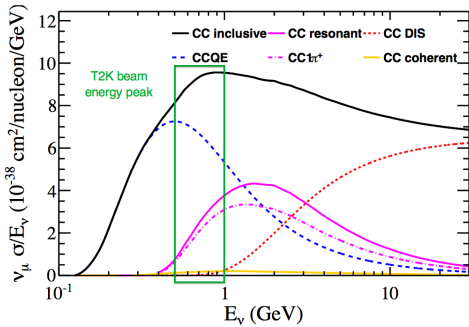


Figure 3.6: Cross sections per nucleon per energy for CC interactions of ν_μ on Carbon as a function of neutrino energy calculated with NEUT, with an approximation of the T2K energy band overlaid, showing that the CCQE channel is enhanced and the backgrounds are reduced. NEUT official plot.

3.3 Near Detectors

In order to study neutrino oscillations of the off-axis muon neutrino beam between its production point and the far detector Super-Kamiokande, it is essential to characterize the unoscillated beam with a precise measurement of the neutrino energy spectrum, flavour content and interaction rates before oscillation. In the T2K experiment, these measurements are performed by a set of detectors situated at 280 m from the target station. These detectors are separated according to their position: there is an on-axis detector (INGRID) and an off-axis complex of detectors (ND280) as illustrated in Fig. 3.7, which shows the near detector complex in the pit. The ND280 off-axis detectors are located in the upper level (about 24 m below the surface) and the modules of the on-axis detector INGRID are located on the level below (about 33 m deep for the horizontal modules). This design allows off-axis angles in the range 2° - 2.5° , constrained by the requirement that the beam axis crosses the central area of the on-axis detector.

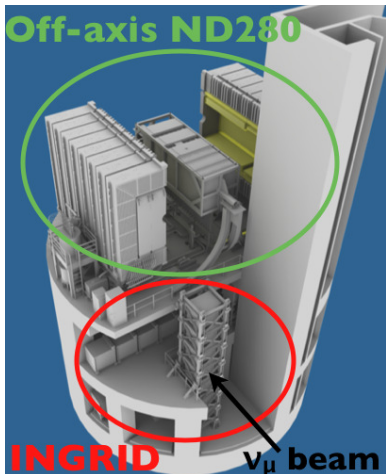


Figure 3.7: The near detector complex in the near detector pit situated 280 m from the target station: the NC280 off-axis detectors are located in the upper level (about 24 m below the surface) and the modules of the on-axis detector INGRID are located on the level below (about 33 m deep for the horizontal modules). Figure from [82].

3.3.1 INGRID On-Axis Detector

The INGRID (Interactive Neutrino GRID) detector is an on-axis near detector placed at the near detector facility, on the neutrino beam axis. This detector has been designed to measure the neutrino beam direction and intensity in a daily basis by means of neutrino interactions in iron.

The INGRID detector configuration is shown in Fig. 3.8. INGRID is composed of 16 identical modules, 14 of them arranged as two groups of 7 modules each along the horizontal and vertical axes, forming a cross. The other two modules are placed at off-axis positions off the main cross. With this structure, INGRID is designed to sample the beam in a transverse section of $10\text{ m} \times 10\text{ m}$, sufficiently covering the neutrino beam profile. The centre of the INGRID cross coincides with the centre of the neutrino beam, defined as 0° with respect to the proton beamline. An extra module, different from the rest, is placed in the centre of the INGRID cross, between the central modules in the horizontal and vertical groups. This module is called Proton Module and is composed of scintillator planes (with a different size for the scintillator bars to improve the tracking) and no iron plates in order to detect the protons together with the muons produced in the charged current neutrino interactions.

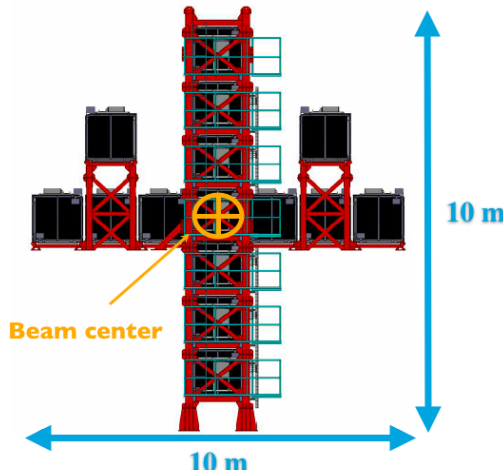


Figure 3.8: The INGRID detector configuration: 14 identical modules are arranged as two groups along the horizontal and vertical axes, forming a cross, and two modules are placed off-axis, off the main cross. The total transverse section covered with this configuration is $10\text{ m} \times 10\text{ m}$. Figure from [82].

Each INGRID module is a sandwich structure of 9 iron plates, which act as a target for the neutrino interactions, and 11 tracking scintillator planes placed in between the iron plates (except the last two scintillator layers, with no iron plate in between due to weight restrictions). Figure 3.9 shows a drawing of one INGRID module (left side), where the blue planes are the iron layers and the tracking planes are coloured in grey. The ensemble of iron and scintillator planes is surrounded by veto scintillator planes as shown in Fig.3.9 (right side) to reject charged particles that enter the modules from outside. Each iron plate is a square of 124×124 cm 2 and 6.5 cm thickness, with a total of 7.1 tons of iron mass serving as neutrino target per module. Each tracking plane is composed of 24 scintillator bars in the horizontal axis and 24 in the vertical axis and has a box for the front-end electronics board attached to its top-right side. The scintillation light is collected and transported with a wavelength shifting (WLS) fibre and read out by a Multi-Pixel Photon Counter (MPPC) attached to the end of the fibre.

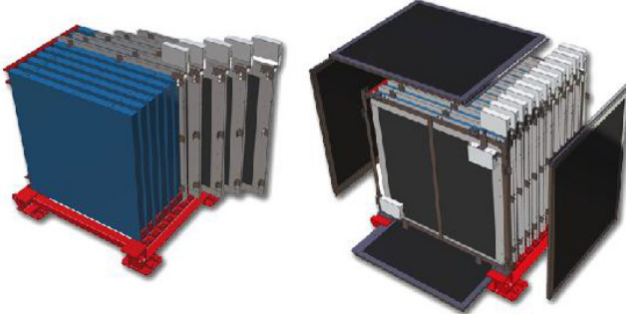


Figure 3.9: Drawings of an INGRID module: a sandwich structure of 9 iron plates (left side, blue) and 11 tracking scintillator planes placed in between the iron plates (grey). The sandwich of iron+scintillator planes is surrounded by veto scintillator planes (right side, black). Figure from [82].

A typical neutrino event in the INGRID detector is shown in Fig. 3.10, with a neutrino entering from the left and the interaction happening in the Proton Module (left module), producing charged particles whose tracks are shown as red circles with different sizes depending on the signal created. In Fig. 3.10, green lines are scintillator planes, blue lines are veto scintillator planes and grey boxes are the iron plates; the long track exiting the Proton Module corresponds to a muon while the short one corresponds to a proton.

The beam centre is measured by the INGRID detector using the number of observed neutrino events in each module, which are identified by detecting muon

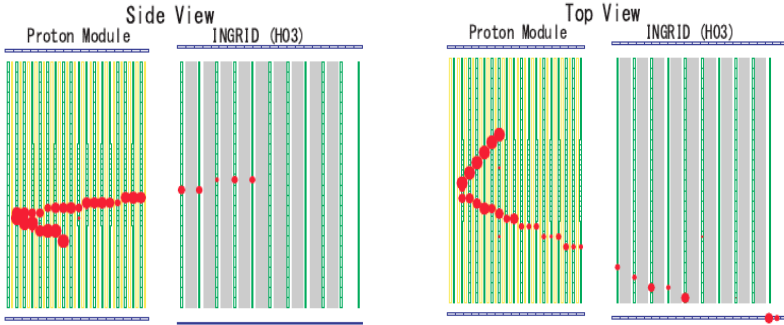


Figure 3.10: Typical neutrino event in the INGRID detector: the neutrino enters from the left and the interaction happens in the Proton Module (left module), producing charged particles whose energy depositions are shown as red circles. Figure from [82].

tracks. The precision of the measurement of the beam centre is better than 10 cm (0.4 mrad precision at the near detector complex), defined by the systematic error due to the uncertainty on the neutrino event rate, and stable within the statistical error of ~ 2 cm measured everyday with a beam power of 200 kW. The observed profiles (number of events vs position from INGRID centre) in the x and y directions are fitted with Gaussian functions, and the beam centre is defined as the peak of the fit. The two modules off the main cross are used to check the axial symmetry of the neutrino beam. Cosmic ray data and beam data were used for the calibration of the INGRID detector. The history of the neutrino beam intensity along the different data taking periods will be presented in Section 4.1, showing the great stability of the neutrino beam intensity and direction during every period. More details about the performance, calibration and simulations for INGRID can be found in [91].

3.3.2 ND280 Off-Axis Detector

The ND280 off-axis near detector serves to characterize the neutrino beam before oscillation, measuring the energy spectrum and flavour composition of the neutrino beam, providing also measurements of the different interaction channels. Figure 3.11 illustrates the different sub-detectors that comprise the off-axis ND280 detector. Firstly, in the inner part, there is a detector called P \otimes D, optimized to reconstruct neutral pions, and a tracker composed of time projection chambers (TPCs) interleaved with fine grained detectors (FGDs). Both the tracker and the P \otimes D detector are placed inside the basket, a metallic container opened at the top, with

dimensions of $6.5 \text{ m} \times 2.6 \text{ m} \times 2.5 \text{ m}$. Three groups of electromagnetic calorimeters (ECAL) surround the basket, and finally the recycled UA1 magnet with the side muon range detector (SMRD) inserted in its air gaps encircles all the other detectors. The active target mass for neutrino interactions in the off-axis ND280 is concentrated in the FGDs and PØD.

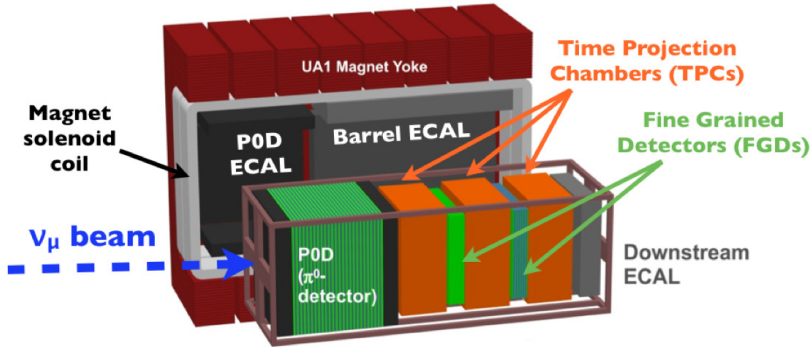


Figure 3.11: The off-axis ND280 set of detectors: the PØD detector, optimized to reconstruct neutral pions; the tracker composed of time projection chambers (TPCs) interleaved with fine grained detectors (FGDs); the electromagnetic calorimeters (ECAL) surrounding the basket containing the tracker and the PØD; and the recycled UA1 magnet with the side muon range detector (SMRD) inserted in its air gaps encircling all the other detectors. Original figure from [82].

ND280 Magnet and Side Muon Range Detector (SMRD)

The off-axis ND280 detectors are enclosed by the recycled CERN UA1/NOMAD magnet. This magnet consists of two mirror-symmetric halves composed of water-cooled coils made of aluminium bars that create a horizontal oriented dipole field, and a return yoke which serves as mechanical support for the coils, electrically isolated from them. A dipole magnetic field of 0.2 T is created by the magnet with the aim of measuring with good resolution the momenta and sign of charged particles produced in the neutrino interactions.

A dedicated mapping procedure was performed using Hall probes to precisely measure the magnetic field of the ND280 magnet. This measurement is specially important in the region of the TPCs in order to understand and correct spatial distortions that could appear in the reconstruction of charged particle tracks. Figure 3.12 illustrates an example of slice of the magnetic field mapped in the TPC region at the centre of the basket ($x = 0$), showing that the field is very homogeneous in

the centre of the magnet but increasingly varies as it gets closer to the edge of the TPC region (downstream).

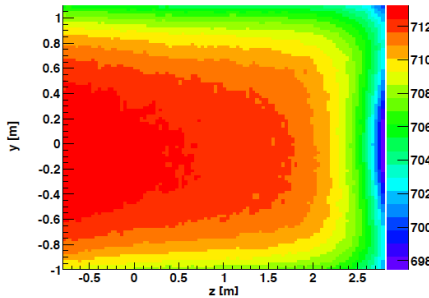


Figure 3.12: Slice of the magnetic field mapped (colours represent the magnetic field in units of Gauss) in the TPC region at the centre of the basket ($x = 0$). The field is very homogeneous in the centre of the magnet but increasingly varies as it gets closer to the edge of the TPC region (downstream). Figure from [82].

The magnet yokes consist of 16 iron plates spaced with 17 mm air gaps. In these air gaps, layers of plastic scintillator were inserted. These scintillator modules (440 in total) form the Side Muon Range Detector (SMRD), whose main goal is to detect muons produced in the neutrino interactions that escape the inner detectors at large angles with respect to the beam direction, measuring also their momenta. Furthermore, the SMRD provides a trigger for cosmic rays entering the ND280 detector and used for calibration thereof, and serves to identify background events from beam neutrino interactions occurring in the magnet or the surrounding walls.

A significant fraction of muons produced in CCQE interactions intersect the SMRD according to MC studies [92]. Muons emitted with large angles often leave a short track or no tracks in the TPCs. The momenta and direction for these muons can be inferred from the SMRD measurements, using the information from its plastic scintillation counters. Each SMRD polystyrene-based scintillator layer incorporates a wavelength shifting (WLS) fibre connected to a multi-pixel photon counter (MPPC).

Electromagnetic Calorimeter (ECal)

The ND280 Electromagnetic Calorimeter (ECal) consists of layers of plastic scintillator bars, serving as active material, interleaved with lead absorber sheets. It provides a near-hermetic coverage for the particles exiting the inner detector volume

that the ECAL surrounds, composed of P \oslash D, TPCs and FGDs. Similarly to the SMRD layers, each ECal plastic scintillator bar, made of doped polystyrene, is read by a WLS fibre connected to one or two MPPCs depending on the length of the bar.

The ECal is composed of 13 independent modules separated in 3 groups depending on their position, arranged as shown in Fig. 3.11: there are six modules surrounding the tracker volume (called Barrel-ECal) distributed in the four sides parallel to the neutrino beam axis; one downstream module (Downstream-ECal or Ds-ECal) placed at the downstream exit of the tracker volume, inside the basket and perpendicular to the neutrino beam axis; and six modules surrounding the P \oslash D detector (P \oslash D-ECal) distributed in the four sides parallel to the neutrino beam axis. There are two modules at the top and bottom sides for the P \oslash D-ECal and Barrel-ECal, following the magnet division in two halves, to allow the opening and access to the inner sub-detectors.

The main goal of the ECal is the detection of photons, primarily from π^0 production, and the measurement of their energy and direction. Thus, the ECal is a key element in the reconstruction of neutral pions produced in the neutrino interactions in the tracker or the P \oslash D. The P \oslash D-ECal serves as a veto for entering particles and complements the P \oslash D reconstruction with information on escaping energy, detecting muons and photons exiting the P \oslash D without being reconstructed. Furthermore, the ECal detector also provides information of charged particles, helping to identify them and to distinguish between electrons, muons and pions combined with the TPC dE/dx particle identification, complementing in this way the inner detectors in full event reconstruction.

Pi-zero Detector (P \oslash D)

The Pi-zero Detector (P \oslash D) is placed inside the basket, at the upstream end of the magnet. The active region of the P \oslash D consists of the structural elements called P \oslash Dules; they are made of two perpendicular arrays (in the x and y directions) of doped polystyrene triangular scintillator bars, each one read out by a WLS fibre attached to MPPC photosensors, and sandwiched between sheets of high-density polyethylene (HDPE) forming a plane. Fillable water bags and lead and brass sheets are placed in between the scintillator planes or P \oslash Dules.

The entire P \oslash D detector is structured in four sections or Super-P \oslash Dules as shown in Fig. 3.13: the Upstream ECal section, followed by the Upstream and Central Water Targets, and the Central ECal section. The water target consists of fillable water bags and corresponds to the two central sections.

The P \oslash D has been optimized for π^0 detection and its main goal is to precisely measure the neutral current process: $\nu_\mu + N \rightarrow \nu_\mu + N + \pi^0 + X$. An accurate measurement of the cross section for this process is of high importance since events

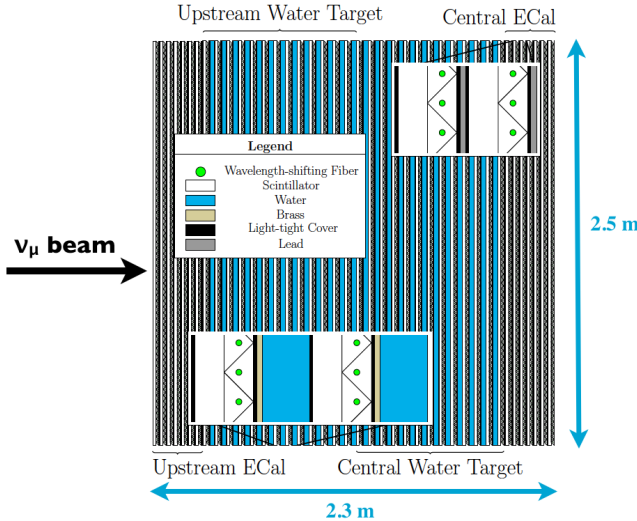


Figure 3.13: A schematic view of the PØD design, showing the four Super-PØDule modules and their composition. The beam direction is left to right. Figure from [82].

containing π^0 's are one of the main backgrounds to the $\nu_\mu \rightarrow \nu_e$ appearance signal at Super-Kamiokande. As the PØD operates with the water target bags filled or emptied, a subtraction method can be used to determine the cross section for the neutral current π^0 interactions on water [93].

As for the other detectors, minimum ionizing particles from cosmic ray muons were used to calibrate the PØD detector. More details about its design, performance and calibration can be found in [94].

Time Projection Chambers (TPCs)

The Time Projection Chambers (TPCs) form with the Fine Grained Detectors (FGDs) the tracker of the ND280 detector, which is a sandwich of three TPCs with two FGDs interleaved.

The three TPCs [95] are gaseous ionization chambers with a rectangular double box design, in which the walls of the outer box (made from composite panels with Al skins) are at ground potential, and the walls of the inner box (made from composite panels and copper strip pattern) form the field cage. The volume enclosed in the inner box is filled with an specific Ar-based gas mixture (Ar:CF₄:iC₄H₁₀ in 95:3:2 proportions), selected for its high drift speed, low diffusion and good performance with micromegas (MM) detectors. The space between the inner and

outer boxes is filled with CO₂ acting as insulator. A gas system connected to the TPCs is designed to maintain a stable mixture in the inner volume and a positive pressure with respect to the outer volume. The inner box is divided by a central cathode plane in its midpoint which is at -25 kV and produces, together with the copper strip pattern, a uniform electric field in the active drift volume of each TPC. This electric field is roughly aligned with the magnetic field produced by the magnet and serves as drift field for the ionization electrons. On the readout planes, the planes parallel to the cathode at each end of the inner volume, twelve bulk micromegas (MM) modules [96] are arranged in two vertical columns with a small offset between them so that inactive regions are not aligned. A schematic drawing of the TPC structure is presented in Fig. 3.14.

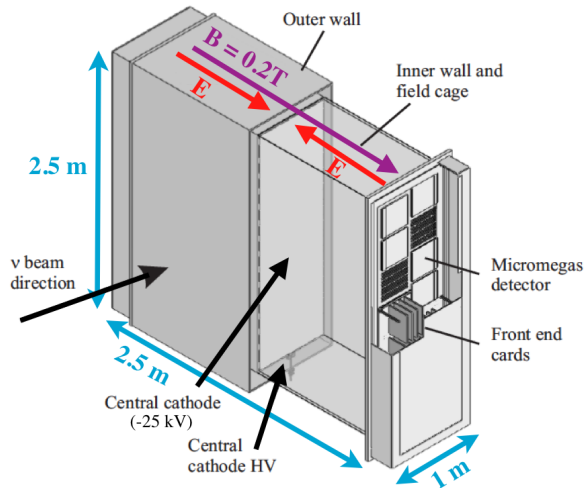


Figure 3.14: Schematic drawing of the TPC structure, showing the main aspects of its double box design. Figure from [82].

When a charged particle crosses a TPC, it produces ionization electrons in the inner gas; these electrons drift towards one of the readout planes due to the electric field and reach the bulk MM detectors, with a 7.0 × 9.8 mm (vertical × horizontal) anode pad segmentation, where the electrons are multiplied and sampled. With the pattern of signals in the pad plane and their arrival time, a complete 3D image of the track of the traversing charged particle can be obtained, by determining the y and z coordinates from the readouts of the anode pads and the x coordinate by the drift time.

The excellent imaging capabilities of the TPCs makes them a fantastic tool to perform three fundamental tasks. Firstly, using the complete 3D image of tracks obtained with them, the number of charged particles and their directions can be precisely determined, allowing the selection of samples of different neutrino interactions with a very high purity. Secondly, using the curvature of the trajectories of the charged particles due to the magnetic field in which the TPCs are embedded, their momenta can be measured and used to estimate the event rate as a function of neutrino energy of the different neutrino interactions prior to oscillation. Thirdly, combining the measured momenta with the amount of energy deposited by ionization by each particle, different types of charged particles can be identified, distinguishing between muons, electrons, protons and pions.

The particle identification is a very important function performed by the TPCs. In order to distinguish between different types of charged particles, the distributions of the energy loss as a function of the momentum are computed using a truncated method² and compared with the expected curves for each kind of particle: muons, electrons, pions and protons. An example of the distribution of energy loss calculated with T2K Run1 data is illustrated in Fig. 3.15, compared to the expected curves for positive (left) and negative (right) particles. The sample of positive particles contains protons, pions and positrons, while the sample of negative particles contains mainly muons and low momentum electrons.

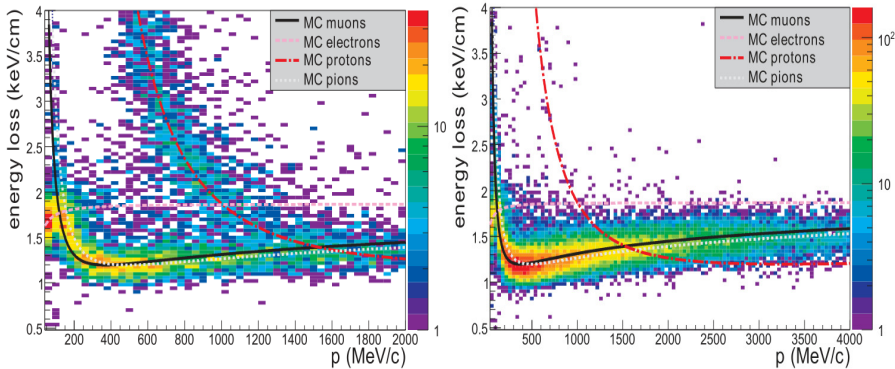


Figure 3.15: Example of the distribution of energy loss as a function of momentum calculated in the TPCs, with the T2K Run1 data, compared to the expected curves for positive (left) and negative (right) particles. The sample of positive particles contains protons, pions and positrons, while the sample of negative particles contains mainly muons and low momentum electrons. Figures from [95].

²The truncated mean is computed using the 70% least energetic clusters forming a track.

The calibration of the TPCs can be divided into two stages, low level and high level calibration, depending on whether reconstruction inputs are used (high level) or not (low level) [97, 98].

For the **low level calibration**, a dedicated test bench was constructed and operated at CERN to characterize the MM modules (building a gain map of each MM and measuring their energy resolution). It consisted of a small drift chamber with a MM implemented on one side and a cathode on the other side. An automated X-Y scanning system allowed to measure the response of individual pads when illuminated by a collimated ^{55}Fe source (185MBq).

Furthermore, the monitor chambers are another important element in the low level calibration. They are two independent mini TPCs (with similar parameters to the large ones) placed at the input and output of the gas system, used to measure both the drift velocity (using two ^{90}Sr sources) and the gas amplification (with one ^{55}Fe source).

One of the aims of the low level calibration is to use the results obtained with these elements to apply basic corrections in the reconstruction. For instance, a correction for the gain variation, resulting from gas density changes (mainly due to atmospheric pressure changes), is very significant in the charge calibration, which is in turn important for particle identification.

On the other hand, the **high level calibration** is also used to apply corrections in the reconstruction.

Data from cosmic rays is used in this calibration step to measure the absolute drift velocity and to estimate the transverse diffusion constants.

In order to measure and monitor the transport of electrons in the TPCs, a photoelectron calibration system was incorporated into the TPC design. A collection of Al targets (dots and strips) with a well defined pattern is located on the central cathodes. When illuminated by the light source provided by a Nd:YAG UV laser, a control pattern of photoelectrons is produced on the central cathodes. The pattern produces an image on the pad plane that is detected and used for the calibration, to measure relative drift velocity, electronics timing uncertainties, MM gain and inhomogeneities and misalignments of B and E fields.

Two sets of laser data with magnetic field on and off can be compared and distortion maps can be built comparing the image of the Al dots in both cases, showing the displacements produced when turning on the magnetic field. Figure 3.16 shows an example of a spatial distortion map where the arrows indicate the displacement appearing when turning on the magnetic field, magnified by a factor of 10.

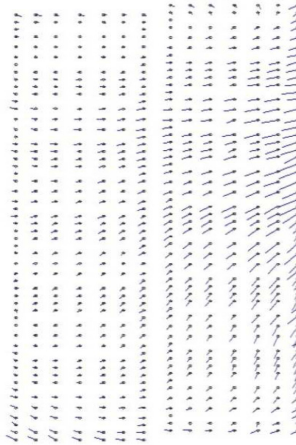


Figure 3.16: Example of spatial distortion map in one TPC computed using laser data. The arrows indicate the displacement appearing when turning on the magnetic field, magnified by a factor of 10. Figure from [95].

Fine-Grained Detectors (FGDs)

There are two Fine-Grained Detectors (FGDs) in the inner part of the ND280 detector, placed in between the three TPCs. The two FGDs have the same geometry, mounting and readout technologies, but FGD1 (upstream) consists of only scintillator bars (5760 in total) while FGD2 (downstream) consists of scintillator bars and thick layers of water (2688 scintillator bars and 15 cm total thickness of water). The FGD scintillator bars are made of extruded polystyrene and they are oriented perpendicular to the beam direction, in the x or y direction. Each scintillator bar incorporates a WLS connected to a MPPC and a light-tight dark box, where the readout electronics are mounted in, surrounds each FGD.

The FGDs perform a double function. On the one hand, they provide target mass for neutrino interactions, both in carbon and water: by comparing interaction rates obtained in the two FGDs, a subtraction method can be used to determine the cross sections separately on carbon and water, since only the second FGD contains water [99]. On the other hand, they serve as tracking devices: with the layers of scintillator bars placed alternating in the x and y direction it is possible to track charged particles produced in the neutrino interactions. Their fine granularity allows to resolve individual particle tracks and to measure short-ranged particles, such as recoil protons.

In addition, the energy loss in the FGD scintillator bars can be used to identify the particle creating a track stopping in an FGD: comparing the measured total

energy deposited by a particle for a given range in the FGD to the theoretical expected curves, muons, protons and pions can be distinguished. This is illustrated in Fig. 3.17, where the deposited energy distribution as a function of the range for particles stopping in FGD1, calculated with T2K Run1-2 data, is compared to the expected curves from MC for protons, muons and pions, using neutrino beam (left) and cosmic rays data (right).

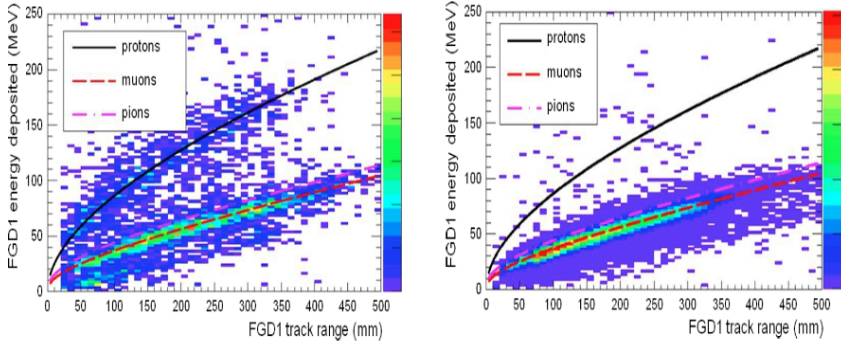


Figure 3.17: Example of the deposited energy distribution calculated with T2K Run1-2 data as a function of the range for particles stopping in FGD1, compared to the expected curves calculated with MC for protons, muons and pions, using neutrino beam data (left) and cosmic rays data (right). Figures from [100].

Studies for Michel electrons have also been performed in the FGDs. These electrons, produced by muons stopping in an FGD, produce a delayed signal after the initial neutrino interaction. The identification of Michel electrons is important to detect events with pions stopping in the FGDs (through the decay chain $\pi \rightarrow \mu \rightarrow e$) and to measure the rate of CC1 π interactions, which would contribute to an incorrect calculation of the neutrino energy. The Michel electron tagging efficiency, computed with cosmic rays, is estimated to be $\sim 61\%$ for MC and $\sim 58.59\%$ for data. More details can be found in [100] and [101].

The three TPCs interleaved with the two FGDs form the ND280 tracker, designed to study charged and neutral current neutrino interactions and optimized to measure charge current quasi-elastic (CCQE) processes, the dominant channel at the T2K neutrino beam energy and the one allowing a full reconstruction of the neutrino energy. Thus, the ND280 tracker is a key element to reconstruct tracks of charged particles (such as the outgoing muon in the CCQE interaction $\nu_\mu + n \rightarrow \mu^- + p$), their momenta, angles and vertexes in order to compute the neutrino energy.

Figure 3.18 shows an example of event display where a muon track crosses the different sub-detectors composing ND280, entering via the upstream side of the P \emptyset D, continuing through the tracker (TPCs and FGDs) and producing secondary particles in the last TPC which are stopped in the ECal detectors.

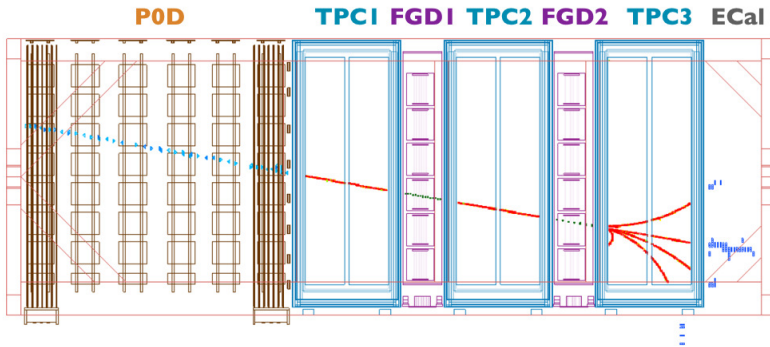


Figure 3.18: Example of event display where a muon track crosses the different sub-detectors composing ND280, entering via the upstream side of the P \emptyset D, continuing through the tracker (TPCs and FGDs) and producing secondary particles in the last TPC which are stopped in the ECal detectors. Figure from [82].

3.4 Far Detector: Super-Kamiokande

Neutrino oscillations are measured at the far detector after neutrinos have travelled a distance of 295 km, the T2K baseline. Super-Kamiokande is the largest land-based water Čerenkov detector in the world, and it serves as far detector in the T2K experiment, to look for $\nu_\mu \rightarrow \nu_e$ appearance and ν_μ disappearance in the T2K ν_μ beam.

Super-Kamiokande [102] is a cylindrical detector with a height of 42 m and 39 m diameter, filled with 50 kton of pure water and placed 1 km deep within the centre of Ikenoyama mountain in the Kamioka Observatory. Its walls are covered with about 13,000 photomultiplier tubes (PMTs), which serve to image neutrino interactions and whose readout electronics were upgraded during the present running period. Figure 3.19 shows the design and location of the Super-Kamiokande detector. It consists of two major volumes, an inner and outer detector, separated by a cylindrical structure of about 50 cm wide, which is composed of a stainless steel scaffold covered by plastic sheets that serve to optically separate the inner and outer detector. The inner detector (ID) volume, with 33.8 m diameter and 36.2 m

of height, incorporates in its walls 11,129 inward-facing PMTs of 50 cm diameter with an effective 40% PMT cathode surface coverage. The outer detector (OD) is the cylindrical space surrounding the ID radially with 2 m thick, instrumented with 1,885 outward-facing 20 cm diameter PMTs. A schematic drawing of the ID and OD and a picture of the inner detector and one PMT can be found in Fig. 3.20.

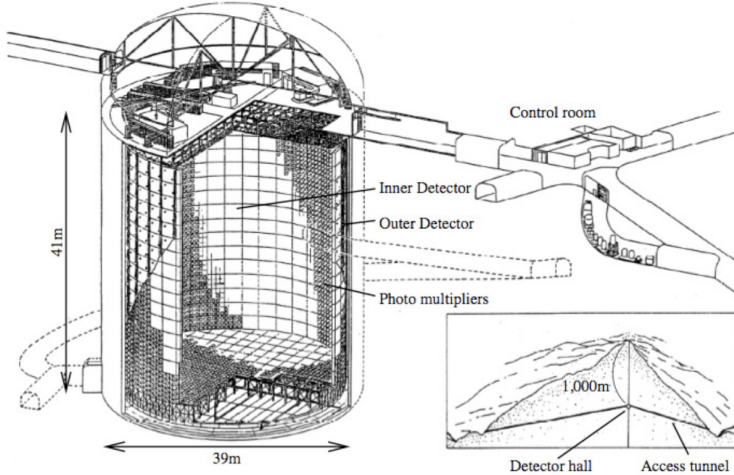


Figure 3.19: Design and location of the Super-Kamiokande detector, a cylindrical Čerenkov detector filled with 50 kton of pure water, instrumented with photomultiplier tubes (PMTs) covering its walls and placed 1 km deep within the centre of Ikenoyama mountain in the Kamioka Observatory. Figure from [82].

Super-Kamiokande has been running since 1996 over four running periods: the initial period SK-I (from April 1996 to July 2001); the SK-II period (from December 2002 to October 2005) that started after a year of rebuilding the detector, with half of the previous tube density, due to an accident that destroyed much of the photo-tubes; the SK-III period (from October 2006 to August 2008) with restored full photo-tube density; and the current SK-IV period (including the T2K experiment) incorporating upgraded PMT readout electronics and data acquisition that allow a higher data processing rate. SK has contributed to measure oscillations in atmospheric, solar and accelerator-produced neutrinos, including confirmation of the solar neutrino deficit [103], the first strong evidence of neutrino oscillation in atmospheric neutrinos [27], and the verification of these neutrino oscillations in an accelerator-produced beam by the K2K experiment [104]. In addition, it has performed studies about proton decays as well, setting limits on partial lifetimes for modes such as $p \rightarrow e^+ \pi^0$ and $p \rightarrow \bar{\nu} K^+$ [105, 106].

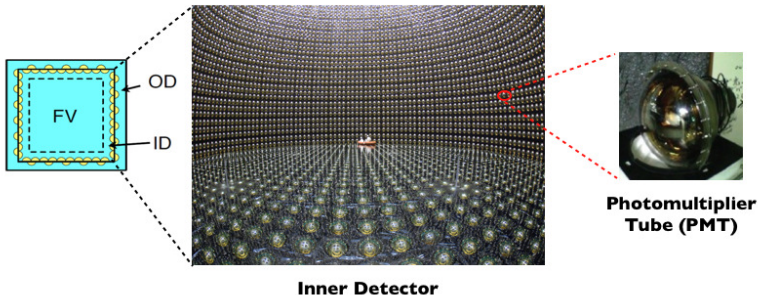


Figure 3.20: Schematic drawing of the division of Super-Kamiokande into inner and outer detector (left), picture of the inner detector (middle) showing the walls instrumented with PMTs and picture of one of those photomultiplier tubes (right). SK official figures.

When charged particles are created in a neutrino interaction with a velocity above the velocity of the light in the medium, c/n , with n the index of refraction of the medium ($n \approx 1.33$ in water) and c is the speed of light in vacuum, they emit a cone of Čerenkov light as they traverse the water filling Super-Kamiokande. The Čerenkov photons reach the PMTs in the walls of the detector and this light, when projected on the flat walls of the detector, produce a ring-shaped hit pattern. Then the PMTs act as pixels detecting the light and giving information about the vertex position, type of charged particles and their momenta, which are computed with the reconstruction techniques described below. With this information about the neutrino interaction occurred, charged current quasi-elastic (CCQE) interactions for muon neutrinos and electron neutrinos can be distinguished and counted based on the different hit pattern of the lepton produced for each flavour (μ in the ν_μ interaction and e in the ν_e interaction), selecting them with the cuts that will be explained in Section 4.5.1. They are then used to determine the flavour composition of the T2K beam after travelling the distance to the far detector, and therefore to measure neutrino oscillations.

3.4.1 SK Reconstruction Techniques

The Super-Kamiokande detector has been calibrated with introduced laser light and cosmic ray particles, and its behaviour and modelling is very well known after its long running operation. T2K analyses rely on the well-known reconstruction techniques developed for SK for other data samples during its many years of running.

The simulation of the SK detector is done with a package called SKDETSIM [107] which is a GEANT3-based simulation package, tuned with SK calibration data [108]. The water absorption and scattering coefficients incorporated in the simulator are calculated using a dye laser beam injected into the water at different wavelengths, and cosmic ray muons are used to monitor the water transparency. The absolute energy scale is determined using mainly muon-decay electrons and stopping cosmic ray muons. The uniformity of the detector response is studied with decay electrons from stopping cosmic ray muons and π^0 's produced by neutrino interactions, and to account for muon polarization in the estimation of the angle (zenith and azimuthal) dependence of the detector gain, electrons decaying perpendicularly to the initial muon direction are used.

A first process of data reduction is used to separate the SK data into three categories: outer detector events (with high activity in the outer detector), low energy events (with total activity less than 200 photoelectrons or a single PMT with more than half of the total charge) and fully contained events (with all their Čerenkov light deposited inside the inner detector). After all events have been classified, they are sent through the SK reconstruction algorithms, which are different for each classification. The data used in the T2K analyses is composed of only fully contained events, so the reconstruction process for this classification will be described, while for the rest it can be found in [108].

The following reconstruction steps, based on charge and hit timing information from the PMTs, are applied to the fully contained events in order to identify their origin and properties:

1. The **vertex** is found in the first step of the reconstruction, determining its position, direction and Čerenkov angle using the PMT hit times (adjusted for the time of flight of the Čerenkov light) with a fitter called TDC-fit, based on [109]. In this fit, a first rough vertex position and direction is found with the timing information, assuming that all the light in the event was produced in a single point. Then, the direction and Čerenkov angle are varied to find an optimal fit to the Čerenkov ring edge, using the charge information as a function of opening angle for different directions. And after this, the vertex is re-fitted [110].
2. The **number of Čerenkov rings** and their directions is determined using a technique based on an iterative Hough transform [111]: a second ring is chosen from the Hough map of possible ring directions and a likelihood is computed to check if the addition of this ring is more consistent with data that just one ring; if that is the case, the procedure is repeated adding as many rings as necessary (up to a maximum of 5 rings).
3. The **particle type** of the final state particles is determined using a particle identification (PID) algorithm, based on the differences in the shape and

opening angles of the Čerenkov rings produced by different particles: the Čerenkov radiation produced by a muon yields a well-defined circular ring since, due to its relatively large mass, muons pass through the detector often unscattered; whereas an electron produces multiple light cones, due to multiple scattering and electromagnetic showers whose particles produce light that overlaps and distorts the pattern, yielding a diffuse ring. At low momentum, the Čerenkov opening angle is used to separate muon and electron rings. This opening angle, defined as $\cos \theta = \frac{1}{n\beta}$, with β the velocity of the particle and n the refraction index (being the maximum opening angle about 42° for $\beta=1$), is smaller for muons than for electrons, as the muon mass is larger than the mass of the electron and therefore $\beta(\mu) < \beta(e)$. Figure 3.21 shows typical displays of different kinds of simulated events: a ν_μ CCQE event (top plot) with a single well-defined ring produced by the muon; a ν_e CCQE event (middle plot) with a single fuzzy ring produced by the electron; and a ν_μ NC1 π^0 interaction (bottom plot) with its two characteristic diffuse rings. In Fig. 3.21 the light pattern produced at the ID wall is shown with the cylindrical wall represented as a flat projection and using different colours according to the amount of charge detected by the PMTs, with purple indicating the least amount of charge and red the most. This method gives a distribution of a likelihood variable (or PID parameter) used to efficiently discriminate the particle type, with a misidentification probability of 0.7% (0.8%) for single ring electrons (muons), and has been validated with a scaled detector in a beam test experiment at KEK [112].

4. The **Čerenkov rings are re-fitted** after the particle identification is performed, taking into account the expected light pattern of the corresponding particle. This fit is performed by a more precise fitter called MS-fit described in [113].
5. The **momentum** is assigned to each ring based on its sum of Čerenkov photons. The first step for multi-ring events is to divide the charge from each PMT into a fraction assigned to each ring, process specially important when the rings overlap. This separation is done according to the expected charge distribution for each ring assuming a uniform distribution of light azimuthally around the particle direction, depending only on the opening angle [110]. Once the rings are separated, the momentum of each particle is computed with the total number of photoelectrons within a 70° half-angle cone with respect to the particle track direction, correcting for light attenuation and PMT angular acceptance.

A new reconstruction algorithm is being developed based on an extension of the model used at MiniBooNE [114] and it has been indeed used in the latest T2K ν_e appearance analysis and in the joint oscillation analysis presented in Chapter

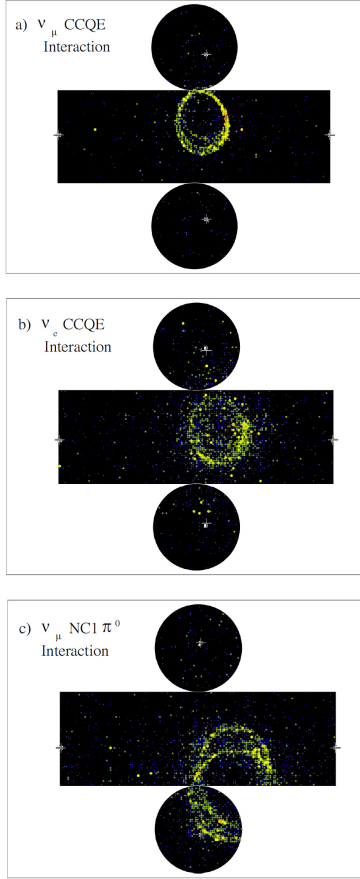


Figure 3.21: Event display examples for the SK simulation of a ν_μ CCQE event (top), a ν_e CCQE event (middle) and a ν_μ NC1 π^0 interaction (bottom), showing the light pattern produced at the ID wall (with the cylindrical wall represented as a flat projection), with different colours according to the amount of charge detected by the PMTs (purple indicates the least amount of charge and red the most). Figures from [2].

5, as it has been employed to remove π^0 background events in the final selection criterion of the single ring e-like event selection that will be described in Section 4. This new algorithm uses the observed charge and time information from every PMT hit [115, 116], and builds the charge and time probability density functions (PDFs) for a given particle hypothesis for every event. A set of 7 parameters is used

for the single ring hypothesis³: vertex position, timing, direction and momentum. The charge contribution from each constituent particle in the event is added and then a simultaneous fit of track parameters is performed, taking automatically into account correlations between parameters, by maximizing the likelihood function:

$$L(x) = \prod_j^{unhit} P_j(unhit|x) \prod_i^{hit} [1 - P_i(unhit|x)] f_q(q_i|x) f_t(t_i|x) \quad (3.4)$$

where the indexes i, j represent the i^{th} , j^{th} PMT, running over the PMTs which are hit or not respectively, x are the parameters in the fit, $P_j(unhit|x)$ is the unhit probability (and therefore $[1 - P_i(unhit|x)]$ is the hit probability), f_q is the charge likelihood (with q_i the charge in the i^{th} PMT) and f_t is the time likelihood (with t_i the time in the i^{th} PMT).

The particle identification of the final state particles is performed by comparing the best-fit likelihood results of the fit under each hypothesis, so that two particles can be distinguished by a cut on the ratio of the best-fit likelihood values for each particle hypothesis as illustrated in Fig. 3.22. Figure 3.22 shows the e/μ separation with this new algorithm, where electron events are represented in blue and muon events in red. A simple cut in $\ln(L_e/L_\mu)$ as a function of the fit momentum, represented by a line in Fig. 3.22, yields an effective e/μ separation, being the misidentification rate $\sim 0.2\%$ for electrons and $\sim 0.85\%$ for muons [116].

The new algorithm is currently used to remove π^0 background events, which are one of the main backgrounds in the ν_e CCQE signal as they are frequently mis-identified as a single electron ring when one of the two γ rings produced in the π^0 decay is not reconstructed (usually due to its low energy). To remove π^0 events, both the reconstructed π^0 mass (m_{π^0}) and the ratio of the best-fit likelihood values of the π^0 and electron fits (L_0/L_e) are used. Figure 3.23 shows the two dimensional distribution of the ratio of the best-fit likelihood values of the π^0 and electron hypothesis $\ln(L_0/L_e)$ vs m_{π^0} for signal CC ν_e events (boxes) and events containing π^0 (blue) in the MC sample, as well as the rejection cut line (red line). Since this new algorithm can reconstruct the low energy γ ring very efficiently, the π^0 background is reduced by $\sim 70\%$ compared with the previous π^0 fit algorithm used [5], which was searching for a second γ ring without using the timing information of the PMTs.

³There are other possible hypothesis, like for instance the π^0 hypothesis with 12 parameters.

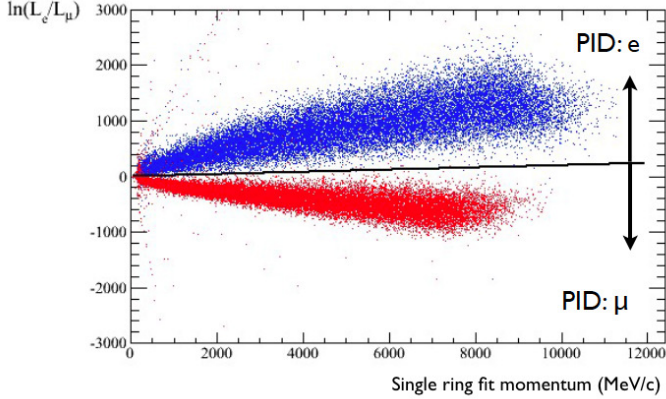


Figure 3.22: Example of the e/μ separation with the new SK reconstruction algorithm, where electron events are represented in blue and muon events in red. The cut in $\ln(L_e/L_\mu)$ as a function of the fit momentum that serves to effectively separate them is represented by a line. Figure from [116].

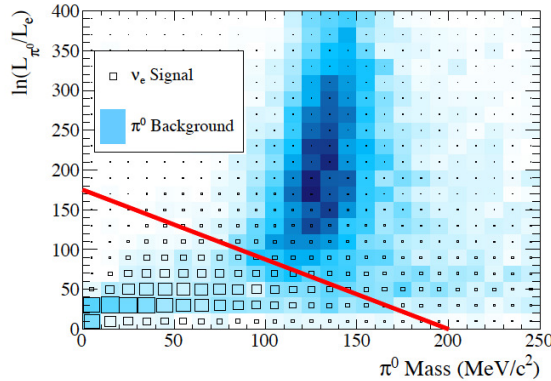


Figure 3.23: Two dimensional distribution of the ratio of the best-fit likelihood values of the π^0 and electron hypothesis $\ln(L_0/L_e)$ vs m_{π^0} for signal CC ν_e events (boxes) and events containing π^0 (blue) in the MC sample, as well as the rejection cut line (red line). Figure from [5].

Chapter 4

T2K Predictions and Measurements for the Joint Oscillation Analysis

In this chapter, a description is given of different T2K predictions and measurements that are used as inputs to the joint oscillation analysis. Firstly, a summary of the T2K beam data taking is presented. The prediction of the flux and spectrum of neutrinos in the T2K detectors (INGRID, ND280 and SK), based on a simulation using different MC packages and combining measurements from the several T2K monitors (of protons, muons and neutrinos) and external hadron production data will be explained along with its uncertainties. Then, the models adopted in the MC simulation of neutrino interactions used for the T2K oscillation analyses will be summarized, as well as the uncertainties related to them. In addition, the measurements performed in the near detector will be described along with the fit performed to constrain the flux and some cross section uncertainties. Finally, the selections made in SK to obtain the neutrino event candidates and the uncertainties and efficiencies in the process will be explained.

4.1 T2K Beam Data Taking Summary

The T2K physics data taking started in January 2010, and since then a total dataset corresponding to 6.57×10^{20} protons on target (POT) has been collected during four run periods until May 2013¹. Table 4.1 presents a summary of the different T2K data taking periods, showing the horn current, beam power and accumulated POT for each of them. The data taking was stopped for about one year due to the

¹More data has been taken afterwards by the T2K experiment, not used for this analysis.

Tohoku earthquake on March 11th 2011 and the recovery work necessary afterwards. The Run3 period is divided into three sub-runs corresponding to different horn currents, with a special run called Run3a (December 2011-January 2012), not used for oscillation analyses, in which the horn current was 0 kA. The beam power has been continuously increasing (see Tab. 4.1) and it will keep augmenting until it reaches the 750 kW design value.

Run #	Period	Horn current (kA)	Beam power (kW)	POT ($\times 10^{20}$)
Run1	Jan. - June 2010	250	50	0.323
Run2	Nov. 2010 - March 2011	250	145	1.108
Run3a*	Dec. 2011 - Jan. 2012	0	190	(0.097)*
Run3b	March 2012	205	190	0.214
Run3c	April - June 2012	250	190	1.365
Run4	Oct. 2012 - May 2013	250	235	3.560
Total	Jan. 2010 - May 2013			6.57

Table 4.1: Summary of the different T2K data taking periods, showing the horn current, beam power and accumulated POT for each of them. *Run3a was not used for oscillation analyses.

Figure 4.1 presents the history of the number of total accumulated protons (blue line) and the number of protons per pulse (red dots), showing the different values of the beam power. During the first data taking period, Run1, there were 6 bunches per beam spill, while 8 bunches were used in subsequent periods.

The horn currents and the proton and neutrino beams were monitored by the different detectors located along the T2K beamline and by the INGRID near detector. The measurements of the T2K neutrino beam intensity and position by INGRID during the four data taking periods is illustrated in Fig. 4.2, which shows on the top plot the stability of the neutrino event rate per 10^{14} protons on target (POT). During a short period of time, called Run3b (March 2012), the horns were working with a current of 205 kA instead of the nominal 250 kA. The bottom part of Fig. 4.2 shows the history of neutrino beam centres in the horizontal and vertical directions measured by the INGRID detector as a function of time. These beam centres are measured in a monthly basis and stay well inside the required range of 1 mrad as maximum angular deviation.

The stability of the neutrino beam position can be also checked in terms of the muon profile measurement performed by MUMON, as it will be shown.

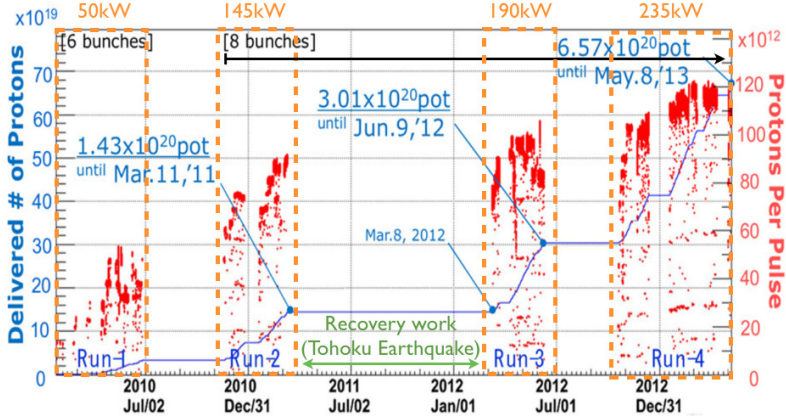


Figure 4.1: History of the number of total accumulated protons (blue line) and the number of protons per pulse (red dots), showing the different values of the beam power. During the first data taking period, Run1, there were 6 bunches per beam spill, using afterwards the 8 bunches structure. Figure from [176].

4.2 T2K Neutrino Flux Prediction

The knowledge of the neutrino flux and spectrum in the T2K detectors (INGRID, ND280 and SK) is essential to predict neutrino interaction rates and thus to perform neutrino oscillation and cross section measurements. The neutrino flux prediction is based on FLUKA (FLUktuierende KAskade) [118] and GEANT3 [119] simulations, and combines data from the several T2K monitors (of protons, muons and neutrinos) and from external hadron production experiments to successfully describe the physical processes occurring from the interaction of protons in the graphite target to the neutrino-producing decays of hadrons and leptons.

4.2.1 Monitor Measurements

The neutrino flux prediction is driven by the measurements of the proton beam profile, the magnetic field produced by the horns and the neutrino beam profile.

The centre position and angle of the proton beam are measured prior to the collision onto the target at the upstream surface of the baffle (placed between the beam window separating the primary beamline and the target station and the Optical Transition Radiation monitor (OTR) as shown in Fig. 4.3), by extrapolating the centre positions measured with the OTR, the electrostatic monitors (ESMs) and the segmented secondary emission monitors (SSEMs). The SSEMs are only

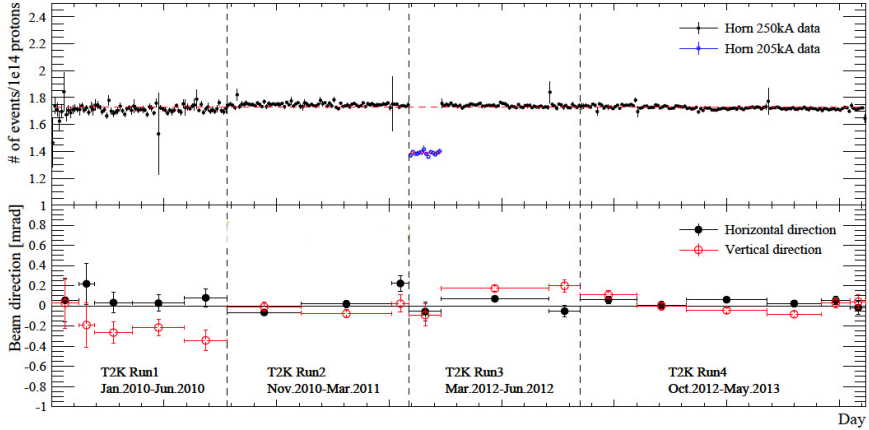


Figure 4.2: Top: History of the neutrino event rate per 10^{14} protons on target (POT) along the four Run periods measured by the INGRID detector as a function of time. During a short period of time, called Run3b (March 2012), the horns were working with a current of 205 kA instead of the nominal 250 kA. Bottom: History of the neutrino beam centres in the horizontal and vertical directions measured by the INGRID detector as a function of time. Figure from [176].

inserted into the beamline to measure the beam profiles for 100 spills when the beam conditions change and removed during data taking since they cause beam loss. The measurements of the proton beam properties at the baffle (centre position, angle, width, emittance and Twiss²) for each run period are obtained by reconstructing them for each spill and summing the spill-by-spill profiles weighted by the number of protons in each spill [83].

The three magnetic horns used in the T2K secondary beamline to collect and focus the positive pions and kaons generated at the target (in neutrino beam mode) are usually operated at a current of 250 kA³. It was observed that the values of the horn current drifted within 2% during the data taking periods [83], most likely due to temperature dependence in the operation of the monitoring hardware, although variations of the actual horn current might still be possible. A detailed description of the design concept of the T2K horn system can be found in [117].

The neutrino beam profile is monitored in two ways: i) a direct measurement of the intensity, stability and direction of the neutrino beam (as illustrated in Fig.

²The Twiss parameters define the shape and orientation of the ellipsoid characterizing the beam phase space of emittance [120].

³There was a short period of time called Run3b (March 2012) when the horns were working with a current of 205 kA instead of the nominal one.

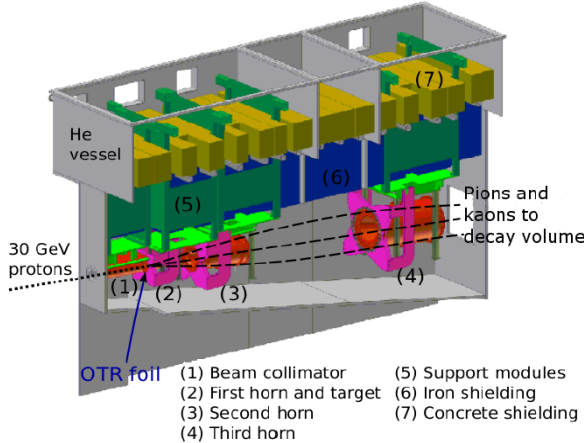


Figure 4.3: Drawing of the T2K target area. Figure from [121].

4.2) is provided by the INGRID detector by means of neutrino interactions in iron as explained in Section 3.3.1; and ii) an indirect measurement is made through the detection of muons at MUMON, which is a muon monitor located right after the beam dump at the end of the secondary beamline, as described in Section 3.2.3. MUMON provides meaningful measurements in a spill-by-spill basis, whereas, at the designed beam power, INGRID it is only able to monitor in a day-by-day basis. Figure 4.4 presents the time history of the measurement of the muon profile centre in the horizontal (top plot) and vertical (bottom plot) directions at MUMON in the first four T2K data taking periods; as observed, all measurements are well controlled within 1 mrad band, as required to maintain the neutrino energy spectrum, which depends on the off-axis angle as illustrated in Fig. 3.4, to the value adequate to achieve the T2K physics goals as explained in Section 3.2.4.

With the previous measurements, a good quality beam data for physics analysis can be selected with the following requirements (besides every hardware component working normally):

- The deviation of all horn currents must be within ± 5 kA with respect to the mean value.
- The deviation of the beam angle measured by MUMON must be within 1 mrad with respect to the mean value.
- The deviation of the total muon yield measured by MUMON must be within $\pm 5\%$ with respect to the mean value.

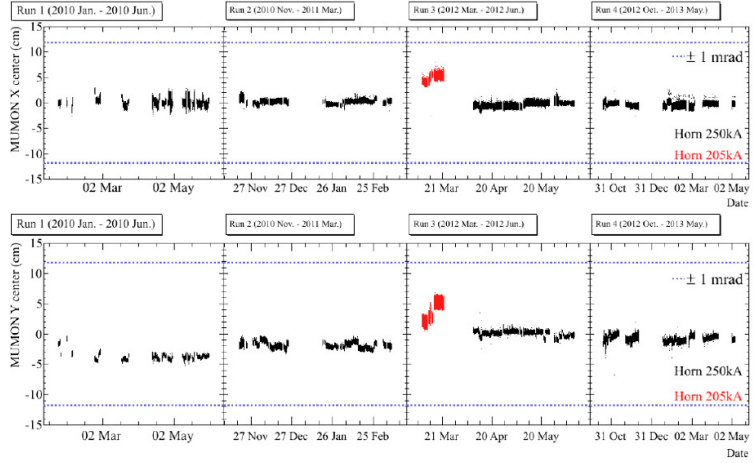


Figure 4.4: Time history of the measurement of the muon profile centre in the horizontal (top plot) and vertical (bottom plot) directions at MUMON in the first four T2K Run periods. As observed, all measurements are well controlled within 1 mrad band (dashed lines). T2K official plot.

4.2.2 Flux Simulation

Based on the measurements of the proton beam profile, the magnetic fields of the horns and the neutrino beam profile, the prediction of the flux and spectrum of neutrinos at the T2K detectors is simulated. This simulation starts with the interaction of primary protons in the target and goes to the final production of neutrinos in the decay of hadrons and leptons, and can be divided into three stages.

Firstly, the interaction of the primary proton beam with the graphite in the target and baffle is simulated using FLUKA 2008.3d, a FORTRAN-based stand-alone Monte Carlo simulation package. The protons are generated with a kinetic energy of 30 GeV, following the measured proton beam spatial distribution and divergence. This package simulates the production of secondary pions and kaons in the target, and it was selected since it has been found to have the best agreement with external hadron production data. The particles emitted are traced until they emerge from the model geometry (a graphite block for the baffle and a graphite cylinder for the target, surrounded by He gas), and their kinematic information is stored and transferred to the next step.

The second step uses JNUBEAM, a Monte Carlo simulation package based on GEANT3 for particle propagation, and GCALOR [122] for hadronic interactions. The geometry of the baffle, target, magnetic horns, helium vessel, decay volume, beam dump and muon monitor is simulated according to the final con-

Particle	Decay products	Neutrino flavour	Branching ratio (%)
π^+	$\rightarrow \mu^+ \nu_\mu$	ν_μ	99.99
	$\rightarrow e^+ \nu_e$	ν_e	1.23×10^{-4}
π^-	$\rightarrow \mu^- \bar{\nu}_\mu$	$\bar{\nu}_\mu$	99.99
	$\rightarrow e^- \bar{\nu}_e$	$\bar{\nu}_e$	1.23×10^{-4}
μ^+	$\rightarrow e^+ \bar{\nu}_\mu \nu_e$	$\nu_e, \bar{\nu}_\mu$	100
	$\rightarrow e^- \bar{\nu}_e \nu_\mu$	$\nu_\mu, \bar{\nu}_e$	100
K^+	$\rightarrow \mu^+ \nu_\mu$	ν_μ	63.55
	$\rightarrow \pi^0 \mu^+ \nu_\mu$	ν_μ	3.35
	$\rightarrow \pi^0 e^+ \nu_e$	ν_e	5.07
K^-	$\rightarrow \mu^- \bar{\nu}_\mu$	$\bar{\nu}_\mu$	63.55
	$\rightarrow \pi^0 \mu^- \bar{\nu}_\mu$	$\bar{\nu}_\mu$	3.35
	$\rightarrow \pi^0 e^- \bar{\nu}_e$	$\bar{\nu}_e$	5.07
K_L^0	$\rightarrow \pi^- \mu^+ \nu_\mu$	ν_μ	27.04
	$\rightarrow \pi^- e^+ \nu_e$	ν_e	40.55

Table 4.2: List of neutrino-producing decays considered in JNUBEAM with their branching ratio in percentage.

structed beamline. The INGRID, ND280 and SK detectors are positioned in the simulation using the latest survey results. Particles are generated in JNUBEAM with the information recorded in the previous step and they are tracked through the horns and helium vessel: they are propagated through the horn magnetic field and may interact with horn material, and then they are propagated through the helium vessel, decay volume and surrounding concrete shield (including the beam dump) either until they interact or decay, or until their kinetic energy drops below 10 MeV. The interaction of the particles with matter is modelled by GCALOR. Neutrinos from particle decays considered, listed in Tab. 4.2, are forced to point to SK or a randomly chosen point in the near detector plane, and their kinematic variables and decay probability, based on the decay phase-space density and branching fraction, are saved. From these simulated events, weighted according to the stored probabilities, the flux and energy spectrum are calculated. The kinematic information of the initial proton and the full interaction chain producing the neutrino are saved to perform the re-weighting in the final stage, including probability, neutrino flavour and energy (assigned in the centre of mass frame based on the decay kinematics, then boosted into laboratory frame).

Finally, the chain of hadronic interactions for each simulated neutrino-producing event (modelled with FLUKA in the target and with GCALOR outside) is used to re-weight each event based on hadron interaction measurements, in order to make

the simulations agree with the measurements of hadronic interactions. Data from different sources is used in this re-weighting process:

- Pion and kaon differential production data is mainly coming from the measurements by the NA61/SHINE [123, 124] experiment at the CERN SPS, where a thin graphite target and a proton beam with the same energy as for T2K were used. The NA61/SHINE data covers most of the hadron production phase space relevant for the T2K flux, more than 90% of the pion phase space and a significant fraction for the K^+ phase space (about 60%) as illustrated in Fig. 4.5. An additional dataset without graphite was used to estimate the contamination from interactions outside the target.
- The model predictions in the phase space for kaons not measured by the NA61/SHINE experiment, i.e. forward production of high energy kaons, is re-weighted using the data from measurements by Eichten et al. [125] and Allaby et al. [126].
- Particle interaction and absorption rates are re-weighted using measurements of the inelastic cross sections for proton, pion and kaon beams with carbon and aluminium targets. Those measurements, which come from different sources, are summarized in [83].
- The measurements by Eichten et al. [125] and Allaby et al. [126] are also used to evaluate systematic uncertainties in secondary nucleon production. Systematic uncertainties associated with tertiary pion production are evaluated using data from the BNL-E910 [127] experiment.

Unlike T2K, whose target is thick, these sources use thin targets in their measurements. Thus, a step-by-step re-weighting procedure is necessary to take into account multiple interactions in the target and interactions outside the target. The calculated weights are applied to:

- Differential production of π^\pm , K^\pm and K_L^0 in the interactions of the primary proton beam with the graphite target.
- Interaction rates for p, π^\pm and K^\pm and attenuation of hadrons that can decay into neutrinos.

Details of the re-weighting processes can be found in [83]; the largest effect at low energies is produced by the pion multiplicity re-weighting whereas at high energies the effect of kaon multiplicity re-weighting dominates.

Figure 4.6 shows the flux prediction up to $E_\nu=10$ GeV, although the flux is simulated up to $E_\nu=30$ GeV, for ND280 off-axis (left) and SK (right) detectors separated by neutrino flavour, result of the flux simulation explained above.

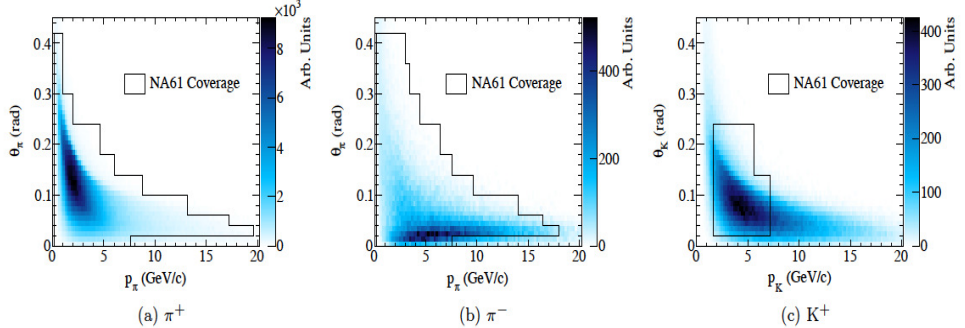


Figure 4.5: The pions (π^+ on the left, π^- on the middle) and kaons (K^+ on the right) phase spaces in terms of production angle vs simulated momentum that contribute to the predicted neutrino flux at SK, with the regions covered by the measurements by the NA61/SHINE experiment overlaid. More than 90% of the pion phase space and a significant fraction for the K^+ phase space relevant for the T2K flux are covered by the NA61/SHINE data. Figures from [83].

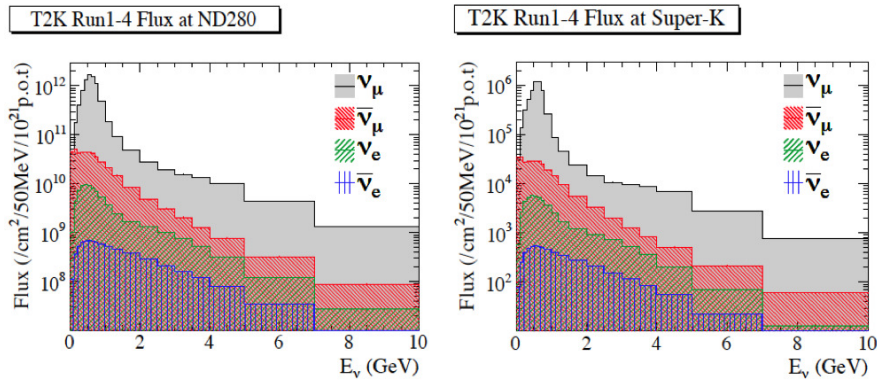


Figure 4.6: The T2K flux prediction for ND280 off-axis (left) and SK (right) detectors separated by neutrino flavour for Run 1-4. Figures from [176].

4.2.3 Flux Uncertainties

The uncertainty on the flux prediction can be grouped into five different sources (ordered according to the steps in the neutrino production) [83]:

- **Proton beam.** The systematic errors for the proton beam centre position and angle (X, θ_X and Y, θ_Y in the horizontal and vertical directions respectively) are due to the position resolution of the proton beam monitors and the uncertainty on their alignment. Their effect on the neutrino flux was studied varying those parameters within their measured errors, taking into account the correlations among different parameters. However, only the vertical centre position (Y) and angle (θ_Y) were found to have a significant effect.
- **Hadron production.** The hadron production uncertainties can be divided into: pion production, kaon production, secondary nucleon production (secondary protons and neutrons which are produced and re-interact in the target) and production cross section uncertainties. Each of them is affected by a variety of uncertainty sources: experimental uncertainties in the data, scaling of the differential production yielding to different incident particle momenta, different target materials due to interactions outside the target, extrapolation to the phase space not covered by data and/or total interaction rate uncertainties. The uncertainty on the SK and ND280 flux was evaluated as a function of neutrino energy by weighting the prediction from the hadron production models used. At low energy, the largest sources of uncertainty on the ν_μ flux are the secondary nucleon production and production cross sections, whereas at high energy the experimental errors on the kaon production dominate. In the future, a ultimate precision on the flux prediction can be achieved through the measurements of hadron emission using a replica of the T2K target (thicker than the current one).
- **Target and horn alignment.** The effect of the uncertainty on the target alignment was studied by rotating the target in JNUBEAM by the observed displacement between the target and the horn axis, surveyed at the downstream end of the target (1.3 mrad in the horizontal plane and 0.1 mrad in the vertical plane). To evaluate the effect of the horn position and angular alignment uncertainties, the effects of horn movements along each coordinate axis and rotations of 0.2 mrad in both horizontal and vertical planes were respectively studied.
- **Horn current and magnetic field.** The total uncertainty on the horn current measurement, combining the uncertainties in the coil calibration and setting, the electronics calibration and the monitor stability, is 1.3 %. The magnetic

field strength, measured using a Hall probe, agrees with the expected nominal field, assumed to have a $1/r$ dependence in the simulation, within 2%. Therefore, the total uncertainty on the absolute field strength is assumed to be 2% (5 kA).

- **Beam direction (off-axis angle).** The effect of the off-axis angle on the neutrino flux is evaluated moving the SK and ND280 detectors in JNUBEAM by 0.4 mrad, the precision on the beam direction achieved by the measurement of the neutrino profile at the INGRID detector.

The effect of these uncertainties on the predicted flux is evaluated by varying the underlying inputs to the flux simulation (such as the hadron production model, the horn currents, etc.) using two approaches. When an error source includes several correlated underlying parameters, re-weighting methods are typically used, in which the underlying parameters are varied according to their covariance and the flux prediction is re-weighted with each set of different values (more than 500 sets are used in general). When a single underlying parameter is enough for evaluating an uncertainty, the flux is typically re-simulated for variations of $\pm 1\sigma$ of the parameter involved. In both cases, the effect on the flux is evaluated by constructing a covariance matrix in bins of neutrino energy, neutrino flavour and detector, using the N re-weighted versions of the flux prediction in the first case, or the re-simulated flux for $+1\sigma$ and -1σ in the second case. The combined total uncertainty on the flux prediction is simply calculated as the sum of the covariances from each independent source of uncertainty. Since the flux covariance is evaluated in bins for near and far detectors, the correlations between the flux prediction at both sites are included, and therefore this covariance can be used directly as extrapolation method or to calculate the uncertainty on a far-to-near ratio.

Figure 4.7 shows an example of the total fractional error in muon neutrino flux at ND280 (left) and SK (right) and its breakdown into different sources of uncertainty, overlaying the MC statistical error, for the first four data taking periods. The value of the total fractional error is typically $\sim 12\%$ around the peak energy for the near and far detectors, dominated by the uncertainties on the hadronic interactions. Around the flux peak there is a significant contribution from the off-axis angle and proton beam uncertainties, since variations of those parameters produce a shift in the peak position of the flux in energy as illustrated in 3.4 (left).

The flux correlations for each neutrino flavour, energy and detector (near and far) bins used in the evaluation of the flux covariance are shown in Fig. 4.8. The correlation and covariance matrices are constructed with 20 true neutrino energy bins for each neutrino flavour ($\nu_\mu, \bar{\nu}_\mu, \nu_e, \bar{\nu}_e$) and detector (near and far detector) which are defined by the following bin edges:

$$E_\nu^{true} (\text{GeV}/c) = [0.0, 0.1, 0.2, 0.3, 0.4, 0.5, 0.6, 0.7, 0.8, 1.0, 1.2, 1.5, 2.0, 2.5, 3.0, 3.5, 4.0, 5.0, 7.0, 10.0, 30.0]$$

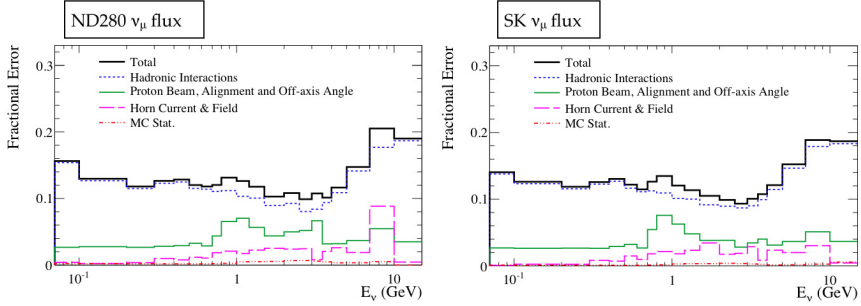


Figure 4.7: Example of the total fractional error in muon neutrino flux at ND280 (left) and SK (right) and its breakdown into different sources of uncertainty, overlaying the MC statistical error, for Run 1-4. The value of the total fractional error is typically $\sim 15\%$ around the peak energy for the near and far detectors, dominated by the uncertainties on the hadronic interactions. Figures from [176].

From this correlation matrix it is clear that there are significant correlations between the ν_μ flux in the near and far detector, which make possible to constrain the uncertainties on the flux in the far detector with a measurement in the near detector; and between ν_μ and ν_e fluxes through the hadron interaction uncertainties, indicating that the measurement of the ν_μ flux can constrain the ν_e contamination in the beam.

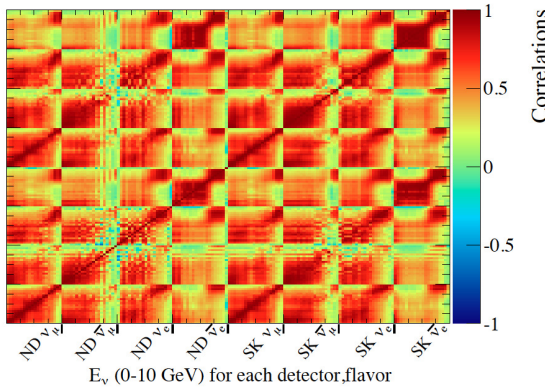


Figure 4.8: The flux correlations for each neutrino flavour, energy and detector (near and far) bins used in the evaluation of the flux covariance (binning in Y and X axis are identical, described in the text). T2K official plot.

The far/near ratio for the flux prediction and its uncertainty can be also calculated from the flux covariance. As shown in Fig. 4.9 taken from [83], the uncertainty on the ratio between the flux predictions at the far and near detectors for the ν_μ flux is $\sim 2\%$ around the energy peak and less than 6% for all energies.

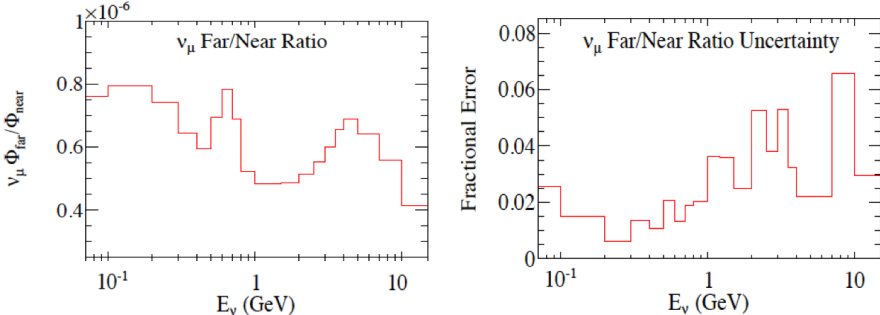


Figure 4.9: The ratio between the flux predictions at the far and near detectors of the ν_μ flux (left) and the uncertainty on the ratio (right). Figures from [83].

4.3 T2K Neutrino Interaction Models

The flux prediction previously described is given as input to a neutrino interaction generator to simulate interactions and predict the event rates at the near and far detectors. The neutrino interaction generator typically used in T2K is NEUT [128], which models neutrino interactions on different nuclei over a range of energies from ~ 100 MeV to ~ 100 TeV, although the GENIE [129] generator was also used in several occasions as an additional cross-check. The results presented in this work, including Chapter 5, were based on the NEUT generator (version 5.1.4.2).

4.3.1 Interaction Models in NEUT

Neutrino interactions in the T2K experiment are simulated using the NEUT neutrino interaction generator [128].

The dominant interaction at the T2K peak energy, as shown in Fig. 3.6, is the charged current quasi-elastic scattering (CCQE), accounting for $\sim 40\%$ of the interactions at ND280 and SK and for up to $\sim 80\%$ of the events passing the ν_e selection cuts at SK (assuming $\sin^2(2\theta_{13}) = 0.1$). This interaction is described by the first Feynman diagram in Fig. 4.10 (left), which represents the process: $\nu_l + n \rightarrow l^- + p$, where l^- is the charged lepton associated to the ν_l neutrino.

Around the T2K beam peak energy there is also an important contribution from single pion producing modes, simulated through the excitation of hadronic resonances for events above the pion production threshold, both from charged current interactions ($\text{CC}1\pi^\pm$, with a fraction of $\sim 16\%$ of the ν_e events at SK) described by the Feynman diagram in Fig. 4.10 (middle) and neutral current interactions ($\text{NC}1\pi$).

Other interactions, such as multi-pion and deep inelastic scattering (DIS) processes described by the Feynman diagram in Fig. 4.10 (right) are dominant at the high energy tail of the T2K flux as shown in Fig. 3.6.

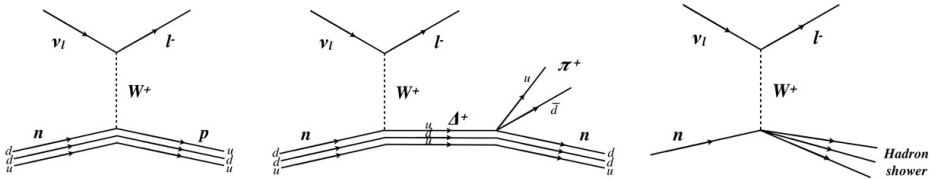


Figure 4.10: Feynman diagrams for charged current nucleon-neutrino interaction modes: charged current quasi-elastic scattering (CCQE) on the left, charged current single charged pion interaction ($\text{CC}1\pi^\pm$) via resonance production in the middle and deep inelastic scattering (DIS) on the right.

The simulation of the interactions of neutrinos with nuclei in NEUT can be divided in two steps: simulation of final state particles and propagation as they traverse the nucleus.

First, neutrino-nucleon interactions are simulated at the interaction vertex and the particles at the final state are determined, following different theoretical models tuned to external neutrino data.

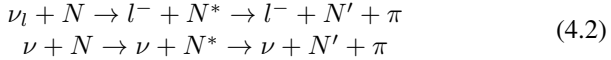
- **Charged Current Quasi Elastic (CCQE).** CCQE interactions are simulated in NEUT using the Llewellyn Smith model [130], with an amplitude described by the product of the hadron and lepton weak currents [131]:

$$T = \frac{G_F}{\sqrt{2}} \bar{u}_l(k_2) \gamma^\mu (1 - \gamma_5) u_\nu(k_1) \langle N'(p_2) | J_\mu^{hadron} | N(p_1) \rangle \quad (4.1)$$

where G_F is the Fermi coupling constant and $p_1(p_2)$ and $k_1(k_2)$ are the initial (final) four-momentum of the nucleon and lepton respectively. The vector and axial-vector form factors in terms of which the hadronic weak

current J^{hadron} is expressed are assumed to have dipole forms, with default characteristic masses of $M_V = 0.84$ GeV and $M_A = 1.21$ GeV respectively. The vector form factors have been precisely measured by electron scattering experiments, but there are inconsistencies between different neutrino experiments for the axial-vector form factors. The default nuclear model used is the **relativistic Fermi gas (RFG) model** of Smith and Moniz [132, 133], with the Fermi surface momentum p_F set to 217 MeV/c (225 MeV/c) and binding energy E_B set to 25 MeV (27 MeV) for carbon (oxygen) nuclei, taking into account Fermi motion of the target nucleon and the Pauli blocking effect, which requires that the outgoing nucleon must have momentum above p_F . A more realistic nuclear model, called **Spectral Function** [134, 135], is being currently included in the T2K simulations as it will be mentioned later.

- **Single pion production (CC1 π and NC1 π).** Single-pion production is simulated in NEUT via excitation of hadronic resonances using the model of Rein and Sehgal [136], in which the single-meson production occurs in two steps, assuming an intermediate resonance N^* :



for the charged current (top) and neutral current (bottom) processes. The simulation of resonance production includes 18 resonances below 2 GeV, along with interference terms, and is dominated by the $\Delta(1232)$ in the energy range relevant for T2K. NEUT also considers de-excitation of the Δ resonances in the nuclear medium without the emission of pions, in which the Δ interacts with a nucleon before it decays, simulating a pion-less Δ decay for 20% of the Δ 's produced. The process of **coherent production of pions**, in which a neutrino interacts with a nucleus X as a whole and produces a pion coherently through $\nu_l + X \rightarrow l^- + \pi^+ + X$, are also simulated in NEUT following Rein and Sehgal model [137]. This process is only possible if the momentum transfer to the nucleus is small, resulting in only a recoil of the nucleus, that remains in the ground state, and tending to produce forward-going pions [138].

- **Multi-Pion and Deep Inelastic Scattering (DIS).** These interactions, corresponding to the process $\nu + N \rightarrow l(\nu) + N' + hadrons$, are simulated in NEUT using Glück-Reya-Vogt-1998 (GRV98) parton distribution functions [139] to calculate their cross section. The final states containing multiple hadrons are simulated in two different ways depending on the

invariant mass of the hadronic system W . A custom program made by the Kamiokande Collaboration [140] is used for the interval $1.3(GeV/c^2) < W < 2.0(GeV/c^2)$, whereas PYTHIA/JETSET [141] is used for $W > 2.0(GeV/c^2)$. Corrections proposed by Bodek and Yang are applied to the small Q^2 region [142]. In order to avoid double counting processes that produce a single pion, the invariant hadronic mass is restricted to be $W < 2.0GeV/c^2$ in the calculation through a resonance described above, and the calculation of the DIS cross section includes in the $W < 2.0GeV/c^2$ region the probability to produce more than one pion only.

As second step, the NEUT **cascade model** is used to simulate the propagation and interaction of final state hadrons (mainly pions and protons) through the nucleus in which they were formed. These **final state interactions (FSI)** can affect the total number of particles observed and their kinematics. In the cascade model, hadrons are propagated through the nuclear medium in finite steps, until an interaction happens or the hadron escapes the nucleus. For each step, an interaction probability is calculated following two different methods depending on the momentum of the particle. For momenta above 500 MeV/c, the nucleons are assumed to be quasi-free and the scattering cross section is modelled using experimental results of scattering of pions on free protons [143], weighted by the nuclear density. Below 500 MeV/c, the method of Salcedo et al. [144] is used to calculate the interaction probability per step, which is a Δ -hole model performing a microscopic, many-body calculation including Pauli blocking and local density approximation for the nuclei.

Particles escaping the nucleus are passed to the GEANT4 [145] or SKDET-SIM (GEANT3-based [119]) simulation packages for ND280 and SK detectors respectively. Inside the detector, the interaction of particles (pion **secondary interactions (SI)**) is simulated with the same cascade model used in NEUT. The **photo-nuclear (PN)** effect [146, 147], describing the absorption of photons by the nucleus in the detector before they convert to e^+e^- pairs and going undetected, is introduced in the simulation as well.

4.3.2 Cross Section Uncertainties

The uncertainties in the neutrino interaction modelling are a significant contribution to the total systematic error in the oscillation analyses. These uncertainties are taken into account through some systematic parameters related to variations in the NEUT neutrino interaction models. Some of the cross section parameters are tuned with external datasets, and some of them are constrained by a fit to the ND280 data.

The cross section parameters used are grouped by interaction type:

CCQE Cross Section

- M_A^{QE} : This is the characteristic mass in the axial-vector dipole form factor for CCQE interactions. The uncertainty on this parameter is driven by the fit to MiniBooNE data that will be explained later.
- **CCQE Normalization:** The normalization of the CCQE cross section separated in three parameters for different energy regions: CCQE E0 for $E_\nu < 1.5$ GeV, CCQE E1 for $1.5 \text{ GeV} < E_\nu < 3.5 \text{ GeV}$ and CCQE E2 for $E_\nu > 3.5 \text{ GeV}$. Below 1.5 GeV the uncertainty of 11 % reported by MiniBooNE [148] was assigned, while a 30 % error was assigned to the parameters above 1.5 GeV to account for the discrepancy in the CCQE cross section between NOMAD [149] at ~ 10 GeV and MiniBooNE at ~ 1 GeV.

Nuclear Model (for CCQE Interactions)

- p_F : The Fermi surface momentum in the relativistic Fermi gas (RFG) model, with central values and uncertainties determined from electron scattering data [150]. The uncertainty for this parameter is assumed to be the ± 30 MeV/c this parameter can be varied inside NEUT.
- E_B : The binding energy in the RFG model, with central values and uncertainties also determined from electron scattering data [150]. The uncertainty for this parameter is assumed to be the ± 9 MeV this parameter can be varied inside NEUT.
- **SF**: This parameter accounts for the difference between the two nuclear models: it switches from the RFG to the Spectral Function (SF) model, which is a more sophisticated and realistic model, as it includes correlations between nucleons and defines the probability distribution of nucleon momenta and binding energies within the nucleus, instead of using a uniform distribution of nucleons with a constant binding energy like in the RFG model. Since the SF model it is not yet implemented in NEUT, the uncertainty is evaluated by comparing RFG with the SF model implemented in the NuWro generator [151].

Resonant Pion Production Cross Section

- M_A^{RES} : Characteristic mass in the axial-vector dipole form factor for resonant pion-producing interactions. The uncertainty on this parameter is driven by the fit to MiniBooNE data.
- **CC1 π Normalization:** Separated in two parameters for different energy regions: CC1 π E0 for $E_\nu < 2.5$ GeV and CC1 π E1 for $E_\nu > 2.5$ GeV. For CC1 π normalization above 2.5 GeV, a conservative 40% error is assigned motivated by NOMAD data [149]. The uncertainty for the low energy parameter is driven by the fit to MiniBooNE data.
- **NC1 π^0 Normalization:** The uncertainty on this parameter is driven by the fit to MiniBooNE data.
- **NC1 π^\pm Normalization:** An uncertainty of 30 % is assumed for this parameter based on the few measurements of neutral current charged pion at the T2K energy made by experiments at Argonne [152] and Gargamelle [153].
- **π -less Δ :** This parameter accounts for the uncertainty on the fraction of de-excitations of the Δ resonances in the nuclear medium without the emission of pions, pion-less Δ decays, occurring when the Δ interacts before it decays. They are considered in NEUT and assumed to be 20% of the Δ 's produced, with an error of 20% independent of energy and target.
- **W shape:** This parameter varies the distribution of invariant mass of the hadronic system (W) in the resonant production model in NEUT, accounting for the uncertainty on the shape of the initial pion momentum distribution (before final state interactions) for NC1 π^0 events. The function used to re-weight these events is defined as:

$$r(W, \Gamma) = \alpha \frac{\Gamma}{(W - M_{N^*})^2 + \Gamma^2/4} P(W; m_\pi, m_N) \quad (4.3)$$

where Γ is the parameter to change its shape, α is a normalization factor to keep the total cross section unchanged, $P(W; m_\pi, m_N)$ is the phase space for two body decay of a particle with mass W into particles with masses m_π and m_N and $M_{N^*} = 1218$ MeV. The uncertainty for this parameter (52%) is defined as the difference between its nominal value (87.7 MeV) and the best-fit value found with the fit to MiniBooNE data.

Other

- **CC coherent Normalization:** Since K2K [154] and SciBooNE data [155] indicated a much less coherent charged pion production by neutrinos below 2 GeV than predicted by models, a 100% uncertainty is assumed for the CC coherent normalization.
- **NC coherent Normalization:** A 30% uncertainty is assigned to the NC coherent normalization factor, estimated from a 15% discrepancy between NEUT and SciBooNE together with a 20% systematic error in those data [156].
- **NC other Normalization:** The same uncertainty of 30% as for $\text{NC}1\pi^\pm$ is assigned to this parameter.
- **CC other shape:** This parameter represents the uncertainty on the CC multi-pion, CC DIS, CC resonant η , K and photon production cross sections. Its uncertainty is taken from MINOS data [157], which gives an error or $\sim 10\%$ for 4 GeV; assuming the error decreases with the neutrino energy ($0.4 \text{ GeV}/E_\nu$)⁴ the error is assigned to be 40% for T2K beam energy.
- **ν_e/ν_μ :** This parameter varies the ratio of the CC ν_e and ν_μ cross sections, with an overall uncertainty of 3% assigned based on calculations over the energy range for T2K [158].
- **$\bar{\nu}/\nu$:** This parameter varies the ratio of the CC $\bar{\nu}$ and ν cross sections. An uncertainty of 20% was assumed for this parameter as a conservative estimation of the difference between the neutrino and anti-neutrino cross sections, based on the latest measurements of anti-neutrino cross sections from MiniBooNE [159] and MINERvA [160].

To constrain the CCQE parameters, the NEUT model was fitted to the MiniBooNE CCQE double-differential cross sections in bins of muon kinetic energy and angle ($T_\mu, \cos \theta_\mu$) [148], following the procedure described in [161]. This fit was intended to complement the information provided by ND280 data, since MiniBooNE data includes backward going muons. However, the best-fit value obtained for M_A^{QE} was significantly larger (1.64 ± 0.04 GeV) than the value obtained by the MiniBooNE collaboration (1.35 ± 0.17 GeV) and the fit poorly reproduced the energy dependency, so the results of this fit were not used directly. Instead, the value of M_A^{QE} was set to the default value in NEUT (1.21 GeV), increasing its uncertainty to the difference with the best fit value obtained from the fit to MiniBooNE (0.43 GeV), and then the fit to ND280 data was performed (see Section 4.4).

⁴Since the threshold for these interactions is ~ 600 MeV, this expression can be assumed with no risk of divergence.

On the other hand, to constrain single pion production parameters, a joint fit was performed to the MiniBooNE CC1 π^+ , CC1 π^0 and NC1 π^0 cross section measurements on light nuclei [162, 163, 164] for the T2K energy range. The fit results were checked with the K2K measurement [165]. The samples in this case were selected based on the presence of a single pion exiting the nucleus in the event, following the definitions used for MiniBooNE samples, instead of using the information of particles produced in the neutrino interaction vertex. The fit was performed to the measured $d\sigma/dQ^2$ spectra from CC1 π^+ and CC1 π^0 samples and the $d\sigma/dp_{\pi^0}$ spectrum from the NC1 π^0 samples, taking into account the uncertainties provided as covariance matrices by MiniBooNE. Figure 4.11 shows the $d\sigma/dQ^2$ spectrum from CC1 π^0 samples on the left and $d\sigma/dp_{\pi^0}$ spectrum from the NC1 π^0 samples on the right for MiniBooNE data with the NEUT nominal and tuned to the best-fit values of the parameters. The nine parameters included in the single pion fits are M_A^{RES} , W shape, CC other shape and the normalizations for CC1 π , CC coherent, NC coherent, NC1 π^0 , NC1 π^\pm and NC other. However, not all of these parameters can be constrained separately by the MiniBooNE data, although the fit can reduce the total parameter space through correlations. The values of M_A^{RES} , NC1 π^0 and CC1 π normalization for low energies were constrained by the fit to the MiniBooNE data. The best-fit values obtained, shown in Tab. 4.3 are used to tune NEUT, and the discrepancy still existing between the tuned NEUT and K2K data is covered by the uncertainties on the single pion production and FSI model. A penalty term was added for the parameters that cannot be directly constrained by the single pion fits to MiniBooNE data to prevent the values of these parameters getting far away from their default values.

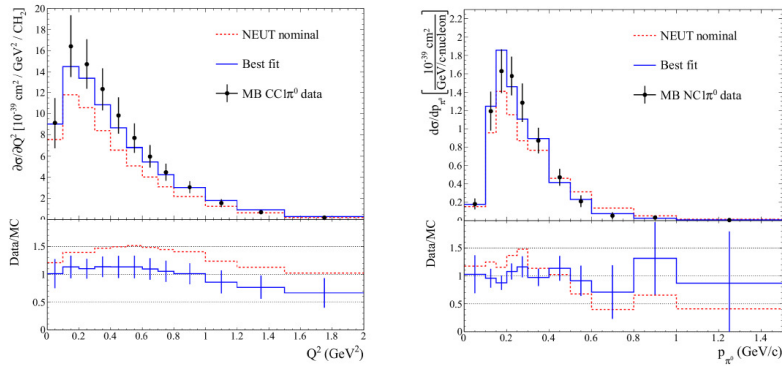


Figure 4.11: Fit to MiniBooNE data for single pion production cross sections: $d\sigma/dQ^2$ spectrum from CC1 π^0 samples on the left and $d\sigma/dp_{\pi^0}$ spectrum from the NC1 π^0 samples on the right. Figure from [166].

Most of the cross section nuisance parameters are absolute normalizations, overall weights that change the nominal prediction of each interaction category independently of energy; among them, two normalizations account for differences between neutrino flavours (ν_e/ν_μ and $\bar{\nu}/\nu$). Other parameters change the absolute normalization and the energy dependence of the interaction cross section, and for them response functions are built for each neutrino flavour, interaction, true and reconstructed energy by a re-weighting method. This method allows to account for variations in the models without re-generating the MC: for a variation in a parameter and for each event, a weight is calculated as the ratio between the nominal value of the cross section and the updated value after the change in the parameter. Then, applying these event-by-event weights to the MC sample works in the same fashion as re-generating the sample, but much faster as it avoids detector simulation and reconstruction processes, and has been validated against re-generated MC samples changing the values of the parameters. In order to save time in our oscillation analyses, response functions with averaged weights are stored for each event interaction mode, flavour, true and reconstructed energy in the MC samples for different values of each parameter, avoiding in this way to run the re-weight process any time a parameter value is varied in our analysis.

Another division for these cross section nuisance parameters can be made according to the detector where the interactions they affect occur. Since neutrino interactions are on different nuclei at ND280 (carbon) and SK (oxygen), some of the cross section parameters described, the ones related to the nuclear model, are only relevant to one of the detectors; whereas others, describing the underlying physics of neutrino interactions independently on the target nucleus, are common to interactions in both the near and the far detector. The axial masses (M_A^{QE} and M_A^{RES}) and the normalizations are correlated between ND280 and SK, and therefore a fit to the ND280 data can constrain the values of these parameters at SK⁵. The parameters related to the nuclear model, p_F , E_B and SF, are not correlated since ND280 and SK have different target nuclei.

Table 4.3 presents a summary of the cross section uncertainties, indicating if they are normalizations or they need response functions (splines), which interaction is affected by them, if they are correlated between ND280 and SK and their input values and uncertainties before the fit to the near detector data (but after the fits to external data, essentially MiniBooNE).

⁵Only the normalizations for CCQE, CC1 π and NC1 π^0 are constrained by the fit to the ND280 data, as it is not sensitive to the rest.

Parameter	Type	Interaction	ND280/SK correlation	Nominal Value	Input Error
M_A^{QE}	shape	CCQE	✓	1.21 (GeV)	37%
M_A^{RES}	shape	CC+NC 1π	✓	1.41 (GeV)	18%
CCQE E0	norm	CCQE	✓	1	11%
CCQE E1	norm	CCQE	✓	1	30%
CCQE E2	norm	CCQE	✓	1	30%
CC 1π E0	norm	CC 1π	✓	1.15	32%
CC 1π E1	norm	CC 1π	✓	1	40%
NC $1\pi^0$	norm	NC $1\pi^0$	✓	0.96	33 %
p_F (^{12}C)	shape	CCQE	-	217 (MeV/c)	14%
p_F (^{16}O)	shape	CCQE	-	225 (MeV/c)	13%
E_B (^{12}C)	shape	CCQE	-	25 (MeV)	36%
E_B (^{16}O)	shape	CCQE	-	27 (MeV)	33%
Spectral function	shape	CCQE	-	0 (OFF)	1 (ON)
π -less Δ decay	shape	CC+NC π	-	0	20%
W shape	shape	NC π	-	1	52%
CC other shape	shape	CC other	-	0	40%
CC coherent	norm	CC coherent	-	1	100%
NC $1\pi^\pm$	norm	NC $1\pi^\pm$	-	1	30%
NC coherent	norm	NC coherent	-	1	30%
NC other	norm	NC other	-	1	30%
$\sigma_{\nu_e}/\sigma_{\nu_\mu}$ ratio	norm	ν_e CC	-	1	3%
$\sigma_{\bar{\nu}}/\sigma_\nu$ ratio	norm	$\bar{\nu}$ CC	-	1	20%

Table 4.3: List of cross section uncertainties indicating type, the interaction they affect, correlation between near and far detector and input value and uncertainties before the ND280 fit (but after the fits to external data).

4.3.3 Final State, Secondary and Photo-Nuclear Interaction Uncertainties

The NEUT model for FSI includes parameters to alter the microscopic pion interaction probabilities in the nuclear medium. Parameters for absorption, charge exchange, QE scattering and inelastic scattering are considered. While charge exchange and QE scattering are considered for all pion momenta (divided into two parameters for low and high momenta), absorption is only considered below 500 MeV/C and inelastic scattering above 500 MeV/c. Fits to pion scattering data are used to evaluate those parameters and their uncertainties [167, 168, 169], giving 16 sets of FSI parameters. The effect of these parameters on the predicted event rates

at ND280 and SK is evaluated by applying weights according to the set of values of the parameters, varying them within their uncertainties from the fit of the pion scattering data, to some observables and calculating the covariance matrix of those predicted observables. Thus, the covariance matrix for ND280 is computed in terms of the two reconstructed parameters used for the ND280 data selection, the momentum and angle of the muon candidate ($p_\mu, \cos \theta_\mu$), whereas for SK bins in reconstructed neutrino energy E_ν^{reco} or reconstructed momentum and angle (only in the ν_e selection) are used depending on the analysis. The covariance matrix is calculated with:

$$V_{ij} = \frac{1}{16} \sum_{k=1}^{16} (p_i^{nom} - p_i^k)(p_j^{nom} - p_j^k) \quad (4.4)$$

where p_i^k is the predicted event rate in the observable i assuming the k -th set of FSI parameters, and p_i^{nom} is the predicted nominal event rate for the observable i .

The parameters for ND280 are included in the fit to ND280 data and marginalized, and the parameters for SK are included in the oscillation fit as it will be explained in Section 5.5.

After leaving the nucleus in which they were formed, pions can interact with other nuclei in the detector, being these interactions called secondary interactions (SI). They are handled in the SK detector simulation using the same cascade model used in NEUT, and their uncertainties are evaluated similarly to the FSI uncertainties, by varying the pion interaction probabilities in the cascade model. They are calculated separately and then combined with the FSI systematic uncertainties at the oscillation analysis level as it will be explained in Section 5.5.

The model for the emission of photons by the de-excitation of nucleus has been updated in the detector simulation to include the absorption of photons by the nucleus, called photo-nuclear (PN) effect. This process affects the detection of π^0 events, since it produces events in which one photon is absorbed and therefore undetected. For this reasons, the uncertainty due to these events has been evaluated for the ν_e selection, obtaining a covariance matrix which is also combined with the FSI and SI systematics.

4.4 Near Detector Fit to Constrain Flux and Cross Section Uncertainties

The flux MC simulation is typically used combined with near detector data to predict the flux at the far detector. The estimates of the uncertainties on the flux and some cross section parameters, based initially on the beam monitors and NA61 data and on fits to external data (essentially from MiniBooNE) respectively, are expected to decrease due to cancellations between ND280 and SK. Thus, a fit to the near detector data can constrain the flux and some of the cross section uncertainties as it will be described in this chapter, whose result is named BANFF output (Beam And ND280 Flux extrapolation task Force), nomenclature that will be used for convenience in the following chapters.

4.4.1 ND280 Data

A sophisticated simulation of the ND280 near detector is implemented based on GEANT4, combining the flux model and the NEUT interaction model previously described with a detailed simulation of the materials and geometry of its different parts, including electronics response, noise and other features such as photon reflections and attenuation in the FGDs and gas ionization and electron diffusion in the TPCs. Then, neutrino event rates and energy spectra are measured by ND280, and this data is used to constrain the flux and some cross section uncertainties in the far detector measurement.

At the ND280 detector, enhanced ν_μ CC data is selected applying a set of cuts, and then is divided into three categories according to the number of pions in each sample. The CC-inclusive data sample is selected using the ND280 tracker reconstruction (other ND280 sub-detectors might be used in the future to improve this selection), requiring a negative muon track present applying the following cuts:

- **Data quality flag.** Only events with all the ND280 off-axis sub-detectors working properly are considered.
- **Time bunching.** Tracks are grouped in bunches according to their times, within 60 nsec from the bunch mean time, effectively eliminating accidental pile-up of events or overlapping events (essentially beam events coinciding with sand muons).
- **One negative track.** There must be at least one good quality (more than 18 vertical TPC clusters) negative track (according to its curvature) starting in the fiducial volume (FV) of FGD1, which is defined by excluding five

scintillator bars (58 mm) at the edges of X and Y layers, using therefore the central 182 bars out of the total 192 bars in the X and Y layers, and excluding the most upstream XY scintillator plane (21 mm) in the Z direction, including the remaining 14 XY modules. The vertex of the track is usually found as the intersection point between the fitted 3D track and the vertical plane of the most upstream FGD hit. If there are more than one negative track, the one with the highest momentum is selected as the muon candidate.

- **Upstream veto.** In order to remove mis-reconstructed events with a particle produced upstream of FGD1 but reconstructed in the FGD1 fiducial volume, it is required that the start position of the highest momentum track which is not the muon candidate must be less than 150 mm upstream from the start position of the muon candidate track.
- **Broken tracks.** This cut is applied to remove external background events in which the muon candidate starts at the downstream edge of FGD1 (two outermost layers) being a piece of a broken track. The cut rejects events with the presence of a “FGD1-only” track (with segments only in the FGD1) with its start position outside FGD1 FV.
- **Muon PID.** The muon TPC particle identification (PID) criteria is applied to the track that has passed the previous cuts, using the dE/dx distribution estimated as a truncated mean⁶ of the energy deposited in the TPC, and comparing it with the expected distribution for the different particle hypothesis of electrons, muons, pions and protons through the pull defined as:

$$Pull_i = \frac{(dE/dx_{measured} - dE/dx_{expected}^i)}{\sigma(dE/dx_{measured} - dE/dx_{expected}^i)} \quad (4.5)$$

To check which particle type is the most probable for a given track (assuming equal priors), the probability of being one particle is defined as the ratio $P_i = \frac{Prob_i}{\sum_j Prob_j}$, where

$$Prob_i = \frac{e^{-Pull_i^2/2}}{\sum_j e^{-Pull_j^2/2}} \quad (4.6)$$

is the Gaussian probability for a given pull value $Pull_i$.

⁶The truncated mean is computed using the 70% least energetic clusters forming a track.

The ν_μ CC-inclusive sample (with a $\sim 91\%$ efficiency of selecting true ν_μ CC-inclusive interactions) is afterwards split according to the number of pions in the event into CC0pi (no pions observed), CC1pi (only one pion observed) and CCother (more than one pion observed) enriched samples, in order to enhance the ability to constraint the CCQE and resonant single pion cross section parameters. The existence of pions in the final state is determined by the PID of the tracks combined with the appearance of delayed hits in the FGDs, which are hits occurring not in time with a beam bunch window and an indication of Michel electrons, electrons coming from the decay of muons, hint in turn of pions in the event. The purity for the samples is calculated using the true information from the MC data selected with these cuts. The muon purity in the CC-inclusive sample is $\sim 90\%$. In summary, this is the division of the CC-inclusive sample:

- **CC0pi.** This sample is defined by the requirement of no pions present in the event final state. Therefore, there must be no tracks in the TPC or the FGD compatible with pions, and no delayed hits in the FGDs. Events with electron or positron TPC tracks are also rejected as they might be generated by CC1 π^0 or NC1 π^0 interactions. The events in this category are mainly CCQE, with a purity of $\sim 64\%$, and CC1 π events where the pion was absorbed in the final state interaction.
- **CC1pi.** This sample is defined by requiring a negative muon and a positive pion in the final state, so the events selected in this category must contain exactly one positive pion. The requirements for this selection is either i) a positive pion track together with the muon candidate track, no delayed hits in FGD (that would indicate the presence of another π^+) and no tracks compatible with e^- , e^+ or π^- ; or ii) delayed hits in the FGD indicating one Michel electron (no more than one) and no positive pion tracks reconstructed. The purity for CC resonance events in this category is $\sim 40\%$.
- **CCother.** This category contains the rest of CC events not included in the previous two samples. The purity for CC deep inelastic scattering (DIS) events in this category is $\sim 68\%$.

Figure 4.12 shows the ND280 data distributions in $(p_\mu, \cos \theta_\mu)$ for CC0pi (left), CC1pi (middle) and CCother (right) with the binning used defined by the edges:

- p_μ for CC0pi and CCother (GeV/c) = [0, 0.3, 0.4, 0.5, 0.6, 0.7, 0.8, 0.9, 1.0, 1.25, 2.0, 3.0, 5.0, 30.0]
- p_μ for CC1pi (GeV/c) = [0, 0.3, 0.4, 0.5, 0.6, 0.7, 0.8, 0.9, 1.0, 1.25, 1.5, 2.0, 5.0, 30.0]
- $\cos \theta_\mu$ = [-1.0, 0.6, 0.7, 0.8, 0.85, 0.9, 0.92, 0.94, 0.96, 0.98, 0.99, 1.0]

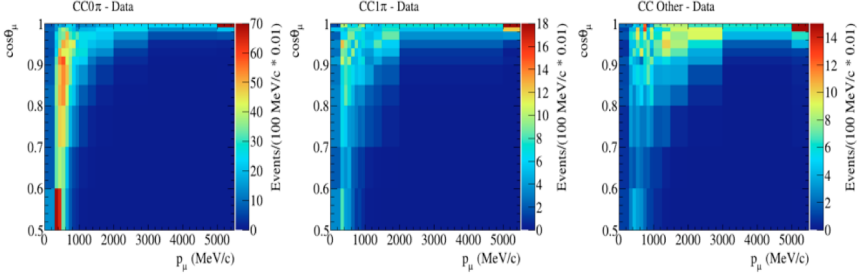


Figure 4.12: The ND280 2-dimensional distributions in $\cos\theta$ vs momentum of the muon candidate for the CC0pi (left), CC1pi (middle) and CCother (right) selected data. T2K official plots.

4.4.2 ND280 Data Fit and Detector Uncertainties

The fit to the ND280 data described in the previous section is performed by minimizing using MINUIT [170] a χ^2 function constructed as a likelihood ratio, where the likelihood function includes the binned likelihood for the ND280 data, the prior constraints on the flux and interaction models and the contribution from the detector systematics. The χ^2 function is described by the following equation:

$$\begin{aligned}
 \chi^2 &= -2 \ln(L_{total}) \\
 &= 2 \sum_i^{(p,\cos\theta)bins} N_i^{pred}(\vec{b}, \vec{x}, \vec{d}) - N_i^{data} + N_i^{data} \ln \left[\frac{N_i^{data}}{N_i^{pred}(\vec{b}, \vec{x}, \vec{d})} \right] \\
 &\quad + \sum_i^{E_\nu bins} \sum_j^{E_\nu bins} (1 - b_i)(V_b^{-1})_{i,j}(1 - b_j) \\
 &\quad + \sum_i^{N_{xsec}} \sum_j^{N_{xsec}} (x_i^{nom} - x_i)(V_x^{-1})_{i,j}(x_j^{nom} - x_j) \\
 &\quad + \sum_i^{(p,\cos\theta)'bins} \sum_j^{(p,\cos\theta)'bins} (d_i^{nom} - d_i)(V_d^{-1})_{i,j}(d_j^{nom} - d_j)
 \end{aligned} \tag{4.7}$$

where N_i^{pred} and N_i^{data} are the predicted and observed number of events respectively; b_i are the flux nuisance parameters, x_i are the cross section nuisance parameters and d_i are nuisance parameters for the detector response; and V_b , V_x and V_d are the covariance matrices containing the pre-fit uncertainties of the flux, cross section and detector models respectively.

ND280 detector systematic	Type
TPC tracking	Efficiency
TPC PID	Reconstructed observable variation
TPC charge confusion	Efficiency
TPC momentum scale	Reconstructed observable variation
TPC momentum resolution	Reconstructed observable variation
TPC quality cut	Efficiency
FGD tracking	Efficiency
FGD PID	Reconstructed observable variation
FGD mass	Normalization
Michel electron	Efficiency
Out of FV	Efficiency
B field distortion	Reconstructed observable variation
TPC-FGD matching	Efficiency
Pile-up	Normalization
Übermerging*	Efficiency
Sand muons	Efficiency
Pion secondary interactions	Efficiency

Table 4.4: List of systematic parameters related to the ND280 detector efficiencies and reconstruction models considered in the ND280 fit with their type. *Übermerging is the systematic caused by two TPC segments from two different particles merged together, producing an incorrect track multiplicity in the event.

The systematic parameters related to the ND280 detector efficiencies and reconstruction models considered in the fit are summarized in Tab.4.4 indicating their type. The uncertainties of these parameters are reduced using data as much as possible (for instance, samples of cosmic rays are used to evaluate TPC-FGD matching). Some systematics are related to reconstruction observables like PID or momentum, which are varied according to the value of the systematic parameter and then the event selection is performed again. Some other detector systematics are associated to the total event normalization and for them the event is simply re-weighted according to the value of the parameter, with no need to re-run the event selection. The rest are efficiencies, and for them events are to be re-weighted differently depending on whether they were correctly reconstructed or not based on their true information. It is important to remark that a dedicated MC simulation with neutrino interactions happening outside the ND280 is used to estimate the sand muons background. Figure 4.13 illustrates for each systematic in which detector and stage of the interaction is applied.

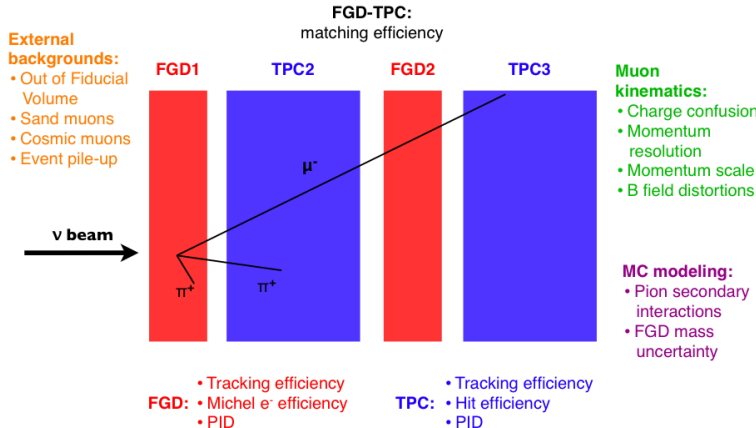


Figure 4.13: Schematic drawing illustrating for each ND280 detector systematic in which detector and stage of the interaction is applied.

The following ND280 detector systematics have a dominant effect in the data selection:

- **Pion secondary interactions:** interactions that the pion undergoes outside the nucleus in which it was formed. These interactions can be divided into: i) absorption, in which the pion is completely absorbed by a nucleus and no other pions are produced; ii) charge exchange, in which the pion interacts with a nucleus and a π^0 is produced; and iii) quasi-elastic scattering, in which the pion interacts with a nucleus and a pion of the same charge exits the interaction. These processes are modelled in GEANT4, but it was found that they significantly differ with respect to the available external data, so that the error associated to these interactions accounts for the difference between the simulation and the external data and the uncertainty on the external data.
- **Out of FV events:** events with true interaction vertex outside the FV of FGD1 but mis-reconstructed as happening inside. They are divided into different categories depending on the physical process; for instance, the following types of events are considered out of FV backgrounds: backward going pions coming from barrel-ECAL and misidentified as forward going muons, pions produced inside the FGD by high energy neutrons and mis-identified as muons, or muons crossing the entire FGD but broken into several tracks and looking like created inside the FGD FV due to a TPC-FGD matching

failure. The systematic error associated to each category is calculated separately: a 20% cross section rate uncertainty, estimated from comparisons of data/MC event rates in the PØD, ECAL and SMRD, is assigned to the categories with the initial neutrino interaction outside the tracker, adding a reconstruction systematic when the relevant control sample is available to measure it.

- **TPC momentum resolution:** The TPC momentum resolution is measured for data and MC using tracks that cross multiple TPCs, by comparing the reconstructed momentum in two consecutive TPCs for the same global track. The difference of the inverse transverse (to the magnetic field) momentum, $1/p_T$, between the two TPCs, corrected by the energy loss in the intermediate FGD, $\Delta(1/p_T)$, is used as the main observable. Its distribution is approximately Gaussian, with mean close to 0, and standard deviation $\sigma_{\Delta(1/p_T)}$, which contains contributions from multiple scattering, energy loss fluctuations and momentum resolution in the two TPCs involved. $\sigma_{\Delta(1/p_T)}$ can be computed for different ranges of position, p_T or angle, as shown in Fig.4.14. From that figure it can be concluded that the momentum resolution is worse in the data, mainly due to an imperfect detector modelling (specially concerning electric field distortions, which are not simulated). Assuming that the momentum resolution is the same in both TPCs, the difference in resolution between data and MC can be computed using the following method: the MC can be smeared track by track and plots like the one shown in Fig.4.14 can be repeated with different smearing factors until data and MC match each other. Performing a numerical χ^2 minimization, the smearing factor and its error are computed.

The detector systematic errors are treated as a vector of systematic parameters d_i , which scale the number of events in the nominal prediction. In order to propagate them in the ND280 data fit, a detector systematic covariance matrix V_d is built, using a coarser binning than the one of the data fit (10 bins for p_μ and 7 bins for $\cos \theta_\mu$). An ensemble of 2000 toy experiments are produced to construct this covariance matrix. For each toy experiment, the values of the systematic parameters are varied following their uncertainties, changing the number of events of the nominal prediction; then, the event selection is repeated and the number of events in each $(p_\mu, \cos \theta_\mu)$ bin is obtained for the three samples.

The flux nuisance parameters b_i are normalization parameters for flux bins in true energy and flavour at both ND280 and SK. The flux input covariance matrix is based on the matrix shown in Fig. 4.8, which is determined as described in Section 4.2. However, the binning in true neutrino energy is different for the ND280 data fit with the aim of having a finer binning around the oscillation maximum and in those regions contributing more to the data sample selected, providing that the

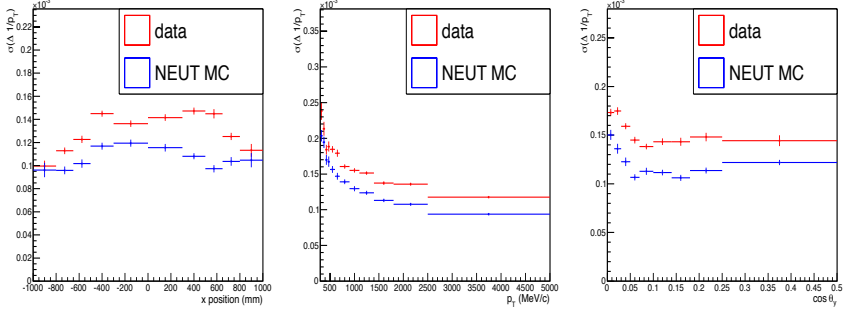


Figure 4.14: Distribution of $\sigma_{\Delta(1/p_T)}$ for the calculation of the TPC momentum resolution as a function of x position (left), p_T (middle) and $\cos \theta_Y$ (right) for data (red) and MC (blue). Figures from [171].

flux error does not change quickly inside one bin and joining together bins that are highly correlated in the original matrix. The new binning for the flux nuisance parameters is different depending on the oscillation analysis for which the output of the ND280 fit must be produced, as defined in Tab. 4.5. For instance, there are no flux bins for ν_e and $\bar{\nu}_e$ considered for the ND280 fit for the ν_μ disappearance analysis since the contribution from these flavours to the SK single muon-like ring sample is very small as it will be shown in Section 5.4. This prior flux covariance matrix is used to apply the prior constraint on the flux nuisance parameters b_i when performing the fit to the ND280 data. Flux weights are applied to each MC event depending on the value of the nuisance parameters and on the true neutrino energy and flavour, changing in this way the prediction.

The relevant cross section nuisance parameters considered in this fit and their uncertainties are presented in Tab. 4.3 (although the uncertainties on $\sigma_{\nu_e}/\sigma_{\nu_\mu}$ and $\sigma_{\bar{\nu}}/\sigma_\nu$ cross section ratios are neglected since the ND280 sample consists almost entirely of ν_μ interactions). For each MC event a weight is applied depending on the true neutrino energy and flavour and the value of the nuisance parameter: for the cross section normalizations, the weight is simply its value; for the shape parameters, the weight must be found through response functions previously calculated with re-weighting as explained previously.

Finally, six parameters are also included in the fit to account for uncertainties in the final state interactions in the near detector: pion production, pion absorption, low and high energy charge exchange and low and high energy inelastic interactions. These parameters are constrained according to their covariance matrix and for each MC event a weight is applied.

Some of the nuisance parameters described are not correlated between the near

Parameter	ν_μ -disappearance	ν_e -appearance	joint
ν_μ flux	[0.0, 0.4, 0.5, 0.6, 0.7, 1.0, 1.5, 2.5, 3.5, 5.0, 7.0, 30.0] (11 bins)	[0.0, 0.4, 0.5, 0.6, 0.7, 1.0, 1.5, 2.5, 3.5, 5.0, 7.0, 30.0] (11 bins)	[0.0, 0.4, 0.5, 0.6, 0.7, 1.0, 1.5, 2.5, 3.5, 5.0, 7.0, 30.0] (11 bins)
$\bar{\nu}_\mu$ flux	[0.0, 0.7, 1.0, 1.5, 2.5, 30.0] (5 bins)	[0.0, 1.5, 30.0] (2 bins)	[0.0, 0.7, 1.0, 1.5, 2.5, 30.0] (5 bins)
ν_e flux	—	[0.0, 0.5, 0.7, 0.8, 1.5, 2.5, 4.0, 30.0] (7 bins)	[0.0, 0.5, 0.7, 0.8, 1.5, 2.5, 4.0, 30.0] (7 bins)
$\bar{\nu}_e$ flux	—	[0.0, 2.5, 30.0] (2 bins)	[0.0, 2.5, 30.0] (2 bins)

Table 4.5: List of true neutrino energy bin edges (in GeV) for the flux nuisance parameters included in the ND280 fit depending on the different oscillation analysis.

and the far detector, and therefore they do not affect the prediction of event rates at SK. For this reason, those parameters are marginalized by performing a numerical integration of the likelihood, assuming that they have a quadratic dependence near the minimum. These parameters are the flux parameters for ND280, detector response systematic parameters and nuclear model-dependent cross section parameters (p_F , E_B and SF for ^{12}C). Some other cross section parameters, which have a negligible effect on the SK prediction, are marginalized as well. The remaining parameters, which include the flux at SK and the cross section parameters listed in Tab.4.6 (a different set of parameters for each analysis), affect the SK event rates and will be constrained by the ND280 fit as described in the next section.

Figure 4.15 (left) shows the input correlation matrix before the ND280 fit for the parameters that are propagated to SK and therefore not marginalized in the fit for the joint oscillation analysis. In this matrix, the prior flux covariance matrix is extended adding the prior uncertainties and correlations for the cross section systematics to be fitted according to Tab. 4.6. In the prior covariance matrix, it is assumed that no correlations exist between the flux and cross section parameters. All the cross section parameters are also considered to be independent from each other except M_A^{RES} , CC1 π E1 and NC1 π^0 : the negative correlations between M_A^{RES} and CC1 π E1 and NC1 π^0 appear because a larger value of M_A^{RES} increases the total normalization and the Q^2 shape in the CC1pi sample, and therefore the values

Parameter	ν_μ -disappearance	ν_e -appearance	joint
M_A^{QE}	✓	✓	✓
M_A^{RES}	✓	✓	✓
CCQE norm. (0-1.5 GeV)	✓	✓	✓
CCQE norm. (1.5-3.5 GeV)	✓	—	✓
CCQE norm. (3.5-30. GeV)	✓	—	✓
CC1 π norm. (0-2.5 GeV)	✓	✓	✓
CC1 π norm. (2.5-30 GeV)	✓	—	✓
NC1 π^0 norm.	—	✓	✓

Table 4.6: List of cross section nuisance parameters included in the ND280 fit for each oscillation analysis.

of CC1 π E1 and NC1 π^0 are forced to decrease; the positive correlation between CC1 π E1 and NC1 π^0 is caused indirectly by the fact that both parameters are affected by M_A^{RES} . Although no NC sample is included in the ND280 data fit, the NC1 π^0 normalization can be also constrained due to its correlation with other cross section parameters.

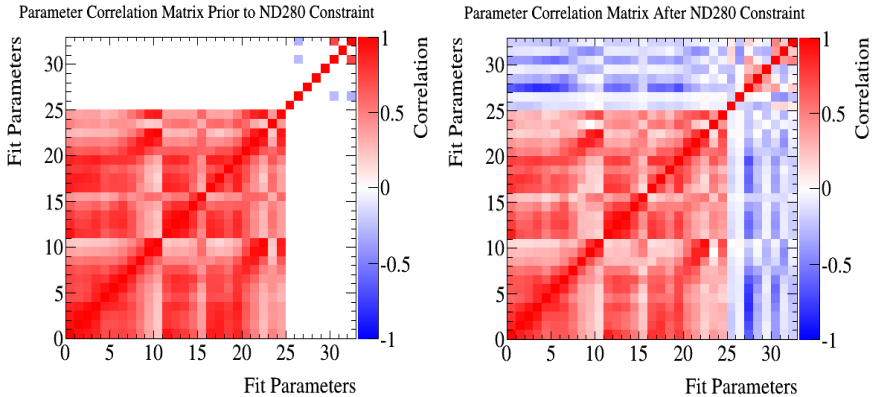


Figure 4.15: Input correlations prior to the ND280 fit (left) and correlations after the ND280 fit of the parameters that are propagated to SK in the joint oscillation analysis. The parameters are ordered as follows: 1-10 SK ν_μ flux parameters, 11-15 SK $\bar{\nu}_\mu$ flux parameters, 16-22 SK ν_e flux parameters, 23-24 SK $\bar{\nu}_e$ flux parameters (as defined in Tab. 4.5), 25 M_A^{QE} , 26 M_A^{RES} , 27-29 CCQE normalization (in the three energy bins: [0-1.5 GeV], [1.5-3.5 GeV], [3.5-30.0 GeV]), 30-31 CC1 π normalization (in two energy bins: [0.0-2.5 GeV], [2.5-30.0 GeV]) and 32 NC1 π^0 normalization. Figures from [172].

As an example of the result of the ND280 fit, Fig. 4.16 shows the momentum distribution of the muon candidate for data (points), MC nominal prediction (blue) and MC after the ND280 fit (red) for the CC0 π sample (left), CC1 π sample (middle) and CCother sample (right) and the ratio between data/MC below each distribution. As expected, the agreement between data and MC distributions is clearly better after the ND280 fit.

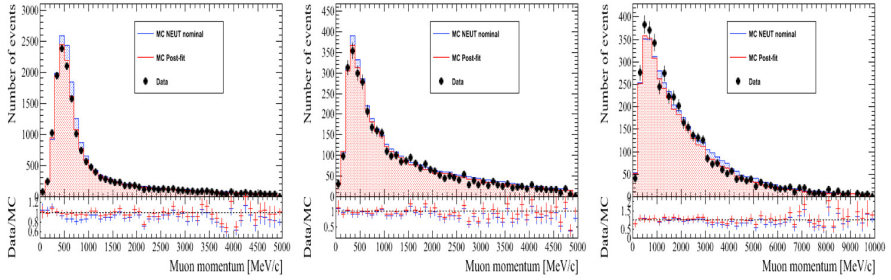


Figure 4.16: Momentum distribution of the muon candidate for data (points), MC nominal prediction (blue) and MC after the ND280 fit (red) for the CC0 π sample (left), CC1 π sample (middle) and CCother sample (right) and the ratio between data/MC below each distribution. Figures from [172].

4.4.3 Constraint on Flux and Correlated Cross Section Uncertainties

As described in previous section, a fit to the ND280 data is performed to constrain some of the parameters used for the SK detector. The covariance matrix relating the flux parameters in the two detectors serves as extrapolation from near to far detector and therefore the flux parameters at the far detector are constrained by the flux parameters at the near detector. Some cross section parameters are common to both detectors so they are also included in the fit and constrained by the ND280 measurement. The prior correlation matrix for the flux and cross section parameters fitted is presented in Fig. 4.15 (left) for the joint analysis with the flux and cross section parameters listed in Tab. 4.5 and Tab. 4.6 respectively. The initial correlations for the flux parameters are obtained from the flux simulation, and the cross section parameters are assumed to be independent with the exception of M_A^{RES} , CC1 π E1 and NC1 π^0 as explained previously. Thus, simultaneous variations of this set of parameters are considered in the fit according to this prior covariance matrix, and a best-fit covariance matrix with new correlations is obtained after performing the fit, as shown in Fig. 4.15 (right).

Figure 4.17 shows the results for the SK flux parameters before and after the ND280 fit separated into the four different flavours. The prior uncertainty is represented with a red band around the nominal values which are 1.0, and the best-fit values after the fit are illustrated as blue points, with the post-fit uncertainties represented by blue bands. There is an obvious reduction in the uncertainties (error bands) of the flux parameters after the ND280 constraint. The uncertainties on the cross section parameters are significantly reduced as well as shown in Tab. 4.7.

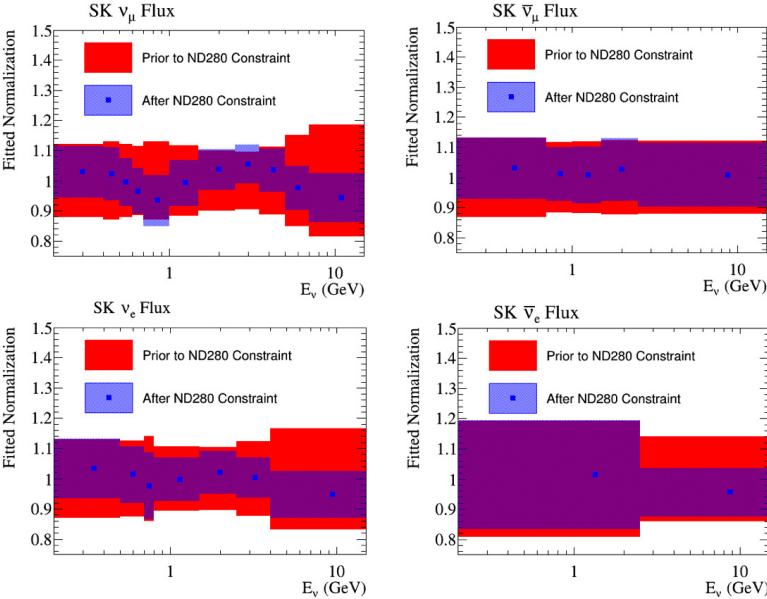


Figure 4.17: SK flux parameters before and after the ND280 fit separated into the four different flavours. The prior uncertainty is represented with a red band around the nominal values which are 1.0, and the best-fit values after the fit are illustrated as blue points, with the post-fit uncertainties represented by blue bands. Figures from [166].

Table 4.7 presents a detailed overview of the result of the ND280 fit for the parameters considered in the joint oscillation analysis, both flux and cross section parameters, including their pre-fit values, best-fit values and uncertainties (1σ error obtained as the square root of the diagonal terms in the covariance matrix) before and after the fit. Notice that the parameters shown in Tab. 4.7 are scaling factors: the best-fit values for the axial masses M_A^{QE} and M_A^{RES} are 1.240 GeV and 0.965 GeV respectively, which correspond to scaling factors of 1.025 and 0.797 respectively⁷. The pre-fit values are the nominal values, 1.0, except for the parameters

⁷The scaling factors are calculated by comparing the best-fit values and the input value 1.21 GeV.

Parameter	Description	Pre-fit value	Best-fit value	Pre/postfit 1σ error
0	ν_μ flux norm, E = 0.0 - 0.4 GeV	1.00	1.029	0.121 / 0.085
1	ν_μ flux norm, E = 0.4 - 0.5 GeV	1.00	1.022	0.130 / 0.088
2	ν_μ flux norm, E = 0.5 - 0.6 GeV	1.00	0.995	0.122 / 0.080
3	ν_μ flux norm, E = 0.6 - 0.7 GeV	1.00	0.966	0.115 / 0.076
4	ν_μ flux norm, E = 0.7 - 1.0 GeV	1.00	0.934	0.129 / 0.085
5	ν_μ flux norm, E = 1.0 - 1.5 GeV	1.00	0.992	0.116 / 0.077
6	ν_μ flux norm, E = 1.5 - 2.5 GeV	1.00	1.037	0.100 / 0.068
7	ν_μ flux norm, E = 2.5 - 3.5 GeV	1.00	1.054	0.095 / 0.065
8	ν_μ flux norm, E = 3.5 - 5.0 GeV	1.00	1.035	0.112 / 0.072
9	ν_μ flux norm, E = 5.0 - 7.0 GeV	1.00	0.975	0.152 / 0.073
10	ν_μ flux norm, E = 7.0 - 30.0 GeV	1.00	0.943	0.187 / 0.082
11	$\bar{\nu}_\mu$ flux norm, E = 0.0 - 0.7 GeV	1.00	1.030	0.133 / 0.102
12	$\bar{\nu}_\mu$ flux norm, E = 0.7 - 1.0 GeV	1.00	1.011	0.117 / 0.090
13	$\bar{\nu}_\mu$ flux norm, E = 1.0 - 1.5 GeV	1.00	1.007	0.119 / 0.094
14	$\bar{\nu}_\mu$ flux norm, E = 1.5 - 2.5 GeV	1.00	1.026	0.123 / 0.104
15	$\bar{\nu}_\mu$ flux norm, E = 2.5 - 30.0 GeV	1.00	1.008	0.122 / 0.107
16	ν_e flux norm, E = 0.0 - 0.5 GeV	1.00	1.033	0.131 / 0.098
17	ν_e flux norm, E = 0.5 - 0.7 GeV	1.00	1.013	0.125 / 0.093
18	ν_e flux norm, E = 0.7 - 0.8 GeV	1.00	0.976	0.141 / 0.110
19	ν_e flux norm, E = 0.8 - 1.5 GeV	1.00	0.998	0.105 / 0.073
20	ν_e flux norm, E = 1.5 - 2.5 GeV	1.00	1.021	0.105 / 0.072
21	ν_e flux norm, E = 2.5 - 4.0 GeV	1.00	1.003	0.123 / 0.067
22	ν_e flux norm, E = 4.0 - 30.0 GeV	1.00	0.947	0.168 / 0.077
23	$\bar{\nu}_e$ flux norm, E = 0.0 - 2.5 GeV	1.00	1.014	0.192 / 0.180
24	$\bar{\nu}_e$ flux norm, E = 2.5 - 30.0 GeV	1.00	0.955	0.142 / 0.080
25	M_A^{QE}	1.00	1.025	0.372 / 0.059
26	M_A^{RES}	1.16	0.797	0.183 / 0.056
27	CCQE norm, E = 0.0 - 1.5 GeV	1.00	0.966	0.110 / 0.076
28	CCQE norm, E = 1.5 - 3.5 GeV	1.00	0.931	0.300 / 0.103
29	CCQE norm, E = 3.5 - 30.0 GeV	1.00	0.852	0.300 / 0.114
30	CC1 π^- norm, E = 0.0 - 2.5 GeV	1.15	1.265	0.317 / 0.163
31	CC1 π^- norm, E = 2.5 - 30.0 GeV	1.00	1.122	0.400 / 0.172
32	NC1 π^0 norm	0.96	1.135	0.328 / 0.248

Table 4.7: List of flux and correlated cross section systematic parameters included in the ND280 fit, with their values and uncertainties (1σ error) before and after the fit.

M_A^{RES} , NC1 π^0 and CC1 π normalization for low energies, whose values are updated with their best-fit values from the fit to MiniBooNE data from Tab. 4.3. The vector of best-fit values of the parameters as in Tab 4.7 and the post-fit covariance matrix is the output of the ND280 fit to be used in the oscillation analysis, also known as BANFF output (Beam And ND280 Flux extrapolation task Force), nomenclature that will be used for convenience in the following chapters. The best-fit values of the BANFF output used in the joint analysis can be found in Fig. 4.18 and the final correlation matrix in Fig. 4.15 (right).

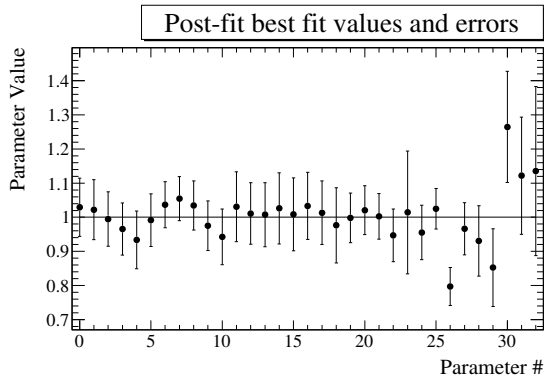


Figure 4.18: Post-fit values and post-fit fractional errors for each of the flux and correlated cross section systematic parameters after the ND280 fit performed for the joint oscillation analysis. The parameters are ordered as in Tab. 4.7.

4.5 Far Detector Event Selection and Efficiencies

In this chapter, the event selections applied to the T2K data currently being taken at SK, performed in order to develop physics analyses, and the related uncertainties, will be described.

4.5.1 SK Neutrino Event Selection

Neutrino event candidates are selected in SK by applying a sequence of cuts that will be described in this section. A CC ν_e interaction ($\nu_e N \rightarrow e^- X$) is identified at SK by detecting a single electron-like (e-like) ring generated by the Čerenkov light cone of the electron produced in the interaction. Similarly, a CC ν_μ interaction ($\nu_\mu N \rightarrow \mu^- X$) is identified by detecting a single muon-like (μ -like) ring. The selection criteria were determined from MC studies before data taking.

Single ring event selection

Neutrino CC interactions typically produce single ring events at SK in the narrow T2K energy range, as most of the particles produced, except the leptons, do not escape the nucleus or are below their Čerenkov threshold. Therefore, there are some preliminary cuts to select a single ring event that are common for both ν_e and ν_μ candidate events:

- **Timing Cuts.** When a beam spill is sent to SK from JPARC, a signal with a corresponding timestamp is sent as well. The signal is read at SK and sent back to JPARC to verify that the data was not corrupted, and if this is the case then the T2K data is separated from the SK data stream and a time window of 1 ms ($\pm 500 \mu\text{s}$ with respect to the expected beam arrival time) is recorded. On-timing events are selected requiring that ΔT_0 is between -2 and +10 μs , with ΔT_0 defined as the timing of the event relative to the leading edge of the spill, corrected to account for the position of the neutrino interaction vertex and the photon propagation time to the PMTs. Figure 4.19 shows the on-timing window ΔT_0 for T2K Run4 compared to T2K Run1+2+3, showing the 8 bunches that compose the spill of a $\sim 5 \mu\text{s}$ duration.

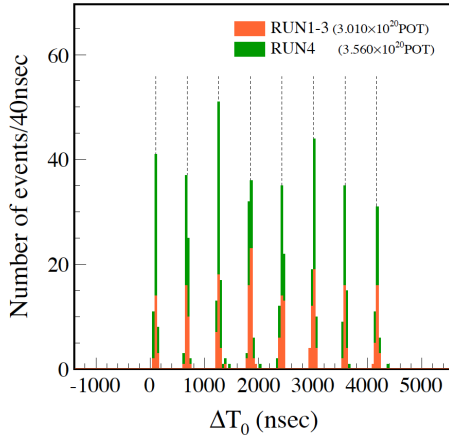


Figure 4.19: On-timing window ΔT_0 for T2K Run4 compared to T2K Run1+2+3, showing the 8 bunches that compose the spill of a $\sim 5 \mu\text{s}$ duration. Figure from [173].

- **Beam and SK data quality cuts.** SK data quality cuts are applied to assure a good spill selection, requiring that the data acquisition (DAQ) at SK works properly and no other problems may affect it or the GPS system. The inefficiency in the SK beam good spill selection is $\sim 1\%$ [173].

- **Fully Contained Fiducial Volume (FCFV) neutrino event cuts.** Events are fully contained (FC) if all their Čerenkov light is deposited inside the SK inner detector (ID), so that their energy can be reconstructed. To select such events it is required that no more than 15 PMT hits (PMTs which register sufficient charge, light above a threshold level set at ~ 0.25 photoelectrons) appear in the outer detector (OD). Events with visible energy (E_{vis}) below 20 MeV, called low energy (LE) events, are also rejected as they are events produced predominantly by solar and supernova neutrinos [174]. The visible energy is computed under the electron hypothesis, assuming that all rings are produced by electrons, defining E_{vis} as the energy of an electromagnetic shower that would produce the observed amount of Čerenkov light. A third cut rejects events in which a single PMT hit has more than half of the total charge to remove events caused by radioactivity very close to the PMT. Then, a flasher test is applied to reject events produced by intermittent light emission inside the phototubes, identifying them from their timing distribution.

A FCFV sample is selected from the FC events by further requiring that $E_{vis} > 30$ MeV and that the reconstructed vertex is at least 2m away from the ID wall.

- **Single ring.** It is required that there is only one reconstructed ring in the event, cut based on the ring counting likelihood parameter calculated with a method based on the Hough transform. If there is at least one reconstructed vertex in the event, events are classified into single- or multi-ring events.

The events passing the single ring event cuts are then separated according to their PID. The shape of the hit pattern produced by the Čerenkov light created by a charged particle serves to identify the particle as described in previous section, so the rings created by muons and electrons can be distinguished, and ν_μ and ν_e candidate events separated with specific cuts.

Single ring muon-like event selection

The cuts to select a CCQE ν_μ enriched sample are the following:

- Single ring event (cuts described previously).
- The reconstructed ring must be muon-like according to the PID parameter, which is based on the shape and the opening angle of the Čerenkov ring [175], applying the cut as shown in Fig. 4.20 (left).
- The reconstructed momentum of the μ candidate particle, estimated measuring the total number of photoelectrons in the Čerenkov ring, must be

$p_\mu > 200$ MeV/c in order to reject events produced by pions and misidentified electrons from the decay of unseen muons and pions, as shown in Fig. 4.20 (right).

- The number of decay electrons (or Michel electrons), identified as time-delayed PMT hits appearing after the primary event, must be less than 2 in order to reject events with non reconstructed pions.

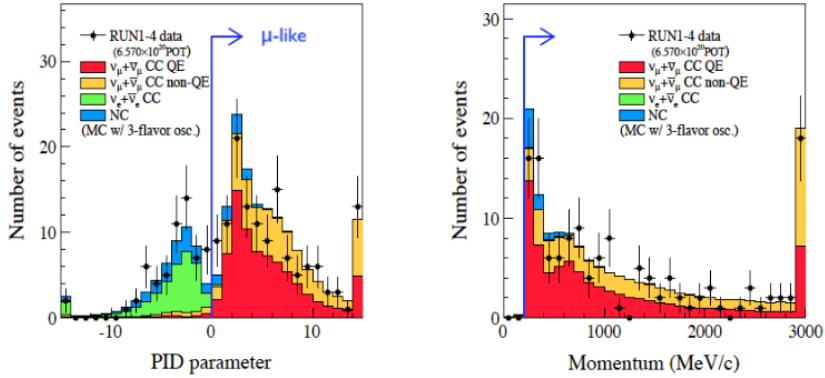


Figure 4.20: PID parameter distribution (left) and reconstructed momentum distribution of the μ candidate particle (right), estimated measuring the total number of photoelectrons in the Čerenkov ring, for the FCFV single ring events and the cuts applied to select muon-like events, showing data and MC prediction overlaid with its breakdown into different categories. Figures from [173].

Single ring electron-like event selection

The cuts to select a CCQE ν_e enriched sample are the following:

- Single ring event (cuts described previously).
- The reconstructed ring must be electron-like according to the PID parameter, applying the cut as shown in Fig. 4.21 (left).
- The visible energy must be $E_{vis} > 100$ MeV in order to remove low energy NC interactions and electrons from unseen muons and pions, as shown in Fig. 4.21 (right).

- There must be no Michel electrons in the event in order to reject events with non reconstructed pions or muons, as shown in Fig. (left).
- The reconstructed neutrino energy must be less than 1250 MeV in order to reduce the high energy tail where the signal is expected to be small and the intrinsic ν_e background is dominant as shown in Fig. 4.22 (right). The reconstructed neutrino energy is calculated assuming CCQE kinematics and neglecting Fermi motion following Eq. 4.8:

$$E_\nu^{reco} = \frac{(m_N - E_B)E_l - m_e^2/2 + m_N E_B - E_B^2/2 + (m_P^2 - m_N^2)/2}{m_N - E_B - E_e + p_e \cos \theta_e} \quad (4.8)$$

where m_p, m_n and m_e are the masses of the proton, neutron and electron respectively, $E_B = 27$ MeV and E_e , p_e and $\cos \theta_e$ are the reconstructed energy, momentum and angle of the electron.

- The invariant mass of the event, reconstructed under a two ring hypothesis, must not be consistent with a π^0 mass in order to reduce NC π^0 events. For this cut, the new reconstruction algorithm described in Section 3.4.1 is used. The final ν_e candidate sample is composed of events that satisfy that the ratio of the best-fit likelihood values under the π^0 and electron hypothesis $\ln(L_0/L_e) < 175 - 0.875 \times m_{\pi^0}$ (parameterization of the red line in Fig. 3.23, illustrating the cut used).

Figure 4.23 shows the data reduction after each cut of the single ring muon-like (left) and electron-like (right) event selection, overlaying T2K Run1+2+3+4 data and MC prediction with typical values of the oscillation parameters and its breakdown into different categories. The MC expectation with oscillations is consistent with the Run 1+2+3+4 data, which after applying all cuts is composed of 120 single ring muon-like events and 28 single ring electron-like events. The detailed effects of each cut in the number of events for signal and the different backgrounds are shown in Tabs. 4.8 and 4.9 for the single ring muon-like events and single ring electron-like events respectively.

The studies of the reduction of each cut for the expected MC events give us information about the purity of the sample after each cut and the background rejection. On the one hand, for the single ring muon-like event selection, if the purity is estimated as the number of $\nu_\mu + \bar{\nu}_\mu$ CCQE events divided by the total number of predicted MC events, after the first muon PID cut, which mainly reduces the $\nu_e + \bar{\nu}_e$ CC and NC backgrounds, the purity of the sample is $\sim 55\%$. Approximately the same purity is obtained after the cut on the momentum, which reduces only

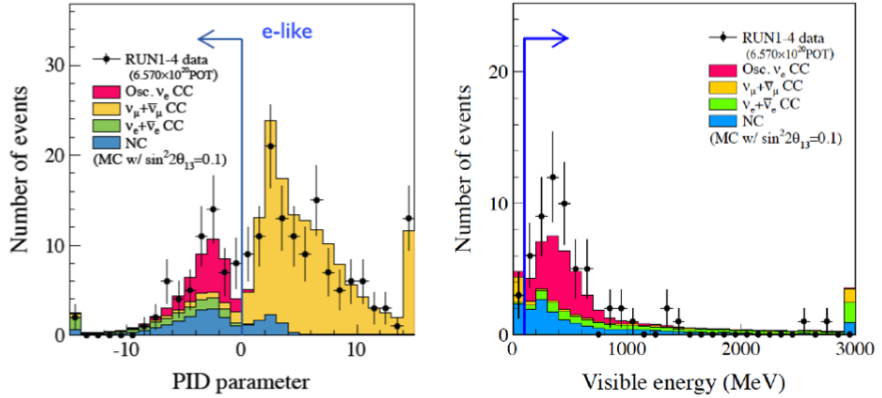


Figure 4.21: PID parameter distribution (left) and visible energy distribution (right) for the FCNV single ring events and the cut applied to select electron-like events, showing data and MC prediction overlaid with its breakdown into different categories. Figures from [173].

a small fraction of NC background events. The last cut on the number of decay electrons improves the purity to $\sim 62\%$ by reducing the $\nu_\mu + \bar{\nu}_\mu$ CCnQE and NC background events.

On the other hand, for the single ring electron-like event selection, the first cut, electron PID, significantly reduces the background contribution, essentially the $\nu_\mu + \bar{\nu}_\mu$ CC background, without almost losing signal events so that the purity of the sample after this cut (computed as the number of signal $\nu_\mu \rightarrow \nu_e$ CC events divided by the total number of predicted MC events) is $\sim 42\%$. The cut in the visible energy reduces the $\nu_\mu + \bar{\nu}_\mu$ CC and NC backgrounds, the cut on the decay number of electrons reduces all the backgrounds, specially the $\nu_\mu + \bar{\nu}_\mu$ CC background, and the cut on the reconstructed energy reduces mainly the $\nu_e + \bar{\nu}_e$ CC and NC backgrounds; the purities after each of those cuts are respectively $\sim 45\%$, $\sim 49\%$ and $\sim 59\%$. The last cut, π^0 rejection, significantly reduces the NC background, so at the end the remaining background contribution is mainly due to the beam ν_e and $\bar{\nu}_e$ contamination and the final purity is $\sim 80\%$.

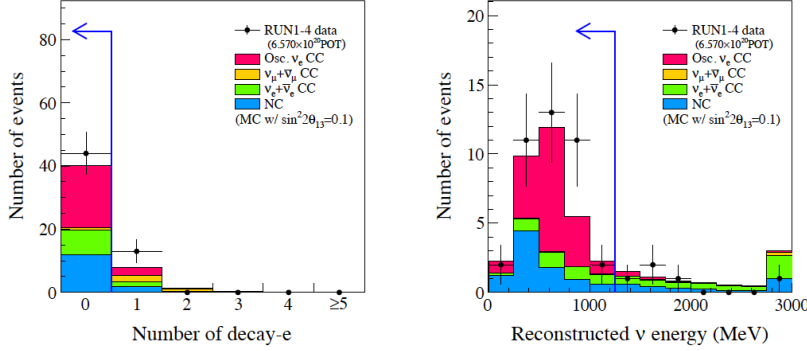


Figure 4.22: Number of decay electrons (left) and reconstructed neutrino energy distribution (right), calculated assuming CCQE kinematics and neglecting Fermi motion, and the cut applied to reduce the high energy tail where the signal is expected to be small and the intrinsic ν_e background is dominant. Figures from [173].

Cut	Data	MC				
		$\nu_\mu + \bar{\nu}_\mu$ CCQE	$\nu_\mu + \bar{\nu}_\mu$ CCnQE	$\nu_e + \bar{\nu}_e$ CC	NC	Total
FCFV	377	85.6	162.2	41.6	83.0	372.4
Single ring	193	80.6	61.9	32.5	23.5	198.4
μ -like PID	133	79.0	57.8	0.4	7.1	144.3
p_μ cut	133	78.8	57.8	0.4	7.0	144.0
Decay-e cut	120	77.9	40.8	0.4	6.8	125.9

Table 4.8: Reduction on the observed data and expected MC events (calculated with typical oscillation parameters) after each cut of the single ring muon-like event selection.

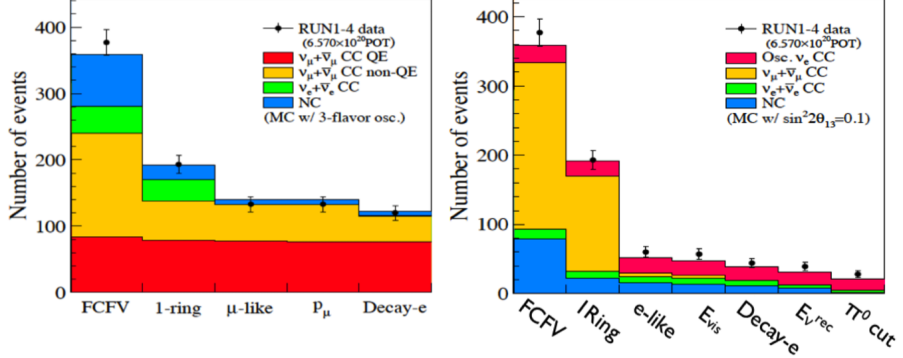


Figure 4.23: SK data reduction after each cut of the single ring muon-like (left) and electron-like (right) event selection, overlaying T2K Run1+2+3+4 data and MC prediction with typical values of the oscillation parameters and its breakdown into different categories. Figures from [173].

Cut	Data	MC				Total	
		Signal		Background			
		$\nu_\mu \rightarrow \nu_e$ CC	$\nu_\mu + \bar{\nu}_\mu$ CC	$\nu_e + \bar{\nu}_e$ CC	NC		
FCFV	377	26.2	247.8	15.4	83.02	372.4	
Single ring	193	22.7	142.4	9.8	23.5	198.4	
e-like PID	60	22.5	5.6	9.7	16.4	51.2	
E_{vis} cut	57	22.0	3.7	9.7	14.0	49.4	
No decay-e	44	19.6	0.7	7.9	11.8	40.0	
E_ν^{rec} cut	39	18.8	0.2	3.7	9.0	31.8	
π^0 cut	28	17.3	0.1	3.2	1.0	21.6	

Table 4.9: Reduction on the observed data and expected MC events (calculated with typical oscillation parameters and $\sin^2 2\theta_{13}=0.1$) after each cut of the single ring electron-like event selection.

Error source	ν_e selection				ν_μ selection
	Osc. ν_e CC	ν_μ CC	ν_e CC	NC	
Fully contained	1%				
Fiducial volume	1%				
Decay-e cut	0.2%	0.4%	0.2%	0.4%	1.0%

Table 4.10: Summary on the uncertainties for the selection cuts other than topological cuts.

4.5.2 SK Detector Uncertainties

The uncertainties on the SK reconstruction and event selection efficiencies have been estimated using control samples. The control samples used are: atmospheric neutrinos, cosmic rays and their decay electrons, muons decaying in flight and "hybrid- π^0 " samples.

The error on the FC event selection is estimated to be 1%, mainly due to the flasher event rejection, whose uncertainty is evaluated from the difference in the cut efficiency between atmospheric neutrino data and MC. The error on the FV event selection is estimated to be 1% by evaluating the difference between reconstructed vertex distributions of observed and simulated cosmic ray muons stopping inside the ID. The uncertainty on the delayed decay electron tagging efficiency is evaluated by comparing the tagging efficiency between cosmic ray stopping muon data and MC samples, and the error on the number of candidate events due to its uncertainty is 0.2% for ν_e events and 1% for ν_μ events.

The uncertainty on the reconstructed energy scale is estimated to be 2.4% by comparing the reconstructed momenta in data and MC events of cosmic ray stopping muons with similar energies to the T2K neutrino events and of their associated decay electrons, and by comparing the reconstructed invariant mass of π^0 produced in atmospheric neutrino interactions in data and MC simulation.

The uncertainties for the selection cuts other than topological cuts are summarized in Tab. 4.10. The uncertainties for the cuts on the p_μ in the ν_μ and the E_{vis} in the ν_e selections are not included since their effect is negligible and the effect in the E_ν^{reco} cut is included in the uncertainty on the reconstructed energy scale.

The **topological cuts**, whose errors are the dominant ones and are estimated from atmospheric neutrino samples, are: ring counting (RC), particle identification and π^0 rejection. The uncertainties for the topological cuts are evaluated separately for the stand-alone ν_μ disappearance and ν_e appearance analyses, defining different control samples. However, a modification was necessary to calculate the uncertainties for the joint analysis taking into account correlations between the ν_μ

and ν_e candidate event selections. Thus, a new definition of control samples and a simultaneous fit to the atmospheric neutrino data have been performed.

The effect of the uncertainties on the topological cuts is evaluated in different categories according to the final state particles exiting the nucleus. Thus, the MC is separated into channels depending on the true interaction type and final particles: ν_e CC single electron, ν_e CC other, ν_μ CC single muon, ν_μ CC other, NC π^0 and NC other. The following five control samples are then defined, all of them from the parent FCFV sample, to perform the fit to the SK atmospheric neutrino data and to estimate the topological cuts uncertainties: two CCQE enriched samples, one for ν_e and one for ν_μ , are defined to evaluate the error on the ν_e CC single electron and ν_μ CC single muon channels respectively; two CCnQE enriched samples, one for ν_e and one for ν_μ , are defined to evaluate the error on the ν_e CC other, and ν_μ CC other channels respectively; and finally a background sample is defined, which is NC π^0 enhanced to constrain the NC normalization. The difference between CCQE enriched and CCnQE enriched samples lies in the number of decay electrons (0 for ν_e CCQE; ≥ 1 for ν_e CCnQE; < 2 for ν_μ CCQE; ≥ 2 for ν_μ CCnQE).

Each of the CCQE, CCnQE enriched samples is then divided into a set of core and tails sub-samples, with the core composed of events passing all topological cuts and tail sub-samples grouping the events failing to pass one of the topological cuts. According to this, there are three tail sub-samples for the ν_e samples (RC, PID and π^0 tails) and only one for the ν_μ samples (RC tail) in order to avoid duplication of sub-samples. Furthermore, the ν_e CCnQE PID tail is slightly different with respect to the definition for the stand-alone appearance analysis: an additional cut is introduced to reject the overlapping events between ν_e CCnQE PID tail and the ν_μ CCQE and CCnQE core sub-samples, using the distance between the expected muon stopping point to the nearest decay electron. Finally a kinematic binning is defined for each sub-sample, dividing them into a different number of E_{vis} bins.

The expected number of events of each sub-sample depends on the efficiency of each topological cut and also on systematic uncertainties on the atmospheric neutrino flux normalization and the cross section of the different interactions. Thus, the fit to the atmospheric control samples is parametrized in terms of those uncertainties, which are allowed to vary in the fit. The parameters representing the uncertainties on the topological cuts are defined as cut parameter shifts and are varied at each fit iteration, and the selection is re-applied with the modified events, so that event migrations across all sub-samples is naturally occurring when changing the values of the topological cut parameters. The variation of the atmospheric neutrino flux and cross section parameters is applied as an event-by-event weighting. The fit was performed using a Markov Chain Monte Carlo (MCMC) method, building a posterior likelihood distribution and marginalizing over the posterior to determine the error for each of those parameters allowed to vary.

Some other special samples are used to calculate the systematic errors of the topological cuts in certain sub-samples. A special MC study of muon decays in flight was done to estimate the systematic error of ν_μ CC events passing the ν_e selection cuts, as these events usually mimic ν_e CC interactions. "Hybrid- π^0 " samples are control samples containing events where a π^0 is reconstructed using one simulated photon ring and a second electron-like ring from the SK atmospheric or cosmic ray samples, choosing the kinematics of the photon ring so that the two rings together mimic the decay kinematics of a π^0 . These events are called hybrid since they mix electron rings from real data and a simulated photon ring, and serve to evaluate the systematic error for the sub-samples containing π^0 in the ν_e selection. In addition, the efficiency of a single photon MC sample was compared to the one of a single electron MC to determine the uncertainty on the neutral current interactions producing a single photon via radiative decays of resonances, background of the ν_e appearance signal.

All the uncertainties described, except the energy scale, are propagated as a covariance matrix to calculate the final SK detector systematic errors to be used in the oscillation analysis. The effect of the energy scale is evaluated independently in the oscillation analysis as it will be explained in Section 5.5. The covariance matrix, which is meant to convert the error on the number of events in the final state samples into a fractional error on the number of events by neutrino flavour, interaction mode and reconstructed energy, is generated with a toy MC method. For each toy MC event a weight is assigned according to a randomly fluctuated value of the systematic uncertainties corresponding to the final state of the event, following a Gaussian distribution to vary the parameters. The weighted events are then summed up in the corresponding output bins, and the process repeated one million times, being the final result a covariance matrix. The output binning in which the covariance matrix is computed is defined in Tab. 4.11 where $1R\mu$ ($1Re$) represents the single ring muon-like (electron-like) samples.

Typical values of the oscillation parameters are used during this toy MC calculation. The resultant correlation matrix for the SK detector systematic errors for the T2K Run1+2+3+4 joint oscillation analysis is presented in Fig. 4.24.

Parameter	Sample	Flavour	Mode	E_{reco} bin
0	1R _μ	$\nu_\mu, \bar{\nu}_\mu$	CCQE	$E_{reco} < 0.4 \text{ GeV}$
1	1R _μ	$\nu_\mu, \bar{\nu}_\mu$	CCQE	$0.4 \text{ GeV} \leq E_{reco} \leq 1.1 \text{ GeV}$
2	1R _μ	$\nu_\mu, \bar{\nu}_\mu$	CCQE	$E_{reco} > 1.1 \text{ GeV}$
3	1R _μ	$\nu_\mu, \bar{\nu}_\mu$	CCnQE	
4	1R _μ	$\nu_e, \bar{\nu}_e$	CC	
5	1R _μ	all	NC	
6	1R _e	osc. ν_e	CC	$E_{reco} < 0.35 \text{ GeV}$
7	1R _e	osc. ν_e	CC	$0.35 \text{ GeV} \leq E_{reco} \leq 0.8 \text{ GeV}$
8	1R _e	osc. ν_e	CC	$0.8 \text{ GeV} < E_{reco} \leq 1.25 \text{ GeV}$
9	1R _e	$\nu_\mu, \bar{\nu}_\mu$	CC	$E_{reco} < 0.35 \text{ GeV}$
10	1R _e	$\nu_\mu, \bar{\nu}_\mu$	CC	$0.35 \text{ GeV} \leq E_{reco} \leq 0.8 \text{ GeV}$
11	1R _e	$\nu_\mu, \bar{\nu}_\mu$	CC	$0.8 \text{ GeV} < E_{reco} \leq 1.25 \text{ GeV}$
12	1R _e	$\nu_e, \bar{\nu}_e$	CC	$E_{reco} < 0.35 \text{ GeV}$
13	1R _e	$\nu_e, \bar{\nu}_e$	CC	$0.35 \text{ GeV} \leq E_{reco} \leq 0.8 \text{ GeV}$
14	1R _e	$\nu_e, \bar{\nu}_e$	CC	$0.8 \text{ GeV} < E_{reco} \leq 1.25 \text{ GeV}$
15	1R _e	all	NC	$E_{reco} < 0.35 \text{ GeV}$
16	1R _e	all	NC	$0.35 \text{ GeV} \leq E_{reco} \leq 0.8 \text{ GeV}$
17	1R _e	all	NC	$0.8 \text{ GeV} < E_{reco} \leq 1.25 \text{ GeV}$

Table 4.11: Binning used for the final output covariance matrix of the SK detector systematic errors, where 1R_μ (1Re) represents the single ring muon-like (electron-like) samples.

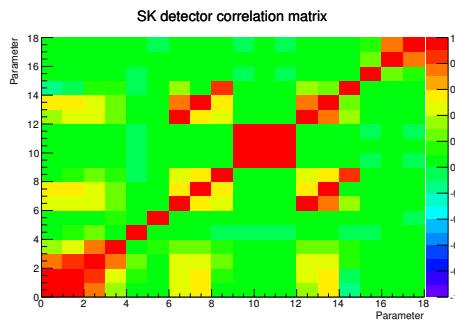


Figure 4.24: SK detector systematic error correlation matrix for the T2K Run1+2+3+4 joint oscillation analysis. Parameters are ordered as in Tab. 4.11.

Chapter 5

T2K Joint Oscillation Analysis

The joint 3-flavour oscillation analysis is a simultaneous fit to the energy spectra of the single ring μ -like and single ring e-like events (ν_μ and ν_e event candidates) from the T2K beam at Super-Kamiokande, in which the atmospheric squared-mass splitting Δm_{32}^2 , the mixing parameters $\sin^2\theta_{23}$, $\sin^2\theta_{13}$ and the CP-violating phase δ_{CP} are jointly determined, avoiding fixing any of them and taking into account all their inter-dependencies. In this chapter, the results of the first T2K joint 3-flavour oscillation frequentist analysis are presented. This analysis was performed on the combined Run1+2+3+4 dataset with 6.57×10^{20} POT described in Section 4.1.

5.1 Motivation

To date, two types of stand-alone oscillation analyses have been performed by the T2K experiment:

- **ν_e appearance analyses**, performed using the SK single e-like ring event sample (ν_e event candidates), in which the best-fit value for $\sin^2 2\theta_{13}$ is usually calculated fixing $\delta_{CP}=0.0$, and the confidence regions in the $(\sin^2 2\theta_{13}, \delta_{CP})$ space are normally built using a *raster scan* method¹. The values of $|\Delta m_{32}^2|$ and $\sin^2 2\theta_{23}$ were typically fixed in these analyses [1], [2].
- **ν_μ disappearance analyses**, in which $|\Delta m_{32}^2|$ and $\sin^2 2\theta_{23}$ are determined simultaneously using the SK single μ -like ring event sample (ν_μ event candidates), usually fixing the values of $\sin^2 2\theta_{13}$ and δ_{CP} [3], [4].

However, the oscillation parameters fixed in each analysis have a non-negligible effect on $P(\nu_\mu \rightarrow \nu_\mu)$ and $P(\nu_\mu \rightarrow \nu_e)$. This is illustrated in Fig. 5.1, which shows

¹In the *raster scan* method, a best-fit value of $\sin^2 2\theta_{13}$ is found for each different fixed value of δ_{CP} , resulting in a line of best-fit points.

the effect of $\sin^2 \theta_{13}$ on $P(\nu_\mu \rightarrow \nu_\mu)$ (left) and the effect of $\sin^2 \theta_{23}$ on $P(\nu_\mu \rightarrow \nu_e)$ (right); and in Fig. 5.2, which shows how the two key observables, $P(\nu_\mu \rightarrow \nu_\mu)$ and $P(\nu_\mu \rightarrow \nu_e)$ depend on $\sin^2 \theta_{23}$ and δ_{CP} for the two mass hierarchies (keeping fixed the other oscillation parameters and the neutrino energy at the oscillation maximum ~ 600 MeV).

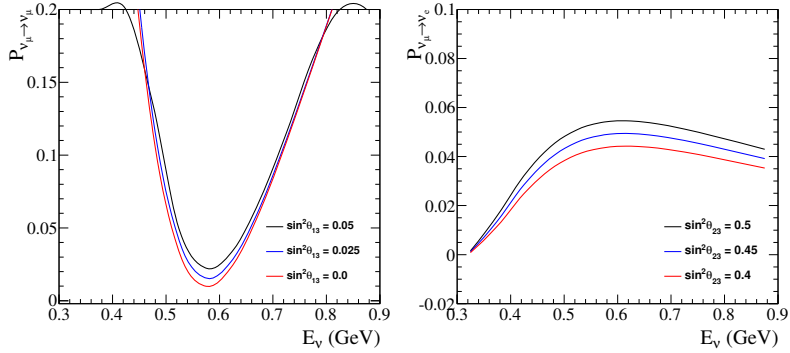


Figure 5.1: Examples of the effect of the interdependence between the oscillation parameters in the oscillation probabilities $P(\nu_\mu \rightarrow \nu_\mu)$ (left) and $P(\nu_\mu \rightarrow \nu_e)$ (right). These probabilities were computed for different values of $\sin^2 \theta_{13}$ (left) or $\sin^2 \theta_{23}$ (right) with the other parameters fixed to $\sin^2 \theta_{23} = 0.45$, $|\Delta m_{32}^2| = 2.4 \times 10^{-3}$ eV $^2/c^4$, $\delta_{CP} = 0$ (left) or $\sin^2 \theta_{13} = 0.025$, $|\Delta m_{32}^2| = 2.4 \times 10^{-3}$ eV $^2/c^4$, $\delta_{CP} = 0$ (right).

Thus, a change in the values of the fixed oscillation parameters in the stand-alone analyses can produce a significant impact on the confidence regions and best-fit values of the parameters measured. This is illustrated in Fig. 5.3, where the 68 % CL regions in the $(\sin^2 2\theta_{13}, \delta_{CP})$ space for the stand-alone appearance analysis on the T2K dataset corresponding to 6.393×10^{20} POT were obtained using different values for $\sin^2 \theta_{23}$, assuming normal mass hierarchy and fixing $|\Delta m_{32}^2| = 2.4 \times 10^{-3}$ eV $^2/c^4$ [177].

In order to avoid neglecting the effect of fixed oscillation parameters and to include all their dependencies, a **joint oscillation analysis** is to be performed. The motivation for the joint oscillation analysis is therefore to prevent fixing any of $|\Delta m_{32}^2|$, $\sin^2 \theta_{23}$, $\sin^2 \theta_{13}$ or δ_{CP} ² and to perform a joint determination of all four oscillation parameters with a simultaneous 3-flavour fit of the single μ -like ring and single e -like ring energy spectra.

²The effect of including the remaining 12-sector parameters, Δm_{21}^2 and $\sin^2 \theta_{12}$, in the T2K joint oscillation analysis has been studied and it found to be negligible (see Appendix B). Therefore, those parameters were kept fixed in the analysis results presented in Chapter 5.

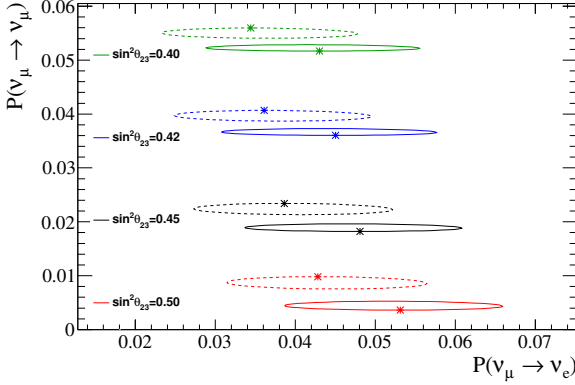


Figure 5.2: The $P(\nu_\mu \rightarrow \nu_\mu)$ and $P(\nu_\mu \rightarrow \nu_e)$ probabilities expected for different values of $\sin^2 \theta_{23}$ and for δ_{CP} in the interval $[-\pi, \pi]$ for normal (solid) and inverted (dashed) mass hierarchy. The highlighted dot on each ellipse is the point for $\delta_{CP} = 0$ and δ_{CP} increases clockwise (anti-clockwise) for normal (inverted) mass hierarchy. The other oscillation parameter values are fixed to $|\Delta m_{32}^2| = 2.4 \times 10^{-3} \text{ eV}^2/c^4$ and $\sin^2 \theta_{13} = 0.0243$ (solar parameters fixed to Tab. B.1) and the neutrino energy is fixed to 600 MeV.

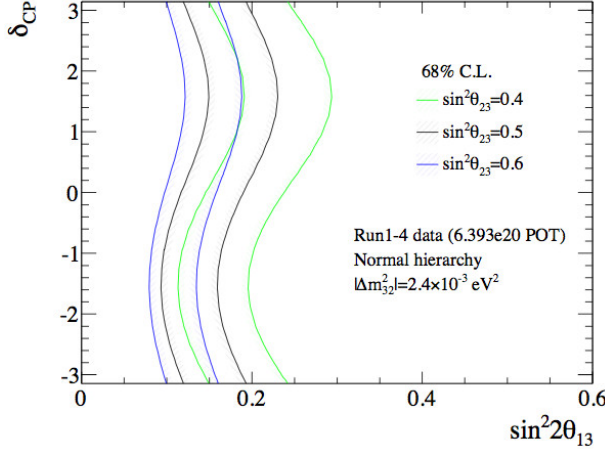


Figure 5.3: The 68% CL regions in the $(\sin^2 2\theta_{13}, \delta_{CP})$ space for the stand-alone appearance analysis on the T2K dataset corresponding to 6.393×10^{20} POT for different values for $\sin^2 \theta_{23}$ ($\sin^2 \theta_{23} = 0.4$ in green, $\sin^2 \theta_{23} = 0.5$ in black and $\sin^2 \theta_{23} = 0.6$ in blue), assuming normal mass hierarchy and fixing $|\Delta m_{32}^2| = 2.4 \times 10^{-3} \text{ eV}^2/c^4$. Figure from [177].

In this chapter, the results of the first T2K joint 3-flavour oscillation frequentist analysis on the combined Run 1+2+3+4 dataset, corresponding to an integrated exposure of 6.57×10^{20} POT, will be presented. In previous chapters, the theoretical framework for the three active neutrino paradigm, the description of the T2K experiment and the studies performed to obtain the necessary inputs to implement the stand-alone and joint oscillation analyses were introduced.

5.2 Oscillation Analysis Overview

Figure 5.4 shows a schematic overview of the oscillation analysis flow, including the necessary inputs described in Chapter 4. The aim of an oscillation analysis is to determine the oscillation parameters by comparing the expected number of neutrino candidate events as a function of neutrino energy with the observation at the far detector.

First of all, the neutrino flux prediction must be constructed as explained in Section 4.2, based on theoretical models integrated in the simulation packages and on T2K data from the different monitors (along the beamline and the INGRID on-axis near detector), constraining it with external data on hadron production from the NA61/SHINE experiment.

The flux simulation at ND280 is combined with the cross section models, constrained by external data (see Section 4.3), and with the simulation of the detector. The ND280 data, separated in three samples according to the number of pions in the final state, is then compared to the prediction to perform a fit, that constrains the flux and some cross section uncertainties at SK (correlated with ND280) as explained in Chapter 4.4.

The flux simulation at SK is also combined with the cross section models in order to build the prediction at SK, fundamental to perform the oscillations analysis. Finally, the neutrino event selection, explained in Chapter 4.5, is applied.

The oscillation fit at SK is performed by varying the oscillation parameters in the simulation and therefore changing the prediction at SK until it best matches the observed data. In this procedure, the systematic uncertainties on the flux prediction and correlated cross sections (Section 4.4.3), independent cross sections (Section 4.3), SK efficiencies (Section 4.5.2) and FSI, SI and PN uncertainties (Section 4.3.3) must be taken into account, including parameters to vary them in the fit.

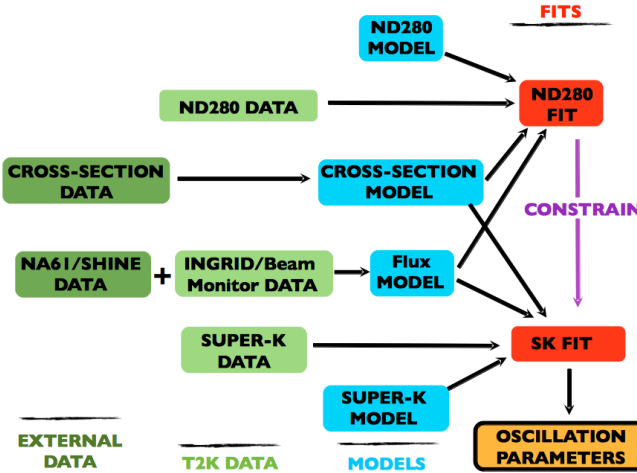


Figure 5.4: Schematic overview of the oscillation analysis flow.

5.3 Oscillation Probability Calculation and Choice of Oscillation Parameters

This analysis uses its own custom software to calculate oscillation probabilities, designed as a complete 3-flavour framework including matter effects in constant density matter, with the possibility of computing also oscillation probabilities in vacuum as cross check. Extensive validations of this framework were performed by comparing the values obtained with those calculated with an alternative formulation in the PDG review [178] and other independent programs, showing a great agreement between the different results.

The 3-flavour neutrino oscillation probabilities in vacuum are calculated from Eq. 2.29 using the PMNS matrix in vacuum defined in Eq. 2.31.

In the calculation of the 3-flavour oscillation probabilities in matter, the formulation described in Section 2.4.2 is used, using $U\bar{M}U^\dagger$ as the effective Hamiltonian matrix describing the neutrino evolution in terms of neutrino flavour eigenstates (see Eq. 2.38) for neutrinos and its complex conjugate for antineutrinos. The matter effects are taken into account by adding (subtracting) the potential $2E\sqrt{2}G_F N_e$ to the real part of the first diagonal element of $U\bar{M}U^\dagger$ (complex conjugate) for neutrinos (antineutrinos). After the addition or subtraction of this potential, $U\bar{M}U^\dagger$ or its complex conjugate is diagonalized. The (real) eigenvalues λ in which the matrix is diagonalized, that represent the effective mass-squared splittings in matter through their differences, are calculated by solving the (cubic) characteristic equa-

tion using the method of del Ferro, Tartaglia and Cardano described in [179]. With these eigenvalues, the eigenvectors are calculated algebraically using the simultaneous equations $UMU^\dagger - \lambda I = 0$ (for neutrinos). The three eigenvectors, normalized, become the columns of the effective mixing matrix in matter [180].

The initial neutrino flavour state, represented by a 1×3 column vector, is then multiplied by the Hermitian conjugate of the mixing matrix in matter, with a resultant 1×3 complex column vector representing the initial mass state. These matter states are then propagated and converted into final flavour states by multiplying by the mixing matrix in matter.

Several choices of the oscillation parameters are possible in the framework used to compute the oscillation probabilities, and different options were considered in the context of a joint 3-flavour oscillation analysis as it is outlined below.

Neutrino mixing parameters

In the stand-alone ν_μ disappearance analysis, $\sin^2 2\theta_{23}$ has been the variable typically measured since it appears in the first-order approximate formula for the ν_μ survival probability:

$$P(\nu_\mu \rightarrow \nu_\mu) \approx 1 - \sin^2 2\theta_{23} \sin^2 \left(\frac{\Delta m_{32}^2 L}{4E_\nu} \right) \quad (5.1)$$

However, in the context of the joint fit it is more natural to use $\sin^2 \theta_{23}$ as it appears in the leading-order term of $P(\nu_\mu \rightarrow \nu_e)$:

$$P(\nu_\mu \rightarrow \nu_e) \approx \sin^2 2\theta_{13} \sin^2 \theta_{23} \sin^2 \left(\frac{\Delta m_{31}^2 L}{4E_\nu} \right) \quad (5.2)$$

Thus, the natural choice for the joint 3-flavour oscillation analysis to fit for $\sin^2 \theta_{ij}$ rather than $\sin^2 2\theta_{ij}$, taking into account in this way the octant for θ_{23} . This choice has been the preferred one for this analysis, although some results were still produced in terms of $\sin^2 2\theta_{13}$.

Regarding the angle θ_{13} , $\sin^2 2\theta_{13}$ appears in the leading term or the $P(\nu_\mu \rightarrow \nu_e)$ oscillation probability in Eq. 5.2, and $\cos^2 \theta_{13}$ appears in the approximate formula for $P(\nu_\mu \rightarrow \nu_\mu)$:

$$\begin{aligned}
 P(\nu_\mu \rightarrow \nu_\mu) &\approx 1 - 4 \sin^2 \left(\frac{\Delta m_{31}^2 L}{4E} \right) c_{13}^2 s_{23}^2 [s_{12}^2 c_{23}^2 + c_{12}^2 s_{13}^2 s_{23}^2 + c_{12}^2 c_{23}^2 + s_{12}^2 s_{13}^2 s_{23}^2] \\
 &= 1 - 4 \sin^2 \left(\frac{\Delta m_{31}^2 L}{4E} \right) c_{13}^2 s_{23}^2 (s_{12}^2 + c_{12}^2) [c_{23}^2 + s_{13}^2 s_{23}^2] \\
 &= 1 - 4 \sin^2 \left(\frac{\Delta m_{31}^2 L}{4E} \right) c_{13}^2 s_{23}^2 [c_{23}^2 + s_{13}^2 s_{23}^2] \\
 &= 1 - \sin^2 \left(\frac{\Delta m_{31}^2 L}{4E} \right) [\cos^2 \theta_{13} \sin^2 2\theta_{23} + \sin^4 \theta_{23} \sin^2 2\theta_{13}]
 \end{aligned} \tag{5.3}$$

Therefore, $P(\nu_\mu \rightarrow \nu_e)$ is approximately linear with $\sin^2 2\theta_{13}$ but $P(\nu_\mu \rightarrow \nu_\mu)$ is not. In the context of global fits like the ones in [181] or [182], the variable used is $\sin^2 \theta_{13}$, and the results of the MINOS joint fit were reported in this variable as well [184]. However, the variable $\sin^2 2\theta_{13}$ was the one historically used to present ν_e appearance results, so it is still useful to produce results in terms of $\sin^2 2\theta_{13}$ in order to compare with previous results and results from other experiment. In any case, several checks were done and it was found that results are identical fitting $\sin^2 2\theta_{13}$ directly or fitting $\sin^2 \theta_{13}$ and making the appropriate re-scaling.

Mass-squared splitting parameters

Previous T2K analyses used the following mass-squared splitting parameters:

$$(|\Delta m_{32}^2|, \Delta m_{21}^2)$$

which are defined as $\Delta m_{ij}^2 = m_i^2 - m_j^2$ according to the PDG notation [178]. The mass hierarchy is set through the sign of Δm_{32}^2 i.e. $\Delta m_{32}^2 = |\Delta m_{32}^2|$ in the normal hierarchy and $\Delta m_{32}^2 = -|\Delta m_{32}^2|$ in the inverted hierarchy. The remaining mass-squared splitting is defined as $\Delta m_{31}^2 = \Delta m_{32}^2 + \Delta m_{21}^2$ for both hierarchies.

In the normal hierarchy (NH) $m_1^2 < m_2^2 << m_3^2$, while in the inverted hierarchy (IH) $m_3^2 << m_1^2 < m_2^2$, i.e. $|\Delta m_{31}^2|$ is the largest mass-squared splitting in the NH, whereas $|\Delta m_{32}^2|$ is the largest in the IH. This means that it is not possible to compare directly in the same plot the two hierarchies if the atmospheric mass-squared difference is input as $|\Delta m_{32}^2|$, as it will be an artificial difference between results due to the solar mass-squared splitting Δm_{21}^2 .

A different convention was considered for the joint analysis, defined by Fogli and Lisi in [181], [183], in which $(|\Delta m_{32}^2|, \Delta m_{21}^2)$ are replaced by:

$$(|\Delta m_{FL}^2|, \Delta m_{21}^2)$$

$$\text{where } \Delta m_{FL}^2 = \left(m_3^2 - \frac{m_1^2 + m_2^2}{2} \right) = \left(\frac{\Delta m_{31}^2 + \Delta m_{32}^2}{2} \right).$$

The parameter Δm_{FL}^2 has the same absolute value for both mass hierarchies and therefore allows results in terms of this quantity to be compared directly for both mass hierarchies in the same plot. The parameter Δm_{21}^2 is the *solar* squared-mass splitting which is known to be positive. When the mass-squared splittings are input as $(|\Delta m_{FL}^2|, \Delta m_{21}^2)$, the mass hierarchy is set through the sign of Δm_{FL}^2 , and Δm_{32}^2 and Δm_{31}^2 are calculated as

$$\begin{aligned}\Delta m_{32}^2 &= \Delta m_{FL}^2 - \frac{\Delta m_{21}^2}{2} \\ \Delta m_{31}^2 &= \Delta m_{FL}^2 + \frac{\Delta m_{21}^2}{2}\end{aligned}$$

for both mass hierarchies.

The convention for mass-squared splitting parameters discussed here, $(|\Delta m_{FL}^2|, \Delta m_{21}^2)$, seems a natural choice for the joint oscillation analysis in order to compare results in different mass hierarchies and it will be extensively used in this chapter. However, final result plots were produced using the convention $|\Delta m^2| = |\Delta m_{32}^2|(NH)$, $|\Delta m_{13}^2|(IH)$, in order to compare with previous results, and Δm_{32}^2 for both mass hierarchies (with opposite signs) for comparisons with results from other experiments in Fig. 5.34.

5.4 Predictions of Single μ -like and e-like Ring Event Reconstructed Energy Spectra in SK

The calculation of the prediction of single μ -like ring and single e-like ring event reconstructed energy spectra in SK is the key element to perform this oscillation analysis and to estimate the values of the oscillation parameters.

5.4.1 Methodology

In this analysis, the oscillation parameters are determined by fitting the reconstructed energy (E_r) spectra of the single μ -like ring and single e-like ring events (ν_μ and ν_e event candidates respectively) observed at SK. The predicted number of events $N_{SK;s,r}$ in the r^{th} reconstructed energy bin in the SK sample s (single μ -like ring or single e-like ring) is computed as follows:

$$N_{SK;s,r}^{exp} = \sum_m \sum_t \sum_{rt} P_{m,t} \cdot T_{s,r,rt,f_{\Delta E},s} \cdot S_{s,m,t,rt,\vec{f}} \cdot N_{SK;s,m,rt,t}^{MC} \quad (5.4)$$

This calculation uses the input SK Monte Carlo (MC) templates, which are 2-dimensional histograms of numbers of events from one interaction mode as a function of true and reconstruct energies. In Eq. 5.4, $N_{SK;s,m,rt,t}^{MC}$ is the input SK MC template containing the number of events in the sample s (single μ -like ring or single e-like ring), with true interaction mode m , and found in the true energy bin t and in the reconstructed energy bin rt . Notice that rt index indicates a SK reconstructed energy bin in absence of a shift in the reconstructed energy scale and the index r indicates a SK reconstructed energy bin after applying a shift in the reconstructed energy scale. The term $S_{s,m,t,rt,\vec{f}}$ in Eq. 5.4 is an overall, multiplicative, systematic error factor depending on the sample s , the interaction mode m , the true energy bin t , the reconstructed energy bin rt and a vector of nuisance (systematic) parameters \vec{f} . A transfer function $T_{r;rt;f_{\Delta E}}$ is describing the migration of events between the reconstructed energy bins r and rt due to the uncertainty on the SK reconstructed energy scale, expressed here in terms of the nuisance parameter $f_{\Delta E}$. Finally, $P_{m,t}$ is the 3-flavour oscillation probability applied in the true energy bin t of the SK MC template which corresponds to the interaction mode m .

5.4.2 Construction of SK Monte Carlo Templates

The nominal SK single μ -like ring or single e-like ring MC templates $N_{SK;s,m,rt,t}^{MC}$ are constructed by applying the corresponding selection cuts for single μ -like ring or single e-like ring events described in Section 4.5.1. The cuts are applied to the official SK MC, based on NEUT, generated using the flux simulation explained in Chapter 4, incorporating the detector simulation described in Section 4.5.

This analysis considers the following seven neutrino species: $\nu_\mu, \bar{\nu}_\mu, \nu_e, \bar{\nu}_e, \nu_\mu \rightarrow \nu_e, \bar{\nu}_\mu \rightarrow \bar{\nu}_e$ and $\nu_e \rightarrow \nu_\mu$. Four of the species, $\nu_\mu, \bar{\nu}_\mu, \nu_e$ and $\bar{\nu}_e$, were generated using the nominal JNUBEAM flux without oscillations. The other three species, $\nu_\mu \rightarrow \nu_e, \bar{\nu}_\mu \rightarrow \bar{\nu}_e$ and $\nu_e \rightarrow \nu_\mu$, were generated re-weighting the sample of the final flavour (from the previous non-oscillated species) with the flux of the initial flavour, so that the flux is considered to be the one for the initial flavour, but interactions are simulated for the final flavour, as if all events in the sample had oscillated from the initial to the final flavour (for instance, all muon neutrinos are assumed to be converted to electron neutrinos in the $\nu_\mu \rightarrow \nu_e$ sample). Therefore, when applying the oscillation probabilities, the corresponding survival probability is to be applied to the first four species, whereas the corresponding appearance probability is to be applied to the other three species. All samples were generated

including the neutrino flux estimates up to 30 GeV. The contribution of the templates for different species at typical oscillation parameters can be found in Tab. 5.1. The oscillated specie $\bar{\nu}_e \rightarrow \bar{\nu}_\mu$ was also considered but finally not used since its contribution is negligible in both the single μ -like ring and the single e-like ring samples, as observed in Tab. 5.1.

The normalization (integrated exposure in terms of POT) of each event sample is calculated from the number of events with a true interaction vertex within the 22.5 kt fiducial volume, N , estimated by:

$$N = \int dS dIdE \cdot \frac{d^3\Phi_{SK}}{dS dIdE_\nu} \cdot \sigma_{H_2O}(E_\nu) \cdot \frac{N_A}{A} \cdot \rho \cdot L \quad (5.5)$$

where $d^3\Phi_{SK}/dS dIdE$ is the number of flux particles for the given neutrino species per neutrino energy bin dE_ν , per unit area in the SK location dS and per POT, $\sigma_{H_2O}(E_\nu)$ is the total interaction cross section in water for the given neutrino species, I is the beam intensity in terms of POT, N_A is Avogadro's number, A is the mass number for water, ρ is the water density and L is the neutrino path length in the water volume. This normalization depends only on the neutrino specie. After being generated from a MC sample corresponding to a calculated integrated beam exposure I , each MC template is normalized to the integrated beam exposure of the Run 1+2+3+4 dataset (6.57×10^{20} POT) by scaling the bin contents of the template with $6.57 \times 10^{20}/I$.

For each SK MC sample, a number of different MC templates is constructed corresponding to different true reaction modes. The joint oscillation analysis presented here uses a different number of MC templates depending on the sample, single μ -like ring or single e-like ring. The division of CC modes is the same for both: CCQE, CC $1\pi^\pm$, CC coherent and CC other. However, the separation of NC modes is different for the single μ -like ring (NC $1\pi^\pm$ and NC other) and the single e-like ring (NC $1\pi^0$, NC coherent and NC other). This separation is intended to identify the neutral current coherent and incoherent π^0 production for the single e-like ring sample on the one hand, since its decay into two γ 's is often mis-identified as an e-like ring and constitutes one of the main backgrounds for the ν_e event candidates at SK; and, on the other hand, to identify charged pions π^\pm produced in neutral current interactions for the single μ -like ring sample, which most probably decay producing μ^\pm and constitute one of the main backgrounds for the ν_μ event candidates at SK. The 36 (40) MC templates used for the single μ -like (e-like) ring sample are the ones included in Tab. 5.2.

Each of these MC templates for the single μ -like ring sample contains 84 true energy bins \times 73 reconstructed energy bins, and each of the MC templates for the single e-like ring sample contains 84 true energy bins \times 25 reconstructed energy bins. The 84 true energy bins, common for both the single μ -like ring and the

single e-like ring samples, are arranged as follows:

- 6 50-MeV bins from 0-0.3 GeV,
- 28 25-MeV bins from 0.3-1 GeV,
- 40 50-MeV bins from 1-3 GeV,
- 5 100-MeV bin from 3-3.5 GeV,
- 1 bin from 3.5-4 GeV,
- 1 bin from 4-5 GeV,
- 1 bin from 5-7 GeV,
- 1 bin from 7-10 GeV and
- 1 bin from 10-30 GeV.

For the single μ -like ring sample the 73 reconstructed energy bins are:

- 60 50-MeV bins from 0-3 GeV,
- 4 250-MeV bins from 3-4 GeV,
- 4 500-MeV bins from 4-6 GeV,
- 4 1000-MeV bins from 6-10 GeV and
- 1 bin >10 GeV

while for the single e-like ring sample the 25 reconstructed energy bins used are uniform 50-MeV bins from 0 to 1.25 GeV. Studies were performed in order to determine this binning scheme, balancing the needs for CPU efficiency and accuracy, so that the selected binning allows enough granularity for precise application of oscillation probabilities and determination of neutrino oscillation parameters, and precise application of the systematic parameters, with a reasonable computation speed at the same time. Comparisons were made against much finer binning schemes and found that the only differences $> 1\%$ occurred for modes with a small contribution to the total reconstructed energy spectra.

The same reconstructed neutrino energy binning is used for the fit of the single μ -like ring reconstructed energy spectrum (73 reconstructed energy bins) and for the single e-like ring reconstructed energy spectrum (25 reconstructed energy bins). The nominal MC templates generated with the nominal flux files are re-weighted to the flux tuned to NA61 hadron production measurements [?]. The re-weighted MC templates are denoted as *NA61-tuned* MC templates in this document and the

effect of this flux tuning on the predicted reconstructed energy spectrum of single μ -like ring events and single e-like ring events is illustrated in Fig. 5.5, showing that the predicted number of single μ -like ring events and single e-like ring events per bin increases when applying the re-weight to the flux tuned to NA61 hadron production with and without oscillations, without altering the general shape of the spectra.

The BANFF flux and cross section parameter tuning explained in Chapter 4.4 is used to re-weight the NA61-tuned MC templates. The MC templates obtained after this second re-weighting process will be denoted as *BANFF-tuned* MC templates in this document. A list of BANFF parameters and their best-fit values is shown in Tab. 4.7. The effect of the BANFF tuning on the predicted reconstructed energy spectra of single μ -like ring and single e-like ring events is discussed in Fig. 5.6, where a reduction on the number of single μ -like ring events and single e-like ring events is observed when applying the BANFF re-weight in the majority of reconstructed energy bins, whereas an increase is produced for some bins, without altering the general shape of the spectra.

The oscillation probabilities, computed in the 3-flavour framework including matter effects in constant density matter previously described, are then applied as a function of true energy to the MC templates of CC interaction modes. The ν_μ NC MC templates for a mode m are proxies for the NC MC templates for the mixture of $\nu_e + \nu_\mu + \nu_\tau$ resulting from 3-flavour ν_μ oscillations for that mode m . The same applies to the $\bar{\nu}_\mu$, ν_e and $\bar{\nu}_e$ NC MC templates. Therefore the NC MC templates are unchanged under standard 3-flavour oscillations.

The MC templates constructed from the unoscillated MC samples are weighted with the corresponding survival probability: the ν_μ templates are weighted with $P(\nu_\mu \rightarrow \nu_\mu)$, the $\bar{\nu}_\mu$ templates with $P(\bar{\nu}_\mu \rightarrow \bar{\nu}_\mu)$, the ν_e templates with $P(\nu_e \rightarrow \nu_e)$ and the $\bar{\nu}_e$ templates with $P(\bar{\nu}_e \rightarrow \bar{\nu}_e)$. The MC templates made from the oscillated $\nu_\mu \rightarrow \nu_e$ MC sample are weighted with $P(\nu_\mu \rightarrow \nu_e)$, the MC templates made from the oscillated $\bar{\nu}_\mu \rightarrow \bar{\nu}_e$ MC sample are weighted with $P(\bar{\nu}_\mu \rightarrow \bar{\nu}_e)$ and the MC templates made from the oscillated $\nu_e \rightarrow \nu_\mu$ MC sample are weighted with $P(\nu_e \rightarrow \nu_\mu)$.

In the standard 3-flavour oscillation framework, oscillations of ν_e and ν_μ can yield ν_τ , while oscillations of $\bar{\nu}_e$ and $\bar{\nu}_\mu$ can yield $\bar{\nu}_\tau$. In this analysis, contributions from ν_τ -CC and $\bar{\nu}_\tau$ -CC were neglected as their energy threshold is around 3.5 GeV and their effect is negligible. Accordingly, no ν_τ -CC and $\bar{\nu}_\tau$ -CC MC templates are used. It should also be mentioned that there are no NC MC templates made from the oscillated species ($\nu_\mu \rightarrow \nu_e$, $\bar{\nu}_\mu \rightarrow \bar{\nu}_e$ and $\nu_e \rightarrow \nu_\mu$). If they were used, the oscillated ν_e (i.e. ν_e coming from ν_μ oscillations), for instance, would be double counted since they are already included in the ν_μ NC MC templates. Finally, it is assumed that CPT is conserved, and the same oscillation parameters are used for neutrinos and antineutrinos.

5.4.3 Predictions of Nominal and Tuned-MC Single μ -like Ring and Single e-like Ring Spectra

In this section, the expected number of events and single μ -like ring and single e-like ring reconstructed energy spectra in SK are presented for various oscillation scenarios. All plots were generated for an integrated exposure of 6.57×10^{20} POT and, unless otherwise stated, the normal hierarchy is assumed and the solar parameters were fixed to the values in Tab. B.1.

The effects of the NA61 and BANFF tunes on the reconstructed energy spectrum of single μ -like ring events (left plots) and single e-like ring events (right plots) are shown in Figs. 5.5 and 5.6 respectively for no oscillations (top plots) and for oscillations with $\sin^2 \theta_{23}=0.5$ and $\Delta m_{FL}^2=2.4375 \times 10^{-3} \text{ eV}^2/\text{c}^4$, $\sin^2 \theta_{13} = 0.0243$, $\delta_{CP}=0$ and the values for the solar parameters in Tab. B.1, and normal mass hierarchy assumed (bottom plots).

The expected number of single μ -like ring events and single e-like ring events is shown in Fig. 5.7 for normal hierarchy for an exposure of 6.57×10^{20} POT after BANFF tuning applied to the MC templates, as a function of the oscillation parameters $\sin^2 \theta_{23}$ and Δm_{FL}^2 with $\sin^2 \theta_{13} = 0.0243$ and $\delta_{CP} = 0$ (top) and as a function of $\sin^2 \theta_{13}$ and δ_{CP} with $\Delta m_{FL}^2 = 2.4375 \times 10^{-3} \text{ eV}^2/\text{c}^4$ (or $\Delta m_{32}^2 = 2.4 \times 10^{-3} \text{ eV}^2/\text{c}^4$) and $\sin^2 \theta_{23} = 0.5$ (bottom). The four plots in this Fig. 5.7 illustrate the characteristic dependency of the expected number of ν_μ and ν_e event candidates with respect to the usual oscillation parameters defining the space where the confidence regions are calculated ($\sin^2 \theta_{23}$, Δm_{FL}^2 and $\sin^2 \theta_{13}$, δ_{CP} respectively), and with respect to the other couple of oscillation parameters.

Predicted single μ -like ring and single e-like ring SK reconstructed energy spectra are shown in Fig. 5.8 for an exposure of 6.57×10^{20} POT after BANFF tuning applied to the MC templates, fixing the systematic parameters to their nominal values, for no oscillations (top plots) and oscillations with $\sin^2 \theta_{23}=0.5$ and $\Delta m_{FL}^2=2.4375 \times 10^{-3} \text{ eV}^2/\text{c}^4$, $\sin^2 \theta_{13}=0.0243$, $\delta_{CP}=0$ and normal hierarchy (bottom plots). The spectrum for the single μ -like ring presents a large peak around the reconstructed energy ~ 600 MeV for no oscillations, which is greatly reduced when oscillations are applied, and an oscillation dip appears at that energy. In both cases the ν_μ CCQE mode is the main contribution, while the main background corresponds to ν_μ CCnQE interactions. The spectra for the single e-like ring is however very different in the oscillation and no oscillation scenarios: obviously, no signal $\nu_\mu \rightarrow \nu_e$ appears when no oscillations are applied, whereas a large contribution, distributed as a peak around the reconstructed energy ~ 600 MeV, appears due to the $\nu_\mu \rightarrow \nu_e$ channel when oscillations are applied. The main contribution in the spectrum without oscillations, and the first after the contribution from the signal $\nu_\mu \rightarrow \nu_e$ in the spectrum with oscillations, is the corresponding to CC interaction modes of beam ν_e and $\bar{\nu}_e$ and osc. $\bar{\nu}_e$.

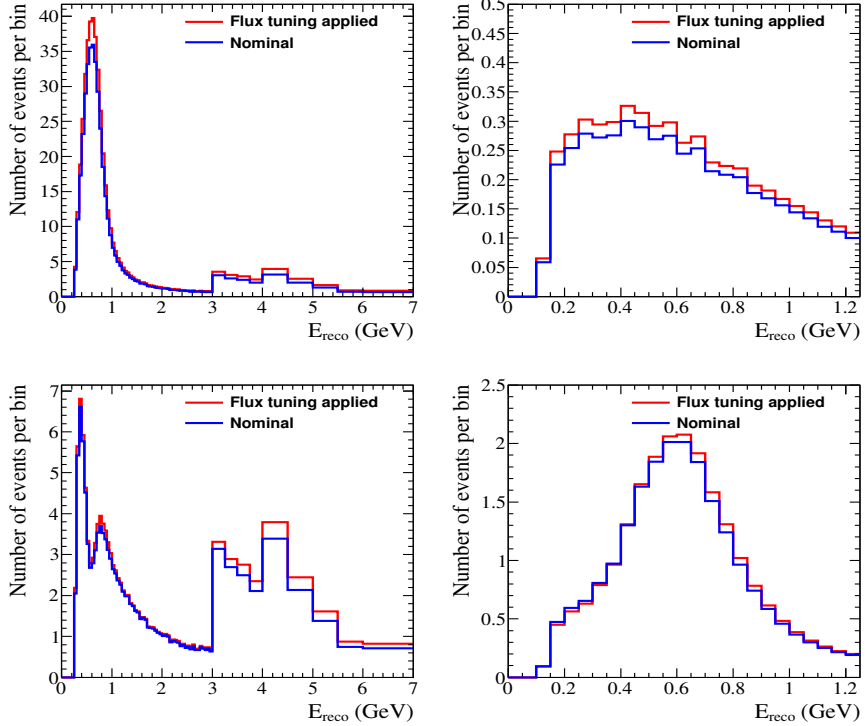


Figure 5.5: Reconstructed energy spectrum of single μ -like ring events (left) and single e -like ring events (right), for an exposure of 6.57×10^{20} POT, both with and without the effect of the NA61 flux tuning of the nominal MC templates. The spectra are shown for no oscillations (top plots) and for oscillations with $\sin^2 \theta_{23}=0.5$ and $\Delta m^2_{FL}=2.4375 \times 10^{-3}$ eV $^2/c^4$, $\sin^2 \theta_{13}=0.0243$, $\delta_{CP}=0$ and the values for the solar parameters in Tab. B.1, and normal mass hierarchy assumed (bottom plots).

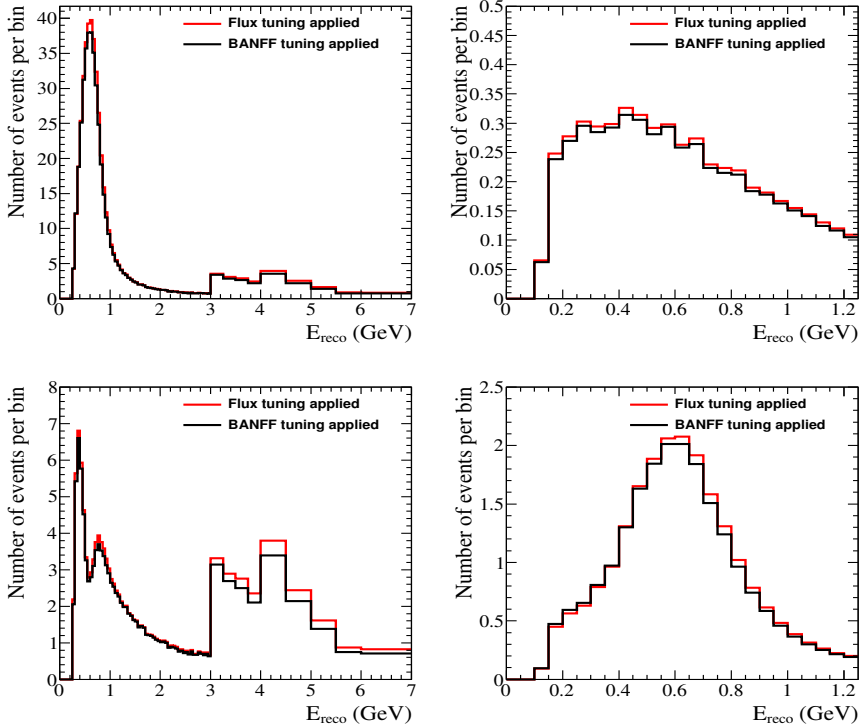


Figure 5.6: Reconstructed energy spectrum of single μ -like ring events (left) and single e -like ring events (right), for an exposure of 6.57×10^{20} POT, both with and without the effect of BANFF flux and cross section tuning on the NA61-tuned flux MC templates. The spectra are shown for no oscillations (top plots) and for oscillations with $\sin^2 \theta_{23}=0.5$ and $\Delta m_{FL}^2=2.4375 \times 10^{-3} \text{ eV}^2/\text{c}^4$, $\sin^2 \theta_{13}=0.0243$, $\delta_{CP}=0$ and the values for the solar parameters in Tab. B.1, and normal mass hierarchy assumed (bottom plots).

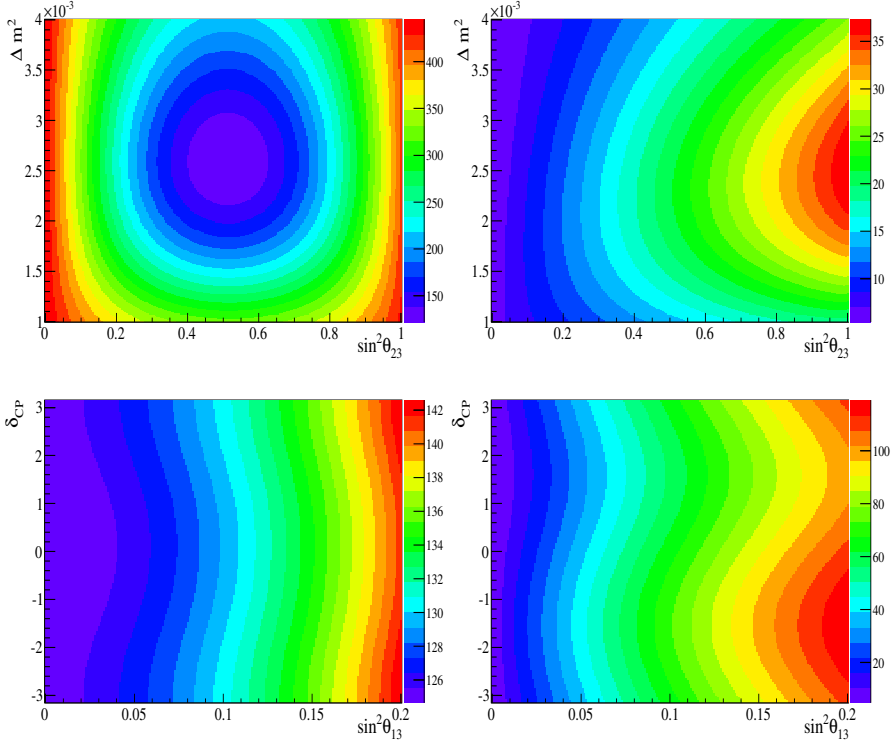


Figure 5.7: Predicted number of single μ -like ring events (left plots) and single e-like ring events (right plots) for an exposure of 6.57×10^{20} POT after BANFF tuning applied to the MC templates as a function of the oscillation parameters $\sin^2 \theta_{23}$ and $\Delta m^2 = \Delta m_{FL}^2$ with $\sin^2 \theta_{13} = 0.0243$ and $\delta_{CP} = 0$ (top plots) and as a function of the oscillation parameters $\sin^2 \theta_{13}$ and δ_{CP} with $\sin^2 \theta_{23} = 0.5$ and $\Delta m^2 = \Delta m_{FL}^2 = 2.4375 \times 10^{-3} eV^2/c^4$ (bottom plots). The solar parameters were fixed to the values in Tab. B.1, the normal hierarchy was assumed and the systematic parameters were fixed to their nominal values.

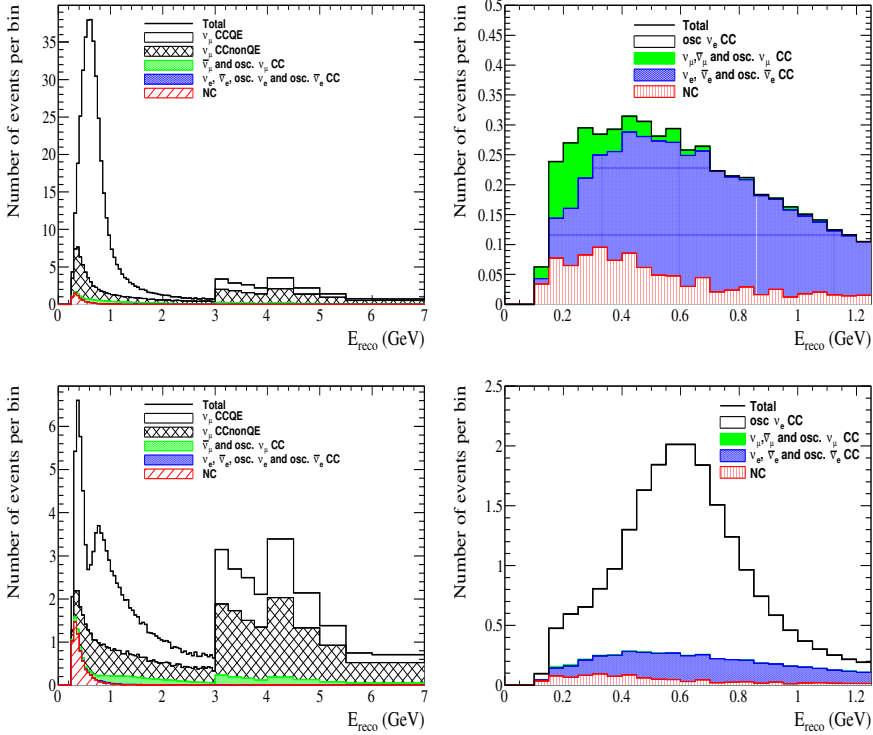


Figure 5.8: Predicted single μ -like ring (left) and single e -like ring (right) SK reconstructed energy spectra showing contributions from various true neutrino interaction modes, for an exposure of 6.57×10^{20} POT after BANFF tuning applied to the MC templates, for no oscillations (top plots) and oscillations with $\sin^2 \theta_{23}=0.5$ and $\Delta m_{FL}^2=2.4375 \times 10^{-3} \text{ eV}^2/\text{c}^4$, $\sin^2 \theta_{13}=0.0243$, $\delta_{CP}=0$ and the values for the solar parameters in Tab. B.1, and normal mass hierarchy assumed (bottom plots). The systematic parameters were fixed to their nominal values in the four plots. Notice that they are stacked plots.

Table 5.1 shows the predicted number of single μ -like ring and single e-like ring events for an exposure of 6.57×10^{20} POT after BANFF tuning applied to the MC templates, fixing the systematic parameters to their nominal values, for oscillations with $\sin^2(\theta_{12}) = 0.306$, $\Delta m_{21}^2 = 7.5 \times 10^{-5}$, $\sin^2(\theta_{23}) = 0.5$, $\Delta m_{FL}^2 = 2.4375 \times 10^{-3} \text{eV}^2/\text{c}^4$, $\sin^2(\theta_{13}) = 0.0243$, $\delta_{CP} = 0$ and normal hierarchy assumed. The predicted number of single μ -like ring events is a very pure ν_μ sample, while the main background is $\bar{\nu}_\mu$ and represents only about $\sim 7\%$ of the number of ν_μ ($\sim 6\%$ of the total) with these oscillation parameters. For the predicted number of single e-like ring events, the main background is due to the beam ν_e contamination, and corresponds to a $\sim 18\%$ of the number of $\nu_\mu \rightarrow \nu_e$ events ($\sim 9\%$ of the total) with these oscillation parameters, followed by the ν_μ background with a $\sim 6\%$ of the number of $\nu_\mu \rightarrow \nu_e$ events ($\sim 4\%$ of the total). As observed in Tab. 5.1, the contribution from the templates $\bar{\nu}_e \rightarrow \bar{\nu}_\mu$ are negligible to both samples, so these templates were finally not used in the analysis.

Number of events	$1R_\mu$		$1R_e$	
	Osc.	No osc.	Osc.	No osc.
Total	124.98	445.98	21.06	4.97
ν_μ	116.46	431.77	0.94	1.38
$\nu_e \rightarrow \nu_\mu$	0.16	0	0.00	0
$\bar{\nu}_\mu$	7.81	13.92	0.05	0.06
$\bar{\nu}_e \rightarrow \bar{\nu}_\mu$	0.01	0	0.00	0
ν_e	0.26	0.27	3.13	3.38
$\nu_\mu \rightarrow \nu_e$	0.26	0	16.55	0
$\bar{\nu}_e$	0.02	0.02	0.15	0.16
$\bar{\nu}_\mu \rightarrow \bar{\nu}_e$	0.00	0	0.22	0

Table 5.1: Predicted number of single muon-like ring and single electron-like ring events for an exposure of 6.57×10^{20} POT after BANFF tuning applied to the MC templates, fixing the systematic parameters to their nominal values, with and without oscillations and with oscillations using the typical parameter values: $\sin^2(\theta_{12}) = 0.306$, $\Delta m_{21}^2 = 7.5 \times 10^{-5}$, $\sin^2(\theta_{23}) = 0.5$, $\Delta m_{FL}^2 = 2.4375 \times 10^{-3}$, $\sin^2(\theta_{13}) = 0.0243$, $\delta_{CP} = 0$ and normal mass hierarchy. The total numbers are broken down into the intrinsic beam and oscillated components. The templates corresponding to $\bar{\nu}_e \rightarrow \bar{\nu}_\mu$ were finally not used in the analysis due to its negligible contribution to both samples.

Table 5.2 shows the number of single μ -like ring events and single e-like ring events using the BANFF-tuned MC templates and the different interaction modes, fixing the systematic parameters to their nominal values, for an exposure of 6.57×10^{20} POT and oscillations with $\sin^2 \theta_{23}=0.5$ and $\Delta m_{FL}^2 = 2.4375 \times 10^{-3} \text{eV}^2/\text{c}^4$, $\sin^2 \theta_{13}=0.0243$, $\delta_{CP}=0$, the values for the solar parameters in Tab. B.1

and normal mass hierarchy. This table gives more details about the main contributing modes for each sample. For the single μ -like ring events, the true interaction modes with the largest contribution to the ν_μ sample are first the CCQE interaction mode and then the CC single pion production. The CCQE and CC single pion production modes are also the modes with the largest contribution to the $\nu_\mu \rightarrow \nu_e$ sample in the single e-like ring events.

5.5 Systematic Effects in the Prediction of the Single μ -like Ring and Single e-like Ring Event Reconstructed Energy Spectra in SK

The estimation of the uncertainties to be included in the oscillation analyses have been described in previous chapters. The flux and cross section uncertainties were described in Chapter 4. The constraint by the fit to the ND280 near detector data (BANFF) on some of the flux and cross section uncertainties was explained in Section 4.4. And the SK detector efficiencies were defined in Section 4.5. In total, there are 64 systematic parameters considered in the joint oscillation analysis presented here, that can be grouped into 4 categories, summarized in Tab. 5.3.

A description of the 64 systematic parameters will be given in this section, explaining the way each systematic is applied and the MC templates that are affected by them. Afterwards, Tab. 5.4 presents a summary of which systematic parameter is applied to each sample (single μ -like ring or single e-like ring) for the stand-alone analyses compared to the joint oscillation analysis.

Finally, the evaluation of the effects of the systematic parameters, on the predicted number of events and on the reconstructed energy spectra, is presented.

	$N_{SK} (1R_\mu)$	$N_{SK} (1R_e)$
Total	124.9776	21.0621
ν_μ CCQE	70.9903	0.0480
ν_μ CC $1\pi^\pm$	29.8033	0.0171
ν_μ CC coherent	0.9083	0.0000
ν_μ CC other	8.5983	0.0010
ν_μ NC $1\pi^\pm$	2.9348	-
ν_μ NC $1\pi^0$	-	0.3924
ν_μ NC coherent	-	0.1539
ν_μ NC other	3.2290	0.3314
Osc. ν_μ CCQE	0.1237	0.0001
Osc. ν_μ CC $1\pi^\pm$	0.0300	0.0000
Osc. ν_μ CC coherent	0.0009	0.0000
Osc. ν_μ CC other	0.0026	0.0000
$\bar{\nu}_\mu$ CCQE	4.6222	0.0009
$\bar{\nu}_\mu$ CC $1\pi^\pm$	2.1332	0.0002
$\bar{\nu}_\mu$ CC coherent	0.2483	0.0000
$\bar{\nu}_\mu$ CC other	0.4855	0.0001
$\bar{\nu}_\mu$ NC $1\pi^\pm$	0.1434	-
$\bar{\nu}_\mu$ NC $1\pi^0$	-	0.0199
$\bar{\nu}_\mu$ NC coherent	-	0.0159
$\bar{\nu}_\mu$ NC other	0.1751	0.0175
ν_e CCQE	0.0352	2.2703
ν_e CC $1\pi^\pm$	0.0228	0.7720
ν_e CC coherent	0.0011	0.0093
ν_e CC other	0.0066	0.0582
ν_e NC $1\pi^\pm$	0.0751	-
ν_e NC $1\pi^0$	-	0.0107
ν_e NC coherent	-	0.0041
ν_e NC other	0.1213	0.0101
$\bar{\nu}_e$ CCQE	0.0020	0.0975
$\bar{\nu}_e$ CC $1\pi^\pm$	0.0013	0.0418
$\bar{\nu}_e$ CC coherent	0.0001	0.0067
$\bar{\nu}_e$ CC other	0.0004	0.0037
$\bar{\nu}_e$ NC $1\pi^\pm$	0.0082	-
$\bar{\nu}_e$ NC $1\pi^0$	-	0.0012
$\bar{\nu}_e$ NC coherent	-	0.0007
$\bar{\nu}_e$ NC other	0.0121	0.0010
Osc. $\bar{\nu}_e$ CCQE	0.0021	0.1715
Osc. $\bar{\nu}_e$ CC $1\pi^\pm$	0.0008	0.0386
Osc. $\bar{\nu}_e$ CC coherent	0.0001	0.0103
Osc. $\bar{\nu}_e$ CC other	0.0000	0.0015
Osc. ν_e CCQE	0.1842	13.9958
Osc. ν_e CC $1\pi^\pm$	0.0689	2.4871
Osc. ν_e CC coherent	0.0049	0.0415
Osc. ν_e CC other	0.0015	0.0302

Table 5.2: Numbers of sing μ -like and e-like ring events (see main text).

SK energy scale systematics (1)

$f_{E;r}^{SK}$	Reconstructed energy scale systematic, with a 2.4% uncertainty.
----------------	---

SK+FSI+SI+PN systematics (18)

Combining SK detector efficiencies, FSI (pion final state interactions / intranuclear hadron transport) and SI (secondary interaction / detector hadron transport) and PN (photo nuclear/ interactions between photons and nuclei) uncertainties. Eighteen correlated parameters are included ($i=0,\dots,17$) corresponding to different modes and reconstructed energy bins.

i	Description	1σ fractional error
0	$1R_\mu$, ν_μ & $\bar{\nu}_\mu$ CCQE, $E_{reco} < 0.4$ GeV	0.020
1	$1R_\mu$, ν_μ & $\bar{\nu}_\mu$ CCQE, $0.4 \text{ GeV} \leq E_{reco} \leq 1.1$ GeV	0.019
2	$1R_\mu$, ν_μ & $\bar{\nu}_\mu$ CCQE, $E_{reco} > 1.1$ GeV	0.020
3	$1R_\mu$, ν_μ & $\bar{\nu}_\mu$ CCnonQE	0.093
4	$1R_\mu$, ν_e & $\bar{\nu}_e$ CC	1.005
5	$1R_\mu$, All NC	0.599
$f_{i;r}^{SK+FSI}$	$1R_e$, osc. ν_e CC, $E_{reco} < 0.35$ GeV	0.110
	$1R_e$, osc. ν_e CC, $0.35 \text{ GeV} \leq E_{reco} \leq 0.8$ GeV	0.031
	$1R_e$, osc. ν_e CC, $0.8 \text{ GeV} < E_{reco} \leq 1.25$ GeV	0.035
	$1R_e$, ν_μ & $\bar{\nu}_\mu$ CC, $E_{reco} < 0.35$ GeV	1.244
	$1R_e$, ν_μ & $\bar{\nu}_\mu$ CC, $0.35 \text{ GeV} \leq E_{reco} \leq 0.8$ GeV	1.216
	$1R_e$, ν_μ & $\bar{\nu}_\mu$ CC, $0.8 \text{ GeV} < E_{reco} \leq 1.25$ GeV	1.229
	$1R_e$, ν_e & $\bar{\nu}_e$ CC, $E_{reco} < 0.35$ GeV	0.068
	$1R_e$, ν_e & $\bar{\nu}_e$ CC, $0.35 \text{ GeV} \leq E_{reco} \leq 0.8$ GeV	0.042
	$1R_e$, ν_e & $\bar{\nu}_e$ CC, $0.8 \text{ GeV} < E_{reco} \leq 1.25$ GeV	0.063
	$1R_e$, All NC, $E_{reco} < 0.35$ GeV	0.524
	$1R_e$, All NC, $0.35 \text{ GeV} \leq E_{reco} \leq 0.8$ GeV	0.247
	$1R_e$, All NC, $0.8 \text{ GeV} < E_{reco} \leq 1.25$ GeV	0.604

The values of fractional errors for each SK+FSI+SI+PN systematic parameter, calculated as the square root of the diagonal terms of the covariance matrix, are shown in Fig. 5.9.

Independent cross section systematics (12)

$f_{pF;t,r}$	Uncertainty of ± 30 MeV/c on the Fermi momentum for ^{16}O .
$f_{bindE;t,r}$	Uncertainty of ± 9 MeV on the binding energy for ^{16}O .
$f_{SF;t,r}$	Nuclear environment modelling systematic: Switches from Fermi Gas (RFG) to Spectral Function (SF) model (0:RFG - 1:SF).
$f_{\pi-less\Delta;t,r}$	Uncertainty of 20% due to the fraction of π -less Δ decays in resonance-production events.
$f_{CCothShape;t,r}$	Uncertainty of 40% on CC multipion, CC DIS and CC resonant η , K and photon production cross section.
$f_{Wshape;t,r}$	Uncertainty of 52% on the shape of the initial pion momentum distribution (before final-state interactions) in resonance interactions.
$f_{CCcoh;t}$	Uncertainty of 100% on the CC coherent cross section.
$f_{NC1\pi^\pm;t}$	Uncertainty of 30% on the NC1 π^\pm cross section.
$f_{NCcoh;t}$	Uncertainty of 30% on the NC coherent cross section.
$f_{NCoth;t}$	Uncertainty of 30% on the NC other (all but single π^\pm for $1R_\mu$ sample or all but single π^0 and coherent for $1R_e$) cross section.
$f_{CC\nu_e;t}$	Uncertainty of 3% on the ν_e / ν_μ CC cross section ratio.
$f_{CC\bar{\nu};t}$	Uncertainty of 20% on the $\bar{\nu} / \nu$ CC cross section ratio.

Correlated flux and cross section systematics (33)

Flux and correlated cross section parameters tuned by the fit to the ND280 near detector data. Thirty-three correlated parameters are included ($i=0,\dots,32$). The list of them with their pre and post fit values and errors in presented in Tab. 4.7 and the correlation matrix is shown in Fig. 4.15

Table 5.3: Summary of systematics included in the joint oscillation analysis.

1. SK reconstructed energy scale

The systematic parameter $f_{E,r}^{SK}$ is included to account for the reconstructed energy scale uncertainty, which was estimated to be 2.4% from data and MC events of cosmic ray stopping muons, decay electrons and atmospheric neutrino interactions (see Section 4.5). This systematic parameter is applied differently to the rest, since it is not applied as a weight in the number of events in each bin. Instead, the uncertainty on the reconstructed energy scale is applied by scaling the bin edges of the MC templates and, assuming uniform distribution of events within the bins, calculating the number of events gained from or lost to neighbouring bins. The effect of the reconstructed energy scale uncertainty is propagated to all the MC templates, applied to all flavour and interaction mode templates for both the single μ -like ring and single e-like ring samples.

2. SK efficiencies & effects of intra-nuclear and secondary re-interactions (FSI+SI) & Photo nuclear effects

These parameters include uncertainties on the efficiencies of the cuts used to select single ring events at SK: the fiducial volume and reduction chain, and the OD, ring-counting, PID, momentum and decay-electron cuts. These uncertainties were evaluated comparing SK-IV atmospheric data with atmospheric neutrino MC, taking into account correlations between the single μ -like ring and single e-like ring samples by using very pure samples of atmospheric neutrinos with either single μ -like ring or single e-like ring events selected at the final state (details are given in Section 4.5). A covariance matrix was calculated using toy MC experiments, which is the input used in the oscillation analyses, and its correlations are presented in Fig. 4.24.

Intranuclear final-state interactions (FSI) have significant effects in the T2K energy range. Uncertainties due to FSI were estimated by simultaneously varying the NEUT parameters that scale the interaction probabilities for quasi-elastic scattering, absorption, charge exchange and pion production using the method described in Section 4.3.3. The secondary pion interactions (SI) uncertainties were also evaluated. Since the same model was used for FSI and SI, it was possible to evaluate the uncertainties in both FSI and SI simultaneously, including variations in the SI interaction probabilities for each FSI parameter set. The effect of the FSI+SI uncertainties was estimated by re-weighting at the same time the single μ -like ring and single e-like selected SK MC events with the same set of parameters. Subsequently, a covariance matrix was calculated for both FSI and SI uncertainties, containing correlations between the two single μ -like ring and single e-like ring samples. The uncertainties related to photo-nuclear (PN) effects (interactions between photons and nuclei) were also taken into account. The identi-

fication of a π^0 relies on the detection of the two photons produced by this particle, but a photon can be absorbed before converting to a e-e⁺ pair and producing Čerenkov light, and would be therefore undetected. This would create an additional uncertainty for the interaction modes where a π^0 is produced, affecting therefore the single e-like ring event selection. A covariance matrix was calculated for the PN uncertainty using the new algorithm for the π^0 cut described in Section 3.4.1, in the same output binning used for the SK and FSI+SI covariance matrices.

The covariance matrices for the SK detector efficiencies and the FSI+SI systematics were created in the same output binning, so that both kind of uncertainties can be combined, adding their covariance matrices linearly. The binning used contains 6 bins for the single μ -like ring sample and 12 for the single e-like ring sample; therefore there are a total of 6+12 of these systematic parameters. Then, the PN covariance matrix was also added linearly to the SK+FSI sub-matrix (12×12) related to the single e-like ring sample. Details of these uncertainties are given in Tab. 5.3, and the final SK+FSI+SI+PN fractional errors are presented Fig. 5.9.

These systematic parameters combining uncertainties on the SK efficiencies, FSI and SI interactions and PN effects, usually referred as SK+FSI (or SK +FSI+SI) for simplicity, are applied to the corresponding templates according to the definition of each parameter given in Tab. 5.3: for instance, f_0^{SK+FSI} , which is defined as the uncertainty on the 1R _{μ} , ν_μ and $\bar{\nu}_\mu$ CCQE with $E_{rec} < 0.4$ GeV, is applied to the single μ -like ring ν_μ CCQE, $\bar{\nu}_\mu$ CCQE and osc. ν_μ ($\nu_e \rightarrow \nu_\mu$) CCQE templates only.

3. Independent cross section parameters

In addition to the correlated cross section systematics constrained by the fit to the near detector data, another 12 cross section systematics are taken into account in the joint oscillation analysis. These additional systematics are considered to have no cancellation between the near and far detector and they are not constrained by the fit to the ND280 data.

The list of independent cross section parameters considered is slightly different for the stand-alone appearance and disappearance analyses. The joint oscillation analysis takes into account the union of all the systematics considered by the two analyses, 12 parameters in total, as presented in Tab. 5.4 and 5.3.

The neutrino interaction generator typically used in T2K is NEUT [128]. As explained in Section 4.3, the nuclear model used is the Relativistic Fermi Gas (RFG), the default nuclear model in NEUT. Two systematic param-

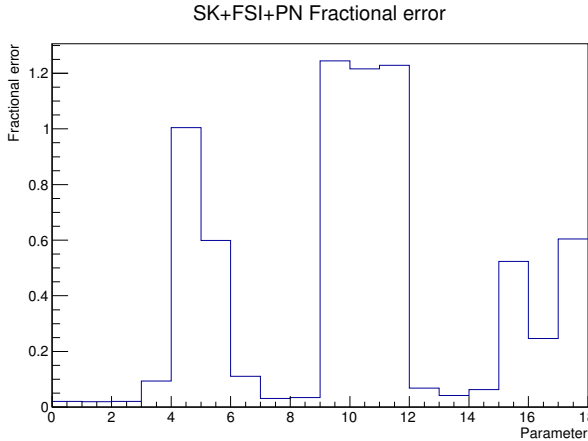


Figure 5.9: Values of the fractional errors for each SK+FSI+PN systematic parameter, defined as listed in Tab. 5.3.

ters take into account the uncertainties on the Relativistic Fermi Gas (RFG) model implementation: the Fermi momentum level $f_{p_F;t,r}$ and the nucleon binding energy $f_{bindE;t,r}$. Another systematic parameter, $f_{SF;t,r}$, accounts for the effect of switching between the RFG model and a more sophisticated and realistic model called Spectral Function (SF), which includes correlations between nucleons and defines the probability distribution of nucleon momenta and binding energies within the nucleus, instead of using a uniform distribution of nucleons with a constant binding energy like the RFG model. Since $f_{SF;t,r}$ switches between the two nuclear models, it needs a special treatment as it will be explained below. To estimate the differences between both methods, the NuWro generator [151] was used, as it contains the SF model. These three parameters are therefore related to the initial-state nuclear environment modelling for CCQE, and they are applied to the CCQE templates of every neutrino flavour for both the single μ -like and single e-like ring samples.

Simple, energy-independent, generator-level uncertainties are considered for the cross sections of the CC coherent and NC interactions and also for the cross section ratios $\sigma_{\nu_e}/\sigma_{\nu_\mu}$ and $\sigma_{\bar{\nu}}/\sigma_\nu$. This analysis uses a 100% uncertainty for the CC coherent cross section, a 30% uncertainty for both the NC1 π^\pm , NC coherent and NC other cross section, a 3% uncertainty on the ν_e / ν_μ CC cross section ratio and a 20% uncertainty on the $\bar{\nu} / \nu$ CC cross

section ratio. The motivation for these values is given in Section 4.3 and the effect of their variation is included in the analysis through the systematic parameters $f_{CCcoh;t}$, $f_{NC1\pi^\pm;t}$, $f_{NCcoh;t}$, $f_{NCoth;t}$, $f_{CC\nu_e;t}$ and $f_{CC\bar{\nu};t}$ respectively, that are applied respectively to the CC coherent, $NC1\pi^\pm$, NC coherent and NC other templates of the neutrino flavour and single ring sample for which those templates exist (for instance, no NC templates are considered for the osc. ν_e flavour, and no NC coherent templates exist for the single μ -like ring sample). The parameter $f_{CC\nu_e;t}$ is applied to the CC templates of the ν_e , $\bar{\nu}_e$, osc. ν_e and osc. $\bar{\nu}_e$ flavours for both the single μ -like and single e-like ring samples. And the parameter $f_{CC\bar{\nu};t}$ is applied to the CC templates of the $\bar{\nu}_\mu$, $\bar{\nu}_e$ and osc. $\bar{\nu}_e$ flavours for both the single μ -like and single e-like ring samples.

The systematic parameter $f_{\pi-less\Delta;t,r}$ accounts for the effect of varying the fraction of π -less Δ decays, which are the de-excitation of resonances without emission of pions produced when the Δ interacts before it decays, to the corresponding MC templates, which are the $CC1\pi$, $NC1\pi^\pm$, $NC1\pi^0$ and NC other (depending on the definition for the single μ -like and single e-like ring sample) templates of every neutrino flavour. These events are considered in NEUT, assuming that 20% of the Δ s produced have a π -less decay, and this analysis takes the uncertainty on this branching fraction to be 100%.

The $f_{CCothShape;t,r}$ systematic represents the uncertainty in the CC multipion, CC deep inelastic scattering and CC η , K and photon production cross sections. From MINOS data, this uncertainty is known to be $\approx 10\%$ at 4 GeV. Using this as a reference point, the uncertainty is estimated as $0.4/E_\nu$, where E_ν is in GeV, and therefore 40% for this analysis. It is applied to the CC other templates of every neutrino flavour for both the single μ -like and single e-like ring samples.

The $f_{Wshape;t,r}$ parameter varies the distribution of invariant mass of the hadronic system (W) in the resonant production model in NEUT, accounting for the uncertainty on the shape of the initial pion momentum distribution (before final state interactions) for $NC1\pi^0$ events as explained in Section 4.3. As the W shape parameter decreases, the pion momentum shifts to lower values, and this increases the probability of pion absorption in a final state interaction. If such an absorption occurs, the event is migrated from $CC1\pi$ (its true initial state) and appears to be CCQE. This uncertainty is driven by the fit to MiniBooNE data and is applied to the $NC1\pi^\pm$, $NC1\pi^0$ and NC other (depending on the definition for the single μ -like and single e-like ring sample) templates of every neutrino flavour.

The effect of the $f_{CCcoh;t}$, $f_{NC1\pi^\pm;t}$, $f_{NCcoh;t}$, $f_{NCoth;t}$, $f_{CC\nu_e;t}$ and $f_{CC\bar{\nu};t}$ systematic parameters is a simple normalization change for the corresponding MC templates and therefore easily implemented. The systematic parameters $f_{pF;t,r}$, $f_{SF;t,r}$, $f_{bindE;t,r}$, $f_{\pi-less\Delta;t,r}$, $f_{CCothShape;t,r}$ and $f_{Wshape;t,r}$ have a complicated non-linear dependence on true and reconstructed energy. These are treated in a similar way to the correlated cross section parameters $f_{25;t,r}^{banff}$ and $f_{26;t,r}^{banff}$, calculating the fractional changes of the number of events in bins of true and reconstructed neutrino energy, for a range of values (- 3.0σ , - 2.5σ , - 2.0σ , ..., + 3.0σ) of the systematic parameters and then using response functions (splines) to interpolate between these event weights.

Some of the latter systematics are special cases:

- $f_{SF;t,r}$ is discrete; it can be either spectral function off (RFG) or spectral function on (SF). Splines are generated with SF off as nominal (0), and SF on as $+1\sigma$. This parameter is restricted to the range between 0 and $+1\sigma$, and linear interpolation is made between the weights for nominal and $+1\sigma$.
- For $f_{Wshape;t,r}$ only $\pm 1\sigma$ errors are evaluated using event re-weighting. Since its error is $\sim 52\%$, it is unphysical to do a tweak of -2σ , as the value of the parameter would become negative. Therefore, weights for positive tweaks are interpolated or extrapolated from the nominal and $+1\sigma$ weights, and weights for negative tweaks are interpolated or extrapolated from the nominal and -1σ weights.
- For $f_{\pi-less\Delta;t,r}$ only $\pm 1\sigma$ errors are evaluated using event re-weighting. Weights for positive tweaks are interpolated or extrapolated from the nominal and $+1\sigma$ weights, and weights for tweaks between nominal and -1σ are interpolated from the nominal and -1σ weights. By default, NEUT simulates a pion-less Δ decay for 20% of the resonance events, with a 20% error, so a tweak of -2σ would be unphysical as it would produce a negative fraction of the number of events. Therefore, weights for tweaks more negative than -1σ are taken to be the same as the -1σ weight.

The 12 independent cross section systematics considered in this analysis are summarised in Tab. 5.3 and were explained in detail in Section 4.3.

4. Correlated flux and cross section (BANFF) parameters

The uncertainties on the flux and some cross sections, correlated between the near and far detectors, which were estimated as explained in Chapter 4, were constrained with the fit to the ND280 near detector data (BANFF) described in Section 4.4.

The number and definition of these parameters is different depending on the oscillation analysis performed: for instance, only the ν_μ and $\bar{\nu}_\mu$ flux parameters were considered for the stand-alone ν_μ disappearance analysis since the effect of the ν_e and $\bar{\nu}_e$ flux parameters is negligible. The uncertainties included in each oscillation analysis are presented in Tab. 4.5 for the flux parameters and in Tab. 4.6 for the cross section parameters. For the joint oscillation analysis, flux bins for ν_μ , $\bar{\nu}_\mu$, ν_e and $\bar{\nu}_e$ and all correlated cross sections were included, the NC1 π^0 normalization parameter is however only applied to the single e-like ring sample templates, because there are no single μ -like ring NC1 π^0 templates. A total of 33 parameters were considered for the joint oscillation analysis, labelled as BANFF parameters and whose pre and post-fit values and uncertainties are presented in Tab. 4.7. The correlation matrix obtained after the fit is shown in Fig. 4.15.

Among the correlated cross section parameters, all but two are simple normalization factors. However, the parameters $f_{25;t,r}^{banff}$ and $f_{26;t,r}^{banff}$, the ones corresponding to the axial masses (CC quasi-elastic, M_A^{QE} , and resonance-production, M_A^{RES} , respectively), have a more complicated non-linear dependence on true and reconstructed neutrino energy. For this reason, event re-weighting methods already described in Chapter 4 were used to obtain the fractional changes of the number of events in bins of true and reconstructed neutrino energy, for a range of values (-3.0 σ , -2.5 σ , -2.0 σ , ..., +3.0 σ) for the $f_{25;t,r}^{banff}$ and $f_{26;t,r}^{banff}$ parameters. Then, in the calculation of probability density functions (p.d.f.) during the analysis, response functions are used for these parameters, handled as cubic splines like the example presented in Fig. 5.10, to obtain the fractional change for any value of these systematic parameters, which can be correctly extrapolated from $\pm 3\sigma$ to $\pm 5\sigma$, maximal values considered in the fit.

These parameters are applied to the MC templates as follows:

- The flux parameters are applied to all interaction mode templates of the given neutrino flavour: for instance, ν_μ flux parameters are applied to all ν_μ templates for both the single μ -like and single e-like ring samples. For the oscillated templates, they are applied according to the initial flavour state, so ν_μ flux parameters are also applied to osc. ν_e ($\nu_\mu \rightarrow \nu_e$) templates.
- The M_A^{QE} axial mass systematic, $f_{25;t,r}^{banff}$, is applied to the CCQE templates of every neutrino flavour for both the single μ -like and single e-like ring samples.
- The M_A^{RES} axial mass systematic, $f_{26;t,r}^{banff}$, is applied to the CC1 π^\pm , CC other, NC1 π^\pm , NC1 π^0 and NC other (depending on the definition

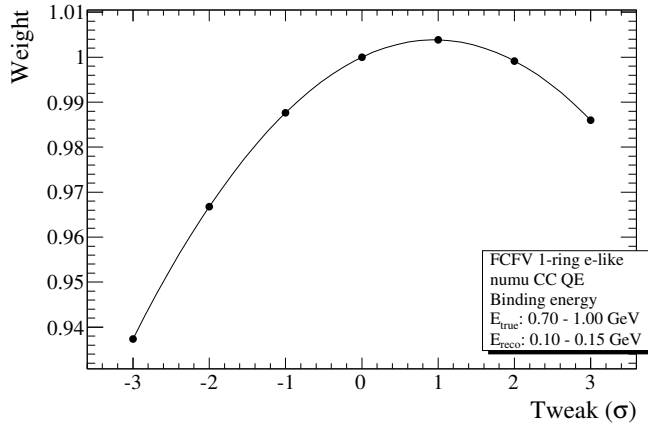


Figure 5.10: Example of response function (cubic spline) showing the weight vs the tweak for the E_B systematic parameter (binding energy) for the 1R_e sample, ν_μ CCQE interaction mode, E_{true} between 0.7-1.0 GeV and E_{reco} between 0.75-0.80 GeV.

for the single μ -like and single e-like ring sample) templates of every neutrino flavour.

- The CCQE normalization systematics, $f_{27;t,r}^{banff} - f_{29;t,r}^{banff}$, are applied to the CCQE templates of every neutrino flavour for both the single μ -like and single e-like ring samples.
- The CC1 π^\pm normalization systematics, $f_{30;t,r}^{banff} - f_{31;t,r}^{banff}$, are applied to the CC1 π^\pm templates of every neutrino flavour for both the single μ -like and single e-like ring samples.
- The NC1 π^0 normalization systematic, $f_{32;t,r}^{banff}$, is applied to the NC1 π^0 templates of each non-oscillated neutrino flavour (ν_μ , $\bar{\nu}_\mu$, ν_e and $\bar{\nu}_e$) of the single e-like ring samples.

Type	Systematics	Comment	Stand-alone ν_μ disap.	Joint OA ν_e app.	1R $_\mu$	1R $_e$	N joint
BANFF	$f_{0;t,r}^{banff} - f_{24;t,r}^{banff}$	ν_μ flux	11	11	11		25
		$\bar{\nu}_\mu$ flux	5	2	5		
		ν_e flux	—	7	7		
		$\bar{\nu}_e$ flux	—	2	2		
	$f_{25;t,r}^{banff}$	CCQE axial mass	1	1	1		8
	$f_{26;t,r}^{banff}$	resonance-production axial mass	1	1	1		
	$f_{27;t,r}^{banff} - f_{29;t,r}^{banff}$	CCQE normalization	3	1	3		
	$f_{30;t,r}^{banff} - f_{31;t,r}^{banff}$	CC1 π normalization	2	1	2		
	$f_{32;t,r}^{banff}$	NC1 π^0	—	1	—	1	
Independent cross sections	$f_{pF;t,r}$	Fermi momentum	1	1	1		12
	$f_{bindE;t,r}$	Binding energy	1	—	1		
	$f_{SF;t,r}$	Nuclear modeling	1	1	1		
	$f_{Wshape;t,r}$	Shape of the π momentum distribution	1	1	1		
	$f_{\pi-less\Delta;t,r}$	π -less Δ decay	1	1	1		
	$f_{CCothShape;t,r}$	CC other shape	1	1	1		
	$f_{CCcoh;t}$	CC coherent cross section	1	1	1		
	$f_{NC1\pi^\pm;t}$	NC1 π^\pm cross section	1	—	1	—	
	$f_{NCcoh;t}$	NC coherent cross section	—	1	—	1	
	$f_{NCoth;t}$	NC other cross section	1	1	1		
	$f_{CC\nu_e;t}$	$\sigma_{\nu_e} / \sigma_{\nu_\mu}$ ratio	1	1	1		
	$f_{CC\bar{\nu};t}$	$\sigma_{\bar{\nu}} / \sigma_\nu$ ratio	1	—	1		
	$f_{E;r}^{SK}$	Reconstructed E scale	1	1	1		1
	$f_{0;r}^{SK+FSI} - f_{5;r}^{SK+FSI}$	1R $_\mu$ efficiencies	6	—	6	—	6
	$f_{6;r}^{SK+FSI} - f_{17;r}^{SK+FSI}$	1R $_e$ efficiencies	—	12	—	12	12
Total			41	49	64		

Table 5.4: List of all systematic parameters included in the joint oscillation analysis, indicating whether the systematic parameter is applied on the single μ -like ring and single e -like ring MC templates.

5.5.1 Evaluation of Effects of the Systematic Parameters

The effects of the systematic uncertainties on the predicted number of events are summarized in Tab. 5.5, for oscillations with $\sin^2 \theta_{12}=0.306$, $\sin^2 \theta_{13}=0.0243$, $\sin^2 \theta_{23}=0.5$, $\Delta m_{21}^2=7.5 \times 10^{-5} \text{ eV}^2/c^4$, $|\Delta m_{FL}^2|=2.4375 \times 10^{-3} \text{ eV}^2/c^4$, $\delta_{CP}=0$ and with the normal mass hierarchy assumed. An ensemble of 10^6 toy experiments were generated with all systematic parameters in the given category randomized using their corresponding p.d.f., fixing the rest to their nominal values. The uncertainty is calculated as the one standard deviation of the 10^6 toy experiments. These results were generated for an integrated exposure of 6.57×10^{20} POT and the BANFF-tuned MC templates were used.

The effects of the systematic uncertainties on the reconstructed energy spectrum of single μ -like ring events and single e-like ring events are illustrated in Fig. 5.11 for the typical oscillation scenario used. Figure 5.11 shows the total error envelope combining all systematic uncertainties, calculated as the $\pm 1\sigma$ spread of bin contents from 10^6 MC toy experiments generated with randomized systematic parameters, taking into account all correlations between them, before and after applying the constraint from the fit to the near detector data, showing the clear reduction of the error envelope when the constraint is applied. The $\pm 1\sigma$ spread in each bin i in Fig. 5.11 is calculated with respect to the nominal

spectrum, computed as $\sigma_i = \sqrt{\frac{\sum_{\alpha}^{m_{exp}} (N_i^{\alpha} - N_i^{nom})^2}{m_{exp}}}$, where N_i^{α} is the number of events for the α^{th} MC toy experiment in the i^{th} bin where σ is being calculated, N_i^{nom} is the number of events in the i^{th} bin for the nominal spectrum (without all systematic parameters set to their nominal values) and m_{exp} is the number of MC toy experiments.

5.6 Neutrino Oscillation Fitting Method

As it has been already explained in Section 5.3, this joint oscillation analysis fits for $\sin^2 \theta_{23}$ in order to take into account the effect of the octant of this parameter. Regarding the angle θ_{13} , results can be presented in either $\sin^2 \theta_{13}$ or $\sin^2 2\theta_{13}$ in order to compare to previous results and results from other experiments. Concerning the convention for the mass-squared splitting parameters, this analysis initially fitted for the Fogli-Lisi convention described in Section 5.3, but final results were produced using the convention $|\Delta m^2| = |\Delta m_{32}^2|(NH)$, $|\Delta m_{13}^2|(IH)$, in order to compare with previous results, and Δm_{32}^2 for both mass hierarchies (with opposite signs) for comparisons with other experiments in Fig. 5.34.

The joint oscillation analysis presented here uses a binned likelihood-ratio method. Measurements of the oscillation parameters $\sin^2 \theta_{23}$, $|\Delta m^2|$, $\sin^2 \theta_{13}$ and δ_{CP} ³ are obtained by comparing the observed and predicted SK reconstructed energy spectra for single μ -like ring events and single e-like ring events.

³As already mentioned, a study was made in which $\sin^2 \theta_{12}$ and Δm_{21}^2 were allowed to float in the fit and the results are shown in Appendix B. The effect was negligible and it was decided to keep them fixed to the values in Tab.B.1.

Source of uncertainty	$1R\mu \delta N_{SK}/N_{SK}$	$1Re \delta N_{SK}/N_{SK}$
SK+FSI+SI(+PN)	5.0%	3.7%
SK	4.0%	2.7%
FSI+SI(+PN)	3.0%	2.5%
Flux and correlated cross sections		
(w/o ND280 constraint)	21.7%	26.0%
(w ND280 constraint)	2.7%	3.2%
Independent cross sections	5.0%	4.7%
Total		
(w/o ND280 constraint)	23.5%	26.8%
(w ND280 constraint)	7.7%	6.8%

Table 5.5: Effect of 1σ systematic parameter variation on the number of single μ -like ring and single e-like ring events using an ensemble of 10^6 toy experiments with oscillations with typical values with all systematic parameters in the given category randomized using their corresponding p.d.f., fixing the rest to their nominal values. The uncertainty is calculated as the one standard deviation of the 10^6 toy experiments.

Let N_μ and N_e be the number of reconstructed energy bins considered for the single μ -like ring and single e-like ring samples respectively, and \mathbf{f} be a $(1 \times N_s)$ -dimensional array of the systematic parameters that affect the SK reconstructed energy spectrum prediction of either sample, which were described in previous section, where s denotes the sample (single μ -like or single e-like ring). Best-fit values are obtained by minimizing:

$$\begin{aligned} \chi^2 = & \\ & - 2 \ln \lambda(|\Delta m^2|, \sin^2 \theta_{23}, \sin^2 \theta_{13}, \delta_{CP}; \mathbf{f}) = \\ & 2 \cdot \sum_{r=0}^{N_\mu-1} \left[(N_{SK;\mu,r}^{exp} - N_{SK;\mu,r}^{obs}) + N_{SK;\mu,r}^{obs} \cdot \ln \left(\frac{N_{SK;\mu,r}^{obs}}{N_{SK;\mu,r}^{exp}} \right) \right] \\ & + 2 \cdot \sum_{r=0}^{N_e-1} \left[(N_{SK;e,r}^{exp} - N_{SK;e,r}^{obs}) + N_{SK;e,r}^{obs} \cdot \ln \left(\frac{N_{SK;e,r}^{obs}}{N_{SK;e,r}^{exp}} \right) \right] \\ & + (\mathbf{f} - \mathbf{f}_0)^T \cdot \mathbf{C}^{-1} \cdot (\mathbf{f} - \mathbf{f}_0) \end{aligned} \quad (5.6)$$

where $N_{SK;\mu,r}^{obs}$ ($N_{SK;e,r}^{obs}$) is the observed number of single μ -like ring (single e-like ring) events in the r^{th} bin, and $N_{SK;\mu,r}^{exp}$ ($N_{SK;e,r}^{exp}$) is the corresponding expected number of events. The expected number of events is a function of $|\Delta m^2|$, $\sin^2 \theta_{23}$, $\sin^2 \theta_{13}$ and δ_{CP} and the vector of systematic parameters \mathbf{f} . The vector \mathbf{f}_0 is also a $(1 \times N_s)$ -dimensional

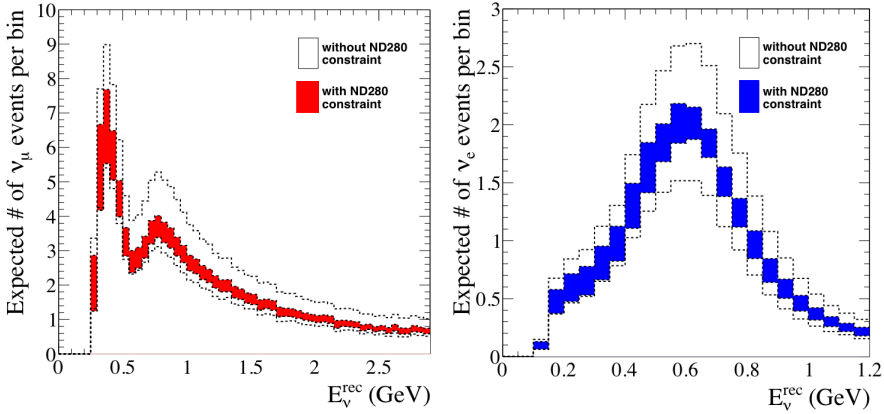


Figure 5.11: Total error envelope of the single μ -like ring and single e-like event reconstructed energy spectra, for oscillations with typical values (as in Tab. 5.5) and the normal mass hierarchy assumed, for an exposure of 6.57×10^{20} POT. The error envelope was calculated as the $\pm 1\sigma$ spread of bin contents using an ensemble of 10^6 MC toy experiments generated with all systematic parameters randomized, taking into account their correlations, before and after applying the constraint from the fit to the near detector data.

array containing the nominal values of the systematic parameters, \mathbf{f}^T is the transpose of \mathbf{f} , and \mathbf{C} is the systematic parameter covariance matrix of dimension $(N_s \times N_s)$.

The minimization is performed with MINUIT [170], using the MIGRAD algorithm, which is a stable variation of the Davidon-Fletcher-Powell [185] variable-metric method and the best minimizer for nearly all functions. This algorithm works updating at each step the approximated error matrix and gradient vector at the current best-fit point, until it converges to the final error matrix as it converges to the function minimum. If MIGRAD does not converge, the fit is performed again changing the initial values of the oscillation parameters, randomly inside their allowed ranges, up to 25 attempts, after which the SIMPLEX algorithm is used, which is a simpler multidimensional minimization routine that does not use first derivatives in the calculations. The search for the minimum value of $-2 \ln \lambda(|\Delta m^2|, \sin^2 \theta_{23}, \sin^2 \theta_{13}, \delta_{CP}; \mathbf{f})$ is performed in the range $1.0 \times 10^{-3} \text{ eV}^2/c^4 \leq |\Delta m^2| \leq 6.0 \times 10^{-3} \text{ eV}^2/c^4$, $0.0 \leq \sin^2 \theta_{23} \leq 1.0$, $0.0 \leq \sin^2 \theta_{13} \leq 1.0$ and $-\pi \leq \delta_{CP} \leq \pi$. After a successful fit, the HESSE algorithm, which finds the covariance matrix error by inverting the second derivative matrix, is called to improve the estimation of the errors on the fitted parameters made by MIGRAD.

In order to find a solution in each one of the two octants for θ_{23} , each fit is repeated twice, because the solution from MINUIT is usually in the same octant the initial value for $\sin^2 \theta_{23}$ was selected: in the first fit, the initial value is $\sin^2 \theta_{23} = 0.6$; then, in the second fit, the initial value is set as the mirror point of the best fit of $\sin^2 \theta_{23}$ found in the first fit (taking into account the best-fit value of $\sin^2 \theta_{13}$ from the first fit to calculate the correct mirror point: $(\sin^2 \theta_{23})_{\text{mirror}} = c \pm |c - (\sin^2 \theta_{23})_{\text{bf}}|$ where the center of symmetry, value

of maximal disappearance, is calculated as $c = (2(1 - (\sin^2 \theta_{13})_{bf}))^{-1}$ as explained in Appendix E). A simpler method, setting initial values $\sin^2 \theta_{23} = 0.6$ and $\sin^2 \theta_{23} = 0.4$ for the two fits, was also tested, with consistent results.

All the 64 systematic parameters are allowed to float in the fit, and are restricted to the range $[-5\sigma_s, +5\sigma_s]$ where σ_s is the one standard deviation error assigned to each systematic parameter except the systematic parameter f_{SF} , which parametrizes the uncertainty on nuclear modelling, switching between the Relativistic Fermi Gas (RFG) and Spectral Function (SF) models, and for which the allowed range in the oscillation fit is [0,1].

5.6.1 Treatment of solar (12-sector) oscillation parameters

A study was made allowing $\sin^2 2\theta_{12}$ and Δm_{21}^2 to float in the joint oscillation fit. It was found that when these parameters were allowed to float freely, the fitter returned extreme values of these parameter because there is no sensitivity in the single μ -like ring sample nor the single e-like ring sample to constrain them, being those extreme values far away from the values established by different experiments. When they were instead allowed to float including the constraints known from well established measurements, there was no effect in the results obtained (details of these tests are given in Appendix B). For this reason, these parameters were fixed throughout this analysis to the values in Tab. B.1.

5.6.2 Adding Reactor Constraint

The final results of the Run 1+2+3+4 dataset will be presented in two ways: firstly, fitting only the T2K dataset, and secondly, including the reactor constraint in the fit, to incorporate the result of the measurements of θ_{13} obtained by the reactor experiments. This constraint works adding a penalty term to the χ^2 function in Eq. 5.6, proportional to the difference between the best-fit value of $\sin^2 2\theta_{13}$ and the one used as constraint. The $\chi^2_{reactor}$ is calculated following Eq. 5.7, where the values of $(\sin^2 2\theta_{13})_{reactor}$ and $\sigma_{reactor}$ used were the latest 2013 PDG values, coming from a weighted average of the results from the three reactor experiments Daya Bay, RENO and Double Chooz [86]: $(\sin^2 2\theta_{13})_{reactor} = 0.095$ and $\sigma_{reactor} = 0.01$.

$$\chi^2_{reactor} = \left(\frac{\sin^2 2\theta_{13} - (\sin^2 2\theta_{13})_{reactor}}{\sigma_{reactor}} \right)^2 \quad (5.7)$$

5.6.3 Validation

Extensive validation tests were done for the fitter used in the joint oscillation analysis, checking the fitter performance and fitting toy datasets. Detailed summaries of these tests are presented in Appendixes C and D.

Firstly, studies on residuals and pulls were done to test the fitter performance. For these studies, a sufficiently large ensemble of toy experiments (5000 toys) was used, including statistical fluctuations and systematic variations, in different oscillation points trying to

avoid physical boundaries ($\sin^2 \theta_{23} = 0.5263$ and $\sin^2 \theta_{13} = 0.05$). An example of the distribution of residuals for the four oscillation parameters is given in Fig. 5.12. The distributions present the difference between the true input value and the best-fit value obtained after the fit for each oscillation parameter. Several features appeared in these distribution, namely a three peak structure in the residuals for $\sin^2 \theta_{23}$ and an intrinsic asymmetry in $\sin^2 \theta_{13} - \delta_{CP}$, but they were understood in terms of physical reasons (see details in Appendix C).

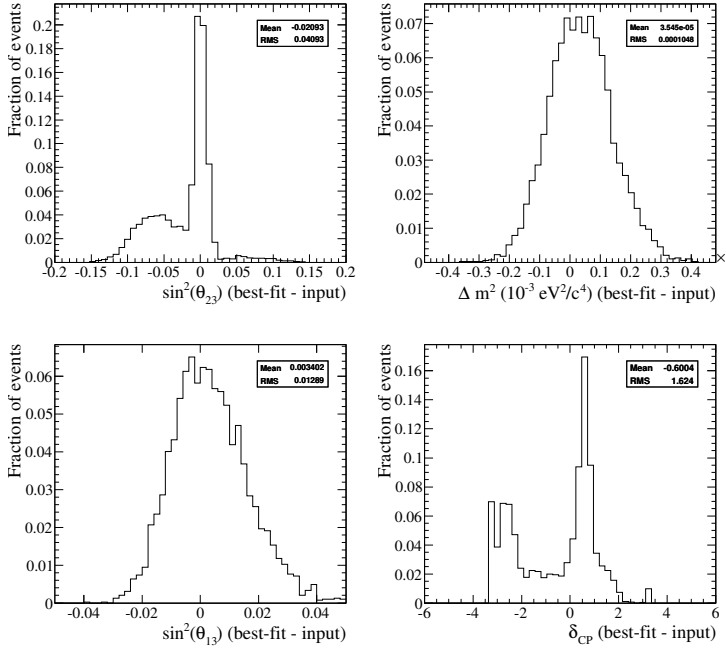


Figure 5.12: Distribution of residuals of the four oscillation parameters at the oscillation point $\sin^2 \theta_{23} = 0.5263$, $\sin^2 \theta_{13} = 0.05$, $\Delta m_{FL}^2 = 2.4 \times 10^{-3} \text{eV}^2/\text{c}^4$ and $\delta_{CP} = 0$ and normal hierarchy for an ensemble of 5k toy MC experiments.

The distributions of pulls and residuals for all the systematic parameters were also checked in these validation tests. Figure 5.13 shows an example of the mean and RMS of the pulls of the 64 systematic parameters, illustrating that in general all systematic parameters present a good behaviour with $\text{mean} \approx 0$ and $\text{RMS} \approx 1$. This plot was created before and after including correlations in the SK efficiency systematics, to check that the effect of these correlations between the $1R\mu$ and $1Re$ samples is indeed very small. There are some small biases in the pull distributions for some systematic parameters, the spectral function, the π -less Δ decay cross section, the reconstructed energy scale and the $1R\mu$ NC SK(+FSI+SI) efficiency, which are explained in terms of physical reasons in Appendix C.

Furthermore, several toy experiments were created for an exposure of 6.57×10^{20} POT at different values of the oscillation parameters, with nominal or random values of the systematic parameters, and they were fitted as real data, with and without reactor constraint, in order to check that no problems appear in the calculation of best-fit values and confidence regions. Table 5.6 shows a summary of the toy experiments created in the validation test, with their true input values and the best fit values obtained after the fit with and without reactor constraint, indicating if the values of the systematic parameters were nominal or random (all toys included statistical fluctuations). A complete set of best-fit spectra, pulls, $\Delta\chi^2$ surfaces and confidence regions plots for one of the toy experiments is presented in Appendix D. The same procedure was followed for the rest of toy experiments, and complete set of plots were also produced, with different mass hierarchy assumptions, with and without reactor constraint, and no problems were identified in any of these fits.

Thus, no unexpected features appeared in these validation tests, showing that the fitter performs as expected.

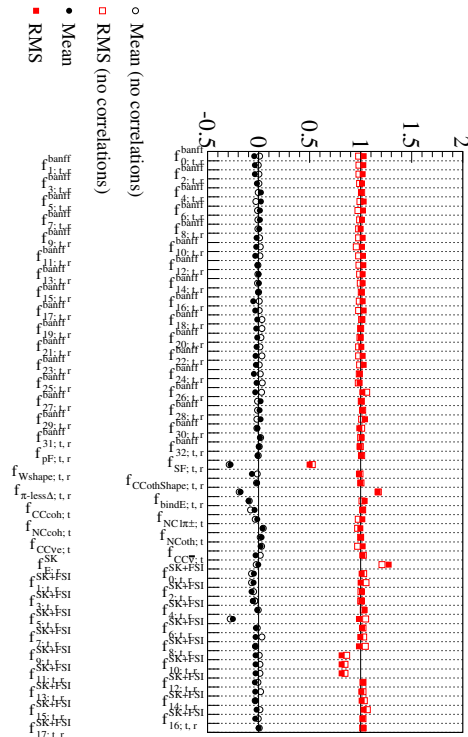


Figure 5.13: Summary of mean and RMS for the distribution of pulls of the 64 systematic parameters with and without correlations.

Toy	Fit	Constraint	MH ($\times 10^{-3}$ eV 2 /c 4)	$ \Delta m_{FL}^2 $	$\sin^2 \theta_{23}$	$\sin^2 2\theta_{13}$	δ_{CP}	χ^2 (ndf = 94)	Systematics
0	true	-	NH	2.4375	0.513	0.098	0.0	-	Nominal
	$\sin^2 2\theta_{13}$	NO	NH	2.413	0.513	0.1403	-0.0825	87.877	-
	$\sin^2 2\theta_{13}$	0.098 ± 0.01	NH	2.435	0.550	0.0996	-1.263	88.249	-
1	true	-	NH	2.4375	0.37	0.098	0.0	-	Random
	$\sin^2 2\theta_{13}$	NO	NH	2.327	0.619	0.0599	1.592	104.764	-
	$\sin^2 2\theta_{13}$	0.098 ± 0.01	NH	2.327	0.402	0.0981	1.599	104.77	-
2	true	-	NH	2.750	0.513	0.098	0.0	-	Random
	$\sin^2 2\theta_{13}$	NO	NH	2.578	0.508	0.0728	-0.0179	90.792	-
	$\sin^2 2\theta_{13}$	0.098 ± 0.01	NH	2.580	0.498	0.0973	0.802	90.977	-
3	true	-	NH	2.4375	0.513	0.1536	0.0	-	Random
	$\sin^2 2\theta_{13}$	NO	NH	2.583	0.568	0.2157	1.087	73.952	-
	$\sin^2 2\theta_{13}$	0.1536 ± 0.01	NH	2.590	0.569	0.1547	-1.013	74.533	-
4	true	-	NH	2.4375	0.513	0.098	$-\pi/2$	-	Nominal
	$\sin^2 2\theta_{13}$	NO	NH	2.466	0.526	0.1768	-2.564	76.768	-
	$\sin^2 2\theta_{13}$	0.098 ± 0.01	NH	2.464	0.542	0.105	-1.615	81.003	-
5	true	-	IH	2.4375	0.513	0.098	0.0	-	Nominal
	$\sin^2 2\theta_{13}$	NO	IH	2.530	0.511	0.0962	2.367	111.203	-
	$\sin^2 2\theta_{13}$	0.098 ± 0.01	IH	2.530	0.511	0.0979	2.323	111.214	-

Table 5.6: True input values (shown in bold) and best-fit values for a test ensemble of 6 fake datasets, comparing results with and without including the reactor constraint in $\sin^2 2\theta_{13}$.

5.6.4 Construction of Confidence Regions

In the results presented in this thesis, confidence regions for the 68% and 90% CL limits are reported for each of $|\Delta m^2|$, $\sin^2\theta_{23}$, $\sin^2\theta_{13}$ and δ_{CP} oscillation parameters. In addition, 2-dimensional confidence regions for 68% and 90% CL are shown for the following combinations of parameters: $(\sin^2\theta_{23}, |\Delta m^2|)$, $(\sin^2\theta_{13}, |\Delta m^2|)$, $(\sin^2\theta_{13}, \delta_{CP})$ and $(\sin^2\theta_{23}, \sin^2\theta_{13})$. When introducing the reactor constraint, the following additional 2-dimensional confidence regions are also presented: $(|\Delta m^2|, \delta_{CP})$ and $(\sin^2\theta_{23}, \delta_{CP})$. The method used to build these confidence regions is the constant $\Delta\chi^2$ method described in [178] (pp. 390-401).

The first step to construct confidence contours in an oscillation parameter space is to build the $\Delta\chi^2$ surface in that space. The oscillation parameter space is divided into a regular grid. The grid limits and spacing used in all confidence regions is presented in Tab. 5.7.

Parameter	Min	Max	Step	Bins
$\sin^2\theta_{23}$	0.3	0.7	0.01	41
$ \Delta m^2 (10^{-3}eV^2/c^4)$	2.0	3.0	0.05	21
$\sin^2\theta_{13}$	0.0	0.1	0.005	21
$\sin^22\theta_{13}$	0.0	0.4	0.02	21
$\sin^2\theta_{13}$ (reactor)	0.015	0.035	0.001	21
$\sin^22\theta_{13}$ (reactor)	0.06	0.14	0.004	21
δ_{CP}	$-\pi$	π	$2\pi/50$	51

Table 5.7: Grid limits and spacing used in all confidence regions.

For the joint 3-flavour analysis confidence regions, the χ^2 is minimized at each grid point with respect to all 64 nuisance parameters considered in this analysis and all oscillation parameters not shown on the plot (and not considered to be fixed). Thus, for instance, at each grid point of the $(\sin^2\theta_{23}, |\Delta m^2|)$ parameter space, the 64 systematic parameters, $\sin^2\theta_{13}$ and δ_{CP} are fitted.

The confidence regions for the joint analysis are constructed by finding the global best-fit point (fitting all oscillation parameters and all systematic parameters at the same time) and calculating the lines of *constant* $\Delta\chi^2$ from this point⁴. A special procedure is followed to construct the confidence regions in the $(\sin^2\theta_{13}, \delta_{CP})$ space, called *raster scan*, where a best-fit value of $\sin^2\theta_{13}$ is found for each fixed value of δ_{CP} , resulting in a line of best-fit points instead of a single best-fit point. Then, confidence intervals in $\sin^2\theta_{13}$ at a fixed δ_{CP} are found with respect to each best-fit $\sin^2\theta_{13}$ using the 1D $\Delta\chi^2$ critical values.

An approach based on Feldman-Cousins [186] was used to calculate confidence regions for δ_{CP} . First, 3D $\Delta\chi^2$ surfaces (one for each mass hierarchy) are calculated as any of the usual 2D $\Delta\chi^2$ surfaces used to build confidence regions, adding one extra dimension: in

⁴For 1 fit parameter, the critical values of $\Delta\chi^2$ used are 1.00 (68% CL), 2.71 (90% CL), 3.84 (95% CL), 6.63 (99% CL). For 2 parameters fitted simultaneously, the critical values of $\Delta\chi^2$ used are 2.30 (68% CL), 4.61 (90% CL), 5.99 (95% CL), 9.21 (99% CL).

each bin of fixed values of ($\sin^2 2\theta_{13}$, $\sin^2 \theta_{23}$, $|\Delta m^2|$) a fit to the Run1+2+3+4 dataset including the reactor constraint is performed, fitting δ_{CP} and the systematic parameters, and the best-fit value of χ^2 obtained is compared to the global best-fit value (when all oscillation and systematic parameters are fitted) to calculate the $\Delta\chi^2$ in that grid point. Then, at fixed values of δ_{CP} in the range $[-\pi, \pi]$ (divided into 51 bins), 4k toy experiments were created with statistical fluctuations, random Poissonian fluctuations of the number of events in each bin, and systematic variations, which are variations obtained with gaussian distributions and applying the corresponding covariance matrix for the systematic errors. The other oscillation parameters ($\sin^2 2\theta_{13}$, $\sin^2 \theta_{23}$ and $|\Delta m^2|$) are varied when creating the toy experiments following the likelihood from the corresponding 3 dimensional $\Delta\chi^2$ surface, with the form of $\exp(-\Delta\chi^2/2)$, so that for the total ensemble of toy experiments, the most probable values of $\sin^2 2\theta_{13}$, $\sin^2 \theta_{23}$ and $|\Delta m^2|$ they are created with are those with a larger likelihood (or smaller χ^2). This is achieved by calculating the cumulative likelihood for each bin n of the 3 dimensional space, summing up the likelihood from the bins 0- n , and divided by the total likelihood, calculated as the sum of the likelihood of all the bins. Then a random number is selected following a uniform distribution between 0 and 1, choosing the bin whose cumulative likelihood divided by the total likelihood is closer to that number, and the values of $\sin^2 2\theta_{13}$, $\sin^2 \theta_{23}$ and $|\Delta m^2|$ corresponding to that bin are the ones used for the toy experiment.

For each toy experiment, two first fits were performed, assuming the true hierarchy and fitting the four oscillation parameters and the systematic parameters, one fit starting in each one of the two octants for θ_{23} . The minimum value χ^2_{min} is found from these two first fits. Then, another four fits are performed for each toy experiment, fitting the 3 oscillation parameters and systematics, but keeping δ_{CP} fixed to its true input value, repeating the fit for each mass hierarchy assumption and initializing in each one of the two octants for $\sin^2 \theta_{23}$ (four combinations). From these four fits, the minimum χ^2_{true} is found. Finally for each toy experiment $\Delta\chi^2 = \chi^2_{true} - \chi^2_{min}$ is calculated. The critical $\Delta\chi^2_c$ for 68 % CL (90 % CL) is found at each value of δ_{CP} as the value for which 68 % (90 %) of the toy experiments created at that point have a $\Delta\chi^2 < \Delta\chi^2_c$.

5.7 Results of the Joint Oscillation Analysis on the Run 1+2+3+4 (6.570×10^{20} POT) dataset

This section presents the results of the T2K joint 3-flavour oscillation analysis on the Run 1+2+3+4 (6.570×10^{20} POT) dataset. The fit was performed with the choice of oscillation parameters discussed in Section 5.3, and using the method explained in Section 5.6. In order to obtain the values of the oscillation parameters, the observed energy spectra of the single e-like ring and single μ -like ring events is compared with the predicted spectra, obtained as described in Section 5.4, including the systematic errors defined in Section 5.5.

5.7.1 Results with T2K Data Only for Normal and Inverted Hierarchy

The joint 3-flavour oscillation fit found $|\Delta m_{32}^2| = 2.512 \times 10^{-3} \text{ eV}^2/c^4$, $\sin^2 \theta_{23} = 0.524$, $\sin^2 \theta_{13} = 0.0422$ and $\delta_{CP} = 1.909$ (p-value = 0.921) to be the best-fit values for the Run 1+2+3+4 dataset for normal hierarchy and $|\Delta m_{13}^2| = 2.488 \times 10^{-3} \text{ eV}^2/c^4$, $\sin^2 \theta_{23} = 0.523$, $\sin^2 \theta_{13} = 0.0491$ and $\delta_{CP} = 1.005$ (p-value = 0.952) for inverted hierarchy. Between the two best-fit points, the one with a smaller value of χ^2 is the one with inverted hierarchy (with a difference in χ^2 of only 0.01). Table 5.8 summarizes the best-fit values for the two mass hierarchies. The number of best-fit single μ -like ring and e-like ring events is very close to the observed number of events in the Run 1+2+3+4 dataset: 120 single μ -like ring events and 28 single e-like ring events.

MH	$ \Delta m_{32}^2 $ (NH) or $ \Delta m_{13}^2 $ (IH) $10^{-3} \text{ eV}^2/c^4$	$\sin^2 \theta_{23}$	$\sin^2[2]\theta_{13}$	δ_{CP}	$N_{exp}^{1R\mu}$	N_{exp}^{1Re}	χ^2/ndf	
$\sin^2 \theta_{13}$	NH	2.512	0.524	0.0422	1.909	119.92	27.999	84.54/94
$\sin^2 2\theta_{13}$	NH	2.512	0.524	0.162	1.909	119.92	27.999	84.54/94
$\sin^2 \theta_{13}$	IH	2.488	0.523	0.0491	1.005	119.95	27.998	84.53/94
$\sin^2 2\theta_{13}$	IH	2.488	0.523	0.187	1.005	119.95	27.998	84.53/94

Table 5.8: Summary of best-fit values of the oscillation parameters for the joint 3-flavour oscillation fit to the Run 1+2+3+4 dataset, for each mass hierarchy assumption. The quoted best-fit χ^2 values were computed from the test-statistic minimized in the fit (likelihood ratio in Eq. 5.6) with the reconstructed energy binning used in each fit described in Section 5.4. The fit was repeated using $\sin^2 2\theta_{13}$ and no difference was found with respect to the results using $\sin^2 \theta_{13}$.

The pull for each systematic parameter f included in the fit was calculated as

$$\frac{f_{bf} - f_{nom}}{\sigma_{bf}}, \quad (5.8)$$

where f_{bf} is the best-fit value of the systematic parameter, f_{nom} is the nominal value of the parameter (corresponding to no systematic variation), and σ_{bf} is the output error from

MINUIT after using its HESSE method, which finds the covariance matrix error by inverting the second derivative matrix. The pulls of all systematic parameters allowed to float in the joint 3-flavour oscillation fit to the Run 1+2+3+4 dataset are shown in Fig. 5.14 assuming normal hierarchy (top) and inverted hierarchy (bottom). All systematic parameters are allowed to float in the fits between $[-5\sigma, 5\sigma]$, and it is clear from Fig. 5.14 that most of them barely move from their nominal values and few move by more than $\pm 0.1\sigma$. The reason is that only certain systematics are able to change the predicted reconstructed energy spectrum to a sufficient extent to offset the penalty term due to its variation.

The reconstructed neutrino energy distribution of single μ -like ring and single e-like ring events in the Run 1+2+3+4 dataset is shown in Fig. 5.15 along with the best-fit prediction of the joint 3-flavour oscillation analysis, assuming normal hierarchy, and overlaid with the non-oscillation prediction. Similarly for inverted hierarchy in Fig. 5.16. The distributions are shown with the reconstructed neutrino energy binning that was used in the fitting procedure. Figures 5.15 and 5.16 also present the ratio of the best-fit reconstructed neutrino energy distribution of single μ -like ring and single e-like ring events to the non-oscillation prediction.

The profiled $\Delta\chi^2$ distribution as function of each of $|\Delta m^2| = |\Delta m_{32}^2|$ (NH), $|\Delta m_{13}^2|$ (IH), $\sin^2\theta_{23}$, $\sin^2\theta_{13}$ and δ_{CP} oscillation parameters for the joint 3-flavour oscillation fit to the Run 1+2+3+4 dataset was calculated for each mass hierarchy, and the results for both mass hierarchy assumptions are compared in Fig. 5.17. This profiled $\Delta\chi^2$ distributions are calculated by minimizing χ^2 (or maximizing the likelihood) over the remaining parameters, so that for instance the profiled $\Delta\chi^2$ distribution as a function of $|\Delta m^2|$ is found by minimizing it over $\sin^2\theta_{23}$, $\sin^2\theta_{13}$, δ_{CP} and the systematic parameters at each fixed value of $|\Delta m^2|$. As expected, each minimum of the profiled $\Delta\chi^2$ distributions coincide, within the binning specified, with the best-fit value of the oscillation parameters found in the 4-dimensional fit summarized in Tab. 5.8. From these plots, the 90% (68%) CL allowed region for the four oscillation parameters can be expressed as

- 2.320×10^{-3} (2.394×10^{-3}) $eV^2/c^4 < |\Delta m_{32}^2| < 2.697 \times 10^{-3}$ (2.623×10^{-3}) eV^2/c^4 ,
- 0.435 (0.465) $< \sin^2\theta_{23} < 0.608$ (0.581),
- 0.018 (0.021) $< \sin^2\theta_{13} < 0.063$ (0.055) and
- $-\pi$ ($-\pi$) $< \delta_{CP} < \pi$ (π)

for normal hierarchy and

- 2.292×10^{-3} (2.370×10^{-3}) $eV^2/c^4 < |\Delta m_{13}^2| < 2.672 \times 10^{-3}$ (2.605×10^{-3}) eV^2/c^4 ,
- 0.434 (0.458) $< \sin^2\theta_{23} < 0.596$ (0.578),
- 0.022 (0.028) $< \sin^2\theta_{13} < 0.076$ (0.064) and
- $-\pi$ ($-\pi$) $< \delta_{CP} < \pi$ (π)

for inverted hierarchy.

The correlations between the oscillation parameters were also studied. The 68% and 90% CL regions in the following four 2-dimensional oscillation parameter spaces were calculated for normal and inverted hierarchy: $(\sin^2\theta_{23}, |\Delta m^2|)$, $(\sin^2\theta_{13}, |\Delta m^2|)$, $(\sin^2\theta_{13}, \delta_{CP})$,

δ_{CP}) and $(\sin^2\theta_{23}, \sin^2\theta_{13})$. Comparisons between the confidence regions obtained from the joint 3-flavour oscillation fits under different mass hierarchy assumptions are shown in Fig. 5.18. Confidence regions in both mass hierarchy assumptions for Fig. 5.18 were constructed with respect to a common best-fit point, the one from the fit with inverted hierarchy, as it is the one with the smallest value of χ^2 . In the $(\sin^2\theta_{13}, \delta_{CP})$ parameter space, the method called *raster scan*, in which the best fit value of $\sin^2\theta_{13}$ is found for each fixed value of δ_{CP} , was used since there is no much information on δ_{CP} with T2K data alone as it can be observed in Fig. 5.17.

Goodness-of-fit tests were performed by calculating p-values using the reconstructed energy distributions in a very coarse binning scheme, to ensure sufficient number of events in each bin. For the single μ -like ring sample, 5 reconstructed energy bins were used: 0-0.4, 0.4-0.7, 0.7-1.0, 1.0-2.0 and 2.0-30.0 GeV. For the single e-like ring sample, 3 reconstructed energy bins were used: 0-0.35, 0.35-0.80, 0.80-1.25 GeV. The goodness-of-fit tests were built using 1000 toy MC experiments created at the best-fit point to test, with statistical and systematic fluctuations. Then, each toy MC experiment is fitted in the coarse binning described, including the four oscillation parameters and all the systematics.

Fig 5.19 shows the result of the goodness-of-fit tests with 1000 toy experiments at the best-fit point for normal (top) and inverted (bottom) hierarchy, overlaying as a red line the value of χ^2_{gof} (in the coarse binning) for the best-fit to the data. The p-values were calculated directly from these plots as the number of toy experiments for which $\chi^2_{gof} > (\chi^2_{gof})_{data}$ divided by the total number of toy experiments.

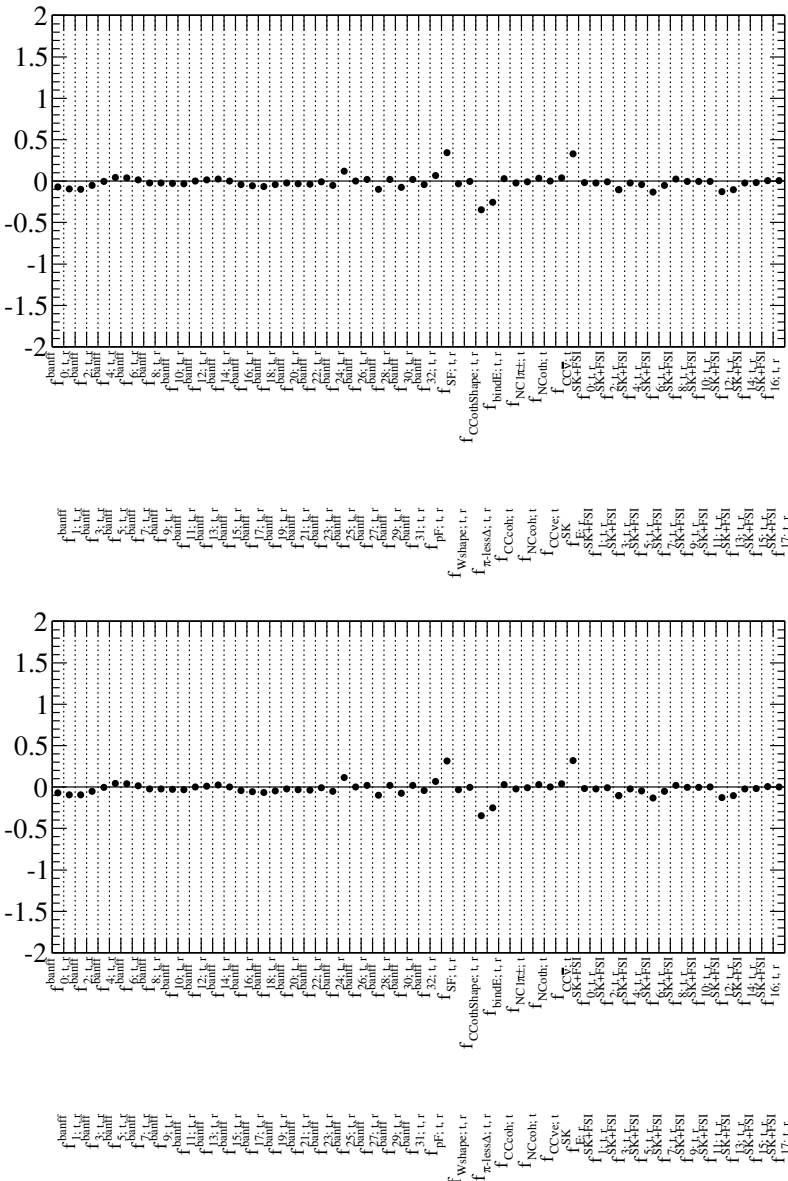


Figure 5.14: Systematic parameter pulls for the 64 systematics allowed to float in the Run 1+2+3+4 joint 3-flavour oscillation fit with normal hierarchy (top) and inverted hierarchy (bottom).

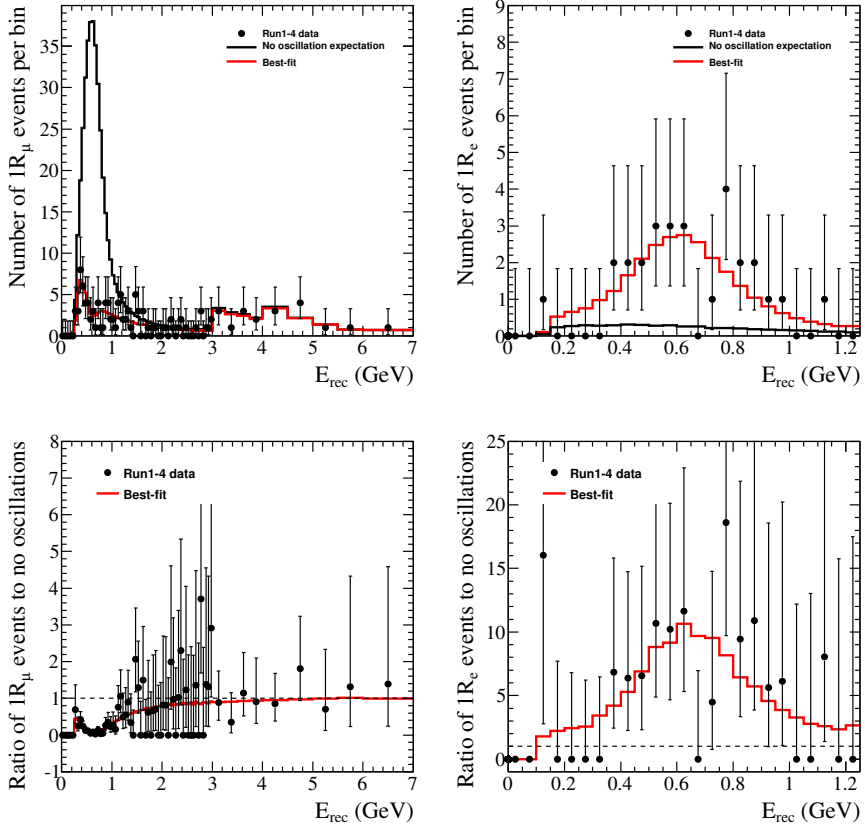


Figure 5.15: Reconstructed neutrino energy distribution of single μ -like ring and single e -like ring events in the Run 1+2+3+4 dataset along with the best-fit prediction of the joint 3-flavour oscillation analysis, assuming normal hierarchy, and overlaid with the non-oscillation prediction. Bottom plots show the ratio of the best-fit reconstructed neutrino energy distribution of single μ -like ring and single e -like ring events to the non-oscillation prediction.

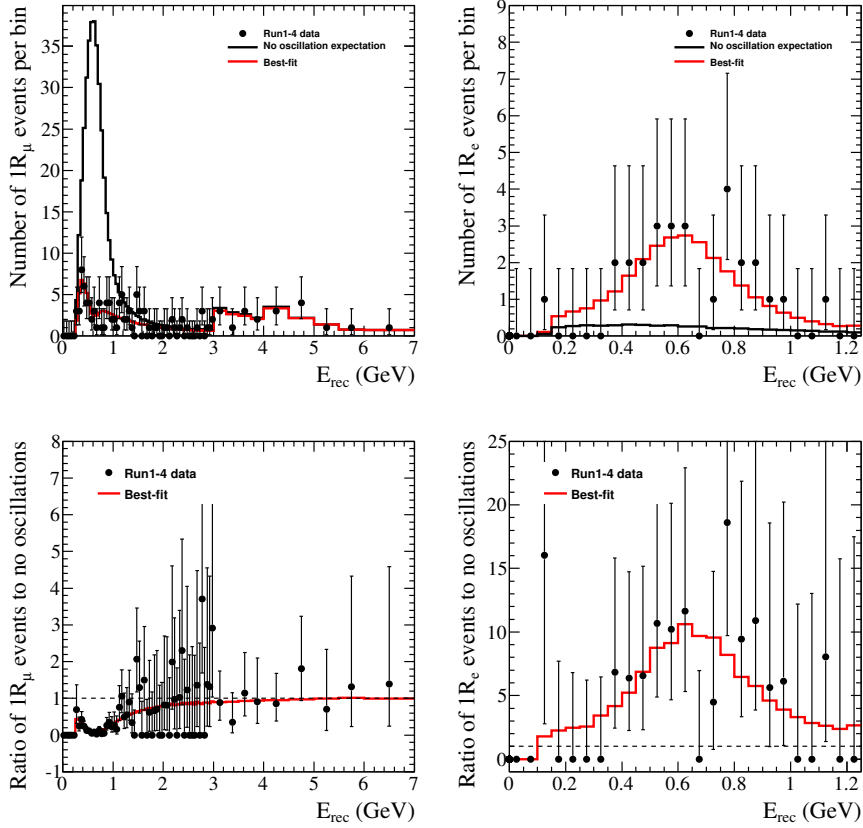


Figure 5.16: Reconstructed neutrino energy distribution of single μ -like ring and single e -like ring events in the Run 1+2+3+4 dataset along with the best-fit prediction of the joint 3-flavour oscillation analysis, assuming inverted hierarchy, and overlaid with the non-oscillation prediction. Bottom plots show the ratio of the best-fit reconstructed neutrino energy distribution of single μ -like ring and single e -like ring events to the non-oscillation prediction.

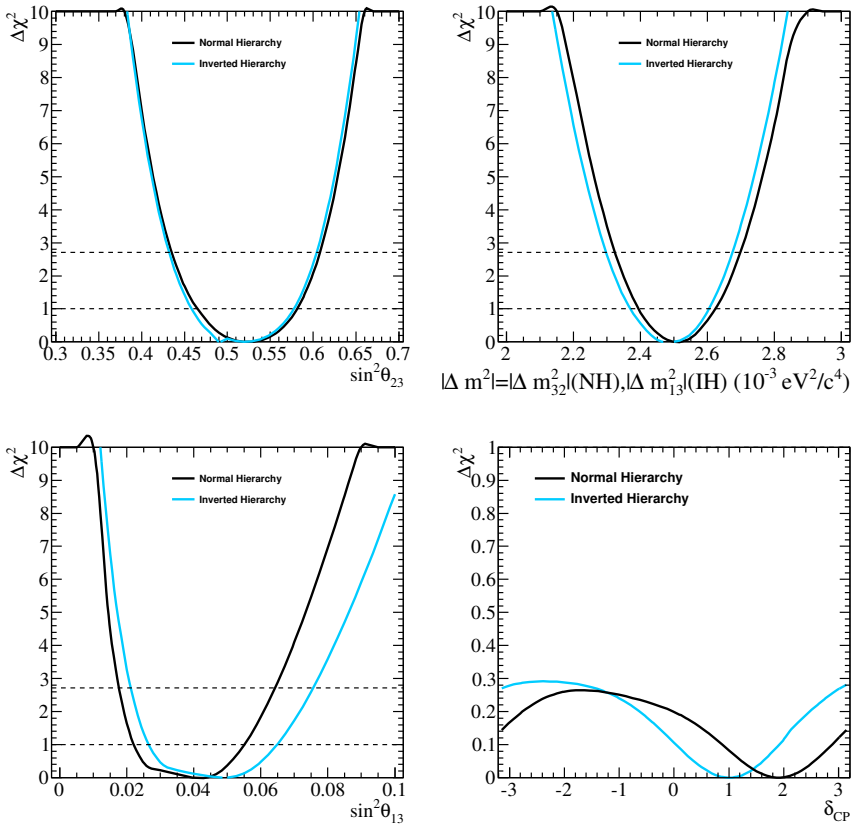


Figure 5.17: Comparison of profiled $\Delta\chi^2$ distributions as function of each of $|\Delta m^2| = |\Delta m^2_{32}|(NH), |\Delta m^2_{13}|(IH), \sin^2\theta_{23}, \sin^2\theta_{13}$ and δ_{CP} for the joint 3-flavour oscillation fit to the Run 1+2+3+4 dataset with normal and inverted hierarchies.

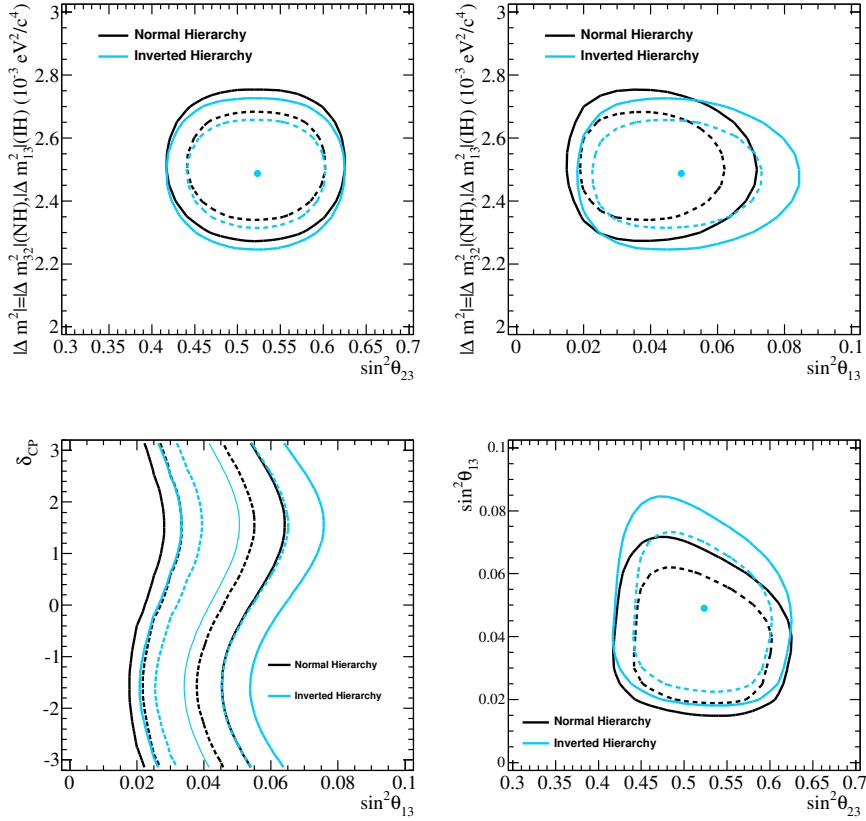


Figure 5.18: Comparison of 68% and 90% CL regions for the Run1+2+3+4 dataset fit with different mass hierarchy assumptions. A common best-fit point, the one from the fit with inverted hierarchy (the one with the smallest value of χ^2), was used to build confidence regions in both mass hierarchy assumptions. In the $(\sin^2 \theta_{13}, \delta_{CP})$ parameter space the method called *raster scan* was used.

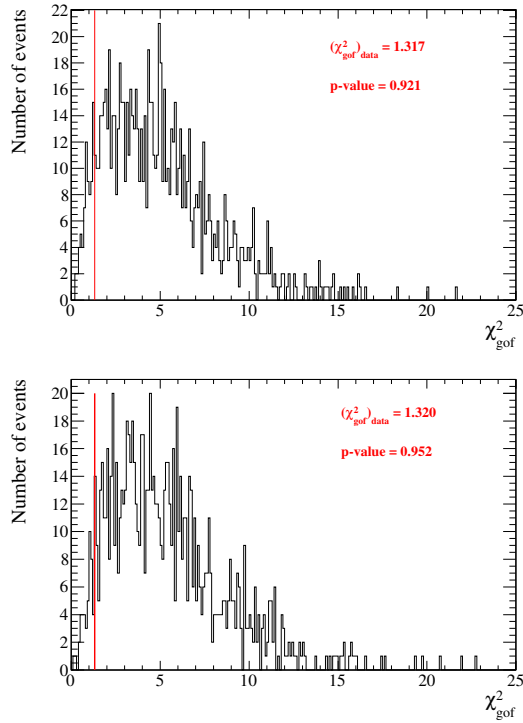


Figure 5.19: Result of the goodness-of-fit tests with 1000 toy experiments at the best-fit point for normal hierarchy (top) and inverted hierarchy (bottom), overlaying as a red line the value of χ^2_{gof} for the best-fit to the data. The p-value was calculated directly from these distributions as the number of toy experiments for which $\chi^2_{gof} > (\chi^2_{gof})_{data}$ divided by the total number of toy experiments.

5.7.2 Results Including the Reactor Constraint

The reactor constraint is included in the Run1+2+3+4 dataset joint fit as it was explained in 5.6.2. Since the weighted average result from reactor experiments is expressed in terms of $\sin^2 2\theta_{13}$, this will be the variable used for these results.

This analysis found $|\Delta m_{32}^2| = 2.509 \times 10^{-3} \text{ eV}^2/c^4$, $\sin^2 \theta_{23} = 0.527$, $\sin^2 2\theta_{13} = 0.0967$ and $\delta_{CP} = -1.554$ to be the joint 3-flavour oscillation best-fit values for the Run 1+2+3+4 dataset combined with the reactor constraint for normal hierarchy and $|\Delta m_{13}^2| = 2.481 \times 10^{-3} \text{ eV}^2/c^4$, $\sin^2 \theta_{23} = 0.533$, $\sin^2 2\theta_{13} = 0.0984$ and $\delta_{CP} = -1.556$ for inverted hierarchy.

Table 5.9 shows the best-fit values obtained the Run1+2+3+4 dataset fit with the two mass hierarchy assumptions, with and without reactor constraint. As expected, the value of $\sin^2 2\theta_{13}$ stays close to the reactor value due to the penalty term, resulting in a variation of the values of the other oscillation parameters accordingly. The χ^2 values found at the best-fit point are larger when the reactor constraint is applied as expected, and now there is a preference for the best-fit point with normal hierarchy, which will be the one used as common best-fit point when comparing confidence regions in the two mass hierarchies.

Reactor	MH	$ \Delta m_{32}^2 $ (NH) or $ \Delta m_{13}^2 $ (IH) $10^{-3} \text{ eV}^2/c^4$	$\sin^2 \theta_{23}$	$\sin^2 2\theta_{13}$	δ_{CP}	$N_{exp}^{1R\mu}$	N_{exp}^{1Re}	χ^2/ndf
NO	NH	2.512	0.524	0.162	1.909	119.915	27.999	84.5395/94
YES	NH	2.509	0.527	0.0967	-1.554	120.383	25.870	85.067/94
NO	IH	2.488	0.523	0.187	1.005	119.948	27.998	84.529/94
YES	IH	2.481	0.533	0.0984	-1.556	121.204	23.571	85.931/94

Table 5.9: Best-fit parameters for the joint 3-flavour oscillation fit to the Run 1+2+3+4 dataset comparing with and without reactor constraint.

The reconstructed neutrino energy distribution of single μ -like ring and single e-like ring events for the Run 1+2+3+4 dataset with the best-fit predictions of the joint oscillation analysis with and without reactor constraint are presented in Fig. 5.20 for normal hierarchy and in Fig. 5.21 for inverted hierarchy. The profiled $\Delta\chi^2$ distribution as a function of each of $|\Delta m^2| = |\Delta m_{32}^2|(NH)$, $|\Delta m_{13}^2|(IH)$, $\sin^2 \theta_{23}$, $\sin^2 2\theta_{13}$ and δ_{CP} oscillation parameters for the joint 3-flavour oscillation fit to the Run 1+2+3+4 dataset with reactor constraint, comparing both mass hierarchies, are presented in Fig. 5.22.

The 68% and 90% CL regions with reactor constraint in the following four 2-dimensional oscillation parameter spaces are calculated for normal and inverted hierarchy and then compared in Fig. 5.23: $(\sin^2 \theta_{23}, |\Delta m^2|)$, $(\sin^2 2\theta_{13}, |\Delta m^2|)$, $(\sin^2 2\theta_{13}, \delta_{CP})$ and $(\sin^2 \theta_{23}, \sin^2 2\theta_{13})$. Also, confidence regions are also presented in the parameter spaces: $(\sin^2 \theta_{23}, \delta_{CP})$ and $(|\Delta m^2|, \delta_{CP})$ in Fig. 5.24. A common best-fit point, the one from the fit with normal hierarchy (the one with the smallest value of χ^2), was used to build confidence regions in both mass hierarchy assumptions for Figs. 5.23 and 5.24. In the $(\sin^2 2\theta_{13}, \delta_{CP})$ parameter space the method *raster scan* was no longer used.

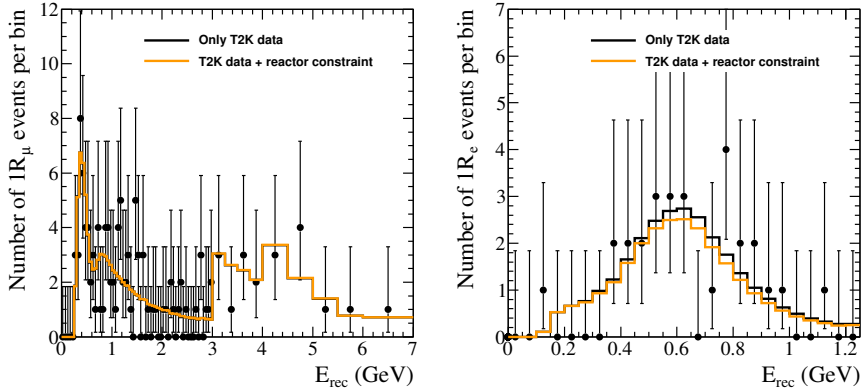


Figure 5.20: Comparison of the best-fit spectra of single μ -like ring and single e-like ring events for the Run 1+2+3+4 dataset for normal hierarchy with and without reactor constraint.

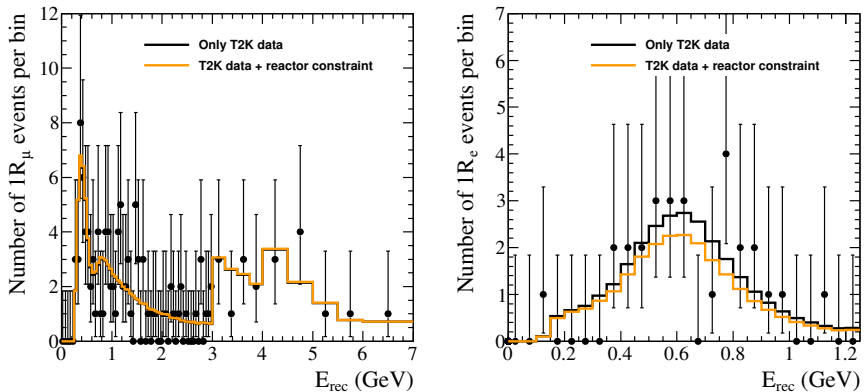


Figure 5.21: Comparison of the best-fit spectra of single μ -like ring and single e-like ring events for the Run 1+2+3+4 dataset for inverted hierarchy with and without reactor constraint.

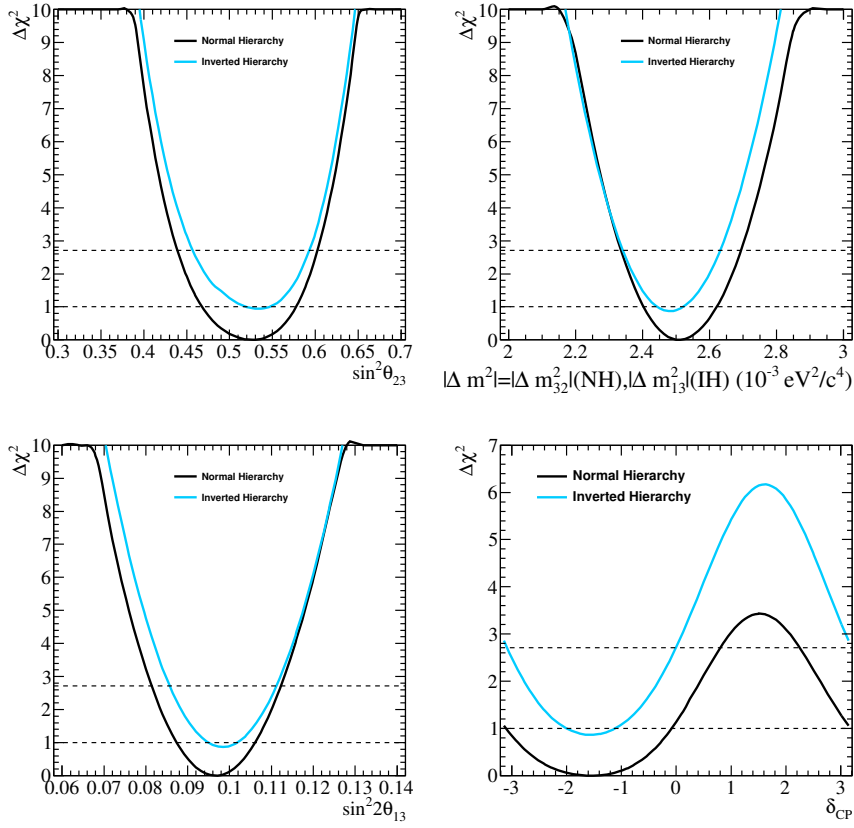


Figure 5.22: Comparison of profiled $\Delta\chi^2$ distributions as a function of each of $|\Delta m^2| = |\Delta m^2_{32}|(NH), |\Delta m^2_{13}|(IH), \sin^2\theta_{23}, \sin^2\theta_{13}$ and δ_{CP} for the joint 3-flavour oscillation fit to the Run 1+2+3+4 dataset with reactor constraint for normal and inverted hierarchies.

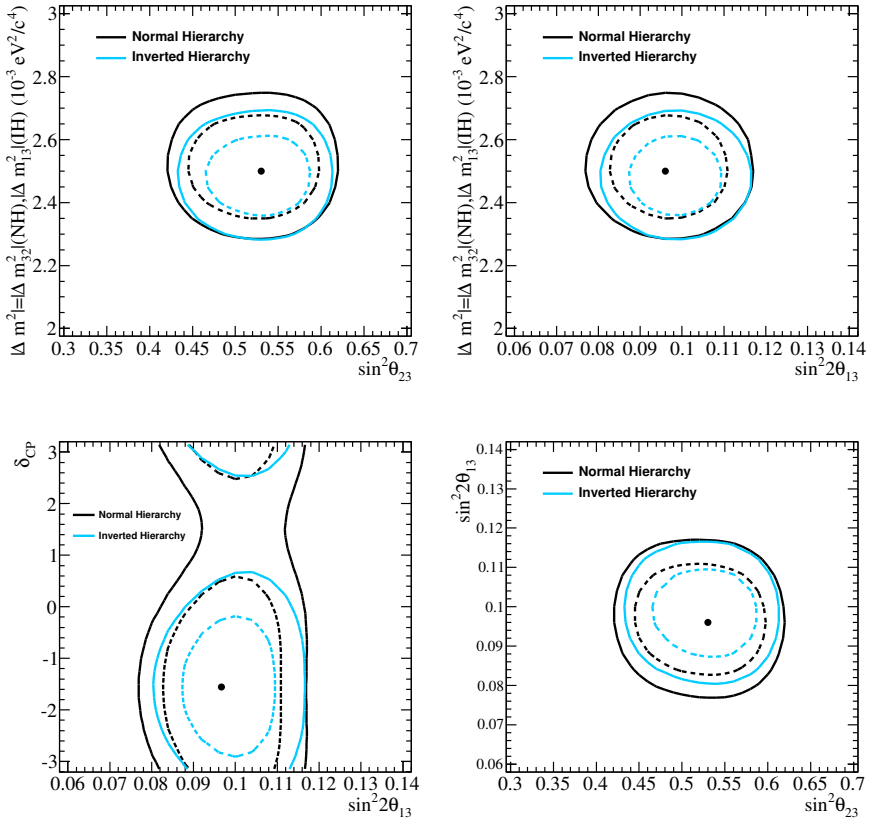


Figure 5.23: Comparison of 68% (dashed lines) and 90% (solid lines) CL regions for the Run1+2+3+4 dataset fit with reactor constraint with different mass hierarchy assumptions. A global χ^2 minimum was used to build confidence regions in both mass hierarchy assumptions.

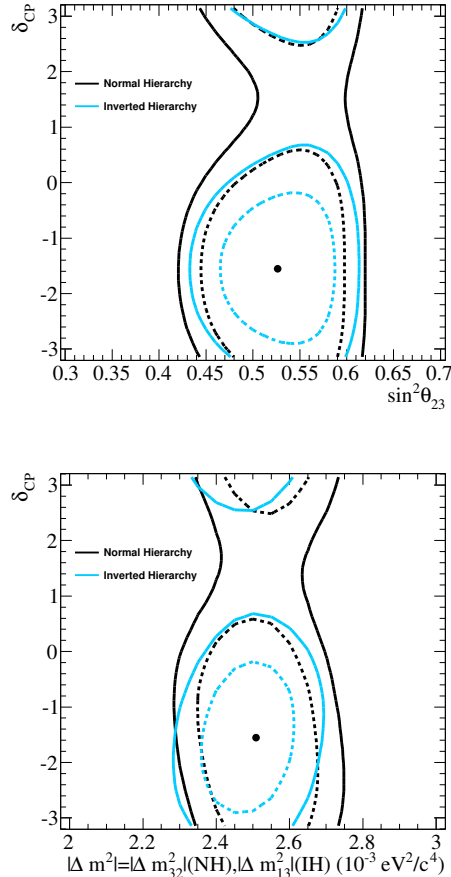


Figure 5.24: Comparison of 68% (dashed lines) and 90% (solid lines) CL regions in the parameter spaces ($\sin^2 \theta_{23}$, δ_{CP}) and ($|\Delta m^2|$, δ_{CP}) for the Run1+2+3+4 dataset fit with reactor constraint with different mass hierarchy assumptions. A global χ^2 minimum was used to build confidence regions in both mass hierarchy assumptions.

Figure 5.25 shows the comparison of 2D confidence regions in the $(\sin^2\theta_{23}, |\Delta m^2|)$ oscillation parameter space with and without reactor constraint for normal hierarchy (left) and inverted hierarchy (right), using independent best-fit points for each mass hierarchy (top) and using a common best fit point (bottom), the one with inverted hierarchy without reactor constraint and with normal hierarchy with reactor constraint. From these figures, it is clear that differences are small in the normal hierarchy assumption when adding the reactor constraint. Larger differences appear in the inverted hierarchy assumption, which are even larger when a common best-fit point is used for both mass hierarchies. This is expected since the best-fit values of $\sin^2\theta_{13}$ of the Run1+2+3+4 dataset fit are larger for the inverted hierarchy, then, when constraining this parameter, larger differences appear. Furthermore, the difference in χ^2 of the best-fit values between the two mass hierarchy assumptions is very small without reactor constraint (≈ 0.01), but becomes significant when adding the reactor constraint (≈ 1), so larger differences appear between confidence regions with and without reactor constraint using a common best-fit point.

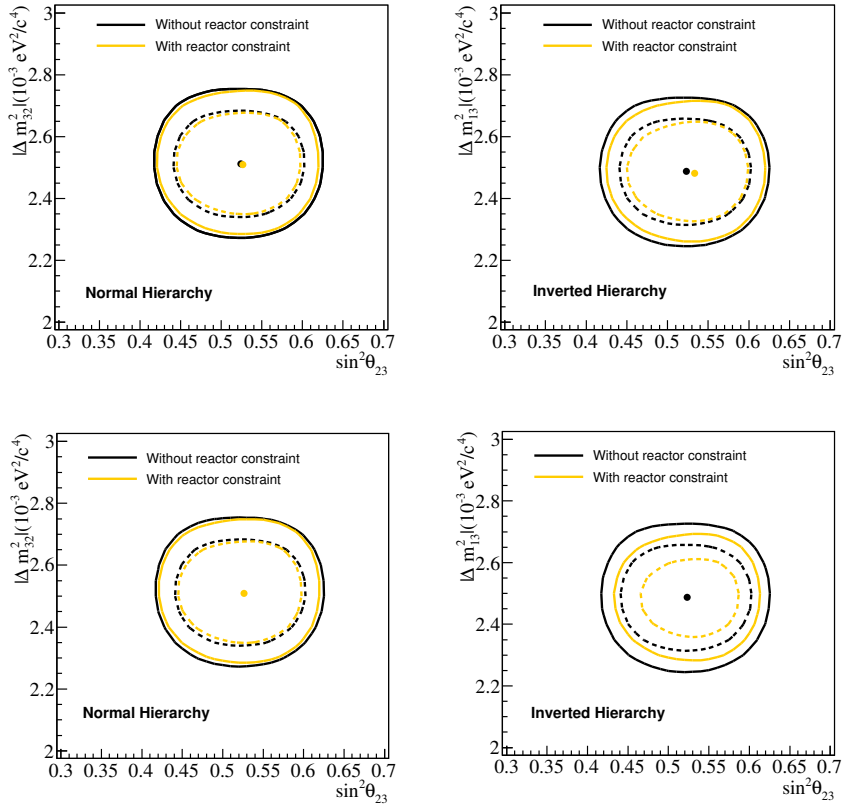


Figure 5.25: Confidence regions in the $(\sin^2 \theta_{23}, \Delta m^2)$ parameters space for the Run1+2+3+4 dataset joint fit with and without reactor constraint for the normal hierarchy (left plots) and the inverted hierarchy (right plots) using independent best-fit points for each mass hierarchy (top plots) and a common best-fit point, the one with inverted hierarchy without reactor constraint and with normal hierarchy with reactor constraint (bottom plots). Solid and dashed lines represent the 90% and 68% CL respectively.

Confidence regions for δ_{CP}

Confidence regions have been calculated for δ_{CP} using a Feldman-Cousins (FC) method [186] in order to have the correct frequentist coverage. This calculation is based on the study already presented in the latest stand-alone ν_e appearance analysis [5]. The approach used to calculate these confidence regions is explained in Section 5.6.4.

Figure 5.26 shows the result of the profiled $\Delta\chi^2$ as a function of δ_{CP} fitting Run1+2+3+4 with reactor constraint in both mass hierarchies taking as common best-fit point the one for normal hierarchy. In this plot the values of critical $\Delta\chi^2_c$ are overlaid. These values of critical $\Delta\chi^2$ were found using a Feldman-Cousins method as it will be explained in Section 5.6.4, and presented as sets of points.

The excluded regions for δ_{CP} can be obtained directly from Fig. 5.26 at the 90% CL:

- $[0.146, 0.825] \pi$ for normal hierarchy
- $[-0.080, 1.091] \pi$ for inverted hierarchy

Figure 5.27 shows the result presented in 5.26 with the excluded regions overlaid.

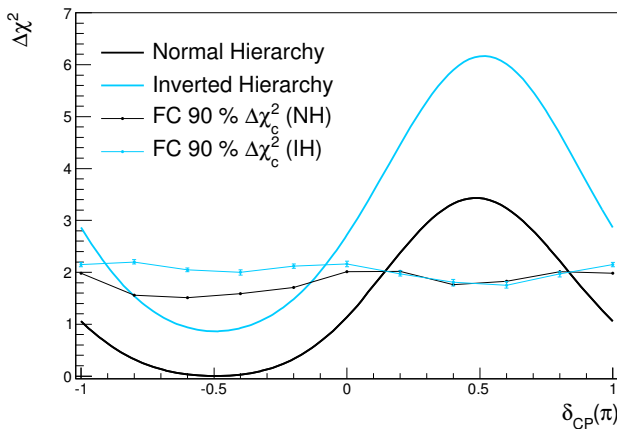


Figure 5.26: Profiled $\Delta\chi^2$ as a function of δ_{CP} with the results of the critical $\Delta\chi^2_c$ values for normal and inverted hierarchy for the Run1+2+3+4 dataset joint fit with reactor constraint.

Sensitivity studies were done to check the result for the profiled $\Delta\chi^2$ as a function of δ_{CP} . In these studies, independent for each mass hierarchy assumption, 500 toy experiments were created at the best-fit values obtained in the fit to the Run1+2+3+4 dataset with reactor constraint, presented in Tab. 5.9, with statistical fluctuations and systematic variations. Then, for each toy experiment, the profiled χ^2 as a function of δ_{CP} was found as

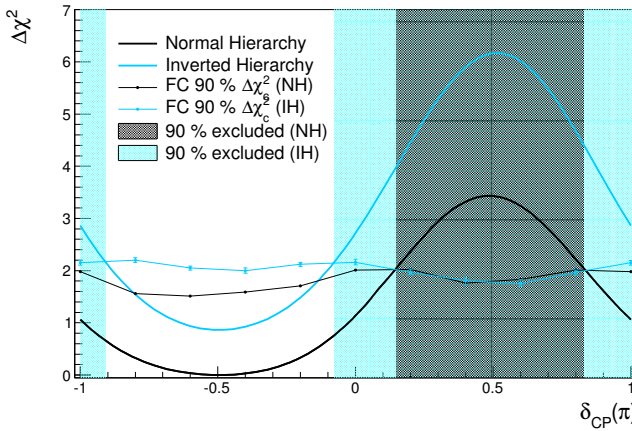


Figure 5.27: Profiled $\Delta\chi^2$ as a function of δ_{CP} with the results of the critical $\Delta\chi^2_c$ values for normal and inverted hierarchy for the Run1+2+3+4 dataset joint fit with reactor constraint, with the excluded regions found overlaid.

for the real data. The results of those sensitivity studies are presented in Fig. 5.28, showing the 500 profiled χ^2 distributions for the toy experiments (black dashed lines) and the one for the Run1+2+3+4 dataset (black solid line). The averaged profiled χ^2 as a function of δ_{CP} from the 500 toy experiments is presented as a blue solid line, and around it, the 1σ band (blue region) was calculated as the band with centre at the averaged distribution that contains 68% of the χ^2 values of the 500 experiments at each value of δ_{CP} (selecting 68% of the values above the averaged one to set the upper limit and 68% of the values below the average to set the lower limit). As observed in this plot, the result for the fit to the Run1+2+3+4 dataset is well inside the 1σ band defined by these sensitivity studies, in both mass hierarchies. Figure 5.29 shows the profiled $\Delta\chi^2$ as a function of δ_{CP} for data (black) and for the averaged profiled χ^2 from Fig. 5.28 (blue).

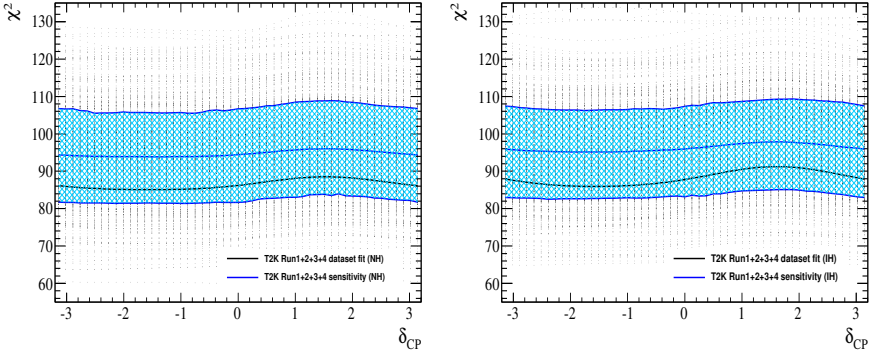


Figure 5.28: Profiled χ^2 as a function of δ_{CP} for the Run1+2+3+4 dataset with reactor constraint (black solid line) and the sensitivity studies performed with 500 toy experiments, showing the averaged profiled χ^2 as a function of δ_{CP} (blue line) and the 1σ band around it for normal hierarchy (left) and inverted hierarchy (right).

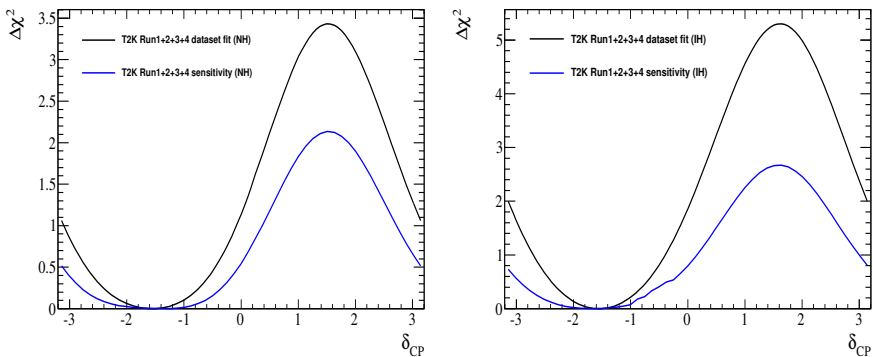


Figure 5.29: Profiled $\Delta\chi^2$ as a function of δ_{CP} for data (black) and for the averaged profiled χ^2 from Fig. 5.28 (blue).

5.7.3 Comparisons of Confidence Regions

Comparisons of confidence regions with stand-alone analyses

Firstly, results of the Run1+2+3+4 dataset joint fit will be compared with the fit to the same dataset in stand-alone ν_μ -disappearance and ν_e -appearance modes.

In Fig. 5.30, the confidence regions in the $(\sin^2\theta_{23}, |\Delta m_{32}^2|)$ or $(\sin^2\theta_{23}, |\Delta m_{13}^2|)$ parameters space for normal hierarchy (left) and inverted hierarchy (right) result of the Run1+2+3+4 dataset joint fit are compared with the results of the ν_μ -disappearance analysis with the same dataset, using the same constant $\Delta\chi^2$ method and a binned likelihood-ratio method for both analyses. Clearly, confidence regions are comparable in size, indicating that, although $\sin^2\theta_{13}$ and δ_{CP} are also included in the fit, the constraint from the SK single e-like ring sample prevents the confidence regions to become larger. Also, there is a small shift to larger values of $\sin^2\theta_{23}$. The reason for this shift is that the best-fit value of $\sin^2\theta_{13}$ for the joint fit is larger than the typical value used for this parameter. Thus, the value for maximal disappearance becomes larger as explained in Appendix E, and the result for the joint fit is also showing a preference for maximal disappearance for the best-fit point.

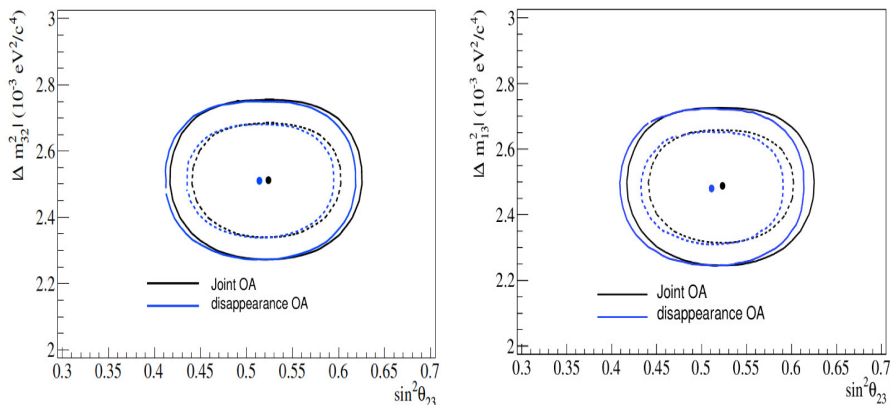


Figure 5.30: Comparison of confidence regions in the $(\sin^2\theta_{23}, |\Delta m_{32}^2|)$ parameter space for the Run1+2+3+4 dataset fit assuming normal hierarchy (left) or inverted hierarchy (right) for the joint oscillation analysis and the ν_μ -disappearance analysis. In both cases the same constant $\Delta\chi^2$ method was used and a binned likelihood-ratio analysis was performed.

In Fig. 5.31 the confidence regions in the $(\sin^2 2\theta_{13}, \delta_{CP})$ parameters space for the Run1+2+3+4 dataset fit with normal hierarchy (left) and inverted hierarchy (right) for the joint oscillation analysis are compared with the results for the latest stand-alone appearance analysis profiling over $|\Delta m_{32}^2|$ and $\sin^2\theta_{23}$, using the *raster scan* method in both analyses. The confidence regions of the appearance analysis profiling over $|\Delta m_{32}^2|$ and $\sin^2\theta_{23}$ are

larger than the ones for the joint fit, clearly visible in this figure, because the latter is including the single μ -like ring sample to constrain those parameters. In addition, the best-fit values (and therefore confidence regions) are shifted for the joint analysis towards smaller values of $\sin^2\theta_{13}$. This is due to the fact that the best-fit values of $\sin^2\theta_{23}$ are larger than 0.5 along the region of the best-fit points in $(\sin^2\theta_{13}, \delta_{CP})$ as it can be observed in Fig. 5.32, where the line of best-fit values in the $(\sin^2\theta_{13}, \delta_{CP})$ space is overlaid on the best-fit values of $\sin^2\theta_{23}$ for normal (left) and inverted (right) hierarchy. Thus, due to the correlation between $\sin^2\theta_{23}$ and $\sin^2\theta_{13}$, and as observed for instance in Fig. 5.3, because $\sin^2\theta_{23} > 0.5$, the line of best-fit points moves to smaller values of $\sin^2\theta_{13}$.

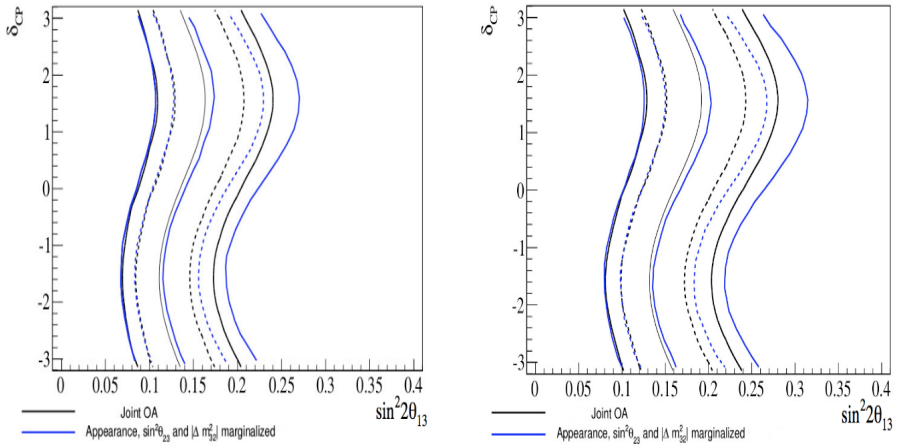


Figure 5.31: Comparison of confidence regions in the $(\sin^2 2\theta_{13}, \delta_{CP})$ parameter space for the Run1+2+3+4 dataset fit assuming normal (left) and inverted (right) hierarchy for the joint oscillation analysis and the latest Run1+2+3+4 ν_e -appearance analysis marginalizing over $|\Delta m^2|$ and $\sin^2\theta_{23}$. In both cases the *raster scan* method was used.

In Fig.5.33, the results are presented adding the excluded regions from the latest stand-alone appearance analyses in [5] ("T2K Nov. 2013 release" in the legend). The excluded regions are larger for the joint oscillation analysis as this includes information of the single μ -like ring and single e-like ring samples simultaneously and it incorporates the constraint in $(\sin^2 2\theta_{13}, \sin^2\theta_{23} \text{ and } |\Delta m^2|)$ for the Run 1+2+3+4 dataset, whereas for the latest stand-alone appearance results in [5] the results for the Run 1+2+3 were used to constrain $(\sin^2\theta_{23} \text{ and } |\Delta m^2|)$.

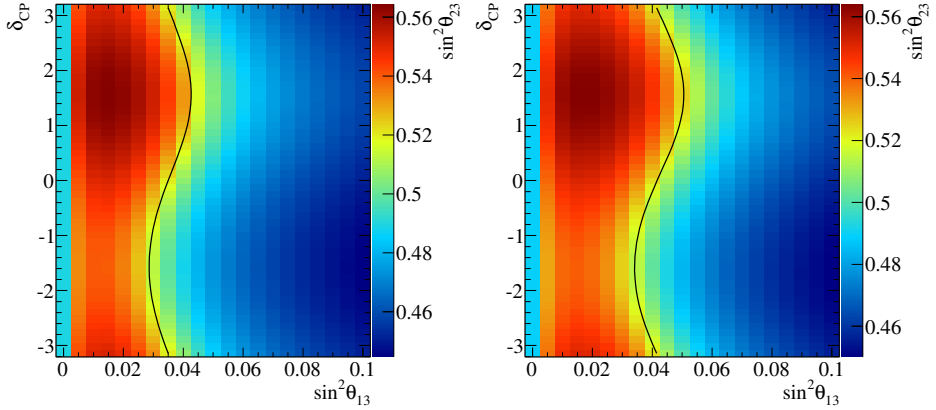


Figure 5.32: Line of best-fit values in the $(\sin^2 \theta_{13}, \delta_{CP})$ space overlaid on the best-fit values of $\sin^2 \theta_{23}$ for normal (left) and inverted (right) hierarchy.

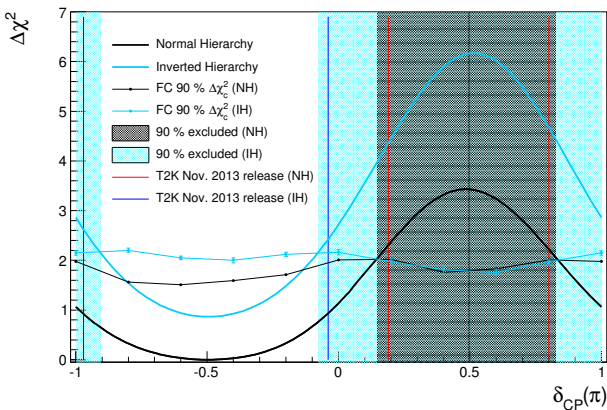


Figure 5.33: Profiled $\Delta\chi^2$ as a function of δ_{CP} with the results of the critical $\Delta\chi_c^2$ values for normal and inverted hierarchy for the Run1+2+3+4 dataset joint fit with reactor constraint, with the excluded regions found overlaid and compared to the excluded regions from the latest stand-alone appearance results in [5].

Comparisons of confidence regions with results from other experiments

A comparison of the confidence regions obtained with the joint analysis with the results from other experiments has been made. Figure. 5.34 shows the comparison of results including the reactor constraint compared to:

- the results of a joint oscillation analysis performed by the MINOS experiment, as presented in [184].
- the preliminary results of a 3-flavour atmospheric neutrino fit from the Super-Kamiokande experiment [187].

The MINOS result was produced combining ν_μ disappearance and ν_e appearance channels in a three flavour formalism. It was obtained using its complete set of accelerator and atmospheric data, in both neutrino and anti-neutrino beam running, with a total of 10.71×10^{20} ν_μ dominated beam, 3.36×10^{20} $\bar{\nu}_\mu$ -enhanced beam and 37.88 kt-yr atmospheric neutrino data. The fit is performed including the reactor constraint on $\sin^2\theta_{13}$ from PDG2013, and fitting δ_{CP} as well, and the best-fit point was obtained for the inverted hierarchy and the first octant for θ_{23} , contrarily to T2K's best-fit, which prefers maximal disappearance and the normal hierarchy with the reactor constraint.

The Super-K 3-flavour joint fit is a zenith angle oscillation fit combining as well ν_μ disappearance and ν_e appearance, and it was done using SK I-IV atmospheric data (more than 11 live-years of atmospheric neutrino data) fixing $\sin^2\theta_{13} = 0.098$ (PDG2012) and fitting δ_{CP} . The results for the SK joint fit weakly prefer the second octant for θ_{23} for both normal and inverted mass hierarchies, and the inverted hierarchy is slightly preferred with $\Delta\chi^2=1.2\sigma$.

Notice that in Fig. 5.34 the results from the Super-K 3-flavour fit are done using independent best-fit points for each mass hierarchy, while a common best-fit point for both mass hierarchies is used for MINOS (inverted hierarchy) and T2K (normal hierarchy).

Finally, the comparison of $\Delta\chi^2$ as a function of δ_{CP} for the T2K joint oscillation analysis with the results of the joint oscillation analysis performed by the MINOS experiment, also combining ν_μ disappearance and ν_e appearance, are presented in Fig. 5.35.

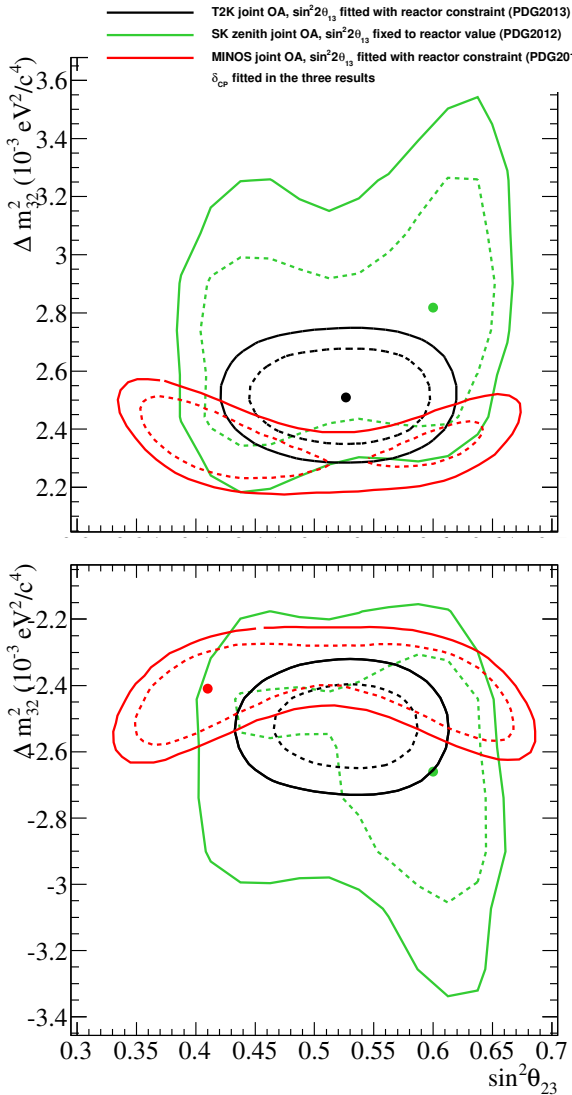


Figure 5.34: Confidence regions in the $(\sin^2 \theta_{23}, \Delta m_{32}^2)$ parameters space for the T2K joint oscillation analysis with the Run1+2+3+4 dataset including reactor constraint (PDG2013) for the two mass hierarchies compared with the preliminary results of a 3-flavour atmospheric neutrino fit from the Super-Kamiokande experiment [187] and results of the joint oscillation analysis performed by the MINOS experiment, also combining ν_μ disappearance and ν_e appearance, as presented in [184]. Notice that the results from the SK 3-flavour fit are done using independent best-fit points for each mass hierarchy.

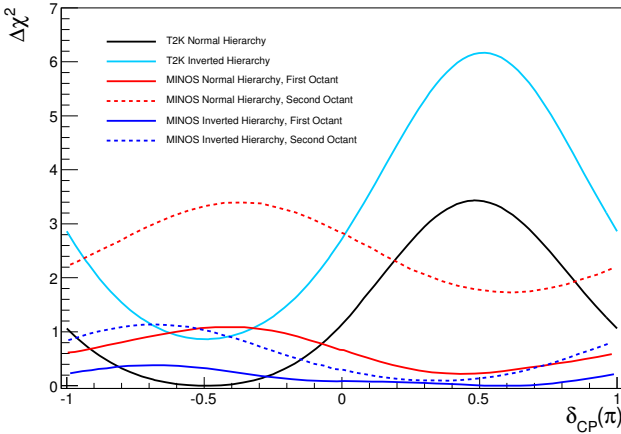


Figure 5.35: Comparison of $\Delta\chi^2$ as a function of δ_{CP} for the T2K joint oscillation analysis with the Run1+2+3+4 dataset including reactor constraint (PDG2013) for the two mass hierarchies compared with the results of the joint oscillation analysis performed by the MINOS experiment, also combining ν_μ disappearance and ν_e appearance, as presented in [184], with different mass hierarchy and θ_{23} octant assumptions.

5.8 Future Improvements for the T2K Joint Oscillation Analysis

There are different aspects that can be explored in order to improve the joint oscillation analysis presented in this chapter.

First of all, additional information can be included concerning the samples used to perform the joint oscillation analysis. On the one hand, the momentum and angle of the lepton in the event candidates can be used as it has been done in the latest stand-alone ν_e appearance analysis [5], not only for the single e-like ring sample but also for the single μ -like ring sample. On the other hand, the addition of extra samples, such as multi-ring samples, can be considered, and presently the inclusion of the antineutrino sample is ongoing as the T2K experiment has already started taking data with an antineutrino beam.

Furthermore, the confidence regions presented in this chapter were obtained using a constant $\Delta\chi^2$ method. The construction of confidence regions could be improved, using other methods to properly deal with physical boundaries. An extension of the Feldman-Cousins [186] method could be studied, although there is no current prescription for applying this method to a 4-dimensional parameter space and it is a CPU-intensive process.

An important source of improvement for this analysis is related to the reduction of the systematic errors, which can be achieved with improvements on the predictions, such as the

measurements of hadron emission using a replica of the T2K target mentioned in Section 4.2, and further measurements to reduce the uncertainties, for instance a more sophisticated data selection in the near detector to further constrain the flux at SK and the correlated cross sections.

Other analyses can be performed as well using the framework of the joint oscillation analysis, including non standard physics studies and searches for sterile neutrinos and non standard matter interactions, which are currently being considered.

Chapter 6

T2K Sensitivity Studies and Prospects

The long term physic goals of the T2K experiment include the investigation of the unknown δ_{CP} value, the mass hierarchy and the θ_{23} octant through high precision measurements of electron neutrino appearance and muon neutrino disappearance. In addition, several cross section measurements are ongoing in the different T2K detectors, and more are expected. Studies for other non standard physics studies are also planned, such as sterile neutrino searches and tests for Lorenz invariance.

Other analyses are possible considering that the future running plan for T2K will likely include a significant fraction of antineutrino beam: anti- ν_μ disappearance and anti- ν_e appearance from an anti- ν_μ beam analyses could be performed, as well as antineutrino cross section measurements.

6.1 T2K Sensitivity Studies

The current dataset accumulated by the T2K experiment (Run1+2+3+4) consist of 6.57×10^{20} POT, which corresponds to a $\sim 8\%$ of the T2K goal 7.8×10^{21} POT. Much higher precision on the measurement of the neutrino oscillation parameters can be achieved with the T2K goal POT, and results to shed light on the still open questions, such as the mass hierarchy, the δ_{CP} value and the θ_{23} octant, can be attained as it has been demonstrated by T2K sensitivity studies (considering the possibility of antineutrino beam running).

The precision obtained for the atmospheric neutrino oscillation parameters is currently very limited by statistics. Sensitivity studies have been performed following the actual T2K oscillation analyses for different values of the POT in order to study the reduction of the 1σ errors for $\sin^2 \theta_{23}$ and Δm_{32}^2 . Figure 6.1 presents an example of such sensitivity studies [188] as a function of POT with a joint oscillation analysis combining ν_μ disappearance and ν_e appearance assuming 50% of neutrino running and 50% of antineutrino running and true values $\sin^2 2\theta_{13} = 0.1$ (being this parameter constrained by $\delta(\sin^2 2\theta_{13}) = 0.005$), $\delta_{CP} = 0$, $\sin^2 \theta_{23} = 0.5$, $\Delta m_{32}^2 = 2.4 \times 10^{-3}$ (eV 2) and the normal mass hierarchy. The solid

lines in Fig. 6.1 were obtained without systematic errors and the red dashed lines assuming a conservative projected systematic error of $\sim 7\%$ for neutrinos (ν_e and ν_μ) and $\sim 14\%$ for antineutrinos ($\bar{\nu}_e$ and $\bar{\nu}_\mu$), and fully correlated errors between neutrinos and antineutrinos.

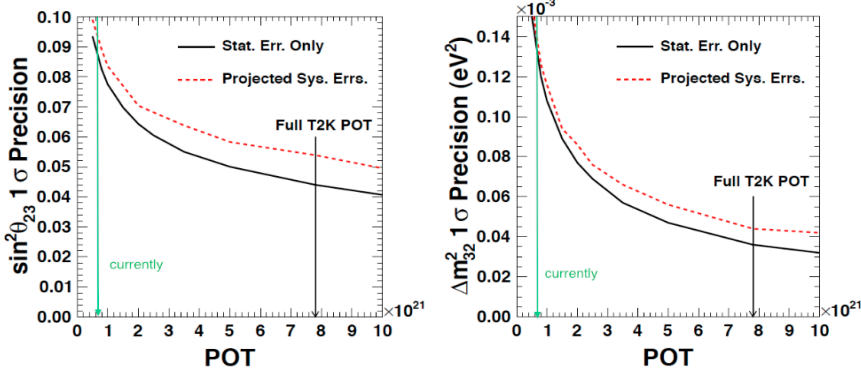


Figure 6.1: Example of T2K sensitivity study showing the value of the 1σ width for $\sin^2 \theta_{23}$ (left) and Δm^2_{32} (right) vs POT with a joint oscillation analysis combining ν_μ disappearance and ν_e appearance assuming 50% of neutrino running and 50% of antineutrino running and true values $\sin^2 2\theta_{13} = 0.1$ (being this parameter constrained by $\delta(\sin^2 2\theta_{13}) = 0.005$), $\delta_{CP} = 0$, $\sin^2 \theta_{23} = 0.5$, $\Delta m^2_{32} = 2.4 \times 10^{-3}$ (eV 2) and the normal mass hierarchy. The solid lines in Fig. 6.1 were obtained without systematic errors and the red dashed lines assuming a conservative projected systematic error of $\sim 7\%$ for neutrinos and $\sim 14\%$ for antineutrinos (fully correlated). Figure from [188].

A similar sensitivity study, also using the joint oscillation analysis and assuming 50% of neutrino running and 50% of antineutrino running, was performed to investigate the T2K sensitivity for resolving $\sin \delta_{CP} \neq 0$, in this case using a realistic assumption for systematic errors based on the 2012 measurements, with $\sim 10\%$ for ν_e , $\sim 13\%$ for ν_μ and equivalent errors for antineutrino with an additional 10% normalization uncertainty. Figure 6.2 presents an example of such a sensitivity study using true values $\sin^2 2\theta_{13} = 0.1$ (being this parameter constrained by $\delta(\sin^2 2\theta_{13}) = 0.005$) and $\Delta m^2_{32} = 2.4 \times 10^{-3}$ (eV 2) for different values of $\sin^2 \theta_{23}$. From Fig. 6.2 it is clear that T2K has sensitivity to the CP-violating phase δ_{CP} at 90% CL over a significant range depending on the value of $\sin^2 \theta_{23}$.

Similarly, sensitivity studies for resolving θ_{23} octant were also performed using the joint oscillation analysis and assuming 50% neutrino and antineutrino running, and realistic systematic errors as for the δ_{CP} study described above. An example is given in Fig. 6.3 for a true value $\sin 2\theta_{23} = 0.4$, and the same true values for other parameters used for the δ_{CP} study, showing how the sensitivity for resolving θ_{23} octant is improved when combining T2K data and results from reactor experiments.

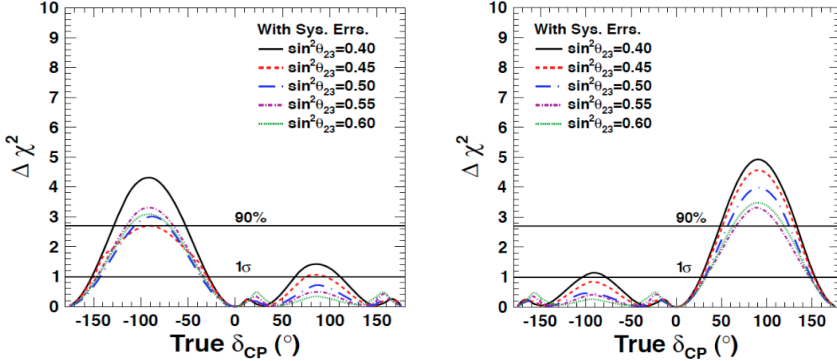


Figure 6.2: Example of T2K sensitivity study for resolving $\sin \delta_{CP} \neq 0$, using joint oscillation analysis and assuming 50% of neutrino running and 50% of antineutrino running and realistic systematic errors based on the 2012 measurements, with true values $\sin^2 2\theta_{13} = 0.1$ (being this parameter constrained by $\delta(\sin^2 2\theta_{13}) = 0.005$) and $\Delta m_{32}^2 = 2.4 \times 10^{-3}$ (eV 2) for different values of $\sin^2 \theta_{23}$ and normal (left) or inverted mass hierarchy (right). Figure from [188].

Furthermore, these sensitivity studies can be performed for T2K combined with the NO ν A experiment [189], with an enhancement of the sensitivities for resolving $\sin \delta_{CP} \neq 0$ and the mass hierarchy as it is shown in Fig. 6.4. For these studies, a modified version of the General Long-Baseline Experiment Simulator (GLoBES) was used [190], [191], with goal POT assumed and a ratio of 50% neutrino and antineutrino running for both T2K and NO ν A¹. The systematic errors used were simply normalization uncertainties of 5% on signal and 10% on background. Figure 6.4 shows an example of sensitivity study for T2K alone, NO ν A alone and T2K+NO ν A for resolving $\sin \delta_{CP} \neq 0$ and the mass hierarchy. From this figure it is clear that the T2K sensitivity can be improved in both cases when combining T2K and NO ν A data.

¹The goal POT assumed for NO ν A is the one stated in its TRD [192], which is the same, 1.8×10^{21} POT, for both neutrino and antineutrino.

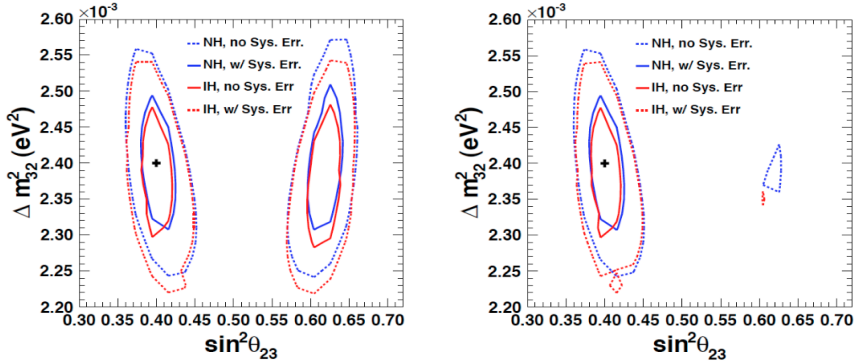


Figure 6.3: Example of sensitivity study for resolving θ_{23} octant with true $\sin 2\theta_{23} = 0.4$, and the true values of the other oscillation parameters $\sin^2 2\theta_{13} = 0.1$, $\delta_{CP} = 0$, $\Delta m_{32}^2 = 2.4 \times 10^{-3}$ (eV^2) and the normal mass hierarchy, without applying reactor constraint (left plot) and applying it through the constraint $\delta(\sin^2 2\theta_{13}) = 0.005$ (right plot), including systematic errors (dashed lines) or not including them (solid lines). Figure from [188].

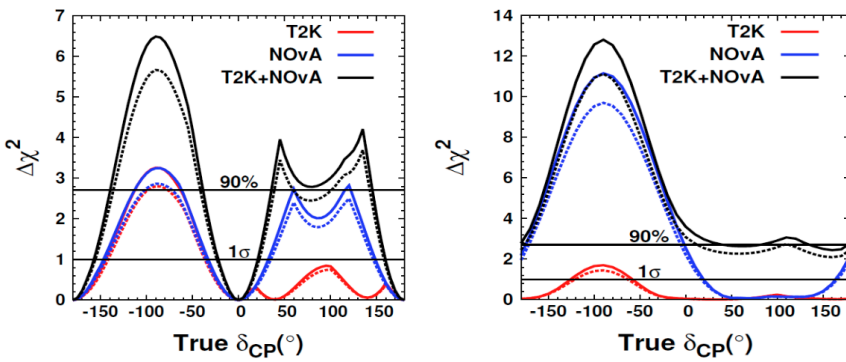


Figure 6.4: Example of sensitivity study for T2K alone (red), NO ν A alone (blue) and T2K+NO ν A (black) for resolving $\sin \delta_{CP} \neq 0$ (left plot) and the mass hierarchy (right plot) without systematics (solid lines) and with systematics (dashed lines) with true values $\sin^2 2\theta_{13} = 0.1$ (being this parameter constrained by $\delta(\sin^2 2\theta_{13}) = 0.005$), $\sin^2 \theta_{23} = 0.5$, $\Delta m_{32}^2 = 2.4 \times 10^{-3}$ (eV^2) and the normal mass hierarchy. Figure from [188].

6.2 Beyond T2K: Hyper-Kamiokande

The Hyper-Kamiokande (Hyper-K) experiment [193] is a proposed next generation neutrino and nucleon decay experiment with an underground water Čerenkov detector of about one Megaton of total volume. It will serve as far detector for a long baseline neutrino oscillation experiment for the upgraded J-PARC, and will be also capable of observing proton decays, atmospheric neutrinos and neutrinos from astronomical origins with a sensitivity far beyond the SK detector. Figure 6.5 shows the schematic view of the Hyper-Kamiokande detector design.

Hyper-K will consist of two cylindrical tanks lying side-by-side with their outer dimensions being 48 m x 54 m x 250 m (width x height x length) and a total mass of 0.99 million metric tons (Megaton) and a fiducial volume of 0.56 Megaton, which is 25 times larger than SK fiducial volume. Its inner detector region will be covered with 99,000 20-inch PMTs, corresponding to the PMT density of 20% photo-cathode coverage (one half of the SK coverage).

The candidate detector site to place Hyper-K detector is in Tochibura Mine, about 10 km south from the Super-Kamiokande location, which is 295 km away from J-PARC, at an underground depth of 1,750 meters water equivalent (m.w.e.).

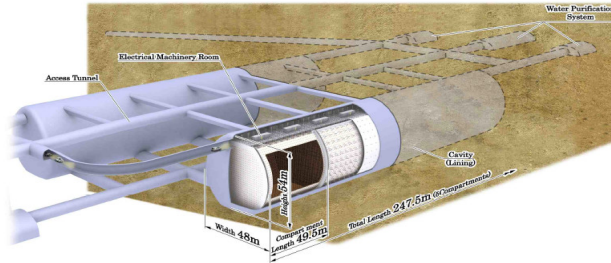


Figure 6.5: Schematic view of the Hyper-Kamiokande detector design. Figure from [193].

The Hyper-K experiment with the upgraded J-PARC beam, whose beam power would be increased up to $\sim 1\text{MW}$, will be able to explore CP violation and greatly improve the recent first measurements of the value of the CP-violating phase δ_{CP} made by the T2K experiment [5]. The experiment will use a proton beam with a power of $\sim 1\text{MW}$ to produce neutrinos and antineutrinos. The beam will be directed to the Hyper-K detector with the same off-axis configuration and 2.5° off-axis angle used by T2K, and near detectors will be used to measure the neutrino beam before oscillations near the production site. The estimation of signal events is approximately 2000 to 4000 for both neutrinos and antineutrinos after running during 10 years with a split of 3:7 between neutrinos and antineutrinos. This high event rate at Hyper-K will also allow precise measurements of the neutrino mixing pa-

rameters. With these estimations, assuming a known mass hierarchy (determined by other means) and a total systematic error of $\sim 5\%$, then the CP-violating phase might be distinguished from $\delta_{CP}=0$ at the 3σ level for 74% of the entire range of δ_{CP} , as illustrated in Fig. 6.6 (left).

In addition, the large statistics sample from the Hyper-K detector will offer a unique opportunity to study atmospheric neutrinos in detail: approximately 10^6 atmospheric neutrino events are expected to be collected in a 10 years period. With atmospheric neutrinos, measuring muon and electron neutrinos and antineutrinos, Hyper-K can shed light on the θ_{23} octant, the mass hierarchy and the CP-violating phase, by combining measurements of the electron and muon neutrino flux variations. As an example, Fig. 6.6 (right) shows the sensitivity to the mass hierarchy as a function of θ_{23} with $\sin^2 2\theta_{13} = 0.098$ fixed for the case of the normal hierarchy, demonstrating that a significance of more than 3σ is expected for the mass hierarchy determination for $\sin^2 \theta_{23} > 0.4$.

Other studies, including low energy neutrino physics and astrophysics (with solar and supernova neutrinos) and nucleon decay modes, will be performed at Hyper-K with promising results expected.

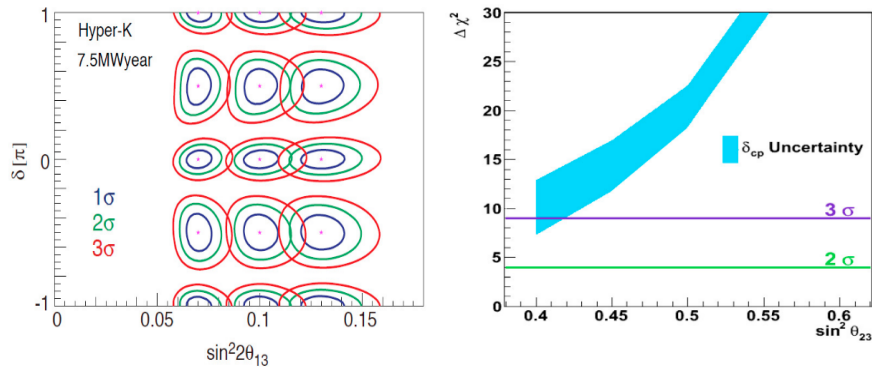


Figure 6.6: Sensitivity studies for the J-PARC to Hyper-K experiment. Left: the 1σ (blue), 2σ (green) and 3σ (red) allowed regions in the space of $\sin^2 2\theta_{13}$ (near its known value) and δ_{CP} assuming normal mass hierarchy. Right: sensitivity study using atmospheric neutrinos to the mass hierarchy as a function of θ_{23} with $\sin^2 2\theta_{13} = 0.098$ fixed for the case of the normal hierarchy, demonstrating that a significance of more than 3σ is expected for the mass hierarchy determination with $\sin^2 \theta_{23} > 0.4$. Figure from [194].

Chapter 7

Conclusion

Since it started taking data in 2010, the T2K experiment has accumulated 6.57×10^{20} protons on target and observed 120 ν_μ and 28 ν_e event candidates at SK. With this dataset, it has obtained the world's most accurate value of the angle θ_{23} and the strongest evidence of ν_e appearance from a ν_μ beam.

The first oscillation analyses performed by the T2K experiment were stand-alone ν_μ disappearance and ν_e appearance analyses, fixing the oscillation parameters not directly measured in each case to some prior values. However, it has been proved that a change in the values of the fixed parameters produces a significant variation on the best-fit values of the parameters measured, stating the importance of the correlations among all oscillation parameters.

In this thesis, the first T2K joint 3-flavour oscillation analysis combining the ν_μ disappearance and the ν_e appearance channels has been presented. This analysis represents a step forward in taking into account the uncertainties in all the oscillation parameters at the same time. It consists in a simultaneous fit to the energy spectra of both the ν_μ and ν_e event candidates from the T2K beam at SK, in which the atmospheric squared-mass splitting Δm_{32}^2 (or Δm_{13}^2), the mixing parameters $\sin^2\theta_{23}$, $\sin^2\theta_{13}$ and the CP-invariance violating phase δ_{CP} are jointly determined. In this way, none of the oscillation parameters is fixed, and all their inter-dependencies are included¹.

The analysis presented in this thesis uses a binned likelihood-ratio method. Measurements of the oscillation parameters are obtained by comparing the observed and predicted SK reconstructed energy spectra for ν_μ and ν_e event candidates, finding their best-fit values by maximizing the likelihood function, which considers the effect of the 64 systematic parameters (related to SK efficiencies, flux and cross section uncertainties) that are allowed to vary in the fit. The fit is repeated four times: for each mass hierarchy assumption, treated as an initial selection, solutions in both octants for θ_{23} are found, choosing the one of the two with the smallest value of χ^2 as the final result for the specified mass hierarchy.

The best-fit values for the T2K Run 1+2+3+4 dataset, with 6.57×10^{20} POT, assuming normal (inverted) mass hierarchy, with their 1σ errors were:

¹The solar mixing parameter $\sin^2\theta_{12}$ and the solar squared-mass splitting Δm_{21}^2 were fixed, as the studies presented in Appendix B demonstrate that their effect is negligible.

$$\begin{aligned}
 \Delta m_{32}^2(\Delta m_{13}^2) &= 2.51_{-0.12}^{+0.11}(2.49_{-0.12}^{+0.12}) \times 10^{-3} eV^2/c^4, \\
 \sin^2 \theta_{23} &= 0.524_{-0.059}^{+0.057}(0.523_{-0.065}^{+0.055}), \\
 \sin^2 \theta_{13} &= 0.042_{-0.021}^{+0.013}(0.049_{-0.021}^{+0.015}) \\
 \delta_{CP} &= 1.91_{-5.05}^{+1.23}(1.01_{-4.15}^{+2.14})
 \end{aligned} \tag{7.1}$$

The confidence regions presented in this thesis were obtained with a frequentist approach, using the constant- $\Delta\chi^2$ method. The 90% CL allowed regions for normal (inverted) mass hierarchy, calculated with the one-dimensional profiled $\Delta\chi^2$ distributions, were:

$$\begin{aligned}
 2.320(2.292) < \Delta m_{32}^2(\Delta m_{13}^2) 10^{-3} eV^2/c^4 &< 2.697(2.672) \\
 0.435(0.434) < \sin^2 \theta_{23} &< 0.608(0.596) \\
 0.018(0.022) < \sin^2 \theta_{13} &< 0.063(0.076) \\
 -\pi(-\pi) < \delta_{CP} &< \pi(\pi)
 \end{aligned} \tag{7.2}$$

Studies combining T2K data with the latest measurements of the angle θ_{13} by experiments with antineutrinos from nuclear reactors were presented as well. The best-fit values including the reactor constraint on $\sin^2 2\theta_{13}$ for normal (inverted) mass hierarchy were:

$$\begin{aligned}
 \Delta m_{32}^2(\Delta m_{13}^2) &= 2.509(2.481) \times 10^{-3} eV^2/c^4 \\
 \sin^2 \theta_{23} &= 0.527(0.533) \\
 \sin^2 2\theta_{13} &= 0.0967(0.0984) \\
 \delta_{CP} &= -1.554(-1.556)
 \end{aligned} \tag{7.3}$$

By constraining $\sin^2 \theta_{13}$ to the reactor value, the T2K joint 3-flavour oscillation analysis led to a first measurement of the δ_{CP} phase: its best-fit value is consistent with $-\pi/2$ and the following values are excluded at the 90% CL (calculated using Feldman-Cousins)

$$\begin{aligned}
 [0.146, 0.825] \pi &\text{ for normal hierarchy} \\
 [-0.080, 1.091] \pi &\text{ for inverted hierarchy}
 \end{aligned}$$

Further T2K data collection and improvements on this joint 3-flavour oscillation analysis will provide more precise, world leading measurements of the four oscillation parameters, and will make possible other non standard physics studies.

Bibliography

- [1] K. Abe et al. (The T2K Collaboration), Indication of Electron Neutrino Appearance from an Accelerator-produced Off-axis Muon Neutrino Beam, Phys. Rev. Lett. 107, 041801 (2011) arXiv:1106.2822 [hep-ex]
- [2] K. Abe et al. (The T2K Collaboration), Evidence of Electron Neutrino Appearance in a Muon Neutrino Beam, Phys. Rev. D 88, 032002 (2013) arXiv:1304.0841 [hep-ex]
- [3] K. Abe et al. (The T2K Collaboration), First Muon Neutrino Disappearance Study with an Off-axis Beam, Phys. Rev. D 85, 031103 (2012) arXiv:1201.1386 [hep-ex]
- [4] K. Abe et al. (The T2K Collaboration), Measurement of Neutrino Oscillation Parameters from Muon Neutrino Disappearance with an Off-Axis Beam, Phys. Rev. Lett. 111, 211803 (2013) arXiv: 1308.0465 [hep-ex]
- [5] K. Abe et al. (The T2K Collaboration), Observation of Electron Neutrino Appearance in a Muon Neutrino Beam, Phys. Rev. Lett. 112, 061802 (2014) arXiv:1311.4750 [hep-ex]
- [6] K. Abe et al. (The T2K Collaboration), Precise Measurement of the Neutrino Mixing Parameter θ_{23} from Muon Neutrino Disappearance in an Off-axis Beam, Phys. Rev. Lett. 112, 181801 (2014) arXiv:1403.1532 [hep-ex]
- [7] J.J. Gómez-Cadenas, Neutrino Physics Lectures, CERN Summer School, 2008
- [8] H. Becquerel, Sur les radiations émises par phosphorescence, Comptes Rendus 122: 420421 (1896)
- [9] J. Chadwick, Intensitätsverteilung im magnetischen Spektrum der β -Strahlen von Radium B+C, Verhandlungen der Deutschen Physikalischen Gesellschaft, 16, p. 383-91, 1914
- [10] J. Chadwick, Possible existence of a neutron, Nature, 129, p. 312, 1932
- [11] E. Fermi, Tentativo di una teoria dell'emissione dei raggi β , La Ricerca Scientifica, 4, p. 491-5, 1933.
- [12] W. Heisenberg, Über den Bau der Atomkerne, Zeitschrift für Physik, 77, p. 1-11, 1932
- [13] D. Iwanenko, Sur la constitution des noyaux atomiques, Comptes Rendues des Séances de L' Académie des Sciences, 195, p. 439-41, 1932
- [14] G. Gamow and E. Teller, Selectrion rules for the β -disintegration, Phys. Rev., 49:895, 1936.
- [15] H. Bethe and R. Peierls, The "neutrino", Nature, 133, p. 532, 1934.

Bibliography

- [16] C. L. Cowan Jr., F. Reines, et al., Detection of the Free Neutrino: a Confirmation, *Science*, 124:103-104, 1956
- [17] R. Davis Jr., An Attempt to Detect the Anti-Neutrinos from a Nuclear Reactor by the $Cl^{37}(n,e^-)Ar^{37}$ Reaction, *Phys. Rev.* 97, 766 (1955)
- [18] E. Majorana, Symmetrical theory of the electron and the positron, *Nuovo Cim.* 5, 171-184 (1937)
- [19] G. Danby et al., Observation of high-energy neutrino reactions and the existence of two kinds of neutrinos, *Phys. Rev. Lett.*, 9(1):36-44, 1962.
- [20] K. Kodama et al. (DONUT Collaboration), Observation of tau neutrino interactions, *Phys. Lett. B*, 504(218), 2001.
- [21] R. J. Davis et al., Search for Neutrinos from the Sun, *Phys. Rev. Lett.*, 20(1205), 1968
- [22] J.N. Bahcall, W. A. Fowler, I. Iben, R. L. Sears, Solar Neutrino Flux, *ApJ*, 137, 344 1963
- [23] W. Hample et. al. (GALLEX Collaboration), Final Results of the Cr^{51} Neutrino Source Experiments in GALLEX, *Phys. Lett. B*, 420:114126, 1998
- [24] K. S. Hirata et al. (KAMIOKANDE II Collaboration), Observation of B-8 solar neutrinos in the Kamiokande-II detector, *Phys. Rev. Lett.* 63 16, 1989
- [25] Q.R. Ahmad et al. (The SNO Collaboration), Measurement of the Rate of $\nu_e + d \rightarrow p + p + e^-$ Interactions Produced by 8B Solar Neutrinos at the Sudbury Neutrino Observatory, *Phys. Rev. Lett.*, 87(071301), 2001.
- [26] B. Pontecorvo, Neutrino Experiments and the Problem of Conservation of Leptonic Charge, *Sov. Phys. JETP* 26, 984 (1968)
- [27] Y. Fukuda, et al. (The SK Collaboration), Evidence for Oscillation of Atmospheric Neutrinos, *Phys. Rev. Lett.* 81 (1998) 1562.
- [28] S. L. Glashow, *Nucl. Phys.* 22, 579 (1961)
- [29] S. Weinberg, *Phys. Rev. Lett.* 19, 1264 (1967)
- [30] A. Salam, Weak and Electromagnetic Interactions, Elementary Particle Theory, Proc. 8th Nobel Symp., 367 (1968)
- [31] M.C. González-García, Neutrino Physics, arXiv:0901.2505 [hep-ph]
- [32] M.C. González-García and M. Maltoni, Phenomenology with Massive Neutrinos, arXiv:0704.1800 [hep-ph]
- [33] P. Hernández, Neutrino Physics (Lectures), arXiv:1010.4131 [hep-ph]
- [34] C. Amslet et. al., *Phys. Lett.* B667 (2008)
- [35] H. Weyl, Electron and gravitation, *Z. Phys.* 56, 330-352, 1929
- [36] Ch. Kraus, B. Bornschein, L. Bornschein, J. Bonn, B. Flatt, et al., Final Results from Phase II of the Mainz Neutrino Mass Search in Tritium Beta Decay, *Eur.Phys.J.* C40, 447/468 (2005). hep-ex/0412056

- [37] V.M. Lobashev, The Search for the Neutrino Mass by Direct Method in the Tritium Beta-Decay and Perspectives of Study it in the Project KATRIN, *Nucl.Phys.* A719, 153/160 (2003)
- [38] V.N. Aseev et al. (The Troitsk Collaboration), An Upper Limit on Electron Antineutrino Mass from Troitsk Experiment, *Phys.Rev.* D84, 112003 (2011). 1108.5034
- [39] G. Drexlin, V. Hennen, S. Mertens and C Weinheimer, Current Direct Neutrino Mass Experiments, arXiv:1307.0101 (2013)
- [40] J. Lesgourgues and S. Pastor, Neutrino Mass from Cosmology, arxiv::1212.6154v1 (2012)
- [41] P.A.R. Ade et al. (The Planck Collaboration), Planck 2013 Results. I. Overview of Products and Scientific Results, arXiv:1303.5062v1 (2013)
- [42] P.A.R. Ade et al. (The Planck Collaboration), Planck 2013 Results. XVI. Cosmological Parameters, arXiv:1303.5076v1 (2013)
- [43] C. Bennett et al., Nine-Year Wilkinson Microwave Anisotropy Probe (WMAP) Observations: Final Maps and Results, arXiv:1212.5225v3
- [44] G. Hinshaw et al., Nine-Year Wilkinson Microwave Anisotropy Probe (WMAP) Observations: Cosmological Parameter Results, arXiv:1212.5226v3
- [45] Particle Data Group, Review of Cosmological Parameters, <http://pdg.lbl.gov/2014/reviews/rpp2014-rev-cosmological-parameters.pdf>
- [46] C. Giunti and C.W. Kim, Fundamentals of Neutrino Physics and Astrophysics, Oxford University Press
- [47] A. Zee, A Theory of Lepton Number Violation, Neutrino Majorana Mass, and Oscillation, *Phys. Lett.* B93, 389 (1980)
- [48] K. S. Babu, Model of "Calculable" Majorana Neutrino Masses, *Phys. Lett.* B203, 132 (1988)
- [49] M. Hirsch and J. W. F. Valle, Supersymmetric Origin of Neutrino Mass, *New J. Phys.* 6, 76 (2004), [hep-ph/0405015]
- [50] M. Hirsch et al., Neutrino Masses and Mixings from Supersymmetry with Bilinear R-Parity Violation: A Theory for Solar and Atmospheric Neutrino Oscillations, *Phys. Rev.* D62, 113008 (2000), [hep-ph/0004115]
- [51] Z. Maki, M. Nakagawa and S. Sakata, Remarks on the Unified Model of Elementary Particles, *Prog. Theor. Phys.* 28 870, 1962
- [52] H. J. Lipkin, Quantum Theory of Neutrino Oscillations for Pedestrians - Simple Answer to Confusing Questions, arXiv: hep-ph/0505141v4, 2006
- [53] G.L.Fogli, E.Lisi et al., Evidence of Theta(13)>0 from Global Neutrino Data Analysis, arXiv:1106.6028 [hep-ph]
- [54] V. Barger, D. Marfatia and K. Whisnant, Breaking Eightfold Degeneracies in Neutrino CP Violation, Mixing, and Mass Hierarchy, *Phys.Rev.* D65 (2002), p. 073023. doi:10.1103/PhysRevD.65.073023

Bibliography

- [55] J. Burguet Castell et al., On the Measurement of Leptonic CP Violation, Nucl. Phys. B, 608, 3001-3008 (2001)
- [56] H. Minakata and H. Nunokawa, Exploring Neutrino Mixing with Low Energy Super-beams, JHEP 0110 (2001)
- [57] L. Wolfenstein, Neutrino Oscillations in Matter, Phys. Rev. D17 (1978) 2369
- [58] B. Kayser, Neutrino Physics, hep-ph 0506165 (2005)
- [59] H. Nunokawa, S. Parke and J.W.F. Valle, CP Violations and Neutrino Oscillations, arXiv: hepph/0710.0554v2, 2008
- [60] A. Cervera et al., Golden Measurements at a Neutrino Factory, Nucl. Phys. B579, 17 (2000), [hep-ph/0002108]
- [61] S.P. Mikheyev and A.YU. Smirnov, Resonant Amplification of Neutrino Oscillations in Matter and Spectroscopy of Solar Neutrinos, Sov. J. Nucl. Phys., 42(913), 1985
- [62] G.L. Fogli, E. Lisi, A. Marrone, D. Montanino, A. Palazzo, et al., Global analysis of neutrino masses, mixings and phases: entering the era of leptonic CP violation searches, Phys.Rev. D86, 013012 1205.5254 (2012)
- [63] F. Capozzi, G.L. Fogli, E. Lisi, A. Marrone, D. Montanino and A. Palazzo, Status of Three-neutrino Oscillation Parameters, circa 2013, arXiv:1312.2878v2 [hep-ph], (2014)
- [64] A. de Gouv  a et al., Neutrinos, arXiv:1310.4340 [hep-ex]
- [65] A. de Gouv  a and H. Murayama, Neutrino Mixing Anarchy: Alive and Kicking, arXiv: hep-ph/1204.1249v1, 2012
- [66] L. J. Hall, H. Murayama and N. Weiner, Neutrino Mass Anarchy, Phys. Rev. Lett. 84, 2572, 2000
- [67] N. Haba and H. Murayama, Anarchy and Hierarchy, Phys. Rev. D 63, 053010, 2001
- [68] C. H. Albright and M-C Chen, Model Predictions for Neutrino Oscillation Parameters, arXiv: hep-ph/0608137v3, 2006
- [69] P. F. Harrison, D. H. Perkins and W. G. Scott, Tri-Bimaximal Mixing and the Neutrino Oscillation Data, Phys. Lett. B 530 (2002) 167
- [70] E. Ma and G. Rajasekaran, Softly Broken A_4 Symmetry for Nearly Degenerate Neutrino Masses, Phys.Rev. D 64, 113012 (2001)
- [71] A. de Gouv  a, Deviation of Atmospheric Mixing from Maximal and Structure in the Leptonic Flavour Sector, Phys. Rev. D 69, 093007, 2004
- [72] H. Georgi and S.L. Glashow, Unity of All Elementary-Particle Forces, Phys. Rev. Lett. 32, 438 (1974)
- [73] K.S. Babu and R.N. Mohapatra, Predictive Neutrino Spectrum in Minimal SO(10) Grand Unification, Phys. Rev. Lett. 70, 2845 (1993)
- [74] C.H. Albright, K.S. Babu, and S.M. Barr, A Minimality Condition and Atmospheric Neutrino Oscillations, Phys. Rev. Lett. 81, 1167 (1998)

- [75] A. Strumia and F. Vissani, Neutrino Masses and Mixing and..., arXiv: hep-ph/0606054v3, 2010
- [76] Particle Data Group, <http://pdg.lbl.gov/2013/tables/rpp2013-rev-neutrino-mixing.pdf>
- [77] W. Buchmuller, R. Peccei, and T. Yanagida, Leptogenesis as the Origin of Matter, arXiv:hep-ph/0502169 (2005)
- [78] A. Aguilar et al. (The LSND Collaboration), Evidence for Neutrino Oscillations from the Observation of $\bar{\nu}_e$ Appearance in a $\bar{\nu}_\mu$ Beam, Phys. Rev. D64 (2001) 112007, arXiv:hep-ex/0104049
- [79] K. Abe et al. (The T2K Collaboration), Search for Short Baseline ν_e Disappearance with the T2K Near Detector, <http://arxiv.org/abs/1410.8811>
- [80] P. Adamson et al. (The MINOS Collaboration), Active to Sterile Neutrino Mixing Limits from Neutral-Current Interactions in MINOS, arXiv:hep-ex/1104.3922v1 (2011)
- [81] K. N. Abazajian et al., Light Sterile Neutrinos: a White Paper, arXiv:hep-ph/1204.5379v1 (2012)
- [82] K. Abe et al. (The T2K Collaboration), The T2K Experiment, Nucl. Instrum. Meth. A (NIMA) DOI number: 10.1016/j.nima.2011.06.067 (2011) arXiv:1106.1238
- [83] K. Abe et al. (The T2K Collaboration), The T2K Neutrino Flux Prediction, Phys. Rev. D 87, 012001 (2013)
- [84] D. Beavis et al., Proposal of BNL AGS E-889, (1995)
- [85] L. Escudero (for the T2K Collaboration), Initial Probe of δ_{CP} by the T2K Experiment with ν_μ Disappearance and ν_e Appearance, Nuclear Physics B - ICHEP 2014 Proceedings (submitted)
- [86] Particle Data Group, <http://pdg.lbl.gov/2013/tables/rpp2013-sum-leptons.pdf>
- [87] K. Abe et al. (The T2K Collaboration), Measurement of the Inclusive Muon Neutrino Charged Current Cross Section on Carbon in the Near Detector of the T2K Experiment, Phys. Rev. D 87. 092003 (2013) arXiv:1302.4908 [hep-ex]
- [88] J-PARC TDR, KEK-Report 2002-13 and JAERI-Tech 2003-044, <http://hadron.kek.jp/accelerator/TDA/tdr2003/index2.html> (2003)
- [89] J-PARC Symposium, http://j-parc.jp/symposium/j-parc2014/abstract_book/July13-PM2/AS-13-PM2/AS-13-PM2-3_Saha_Pranab.pdf
- [90] C. Giganti (for the T2K Collaboration), T2K Experiment: Status and Initial Look at the Data, 22nd Rencontres de Blois, July 17th 2010 (talk)
- [91] K. Abe et al. (The T2K Collaboration), Measurements of the T2K Neutrino Beam Properties Using the INGRID On-Axis Near Detector, Nucl. Instrum. And Meth. A (NIMA) DOI number: 10.1016/j.nima.2012.03.023 (2012) arXiv:1111.3119 [hep-ex]
- [92] S. Aoki et al. (The T2K SMRD Collaboration), The T2K Side Muon Range Detector (SMRD), Nucl. Instrum. And Meth. A (NIMA) DOI number: 10.1016/j.nima.2012.10.001 (2012)

Bibliography

- [93] T. Yuan for the T2K Collaboration, Measuring the ν_μ Charged Current Quasielastic Cross Section on Water using T2K's Near Detector, Neutrino2014, poster
- [94] S. Assylbekov et al. (The T2K PØD Collaboration), The T2K ND280 Off-Axis Pi-Zero Detector, Nucl. Instrum. And Meth. A (NIMA) DOI number: 10.1016/j.nima.2012.05.028 (2012)
- [95] N. Abgrall et al. (The T2K TPC Collaboration), Time Projection Chambers for the T2K Near Detectors, Nucl. Instrum. And Meth. A (NIMA) DOI number: 10.1016/j.nima.2011.02.036 (2011)
- [96] I. Giomataris, et al., Micromegas in a Bulk, Nucl. Instrum. And Meth. A (NIMA) DOI number: 10.1016/j.nima.2005.12.222 (2006)
- [97] L. Escudero, A. Cervera, P. Stamoulis, L. Monfregola, Calibration and Performance of the T2K Time Projection Chambers, Proceedings of NeuTel (Neutrino Telescopes) 2011
- [98] L. Escudero, A. Cervera, P. Stamoulis, L. Monfregola, Calibration and Performance of the T2K Time Projection Chambers, Reunin Bienal de la Real Sociedad Espaola de Fsica 2011 (Proceedings): ISBN: 978-84-86116-41-5 (Fsica de Altas Energias. Fsica Terica. Fsica Nuclear.)
- [99] D. G. Brook-Roberge, Measurements of Neutrino Interactions on Water using a Fine-Grained Scintillator Detector with Water Targets, Thesis Dissertation
- [100] P.-A. Amaudruz et al. (The T2K FGD Collaboration), The T2K Fine-Grained Detectors, Nucl. Instrum. And Meth. A (NIMA) DOI number: 10.1016/j.nima.2012.08.020 (2012)
- [101] J. Kim, Michel Electrons Analysis in the Fine-Grained Detectors for T2K, B.Sc Thesis
- [102] Y. Fukuda, T. Hayakawa, E. Ichihara, M. Ishitsuka, Y. Itow, et al. (The SK Collaboration), The Super-Kamiokande Detector, Nucl. Instrum. And Meth. A (NIMA) DOI number: 10.1016/S0168-9002(2003)00425-X
- [103] Y. Fukuda, et al. (The SK Collaboration), Measurements of the Solar Neutrino Flux from Super-Kamiokande's First 300 Days, Phys. Rev. Lett. 81 (1998) 1158.
- [104] M. H. Ahn et al. (The K2K Collaboration), Measurement of Neutrino Oscillation by the K2K Experiment, Phys.Rev. D 74 (2006) 072003
- [105] M. Shiozawa, et al., Search for Proton Decay via $p \rightarrow e^+ \pi^0$ in a Large Water Cherenkov Detector, Phys. Rev. Lett. 81 (1998) 3319
- [106] Y. Hayato, et al., Search for Proton Decay through $p \rightarrow \bar{\nu} K^+$ in a Large Water Cherenkov Detector, Phys. Rev. Lett. 83 (1999) 1529
- [107] K. Scholberg, Super-K Monte Carlo: Detector Simulation, http://phy.duke.edu/~schol/sk_intro/sk_mc1.html
- [108] Y. Ashie et al. (The Super-Kamiokande collaboration), A Measurement of Atmospheric Neutrino Oscillation Parameters by Super-Kamiokande I, Phys. Rev. D 71, 112005 (2005)

- [109] M. Shiozawa (for the Super-Kamiokande collaboration), Reconstruction Algorithms in the Super-Kamiokande Large Water Cherenkov Detector, NIM A 433 (1999) 240-246
- [110] J. B. Albert, Indication of Electron Neutrino Appearance in an Accelerator-Produced Muon Neutrino Beam, Thesis Dissertation
- [111] E. Davies, Machine Vision : Theory, Algorithms, Practicalities, Academic Press, San Diego, 1997
- [112] S. Kasuga et al., A Study on the e/μ Identification Capability of a Water Čerenkov Detector and the Atmospheric Neutrino Problem, Phys. Lett. B374, 238 (1996)
- [113] L. K. Pick, Thesis Dissertation
- [114] R. B. Patterson et al., The Extended-Track Event Reconstruction for MiniBooNE, Nucl.Instrum.Meth. A608, 206 (2009)
- [115] S. Tobayama (for the T2K and SK collaborations), fitQun: A New Event Reconstruction Algorithm for Super-Kamiokande, Poster at NNN13 (International Workshop on Next generation Nucleon Decay and Neutrino Detectors 2013)
- [116] S. Tobayama (for the T2K and SK collaborations), New Event Reconstruction Algorithm for Super-Kamiokande Water Cherenkov Detector, Talk at WNPPC 2012 (49th Winter Nuclear and Particle Physics Conference 2012)
- [117] A.K. Ichikawa, Design Concept of the Magnetic Horn System for the T2K Neutrino Beam, Nucl. Instrum. And Meth. A (NIMA) DOI number: 10.1016/j.nima.2012.06.045 (2012)
- [118] A. Ferrari, P. R. Sala, A. Fasso and J. Ranft, CERN-2005-010, SLAC-R-773, INFN-TC-05-11
- [119] R. Brun, F. Carminati and S. Giani, CERN-W5013 (1994)
- [120] M. Chung, Twiss Parameters and Beam Matrix Formulation of Generalized Courant-Snyder Theory for Coupled Transverse Beam Dynamics, Fermilab Communication 2010
- [121] S. Bhadra et al., Optical Transition Radiation Monitor for the T2K Experiment, arXiv:1201.1922 [physics.ins-det]
- [122] C. Zeitnitz and T. A. Gabriel, Proc. of International Conference in High Energy Physics (1993)
- [123] N. Abgrall et al. (NA61/SHINE Collaboration), Measurements of Cross Sections and Charged Pion Spectra in Proton-Carbon Interactions at 31 GeV/c, Phys. Rev. C 84 (2011) 034604
- [124] N. Abgrall et al. (NA61/SHINE Collaboration), Measurement of Production Properties of Positively Charged Kaons in Proton-Carbon Interactions at 31 GeV/c, Phys. Rev. C 85 (2012) 035210
- [125] T. Eichten et al., Particle Production in Proton Interactions in Nuclei at 24 GeV/c, Nucl. Phys. B 44 (1972)

Bibliography

- [126] J. V. Allaby et al., High-energy Particle Spectra from Proton Interactions at 19.2 GeV/c, Tech. Rep. 70-12 (CERN, 1970)
- [127] I. Chemakin et al., Pion Production by Protons on a Thin Beryllium Target at 6.4, 12.3, and 17.5 GeV/c Incident Proton Momenta, Phys. Rev. C 77 (2008) 015209
- [128] Y. Hayato, A Neutrino Interaction Simulation Program Library NEUT, Acta Phys. Pol. B 40, 2477 (2009)
- [129] C. Andreopoulos et al., The GENIE Neutrino Monte Carlo Generator, Nucl. Instrum. Methods Phys. Res., Sec. A 614, 87 (2010), arXiv:0905.2517 [hep-ph].
- [130] C. H. Llewellyn Smith, Neutrino Reactions at Accelerator Energies, Phys. Rept. 3, 261 (1972)
- [131] J. Kameda, Review of NEUT, 5th RCCN International Workshop on Sub-dominant Oscillation Effects in Atmospheric Neutrino Experiments p.131-141 Proceedings
- [132] R. Smith and E. Moniz, Neutrino Reactions on Nuclear Targets, Nucl. Phys. B 43, 605 (1972)
- [133] R. Smith and E. Moniz, Neutrino Reactions on Nuclear Targets, Nucl. Phys. B 101, 547 (1975)
- [134] O. Benhar, The Nucleon Spectral Function in Nuclear Matter, Nuclear Physics A, 505, 2, Pages 267-299 (1989)
- [135] O.Benhar, A. Fabrocini, S. Fantoni and I. Sick, Spectral Function of Finite Nuclei and Scattering of GeV Electrons, Nucl. Phys. A. 579, 493-517 (1994).
- [136] D. Rein and L. M. Sehgal, Neutrino-Excitation of Baryon Resonances and Single Pion Production, Annals Phys. 133, 79 (1981)
- [137] D. Rein and L. M. Sehgal, Coherent π^0 Production in Neutrino Reactions, Nuclear Physics B 233 (1983) 29
- [138] D. Scully, Neutrino Induced Coherent Pion Production, Thesis dissertation
- [139] M. Glück, E. Reya, and A. Vogt, Dynamical Parton Distributions Revisited, Eur. Phys. J. C 5, 461 (1998)
- [140] M. Nakahata et al. (Kamiokande Collaboration), Atmospheric Neutrino Background and Pion Nuclear Effect for KAMIOKA Nucleon Decay Experiment, J. Phys. Soc. Japan 55, 3786 (1986)
- [141] T. Sjostrand, High-Energy-Physics Event Generation with PYTHIA 5.7 and JETSET 7.4, Comput. Phys. Commun. 82, 74 (1994)
- [142] A. Bodek and U. Yang, Higher Twist, ξ_W Scaling, and Effective LOPDFs for Lepton Scattering in the Few GeV Region, Nucl. Phys. Proc. Suppl. (2003)
- [143] P. de Perio, NEUT Pion FSI, AIP Conf.Proc. 1405, 223 (2011)
- [144] L. Salcedo, E. Oset, M. Vicente-Vacas, and C. Garcia-Recio, Computer Simulation of Inclusive Pion Nuclear Reactions, Nucl. Phys. A 484, 557 (1988)

- [145] S. Agostinelli et al., GEANT4 - a Simulation Toolkit, Nuclear Instruments and Methods in Physics Research A 506 (2003) 250-303
- [146] V.V.Borog and A.A.Petrukhin, Proc. 14th Int.Conf. on Cosmic Rays, Munich,1975, vol.6, p.1949.
- [147] L.B Bezrukov and E.V.Bugaev, Sov. J. Nucl. Phys., 33, 1981, p.635.
- [148] A. A. Aguilar-Arevalo et al. (MiniBooNE Collaboration), First Measurement of the Muon Neutrino Charged Current Quasi-Elastic Double Differential Cross Section, Phys. Rev. D 81, 092005 (2010)
- [149] V. Lyubushkin et al. (NOMAD Collaboration), A Study of Quasi-Elastic Muon Neutrino and Antineutrino Scattering in the NOMAD Experiment, Eur.Phys. J. C 63, 355 (2009)
- [150] E. Moniz, I. Sick, R. Whitney, J. Ficenec, R. D. Kephart, et al., Nuclear Fermi Momenta from Quasi-Elastic Electron Scattering, Phys. Rev. Lett. 26, 445 (1971)
- [151] A. M. Ankowski and J. T. Sobczyk, Argon Spectral Function and Neutrino Interactions, Phys. Rev. C 74, 054316 (2006)
- [152] M. Derrick et al., Study of Single-Pion Production by Weak Neutral Currents in Low-Energy νd Interactions, Phys. Lett. B 92, 363 (1980)
- [153] W. Krenz et al. (Gargamelle Neutrino Propane Collaboration and Aachen-Brussels-CERN-Ecole Po), Experimental Study of Exclusive One-Pion Production in all Neutrino-Induced Neutral Current Channels, Nucl. Phys. B 135, 45 (1978).
- [154] M. Hasegawa et al. (K2K Collaboration), Search for Coherent Charged Pion Production in Neutrino-Carbon Interactions, Phys. Rev. Lett. 95, 252301 (2005), arXiv:hep-ex/0506008.
- [155] K. Hiraide et al. (SciBooNE Collaboration), Search for Charged Current Coherent Pion Production on Carbon in a Few-GeV Neutrino Beam, Phys. Rev. D 78, 112004 (2008), arXiv:0811.0369 [hep-ex]
- [156] Y. Kurimoto et al. (SciBooNE Collaboration), Improved Measurement of Neutral Current Coherent π^0 Production on Carbon in a Few-GeV Neutrino Beam, Phys. Rev. D 81, 111102 (2010), arXiv:1005.0059 [hep-ex].
- [157] P. Adamson et al. (MINOS Collaboration), Neutrino and Antineutrino Inclusive Charged-Current Cross Section Measurements with the MINOS Near Detector, Phys. Rev. D 81, 072002 (2010)
- [158] M. Day and K. S. McFarland, Differences in quasi-elastic cross sections of muon and electron neutrinos, Phys. Rev., Vol. D86, p. 053003, 2012
- [159] A.A. Aguilar-Arevalo et al. (MiniBooNE Collaboration), First Measurement of the Muon Antineutrino Double Differential Charged Current Quasi-Elastic Cross Section, Phys. Rev. D88, 032001 (2013)
- [160] L. Fields, J. Chvojka et al. (MINERvA Collaboration), Measurement of $d\sigma/dQ^2$ in Muon Anti-Neutrino Quasi-Elastic Scattering on a Hydrocarbon Target, Phys. Rev. Lett. 111, 022501 (2013)

Bibliography

- [161] C. Juszczak, J. T. Sobczyk and J. Zmuda, Extraction of the Axial Mass Parameter from MiniBooNE Neutrino Quasielastic Double Differential Cross-Section Data, Phys. Rev. C, 82, 045502 (2010)
- [162] A. A. Aguilar-Arevalo et al. (MiniBooNE Collaboration), Measurement of Neutrino-Induced Charged-Current Charged Pion Production Cross Sections on Mineral Oil at $E_\nu \sim 1\text{GeV}$, Phys. Rev. D 83, 052007 (2011)
- [163] A. A. Aguilar-Arevalo et al. (MiniBooNE Collaboration), Measurement of ν_μ -Induced Charged-Current Neutral Pion Production Cross sections on Mineral Oil at E_ν in $0.52.0??\text{GeV}$, Phys. Rev. D 83, 052009 (2011)
- [164] A. A. Aguilar-Arevalo et al. (MiniBooNE Collaboration), Measurement of ν_μ and $\bar{\nu}_\mu$ Induced Neutral Current Single π^0 Production Cross Sections on Mineral Oil at $E_\nu \sim O(1\text{ GeV})$, Phys. Rev. D 81, 013005 (2010)
- [165] S. Nakayama et al. (K2K Collaboration), Measurement of Single π^0 Production in Neutral Current Neutrino Interactions with Water by a 1.3 GeV Wide Band Muon Neutrino Beam, Phys. Lett. B 619, 255 (2005)
- [166] T. Dealtry, Controlling Neutrino Interaction Systematics: The T2K Experience, Talk at Neutrino Interactions Conference (NuInt) 2014
- [167] D. Ashery et al., True Absorption and Scattering of Pions on Nuclei, Phys. Rev. C 23, 2173 (1981)
- [168] M. K. Jones et al., Pion Absorption Above the $\Delta(1232)$ Resonance, Phys. Rev. C 48, 2800 (1993)
- [169] R. A. Giannelli et al., Multiproton Final States in Positive Pion Absorption Below the $\Delta(1232)$ Resonance, Phys. Rev. C 61, 054615 (2000)
- [170] F.James, M.Roos, MINUIT: A System for Function Minimization and Analysis of the Parameter Errors and Correlations, Comput.Phys.Commun. 10:343 (1975)
- [171] A. Cervera, Private communication
- [172] K. Ieki, Observation of $\nu_\mu \rightarrow \nu_e$ oscillation in the T2K experiment, Thesis Dissertation
- [173] J. Hignight, T2K Data Reduction at Super-Kamiokande, Lake Louise Winter Institute 2014
- [174] Y. Takeuchi, Low-Energy Neutrino Observation at Super-Kamiokande-III, Proceedings of 10th Int. Conf. on Topics in Astroparticle and Underground Physics (TAUP2007)
- [175] F. Dufour, Precise Study of the Atmospheric Neutrino Oscillation Pattern Using Super-Kamiokande I and II, PhD thesis, Boston University, <http://www-sk.icrr.u-tokyo.ac.jp/sk/pub/fdufour-thesis.pdf>, 2009.
- [176] A. Minamino (on behalf of the T2K Collaboration), New Results from T2K, KEK seminar 18/2/2014 http://seminar.kek.jp/physics/files2013/20140218_minamino.pdf
- [177] A. Kaboro (for the T2K Collaboration), Systematics for Oscillation Analyses at T2K, NuFact 2013

- [178] J. Beringer et al. (Particle Data Group), PR D86, 010001 (2012) (URL: <http://pdg.lbl.gov>)
- [179] J. Kopp, Efficient Numerical Diagonalisation of Hermitian 3x3 matrices, arXiv:physics/0610206
- [180] N. Grant, 3-Flavour Neutrino Oscillations, Institute of Physics HEPP/APP Meeting (April 2012)
- [181] G.L.Fogli, E.Lisi et al., Evidence of theta(13)>0 from global neutrino data analysis, arXiv:1106.6028 [hep-ph]
- [182] M. C. Gonzalez-Garcia, Michele Maltoni, Jordi Salvado, Thomas Schwetz, Global fit to three neutrino mixing: critical look at present precision, arXiv:1209.3023 [hep-ph]
- [183] G.Fogli's talk (pages 4,5,6) in NNN05 conference, <http://nnn05.in2p3.fr/schedule.html>
- [184] P. Adamson et al. (MINOS Collaboration), Combined Analysis of ν_μ Disappearance and $\nu_\mu \rightarrow \nu_e$ Appearance in MINOS Using Accelerator and Atmospheric Neutrinos, submitted to Phys. Rev. Lett. (2014), arXiv:1403.0867 [hep-ex].
- [185] W. C. Davidon, Variable metric method for minimization, SIAM Journal on Optimization 1: 117, doi:10.1137/0801001
- [186] G.J. Feldman and R.D. Cousins, A Unified Approach to the Classical Statistical Analysis of Small Signals, Phys.Rev.D57:3873-3889,1998; physics/9711021
- [187] A. Himmel (for the Super-Kamiokande Collaboration), Recent Atmospheric Neutrino Results from Super-Kamiokande, 7th Intl. Conf. on Interconnection between Particle Physics & Cosmology (PPC 2013) (2013), arXiv:1310.6677 [hep-ex]
- [188] K. Abe et.al. (The T2K Collaboration), Neutrino Oscillation Physics Potential of the T2K Experiment, Progress of Theoretical and Experimental Physics (submitted) arXiv:1409.7469
- [189] The NO ν A Collaboration, Proposal to Build a 30 Kiloton Off-Axis Detector to Study $\nu_\mu \rightarrow \nu_e$ Oscillations in the NuMI Beamline (NO ν A, NuMI Off-Axis ν_e Appearance Experiment), arXiv:hep-ph/0503053
- [190] P. Huber, M. Lindner, W. Winter, Simulation of Long-Baseline Neutrino Oscillation Experiments with GLoBES, arXiv:hep-ph/0407333
- [191] P. Huber, J. Kopp, M. Lindner, M. Rolinec, W. Winter, New Features in the Simulation of Neutrino Oscillation Experiments with GLoBES 3.0, arXiv:hep-ph/0407333
- [192] D. S. Ayres et al. (The NO ν A Collaboration), The NO ν A Technical Design Report, FERMILAB-DESIGN-2007-01
- [193] K. Abe et al. (The Hyper-Kamiokande Working Group), Letter of Intent: The Hyper-Kamiokande Experiment — Detector Design and Physics Potential — arXiv:1109.3262
- [194] The Hyper-Kamiokande Working Group, Hyper-Kamiokande Physics Opportunities, arXiv:1309.0184
- [195] G. L. Fogli, E. Lisi, A. Marrone, A. Palazzo, and A. M. Rotunno, Evidence of $\theta_{13} > 0$ from Global Neutrino Data Analysis, Phys.Rev. D84, 053007 (2011)

- [196] R. D. Cousins and V. L. Highland, Incorporating Systematic Uncertainties Into an Upper Limit, Nucl. Instrum. Methods A320, 331 (1992)
- [197] J. Nieves, I. R. Simo, and M. Vicente Vacas, The Nucleon Axial Mass and the Mini-BooNE Quasi-Elastic NeutrinoNucleus Scattering Problem, Phys.Lett.B 707, 72 (2012)

Appendix A

T2K Latest Results of Stand-alone Analyses

With the datasets obtained during different running periods, T2K has published several stand-alone oscillation analyses (independent ν_μ disappearance and ν_e appearance):

- Run1+2 (1.43×10^{20} POT): indication of ν_e appearance from an accelerator-produced off-axis ν_μ beam in 2011 [1] and first ν_μ disappearance study with an off-axis beam in 2012 [3].
- Run1+2+3 (3.01×10^{20} POT): evidence of ν_e appearance in a ν_μ beam in 2013 [2] and measurement of oscillation parameters from ν_μ disappearance analysis in 2013 [4].
- Run1+2+3+4 (6.57×10^{20} POT): observation of ν_e appearance in a ν_μ beam in 2014 [5] and precise measurement of the neutrino mixing parameter θ_{23} from ν_μ disappearance analysis in 2014 [6].

The latest results of ν_e appearance [5] and ν_μ disappearance [6] with Run1+2+3+4 (6.57×10^{20} POT), observing 28 ν_e and 120 ν_μ events will be summarized in this appendix.

A.1 T2K Latest Results on ν_e Appearance

The latest T2K ν_e appearance analysis [5] was performed with the combined Run1+2+3+4 dataset (6.57×10^{20} POT accumulated), in which 28 ν_e events passing the cuts described in 4.5.1 were observed. This number of events is significantly larger than the expected number of events for $\sin^2 2\theta_{13} = 0$ (4.92 events) and even larger than the expected number of events for $\sin^2 2\theta_{13} = 0.1$ (21.56 events) as detailed in Tab. A.1.

The neutrino oscillation parameters were determined by comparing the expected number of events, calculated in a 3-flavour framework, with the observed number of events, using a binned extended maximum-likelihood fit, where the likelihood is integrated over the nuisance parameters to obtain a marginalized likelihood for the parameters of interest.

	$\sin^2 2\theta_{13} = 0$	$\sin^2 2\theta_{13} = 0.1$
Total	4.92	21.56
osc. ν_e	0.40	17.30
ν_μ	0.94	0.94
$\bar{\nu}_\mu$	0.05	0.05
ν_e	3.37	3.12
$\bar{\nu}_e$	0.16	0.15

Table A.1: Expected number of ν_e events for $\sin^2 2\theta_{13} = 0$ and $\sin^2 2\theta_{13} = 0.1$ at 6.57×10^{20} POT with its breakdown according to neutrino flavour.

A total of 27 systematic parameters for the flux and correlated cross sections, uncorrelated cross sections and SK + FSI + SI + PN systematics were considered in the fit. The uncertainty on the predicted number of ν_e events for each group of systematics under the assumption of $\sin^2 2\theta_{13} = 0$ and $\sin^2 2\theta_{13} = 0.1$ is presented in Tab. A.2, expressed as RMS/mean (%).

Error source	$\sin^2 2\theta_{13} = 0$	$\sin^2 2\theta_{13} = 0.1$
Total	11.1	8.8
Flux and correlated cross sections (w/o ND280 fit)	4.8 (21.7)	2.9 (25.9)
Independent cross sections	6.8	7.5
SK+FSI+SI+PN	7.3	3.5

Table A.2: Uncertainty on the predicted number of ν_e events for each group of systematics under the assumption of $\sin^2 2\theta_{13} = 0$ and $\sin^2 2\theta_{13} = 0.1$, expressed as RMS/mean (%).

The fit was repeated twice, assuming normal and inverted mass hierarchy, fixing the following parameters: $\sin^2 \theta_{12} = 0.306$, $\Delta m_{21}^2 = 7.6 \times 10^{-5}$ (eV 2) from global neutrino fits [195], $\sin^2 \theta_{23} = 0.5$, $|\Delta m_{32}^2| = 2.4 \times 10^{-3}$ (eV 2) from the previous T2K ν_μ disappearance analysis [4] and $\delta_{CP} = 0$. The best-fit value found with its corresponding 68% confidence level (CL) for normal (inverted) hierarchy is: $\sin^2 2\theta_{13} = 0.140^{+0.038}_{-0.032}$ ($0.170^{+0.045}_{-0.037}$). Two independent analyses were performed: one using the (p_e, θ_e) distribution of ν_e candidates and an alternative one using the ν_e reconstructed energy spectrum. Figure A.1 (A.2) shows the best-fit result with normal hierarchy for the (p_e, θ_e) analysis (alternative E_ν^{rec} analysis) with the 28 observed events overlaid.

Two different methods were used to calculate the significance for a non-zero θ_{13} , both giving a significance of 7.3σ (leading to an *observation*). The first method used the difference of the log likelihood values between the best-fit value obtained for θ_{13} and the value $\theta_{13} = 0$. The second method computed the significance by generating a large ensemble of

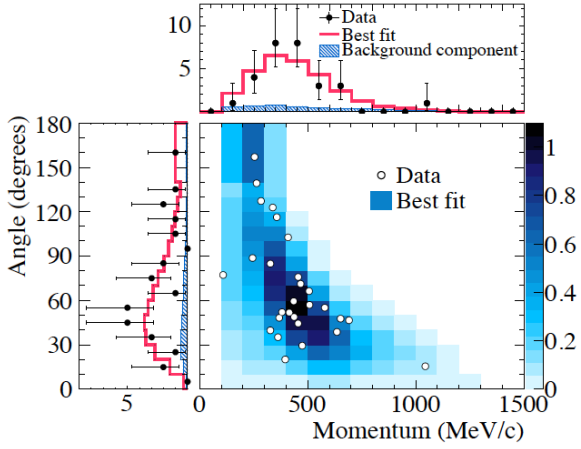


Figure A.1: Best-fit (p_e, θ_e) distribution result with normal hierarchy for the (p_e, θ_e) analysis with the 28 observed events overlaid. Figure from [5].

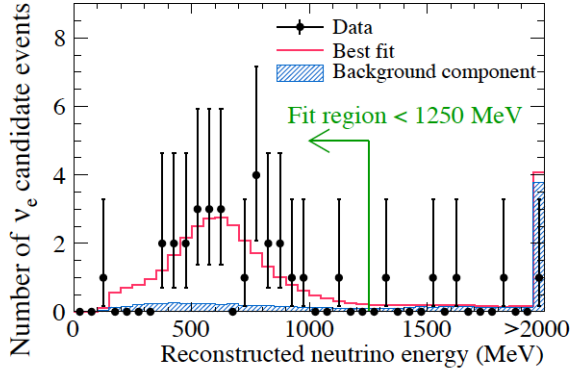


Figure A.2: Best-fit E_ν^{rec} spectrum result with normal hierarchy for the alternative E_ν^{rec} analysis with the 28 observed events overlaid. Figure from [5].

toy MC experiments assuming $\theta_{13} = 0$.

To compute the confidence regions in the $(\sin^2 2\theta_{13}, \delta_{CP})$ parameter space, the uncertainties on θ_{23} and Δm_{32}^2 were also taken into account by adding a term to the likelihood, L_{const} , which is the likelihood as a function of $(\sin^2 \theta_{23}, |\Delta m_{32}^2|)$ obtained from the previous T2K ν_μ disappearance analysis [4], and marginalizing the likelihood over $\sin^2 \theta_{23}$ and

$|\Delta m_{32}^2|$. The hierarchy was assumed a priori and $\sin^2 2\theta_{13}$ was fitted using a *raster scan* method in which the best-fit value of $\sin^2 2\theta_{13}$ was found for fixed values of δ_{CP} for each bin of this parameter. The results for the 68% and 90% CL regions in the $(\sin^2 2\theta_{13}, \delta_{CP})$ parameter space using *raster scan* and marginalizing over $\sin^2 \theta_{23}$ and $|\Delta m_{32}^2|$ are presented in Fig. A.3 for normal hierarchy (top plot) and inverted hierarchy (bottom). The best-fit value obtained from this result at $\delta_{CP} = 0$ is $\sin^2 2\theta_{13} = 0.136^{+0.044}_{-0.033}$ ($0.166^{+0.051}_{-0.042}$), which is very close to the best-fit value obtained fixing $\sin^2 \theta_{23}$ and $|\Delta m_{32}^2|$.

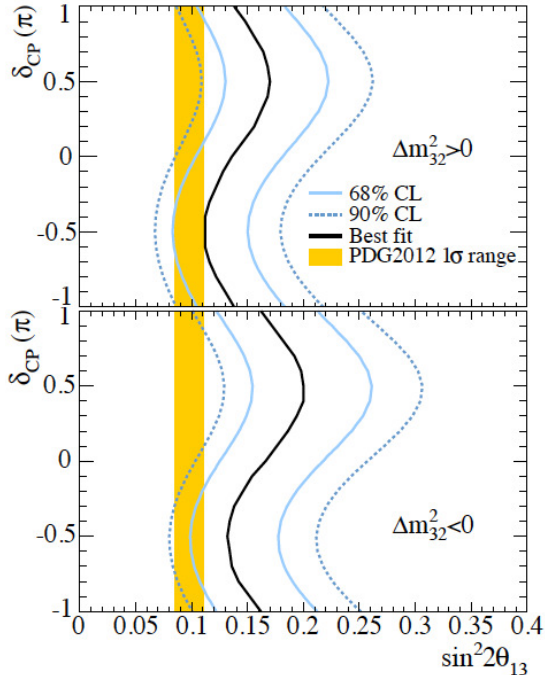


Figure A.3: The 68% and 90% CL regions in the $(\sin^2 2\theta_{13}, \delta_{CP})$ parameter space using the *raster scan* method and marginalizing $\sin^2 \theta_{23}$ and $|\Delta m_{32}^2|$ for normal hierarchy (top plot) and inverted hierarchy (bottom). The solid black line represents the best-fit $\sin^2 2\theta_{13}$ value for given δ_{CP} values. The shaded region shows the averaged $\sin^2 2\theta_{13}$ value from [178]. Figure from [5].

Combining the results of the measurement of θ_{13} by experiments using antineutrinos from nuclear reactors with the T2K data, CP violation, which has yet to be observed in the lepton sector, can be explored, and constraints on δ_{CP} value were obtained. The addition of the reactor constraint was done by adding the likelihood term defined as $\exp[-(\sin^2 2\theta_{13} - 0.098)^2 / 2(0.013)^2]$ where the mean and error values in this term are the averaged values obtained from PGD2012

[178]. The $-2\Delta \ln L$ distribution as a function of δ_{CP} result of the T2K ν_e appearance combined with the reactor constraint is presented in Fig. A.4, showing that the preferred value (with minimum χ^2) is $\delta_{CP} = -\pi/2$. The 90% CL limits shown in Fig. A.4 were obtained using the Feldman-Cousins method [186] and the exclusion regions obtained are $[0.19\pi, 0.80\pi]$ ($[-\pi, -0.97\pi] \cup [-0.04\pi, \pi]$) for normal (inverted) hierarchy.

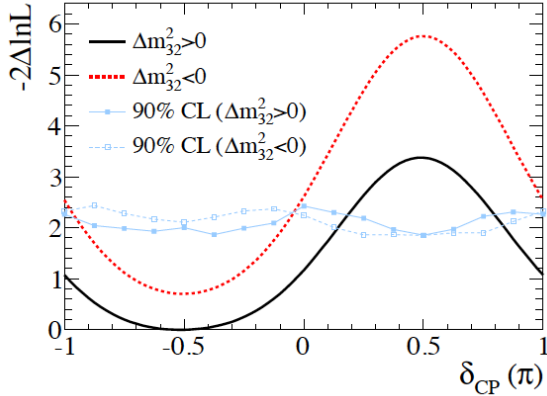


Figure A.4: The $-2\Delta \ln L$ distribution as a function of δ_{CP} result of the T2K ν_e appearance combined with the reactor constraint, showing that the preferred value (with minimum χ^2) is $\delta_{CP} = -\pi/2$. The 90% CL limits shown were obtained using the Feldman-Cousins method [186]. Figure from [5].

A.2 T2K Latest Results of ν_μ Disappearance

The latest T2K ν_μ disappearance analysis [6] was performed with the combined Run1+2+3+4 dataset (6.57×10^{20} POT accumulated), in which 120 ν_μ events passing the cuts described in 4.5.1 were observed. With this analysis, T2K has obtained the most precise measurement to date of the neutrino mixing angle θ_{23} .

The oscillation parameters were determined by comparing the reconstructed energy spectra of the 120 observed events at SK and the expected events, calculated in a 3-flavour framework, depending on the oscillation parameters and based on the flux simulation, neutrino interaction models and detector response explained in previous chapters. Table A.3 shows the predicted number of events for different neutrino interaction modes for the usual values of the oscillation parameters $\sin^2 \theta_{23} = 0.5$ and $|\Delta m^2_{32}| = 2.4 \times 10^{-3} \text{ eV}^2/\text{c}^4$.

In this analysis, the calculation of the oscillation parameters was performed using an unbinned maximum likelihood fit to the SK expected spectrum, with 73 reconstructed energy bins with unequal width, and interpolating the spectrum between bins. An alternative analysis was performed using a binned likelihood ratio method, with consistent results. The

Interaction mode	Number of events
Total	125.85
ν_μ CCQE	77.93
ν_μ CCnQE	40.78
ν_e CC	0.35
NC	6.78

Table A.3: Expected number of ν_μ events for $\sin^2 \theta_{23} = 0.5$ and $|\Delta m_{32}^2| = 2.4 \times 10^{-3}$ eV $^2/c^4$ at 6.57×10^{20} POT for different neutrino interaction modes.

oscillation probabilities were calculated using a full 3-flavour oscillation framework including matter effects and assuming a constant Earth density of $\rho = 2.6$ g/cm 3 . The oscillation parameters fitted were $\sin^2 \theta_{23}$, Δm_{32}^2 (Δm_{13}^2) for the normal (inverted) mass hierarchy assumption; regarding the other oscillation parameters, δ_{CP} was unconstrained in the range $[-\pi, \pi]$ and the rest were fitted with constraints from [86]: $\sin^2 \theta_{13} = 0.0251 \pm 0.0035$, $\sin^2 \theta_{12} = 0.312 \pm 0.016$, $\Delta m_{21}^2 = (7.50 \pm 0.20) \times 10^{-5}$ eV $^2/c^4$. A total of 45 systematic nuisance parameters were also included in the fit to account for the uncertainties in the flux and correlated cross section parameters, independent cross section parameters and SK detector efficiencies and FSI and SI. The uncertainty on the predicted number of ν_μ events for each systematic errors category, and the 1σ effect of the other oscillation parameters, under the assumption of $\sin^2 \theta_{23} = 0.5$ and $|\Delta m_{32}^2| = 2.4 \times 10^{-3}$ eV $^2/c^4$ is presented in Tab. A.4, expressed in terms of RMS/mean (%).

Error source	$\delta n_{SK}^{exp}/n_{SK}^{exp}$ (%)
Total	8.1
Flux and correlated cross sections	2.7
Independent cross sections	4.9
SK+FSI+SI+PN	5.6
δ_{CP} , $\sin^2 \theta_{13}$, $\sin^2 \theta_{12}$ and Δm_{21}^2	0.2

Table A.4: Uncertainty on the predicted number of ν_μ events for each systematic errors category, and the 1σ effect of the other oscillation parameters, under the assumption of $\sin^2 \theta_{23} = 0.5$ and $|\Delta m_{32}^2| = 2.4 \times 10^{-3}$ eV $^2/c^4$, expressed in terms of RMS/mean (%).

Figure A.5 shows the best-fit reconstructed energy spectrum for the ν_μ event candidates at SK, with its breakdown in different neutrino interaction modes and overlaying the spectrum of observed events. The bottom plot in Fig. A.5 shows the ratio to no oscillations for the observed spectrum (points) and the best-fit spectrum (solid line).

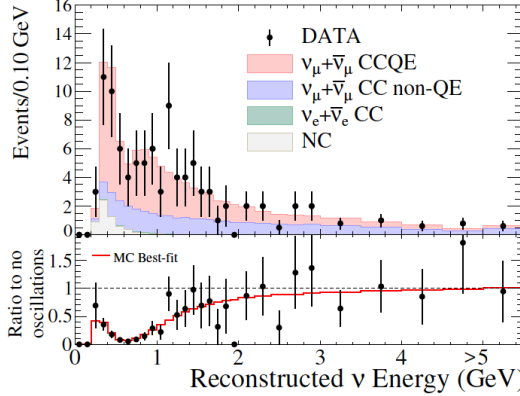


Figure A.5: Best-fit reconstructed energy spectrum for the single ring μ -like events at SK, with its breakdown in different neutrino interaction modes and overlaying the spectrum of observed events. The bottom plot in Fig. A.5 shows the ratio to no oscillations for the observed spectrum (points) and the best-fit spectrum (solid line). Figure from [6].

To construct the confidence regions in the $(\sin^2 \theta_{23}, \Delta m_{32}^2)$ or (Δm_{13}^2) parameter space, the Feldman-Cousins method [186] was used, incorporating systematic parameters with the Cousins-Highland method [196]. Figure A.6 presents the 68% (dashed lines) and 90% (solid lines) C.L. regions of the $(\sin^2 \theta_{23}, \Delta m_{32}^2)$ or (Δm_{13}^2) oscillation parameters result of the latest T2K ν_μ disappearance fit with both the normal (black) and inverted (red) mass hierarchy assumptions. Results of the 90% C.L. regions with normal hierarchy from the SK [187] and MINOS [184] latest analyses were overlaid for comparison in Fig. A.6. The one dimensional limits were calculated based on Feldman-Cousins and Cousins-Highland methods, marginalizing over the second oscillation parameter in each case. For instance, for each value of $\sin^2 \theta_{23}$, toy experiments were created with values of Δm_{32}^2 or Δm_{13}^2 according to the likelihood for the fixed $\sin^2 \theta_{23}$, marginalizing over systematic parameters, and those toy experiments were used to calculate $-2\Delta \ln L_{critical}$; and similarly for $\Delta m_{32}^2/\Delta m_{13}^2$. The 1D profile likelihoods for both mass hierarchies and the $-2\Delta \ln L_{critical}$ MC estimates for NH using this method are included in Fig. A.6 at the top and right plots.

The best-fit values of the oscillation parameters measured in the latest T2K ν_μ disappearance analysis, including the 68% intervals obtained with the method to calculate 1D limits described above are: $\sin^2 \theta_{23} = 0.514^{+0.055}_{-0.056}$ ($\sin^2 \theta_{23} = 0.511 \pm 0.055$) and $\Delta m_{32}^2 = 2.51 \pm 0.10$ ($\Delta m_{13}^2 = 2.48 \pm 0.10 \times 10^{-3} \text{ eV}^2/\text{c}^4$) for normal (inverted) mass hierarchy. The best-fit value of $\sin^2 \theta_{23}$ corresponds to maximal disappearance for the 3-flavour formula with $\sin^2 \theta_{13} = 0.0251$.

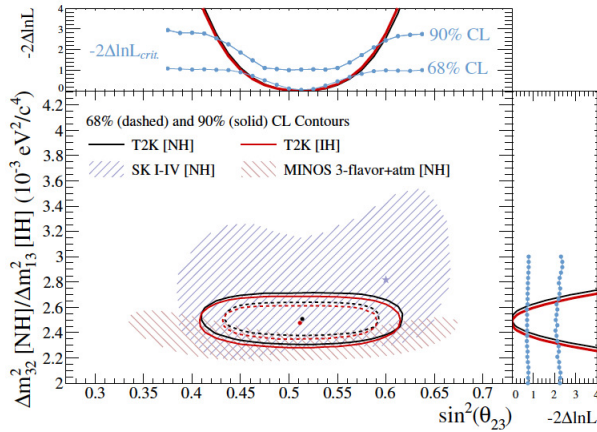


Figure A.6: The 68% and 90% CL regions in the $(\sin^2 \theta_{23}, \Delta m^2_{32}/\Delta m^2_{13})$ parameter space calculated using the Feldman-Cousins [186] and Cousins-Highland [196] methods for normal (black) and inverted (red) mass hierarchies. Results of the 90% C.L. regions with normal hierarchy from the SK [187] and MINOS [184] latest analyses are overlaid for comparison. The 1D profile likelihoods for both mass hierarchies and the $-2\Delta \ln L_{critical}$ MC estimates for NH are shown at the top and right plots. Figure from [6].

The effects of multinucleon interactions, neutrino interactions knocking out multiple nucleons, were considered for the first time in an oscillation experiment. Multinucleon interactions are indistinguishable from quasi-elastic interactions at T2K beam energy since at this energy the final state nucleons produced are below the Čerenkov threshold. However, the additional nucleon in the interaction alters the kinematics of the outgoing lepton, so including multinucleon events in our prediction distorts the reconstructed energy spectrum: since two-body QE kinematics are assumed when calculating the reconstructed neutrino energy (following Eq. 4.8), these events are reconstructed at lower energies as shown in Fig. A.7. The NEUT neutrino generator used in T2K includes an effective model called π -less Δ decay, which models only part of the expected multinucleon cross section. In order to evaluate the effect of the multinucleon interactions in the T2K ν_μ disappearance analysis, a MC study was performed replacing the existing effective model with a more accurate model based on the work by Nieves [197] up to 1.5 GeV. Then fake data sets were made for ND280 and SK with this model, with randomly varied systematic values but without statistical fluctuations, and the same oscillation fit was performed as for the real data for each of them, allowing the ND280 fake data to re-normalize the SK prediction. The mean biases in the oscillation parameters were $< 1\%$ for the ensemble, although the $\sin^2 \theta_{23}$ biases showed a 35% RMS spread.

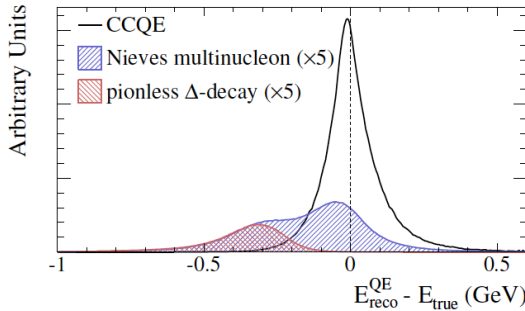


Figure A.7: Difference between reconstructed energy (assuming QE kinematics following Eq. 4.8) and true energy for CCQE events with energies below 1.5 GeV showing a little bias (black), and multinucleon events constructed based on [197] (blue) and NEUT π -less Δ decay (red) models scaled by a factor of five, showing biases to lower energies. Figure from [6].

Appendix B

Effect of the Solar Oscillation Parameters on the Run 1+2+3+4 Joint Oscillation Analysis

Several checks were done in order to test the effect of fitting the solar oscillation parameters $\sin^2 \theta_{12}$ and Δm_{21}^2 on the joint oscillation analysis. Solar parameters are allowed to float in the fit using as initial values and constraints the ones shown in table Tab. B.1. The resulting confidence regions, shown in red in Fig. B.1, are almost identical to the ones obtained fixing the solar parameters (shown in black in Fig. B.1).

Parameter	Value	1σ Error
$\sin^2 2\theta_{12}$	0.8495	0.071
$\sin^2 \theta_{12}$	0.306	0.018
Δm_{21}^2	$7.5 \times 10^{-5} (eV^2/c^4)$	$0.2 \times 10^{-5} (eV^2/c^4)$

Table B.1: Values of the solar oscillation parameters used for the results in this appendix.

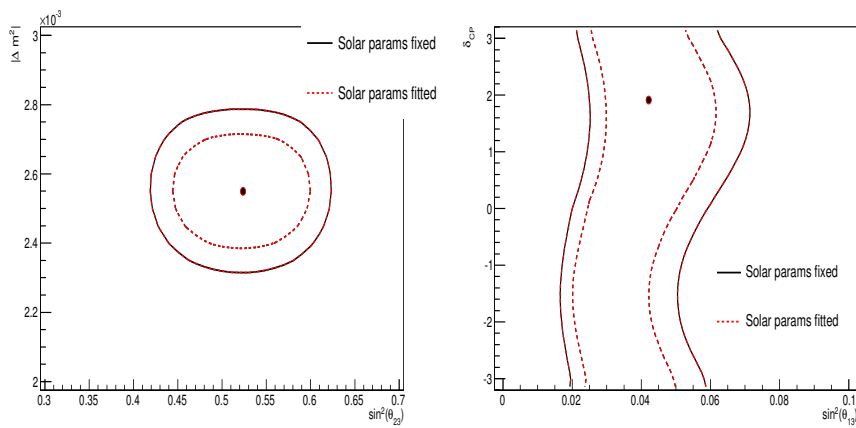


Figure B.1: Comparison of confidence regions in the $(\sin^2 \theta_{23}, |\Delta m^2_{32}|)$ parameter space (left) and $(\sin^2 \theta_{13}, \delta_{CP})$ parameter space (right) for the Run1+2+3+4 dataset fit assuming normal hierarchy with and without fitting the solar parameters $\sin^2 \theta_{12}$ and Δm^2_{21} .

Appendix C

Validation of the Run1+2+3+4 Joint 3-flavour Oscillation Analysis: Fitter Performance

Different studies were made in order to validate the Run1+2+3+4 joint 3-flavour oscillation analysis. In this Appendix, a summary of the studies concerning the fitter performance are presented.

C.1 Residuals and pulls of oscillation parameters

The residuals and pulls presented in this Section were obtained using 5k MC toy experiments generated with statistical fluctuations and variations of all 64 systematic parameters, fitting them using MINUIT with MIGRAD method and HESSE errors. In order to avoid undesired effects due to the proximity to the physical boundaries, the following study was made at the oscillation point $\sin^2 \theta_{23} = 0.5263$ and $\sin^2 \theta_{13} = 0.05$. The value for $\sin^2 \theta_{13}$ was selected to be sufficiently large to avoid the effect of the physical boundary at $\sin^2 \theta_{13} = 0$ that could be observed as an asymmetry in the distribution of residuals if a small value of $\sin^2 \theta_{13}$ is used. For the other angle $\sin^2 \theta_{23}$ the value was selected to be in the point of maximal disappearance given that $\sin^2 \theta_{13} = 0.05$, which is calculated as $\approx (2(1-\sin^2 \theta_{13}))^{-1}$ according to the explanation in App. E. Table C.1 presents the values of the oscillation parameters used for the validation studies presented in this Appendix.

Figures C.1 and C.2 show the distribution of residuals and pulls respectively for the four oscillation parameters at the oscillation point defined in Tab. C.1 for an ensemble of 5k MC toy experiments. Residuals for the events at the central peak in $\sin^2 \theta_{23}$ are presented in Fig. C.3 while for the other two peaks away from the true value of $\sin^2 \theta_{23}$ residuals are shown in Fig. C.4. Since one of the two peaks is reduced in the joint fit, these figures show the distributions from the two independent fits performed with an initial value in each octant, before selecting the one with minimal χ^2 .

Parameter	Value
$\sin^2 \theta_{23}$	0.5263
$\sin^2 \theta_{13}$	0.05
Δm_{FL}^2	$2.4 \times 10^{-3} (eV^2/c^4)$
δ_{CP}	0
Mass hierarchy	Normal

Table C.1: Values of the oscillation parameters used for the fitter performance validation studies presented in this Appendix.

Fig C.5 shows the distribution of residuals of the four oscillation parameters at the oscillation point defined in Tab. C.1 for an ensemble of 4k MC toy experiments fixing δ_{CP} to its true value, and Fig. C.6 selecting only the events which are at the central peak in $\sin^2 \theta_{23}$.

From the study of residuals and pulls the following features can be observed:

- **Three peak structure in $\sin^2 \theta_{23}$**

There is a three peak structure in the distribution of residuals for $\sin^2 \theta_{23}$, with a large peak at 0 (best-fit value close to true value), but also two smaller peaks at each octant¹. This can be explained by considering the effects of statistical fluctuations in the bins near the oscillation maximum in the toy datasets. If there are no statistical fluctuations in these bins, the fitted value of $\sin^2 \theta_{23}$ is similar to the true value, and downward statistical fluctuations also result in a fitted value similar to the input value (maximal disappearance). However, upward statistical fluctuations in these bins in some datasets mean that ν_μ -disappearance is less than maximal, and this results in a fitted value of $\sin^2 \theta_{23}$ far from the true one. The non-maximal values of $\sin^2 \theta_{23}$ returned by the fitter, where the other peaks appear, can be calculated with the ratio between the number of events at the oscillation dip with and without oscillations.

In addition, comparing Fig. C.3 with Fig. C.4 it is clear that the main source for the biases in the distribution of residuals for Δm_{FL}^2 and $\sin^2 \theta_{13}$ comes from the extra peaks away from the true value.

- **Intrinsic asymmetry in $\sin^2 \theta_{13}$ - δ_{CP}**

It was observed that an intrinsic asymmetry exist in the $\sin^2 \theta_{13}$ - δ_{CP} space. Figure C.7 shows the true $\Delta\chi^2$ distribution for the single e-like ring sample in the $(\sin^2 \theta_{13}, \delta_{CP})$ space for a MC toy experiment created at the oscillation point defined

¹ One of the two peaks away from the true value (the one corresponding to the solution in the second octant) is suppressed when the contribution to the total χ^2 coming from the single e-like ring sample is added (it was checked that when using only the χ^2 contribution from the single μ -like ring sample both peaks appeared). The explanation for this suppression will be given in next bullet.

in Tab. C.1 without statistical fluctuations nor systematic variations. In this figure, the region of minimal $\Delta\chi^2$ is clearly not centred at $\delta_{CP} = 0$, $\sin^2 \theta_{13} = 0.05$ (the true value) but it is asymmetric, centred at a value $\delta_{CP} > 0$ and $\sin^2 \theta_{13} > 0.05$. This explains why the δ_{CP} residuals do not have the main peak centred at 0 in Figs. C.1-C.4 (with statistical and systematic fluctuations) but at $\delta_{CP} \approx 0.6$, even when other potential bias sources are removed (fixing $\sin^2 \theta_{23}$ to its true value for instance). The bias in δ_{CP} results in an upward bias in $\sin^2 \theta_{13}$, as deduced also from Fig. C.7, and observed in Figs. C.1-C.4.

This is a direct consequence of the energy spectrum of T2K event candidates convoluted with the oscillation probability $P(\nu_\mu \rightarrow \nu_e)$. Figure C.8 is built as follows. All points in the $(\sin^2 \theta_{13}, \delta_{CP})$ space for which the difference in $P(\nu_\mu \rightarrow \nu_e)$ with respect to the true point $(\Delta(P(\nu_\mu \rightarrow \nu_e))(E_i)) = P(\nu_\mu \rightarrow \nu_e)_{point}(E_i) - P(\nu_\mu \rightarrow \nu_e)_{true}(E_i)$ is smaller than 0.005 are marked. This produces a S-shaped line for each $\Delta(P(\nu_\mu \rightarrow \nu_e))$ value. This process is repeated for different true neutrino energies, which correspond to the centre of the two most populated bins in the energy spectrum (see Fig. C.8, left), and results in a band for each of the two energy values, with red regions indicating those points where all the bands for all energies crossed. Those are therefore points where the $\Delta\chi^2$ value will be approximately the same, minimal with respect to the true oscillation point selected. The shape and position of the red region in the left side of Fig. C.8 describes exactly the asymmetry observed in Fig. C.7.

The true values of other oscillation parameters except δ_{CP} do not affect the position of this region as can be observed in Fig. C.9, where the oscillation point is the one defined in Tab. C.1 but changing $\sin^2 \theta_{13} = 0.03$ (left) and $\sin^2 \theta_{23} = 0.3$ (right).

The distribution changes with the true value of δ_{CP} . For instance, when doing this test with $\sin^2 \theta_{23} = 0.5263$, $\sin^2 \theta_{13} = 0.05$, $\Delta m_{FL}^2 = 2.4 \times 10^{-3} eV^2/c^4$ and $\delta_{CP} = -1$ the position of minimal $\Delta\chi^2$ values along the $(\sin^2 \theta_{13}, \delta_{CP})$ space change as can be observed in Fig. C.10.

This inherent bias in $\sin^2 \theta_{13}$ - δ_{CP} is the cause of the suppression of one of the peaks in the distribution of residuals for $\sin^2 \theta_{23}$: due to the correlation between $\sin^2 \theta_{23}$ and $\sin^2 \theta_{13}$, a positive shift in $\sin^2 \theta_{23}$ is compensated by a negative shift in $\sin^2 \theta_{13}$ as can be observed in Fig. C.4. However, the asymmetry in the minimal $\Delta\chi^2$ values in the $(\sin^2 \theta_{13}, \delta_{CP})$ space produces a tension such that a negative shift of $\sin^2 \theta_{13}$ is penalized (it gets out of the distribution of minimal $\Delta\chi^2$), and therefore the solution in the second octant of $\sin^2 \theta_{23}$ is suppressed. This can be also observed in Fig. C.4, where the two distributions of residuals for $\sin^2 \theta_{13}$ are not symmetric as they would be in the absence of the intrinsic asymmetry.

Another consequence of this intrinsic bias in $(\sin^2 \theta_{13}, \delta_{CP})$ space is the asymmetry observed in the $\sin^2 \theta_{13}$ distributions even when $\sin^2 \theta_{23}$ is fixed to its true value, with a larger tail to positive values of $\Delta(\sin^2 \theta_{13})$, disappearing when δ_{CP} is fixed to its true value as can be observed comparing the bottom left plots of Figs. C.1 and C.5.

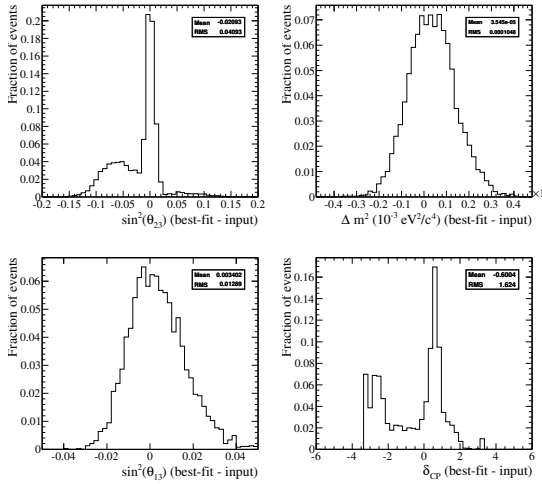


Figure C.1: Distribution of residuals of the four oscillation parameters at the oscillation point defined in Tab. C.1 for an ensemble of 5k toy MC experiments.

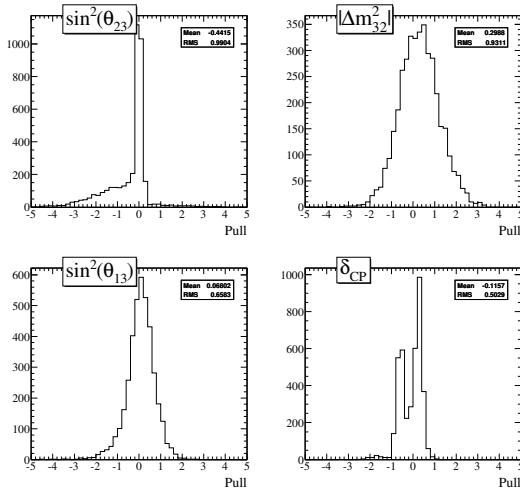


Figure C.2: Pulls of the four oscillation parameters at the oscillation point defined in Tab. C.1 for an ensemble of 5k toy MC experiments.

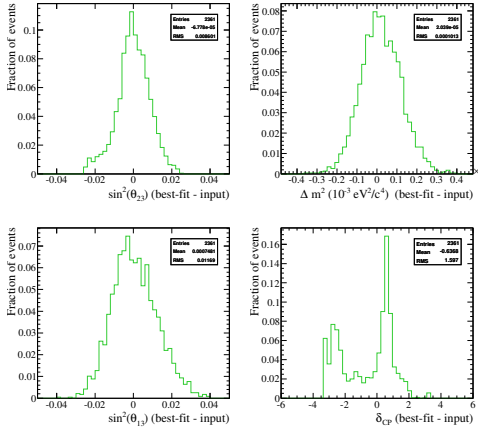


Figure C.3: Distribution of residuals of the four oscillation parameters at the oscillation point defined in Tab. C.1 for an ensemble of 5k toy MC experiments selecting only those experiments with a best-fit value of $\sin^2 \theta_{23}$ in the central peak.

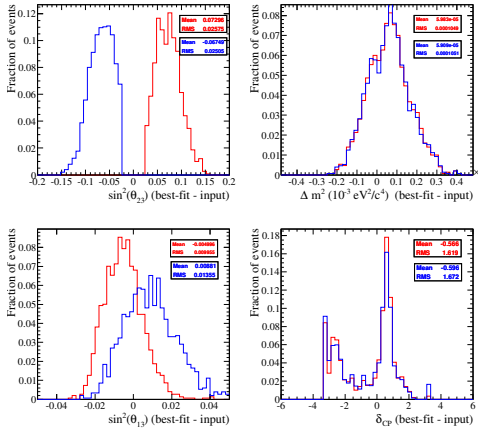


Figure C.4: Distribution of residuals of the four oscillation parameters at the oscillation point defined in Tab. C.1 for an ensemble of 5k toy MC experiments selecting only those experiments with a best-fit value of $\sin^2 \theta_{23}$ in the peaks away from the true value (distributions are from the two independent fits performed with an initial value in each octant, before selecting the one with minimal χ^2).

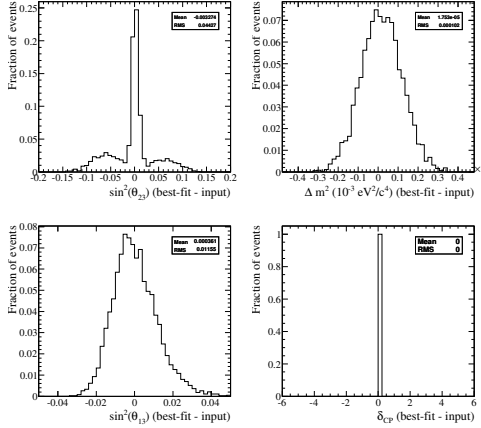


Figure C.5: Distribution of residuals of the four oscillation parameters at the oscillation point defined in Tab. C.1 for an ensemble of 4k toy MC experiments and fixing δ_{CP} to its true value.

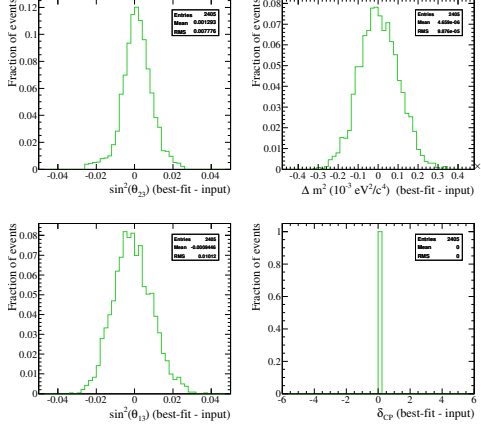


Figure C.6: Distribution of residuals of the four oscillation parameters at the oscillation point defined in Tab. C.1 for an ensemble of 4k toy MC experiments and fixing δ_{CP} to its true value, selecting only those experiments with a best-fit value of $\sin^2 \theta_{23}$ in the central peak.

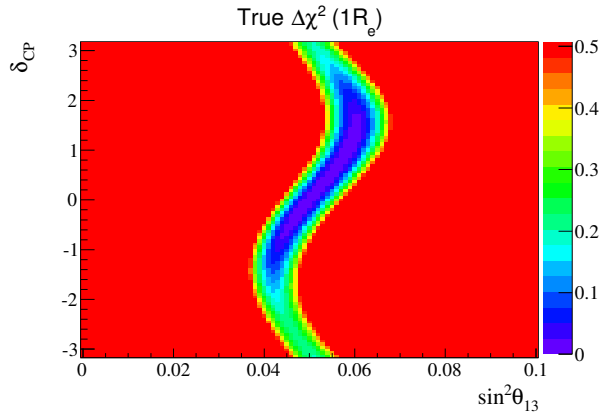


Figure C.7: True $\Delta\chi^2$ distribution for the single e-like ring sample in the $(\sin^2 \theta_{13}, \delta_{CP})$ space for a toy created at the oscillation point defined in Tab. C.1 without statistical fluctuations nor systematic variations.

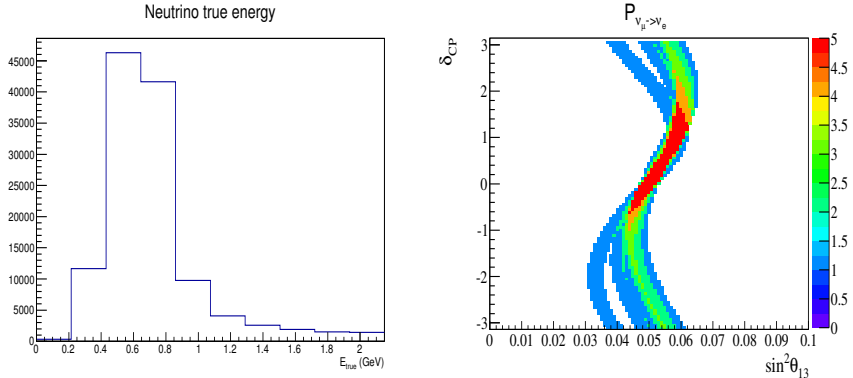


Figure C.8: Left: zoom of the true energy spectrum for the oscillated ν_e events in the single e-like ring sample. Right: All points in the $(\sin^2 \theta_{13}, \delta_{CP})$ space for which the difference in $P(\nu_\mu \rightarrow \nu_e)$ with respect to the true point is smaller than 0.005 are marked. This produces a S-shaped line for each $\Delta(P(\nu_\mu \rightarrow \nu_e))$ value. This process is repeated for the neutrino energies of the two most populated bins in the energy spectrum on the left, and results in a band for each energy value, with red regions indicating those points where they cross.

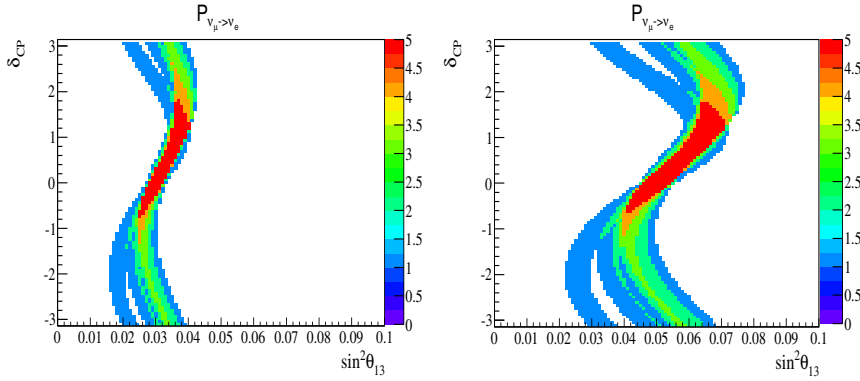


Figure C.9: Lines of equal $P(\nu_\mu \rightarrow \nu_e)$ are drawn for the different values of the true energy at the peak of the spectrum on the left side of Fig. C.8 (from 0.45 GeV to 0.85 GeV) corresponding to the oscillation point defined in Tab. C.1 changing $\sin^2 \theta_{13} = 0.03$ (left) and $\sin^2 \theta_{23} = 0.3$ (right).

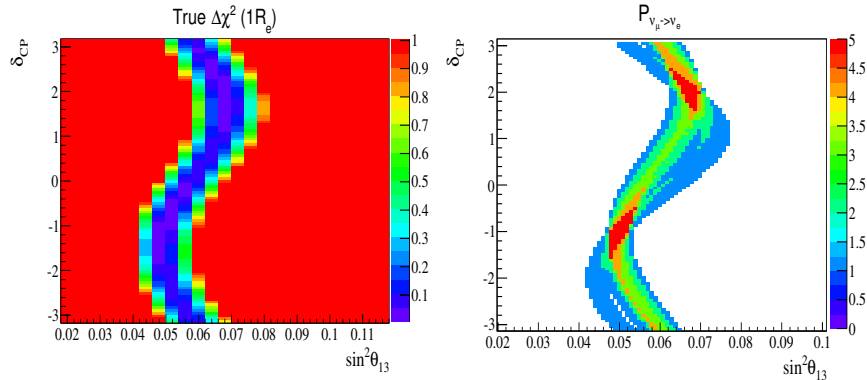


Figure C.10: On the left: true $\Delta\chi^2$ distribution for the single e-like ring sample in the $(\sin^2 \theta_{13}, \delta_{CP})$ space for a toy created at the oscillation point defined in Tab. C.1 changing $\delta_{CP} = -1$ assuming normal hierarchy without statistical fluctuations nor systematic variations. On the right: lines of equal $P(\nu_\mu \rightarrow \nu_e)$ are drawn for the different values of the true energy at the peak of the spectrum on the left side of Fig. C.8 (from 0.45 GeV to 0.85 GeV) corresponding to the oscillation point defined in Tab. C.1 changing $\sin^2 \theta_{13} = 0.03$ and $\delta_{CP} = -1$.

C.2 Residuals and pulls of systematic parameters

Distributions of pulls for the 64 systematic parameters are presented in Figs. C.12-C.18 for an oscillation point with $\sin^2 \theta_{23} = 0.513$, $\sin^2 \theta_{13} = 0.0251$, $\Delta m_{FL}^2 = 2.4 \times 10^{-3} eV^2/c^4$ and $\delta_{CP} = 0$. A summary of the pull mean and RMS is given in Fig. C.11. No problems were identified in the tests done to the fitter, which performed as expected. In general all systematic parameters present a good behaviour with a mean in ≈ 0 and RMS ≈ 1 . There are some small biases in the pull distributions for some systematic parameters, which are understood:

- **Spectral function**

A special treatment is done for this parameter, which is varied following a Gaussian distribution with mean at 0 and $\sigma = 1$ bounded between [0,1] when creating toy experiments. When fitting this parameter, it is limited to the same range [0,1] and a Gaussian constraint in the penalty term is applied. Therefore, a Gaussian distribution of residuals centred at 0 with RMS 1 is not expected for this parameter.

- **π -less Δ decay**

The distribution of pulls for this parameter is biased due to the special procedure followed to calculate the weights for its response functions. In NEUT, 20% of the Δ 's decay through this process, being therefore the uncertainty equal to 20%. That means that this parameter cannot be tweaked to values smaller than -1σ , what would be unphysical, and instead the same weight found for a tweak of -1σ is applied to any tweak smaller than this value, creating an asymmetry and a constant plateau at negative values. Thus, a small negative bias appears for this parameter.

- **SK reconstructed energy scale**

This systematic is different from the others since its effect is not translated into a weight of the number of events in a bin, but a migration of events from one bin to the adjacent ones. The single μ -like ring spectrum is not symmetric and therefore a positive tweak of the reconstructed energy scale parameter has a different effect in the spectrum than a negative one, and there is also an asymmetric effect in the single e-like ring spectrum, more evident in the first and last bins. The RMS of this parameter is larger than 1, issue that can be solved if MINOS errors are computed instead of the ones calculated with the HESSE algorithm, since MINOS errors are different for positive and negative values of the distribution of residuals and they therefore account for the asymmetric effect of this parameter.

- **$1R_\mu$ NC SK efficiency + FSI + SI**

The distribution of pulls for this parameter is biased towards negative values due to the low statistics at current POT, which makes that a downward Poisson fluctuation of the small number of events in the bins around the oscillation dip in the single μ -like ring spectrum is more likely than an upward fluctuation. Thus, since NC events are mainly distributed around the oscillation dip, a movement to a smaller value of this systematic parameter is more probable, and that creates a bias to negative values. The bias disappears when increasing the POT and the number of events at the oscillation dip, reducing the predominance of downward fluctuations.

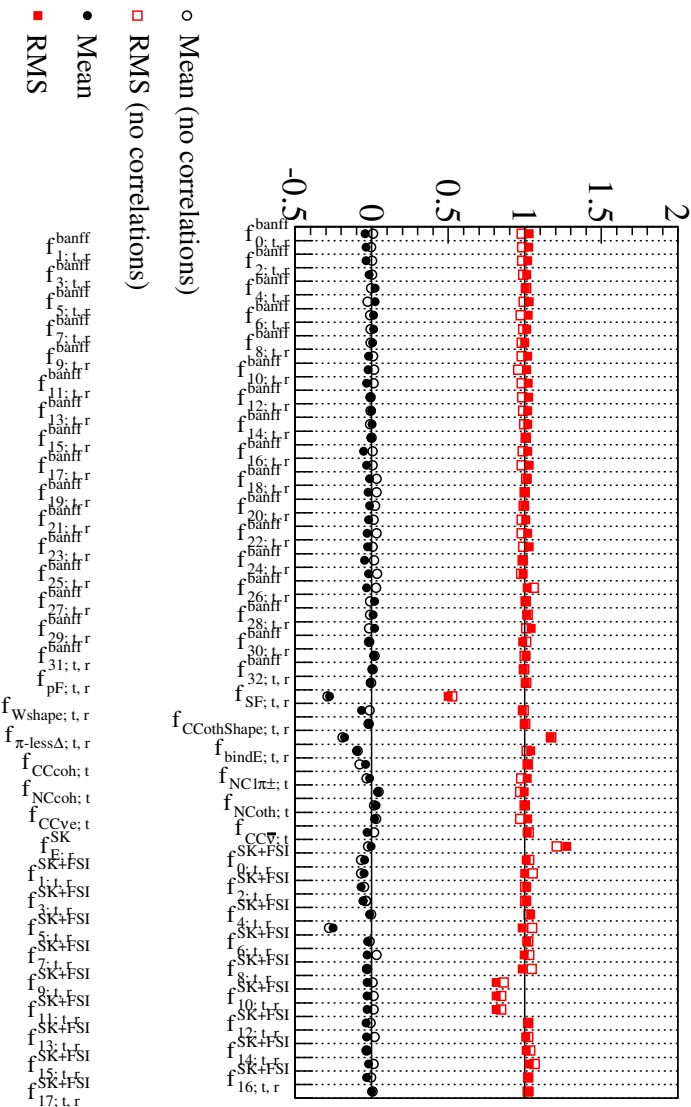


Figure C.11: Summary of mean (black circles) and RMS (red squares) for the distribution of pulls of the 64 systematic parameters with (filled) and without (empty) correlations.

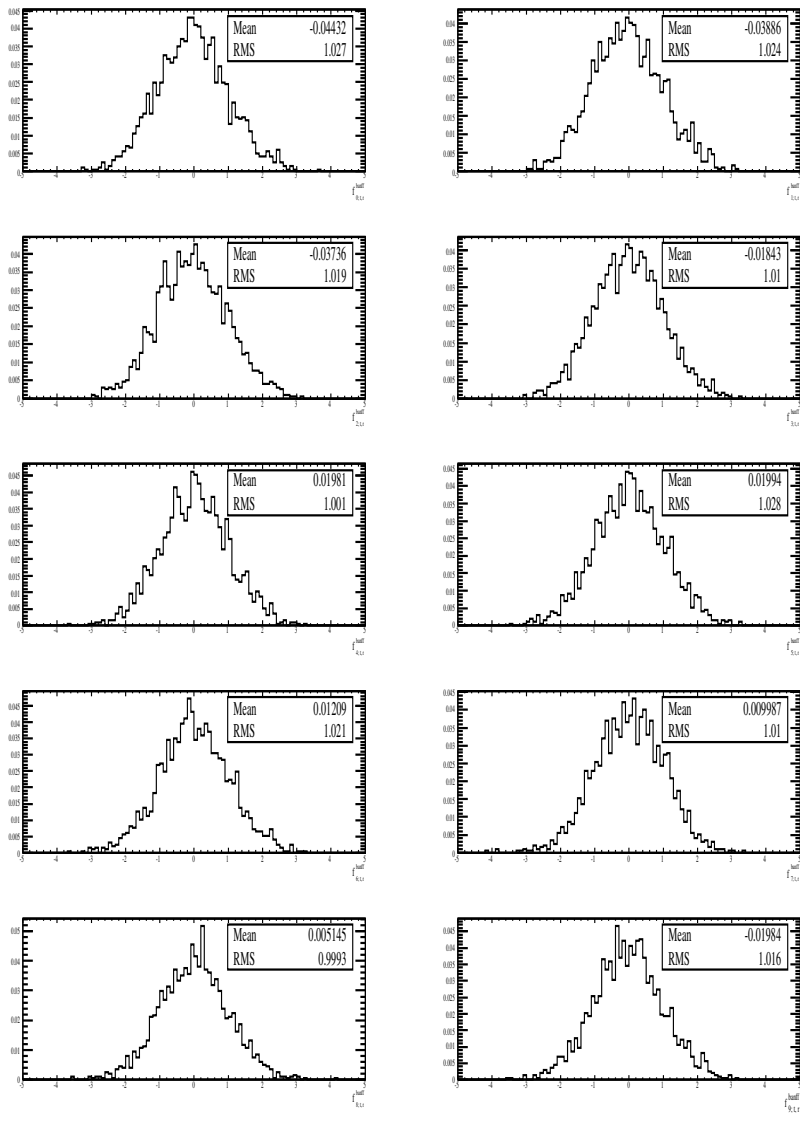


Figure C.12: Distribution of pulls for the systematic parameters BANFF 0 - 9.

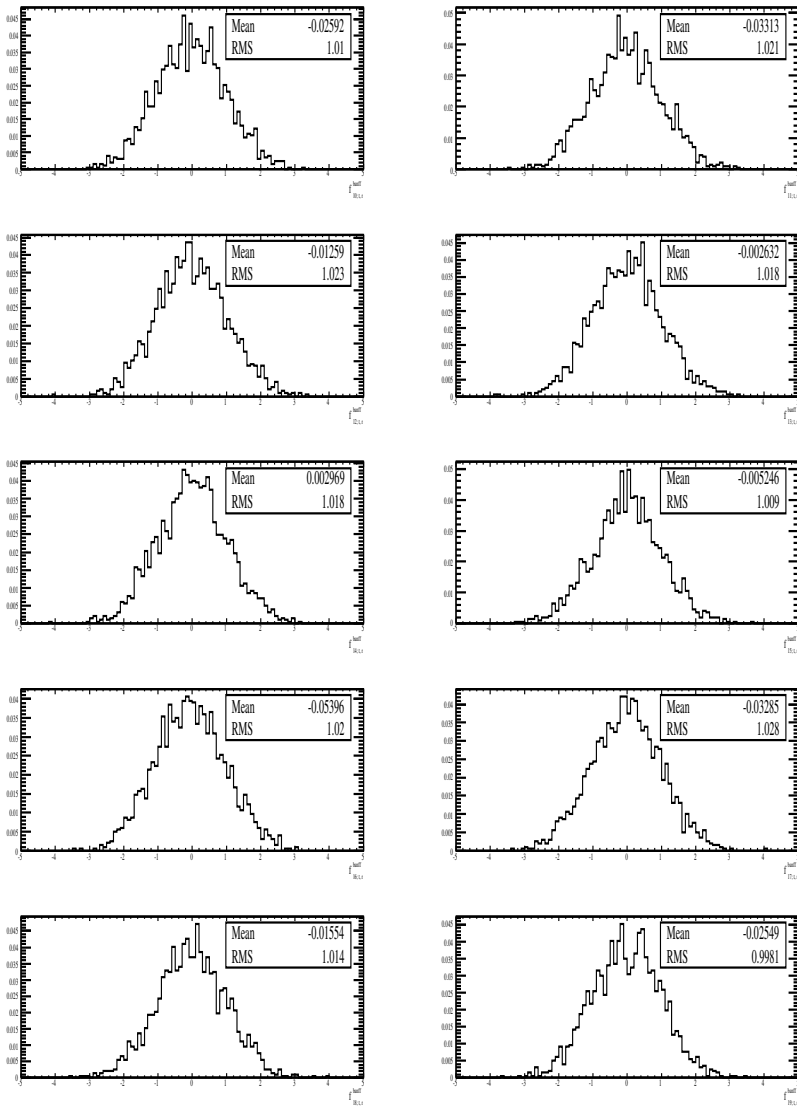


Figure C.13: Distribution of pulls for the systematic parameters BANFF 10 - 19.

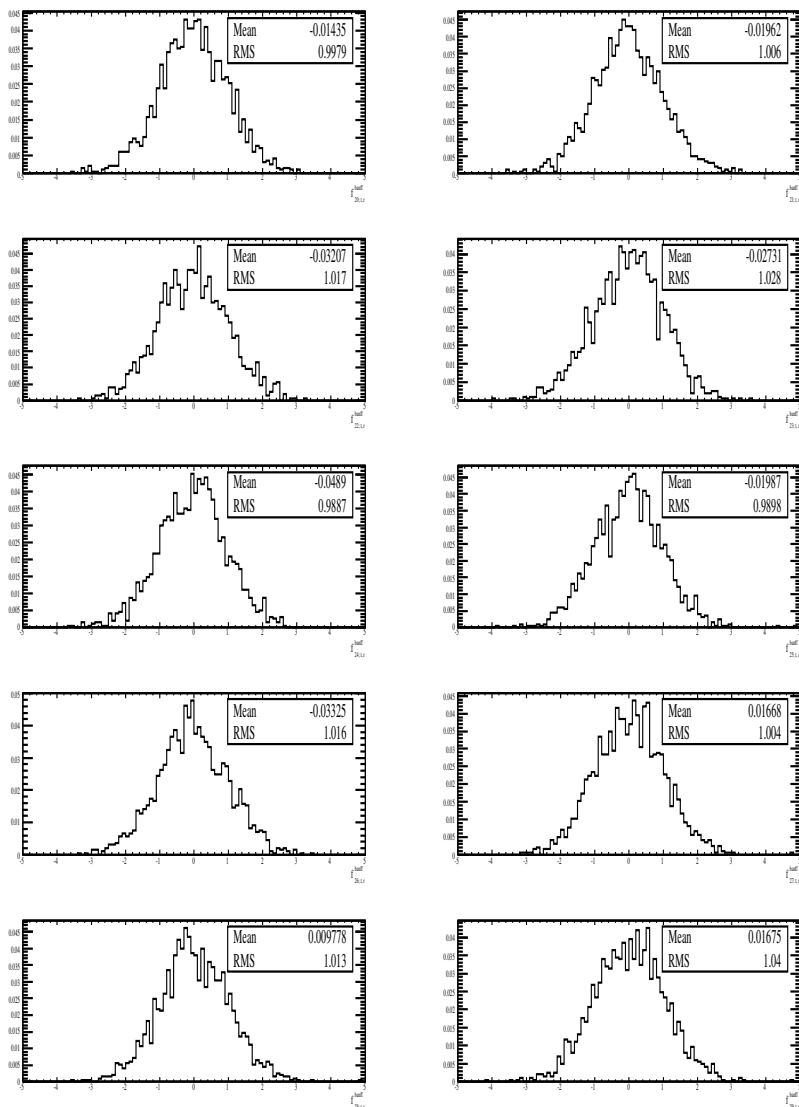


Figure C.14: Distribution of pulls for the systematic parameters BANFF 20 - 29.

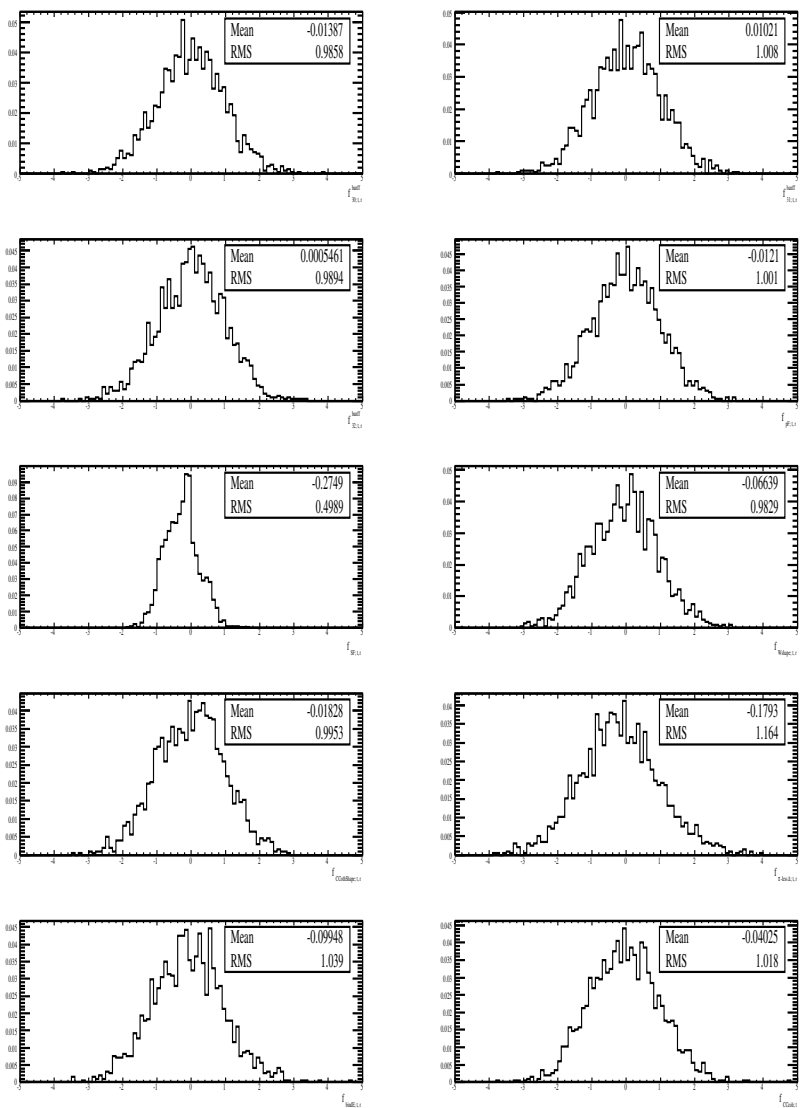


Figure C.15: Distribution of pulls for the systematic parameters BANFF 30 - 32 and some of the independent cross section systematics.

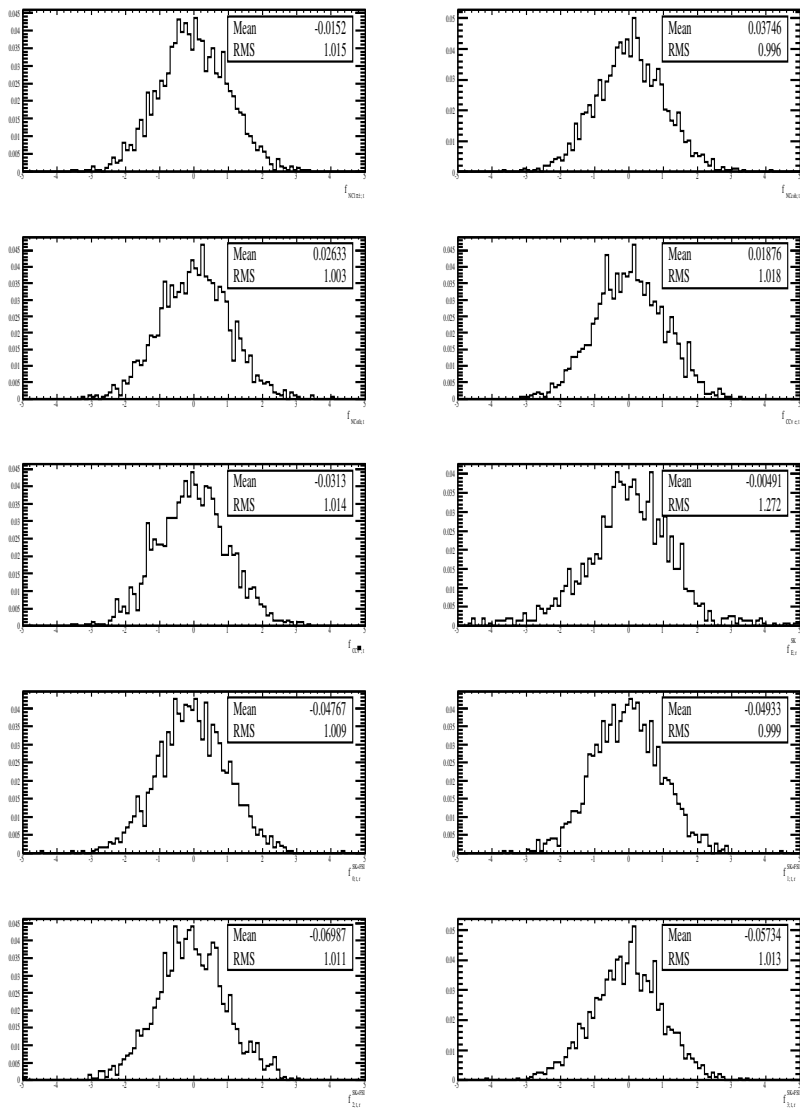


Figure C.16: Distribution of pulls for some of the independent cross section systematics, reconstructed Energy scale and SK+FSI parameters 0-3.

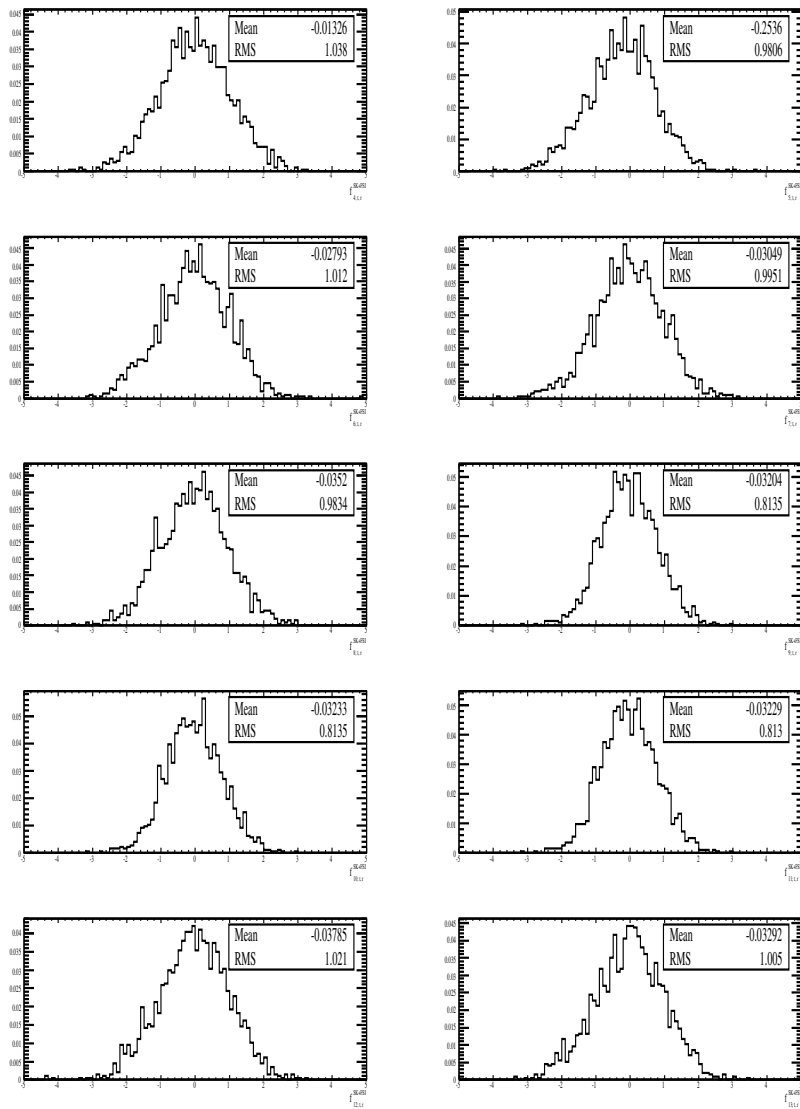


Figure C.17: Distribution of pulls for the systematic parameters SK+FSI 4 - 13.

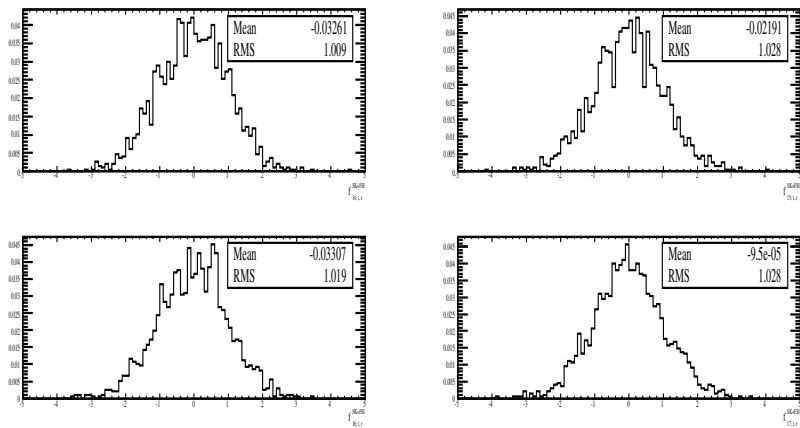


Figure C.18: Distribution of pulls for the systematic parameters SK+FSI 14 - 17.

Appendix D

Validation of the Run1+2+3+4 Joint 3-flavour Oscillation Analysis: Toy Dataset Fits

Different fake single μ -like ring and e-like ring datasets were created for an exposure of 6.57×10^{20} POT in order to validate the Run1+2+3+4 joint 3-flavour oscillation analysis. The values of the oscillation parameters used to create those toy experiments are summarized in Tab. D.1. All the fake datasets were created including statistical fluctuations and some of them included also random variations of all systematic parameters, as indicated in Tab. D.1. They were treated as the real datasets and therefore all the relevant plots were made for each dataset: distribution of pulls, best-fit spectra, marginalized $\Delta\chi^2$ as a function of each oscillation parameter ($|\Delta m_{FL}^2|$, $\sin^2\theta_{23}$, $\sin^2\theta_{13}$ and δ_{CP}), the $\Delta\chi^2$ distributions in the four 2-dimensional parameter spaces and the confidence regions in the four 2-dimensional parameter spaces: $(\sin^2\theta_{23}, |\Delta m_{FL}^2|)$, $(\sin^2\theta_{13}, |\Delta m_{FL}^2|)$, $(\sin^2\theta_{13}, \delta_{CP})$ and $(\sin^2\theta_{23}, \sin^2\theta_{13})$. In this Appendix, only a summary will be presented, and therefore these plots will be included for only one selected toy dataset (#1) in Figs. D.1-D.5. All profile $\Delta\chi^2$ and confidence region plots were built minimizing with respect to all 64 systematic parameters and the oscillation parameters from $(|\Delta m_{FL}^2|, \sin^2\theta_{23}, \sin^2\theta_{13}, \delta_{CP})$ not shown on the plot (as explained in App. B, $\sin^2\theta_{12}$ and Δm_{21}^2 have a negligible effect and they were kept fixed to the value indicated in Tab. B.1). Confidence regions were found with respect to the χ^2 global minimum reported in Tab. D.1 (except for the result in $(\sin^2\theta_{13}, \delta_{CP})$ space where the raster scan was used) using the constant- $\Delta\chi^2$ method (see Section 5.6).

The results presented in this Appendix confirm that the fitter performs correctly, with no unexpected features found.

The best-fit point obtained for each fake dataset is also presented in Tab. D.1. The toy datasets were also fitted including a constraint for $\sin^2 2\theta_{13}$ as explained in Section 5.6.2, using the true input value of the toy experiment as the mean value for the constraint, and the same error used for real data from reactor experiments [86]. Table D.2 summarizes

these fits, comparing results of best-fit values with and without constraint. As expected, for the toy experiments whose best-fit value obtained for $\sin^2 2\theta_{13}$ without constraint is larger (smaller) than the true value, when the constraint is applied the value of $\sin^2 2\theta_{13}$ is forced to get smaller (larger). This forces in turn that the values of $\sin^2 \theta_{23}$ become larger (smaller) and the values of δ_{CP} become negative (positive). In addition, best-fit values of χ^2 are obviously larger when the constraint in $\sin^2 2\theta_{13}$ is imposed.

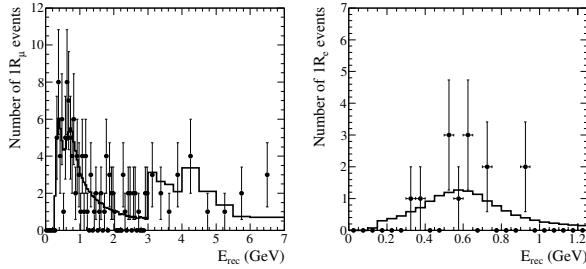


Figure D.1: Single μ -like ring (left) and e-like ring (right) reconstructed energy spectra for fake dataset #1. Points with error bars represent the fake data while the solid line corresponds to the best-fit prediction.

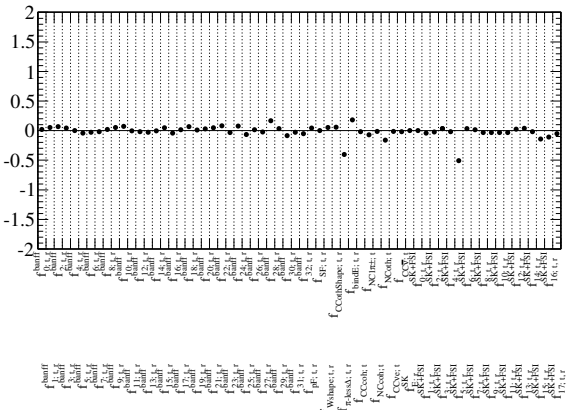


Figure D.2: Systematic parameter pull means for the oscillation fit to fake dataset #1.

Toy	Fit	MH	$ \Delta m_{FL}^2 $ ($\times 10^{-3}$ eV $^2/\text{c}^4$)	$\sin^2 \theta_{23}$	$\sin^2 \theta_{13}$ or $\sin^2 2\theta_{13}$	δ_{CP}	$N_{SK}^{LR\mu}$	$N_{SK}^{LR\bar{\nu}}$	χ^2	Systematics
0	true	NH	2.4375	0.513	0.0251	0.0	123	31	-	Nominal
	$\sin^2 \theta_{13}$	NH	2.413	0.513	0.0364	-0.0825	127.264	30.104	87.877	-
	$\sin^2 2\theta_{13}$	NH	2.413	0.513	0.1403	-0.0825	127.264	30.104	87.877	-
1	true	NH	2.340	0.514	0.0364	-0.105	126.234	29.920	88.942	-
	$\sin^2 \theta_{13}$	NH	2.4375	0.37	0.0251	0.0	138	13	-	Random
	$\sin^2 2\theta_{13}$	NH	2.327	0.619	0.0152	1.585	139.277	13.817	104.765	-
2	true	NH	2.750	0.513	0.0251	0.0	120	17	-	Random
	$\sin^2 \theta_{13}$	NH	2.578	0.508	0.0185	-0.0179	120.354	17.298	90.792	-
	$\sin^2 2\theta_{13}$	NH	2.578	0.508	0.0728	-0.0179	120.354	17.298	90.792	-
3	true	NH	2.4375	0.513	0.04	0.0	112	39	-	Random
	$\sin^2 \theta_{13}$	NH	2.583	0.568	0.0572	1.087	116.335	38.972	73.952	-
	$\sin^2 2\theta_{13}$	NH	2.583	0.568	0.2157	1.087	116.335	38.972	73.952	-
4	true	NH	2.4375	0.513	0.0251	$-\pi/2$	117	38	-	Random
	$\sin^2 \theta_{13}$	NH	2.466	0.526	0.0464	-2.564	120.035	38.414	76.768	-
	$\sin^2 2\theta_{13}$	NH	2.466	0.526	0.1768	-2.564	120.035	38.414	76.768	-
5	true	IH	2.4375	0.513	0.0251	0.0	123	17	-	Nominal
	$\sin^2 \theta_{13}$	IH	2.530	0.511	0.0246	2.367	121.802	16.279	111.201	-
	$\sin^2 2\theta_{13}$	IH	2.530	0.511	0.0962	2.367	121.783	16.278	111.203	-
	$\sin^2 \theta_{13}$	NH	2.557	0.511	0.0205	0.722	121.816	16.226	111.375	-
	$\sin^2 2\theta_{13}$	NH	2.557	0.511	0.0802	0.723	121.814	16.227	111.375	-

Table D.1: True input values (shown in bold) and best-fit values for a test ensemble of 6 fake datasets.

Toy	Fit	Constraint	MH	$ \Delta m_{FL}^2 $ ($\times 10^{-3}$ eV $^2/c^4$)	$\sin^2 \theta_{23}$	$\sin^2 2\theta_{13}$	δ_{CP}	χ^2	Systematics
0	true	-	NH	2.4375	0.513	0.098	0.0	-	Nominal
	$\sin^2 2\theta_{13}$	NO	NH	2.413	0.513	0.1403	-0.0825	87.877	-
	$\sin^2 2\theta_{13}$	0.098 ± 0.01	NH	2.435	0.550	0.0996	-1.263	88.249	-
1	true	-	NH	2.4375	0.37	0.098	0.0	-	Random
	$\sin^2 2\theta_{13}$	NO	NH	2.327	0.619	0.0599	1.592	104.764	-
	$\sin^2 2\theta_{13}$	0.098 ± 0.01	NH	2.327	0.402	0.0981	1.599	104.77	-
2	true	-	NH	2.750	0.513	0.098	0.0	-	Random
	$\sin^2 2\theta_{13}$	NO	NH	2.578	0.508	0.0728	-0.0179	90.792	-
	$\sin^2 2\theta_{13}$	0.098 ± 0.01	NH	2.580	0.498	0.0973	0.802	90.977	-
3	true	-	NH	2.4375	0.513	0.1536	0.0	-	Random
	$\sin^2 2\theta_{13}$	NO	NH	2.583	0.568	0.2157	1.087	73.952	-
	$\sin^2 2\theta_{13}$	0.1536 ± 0.01	NH	2.590	0.569	0.1547	-1.013	74.533	-
4	true	-	NH	2.4375	0.513	0.098	$-\pi/2$	-	Random
	$\sin^2 2\theta_{13}$	NO	NH	2.466	0.526	0.1768	-2.564	76.768	-
	$\sin^2 2\theta_{13}$	0.098 ± 0.01	NH	2.464	0.542	0.105	-1.615	81.003	-
5	true	-	IH	2.4375	0.513	0.098	0.0	-	Nominal
	$\sin^2 2\theta_{13}$	NO	IH	2.530	0.511	0.0962	2.367	111.203	-
	$\sin^2 2\theta_{13}$	0.098 ± 0.01	IH	2.530	0.511	0.0979	2.323	111.214	-

Table D.2: True input values (shown in bold) and best-fit values for a test ensemble of 6 fake datasets, comparing results with and without including constraint in $\sin^2 2\theta_{13}$.

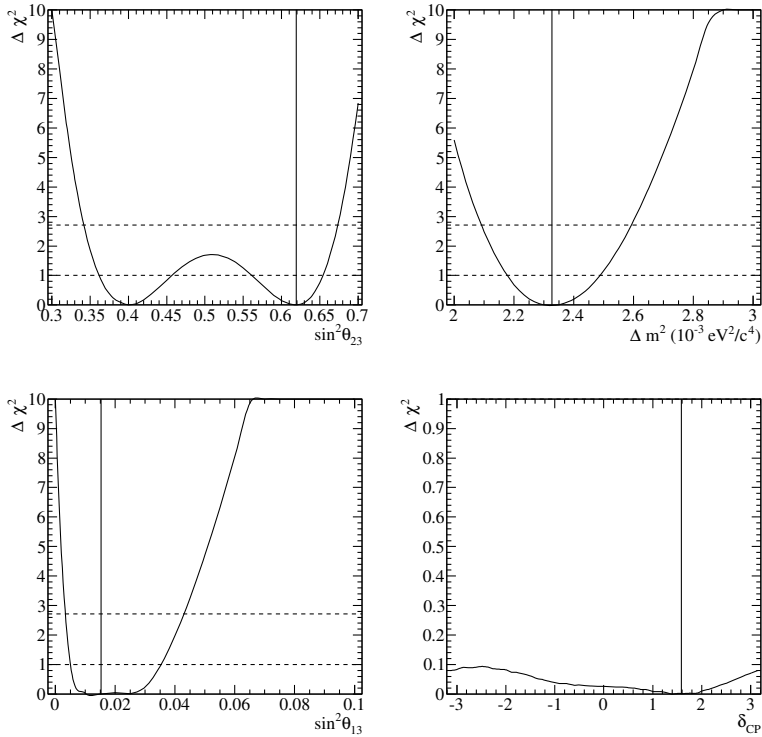


Figure D.3: $\Delta\chi^2$ as function of $\sin^2\theta_{23}, |\Delta m_{FL}^2|, \sin^2\theta_{13}$ and δ_{CP} for fake dataset #1. At each point the χ^2 was minimized with respect to the oscillation parameters not shown in each figure and all 64 systematic parameters.

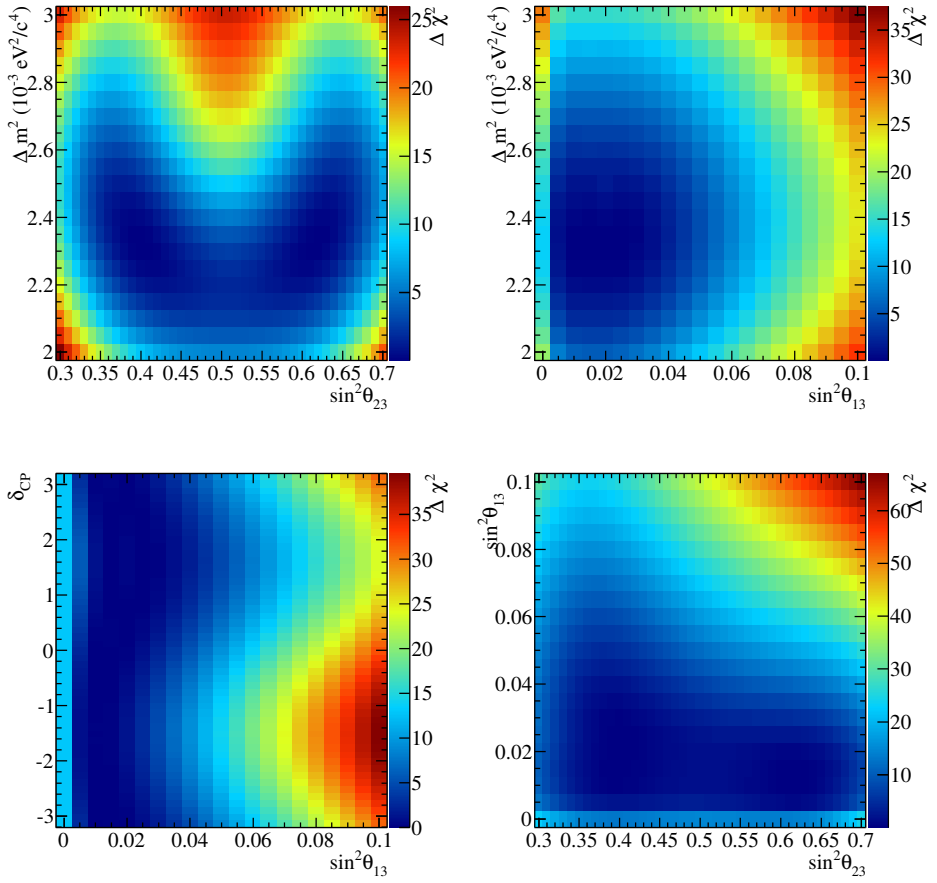


Figure D.4: $\Delta\chi^2$ surface in $(|\Delta m_{FL}^2|, \sin^2\theta_{23})$, $(|\Delta m_{FL}^2|, \sin^2\theta_{13})$, $(\delta_{CP}, \sin^2\theta_{13})$ and $(\sin^2\theta_{13}, \sin^2\theta_{23})$ spaces for fake dataset #1. At each point the χ^2 was minimized with respect to the oscillation parameters not shown in each figure and all 64 systematic parameters.

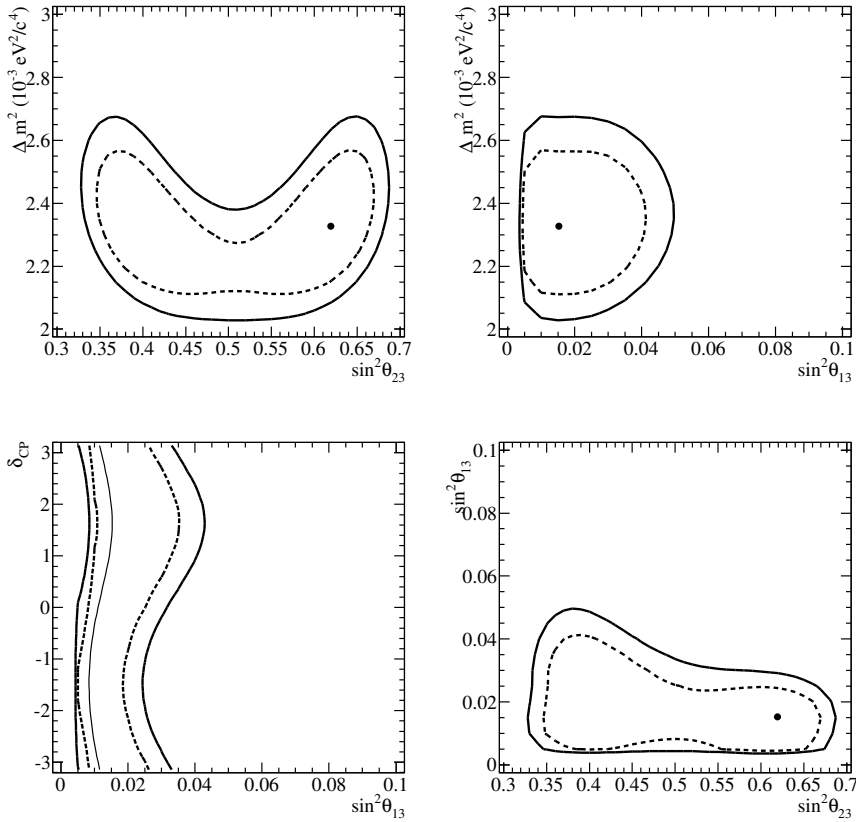


Figure D.5: 68% and 90% CL regions in $(|\Delta m_{FL}^2|, \sin^2 \theta_{23})$, $(|\Delta m_{FL}^2|, \sin^2 \theta_{13})$, $(\delta_{CP}, \sin^2 \theta_{13})$ and $(\sin^2 \theta_{13}, \sin^2 \theta_{23})$ spaces for fake dataset #1. At each point the χ^2 was minimized with respect to the oscillation parameters not shown in each figure and all 64 systematic parameters.

Appendix E

Difference Between $\sin^2\theta_{23}$ Values for Maximal Mixing and Maximal Disappearance

The distribution of $\Delta\chi^2$ as a function of $\sin^2\theta_{23}$ is not always symmetric with respect to $\sin^2\theta_{23} = 0.5$, as it can be observed in Figs. 5.17 or 5.22. The reason for this behaviour will be explained in this appendix.

The distribution of $\Delta\chi^2$ vs $\sin^2\theta_{23}$ has in general two minima which are at values of $\sin^2\theta_{23}$ that are symmetric with respect to a centre of symmetry (see, for example, Fig. D.3). It seems natural to think that this centre of symmetry must be exactly at $\sin^2\theta_{23} = 0.5$ since the value of $\sin^2 2\theta_{23}$ is exactly identical for θ_{23} and $\pi/2 - \theta_{23}$. However, as it will be shown below, the centre of symmetry depends on the value of $\sin^2\theta_{13}$ and that it is 0.5 only when $\sin^2\theta_{13} = 0$.

Although all the results in this thesis include matter effects, the following calculation is made using the 3-flavour vacuum oscillation probabilities so that the algebra is manageable. The general form of the oscillation probability is in this case:

$$P(\nu_\alpha \rightarrow \nu_\beta) = \delta_{\alpha\beta} - 4 \sum_{i>j} \mathcal{Re} [U_{\alpha i}^* U_{\beta i} U_{\alpha j} U_{\beta j}^*] \sin^2 \left(\frac{\Delta m_{ij}^2 L}{4E} \right) + 2 \sum_{i>j} \mathcal{Im} [U_{\alpha i}^* U_{\beta i} U_{\alpha j} U_{\beta j}^*] \sin \left(\frac{\Delta m_{ij}^2 L}{2E} \right) \quad (\text{E.1})$$

where U_{ab} represents the ab element of the PMNS matrix shown in Eq. 2.31.

The ν_μ -survival probability is plotted as a function of $\sin^2(\theta_{23})$ in figure E.1 for different values of $\sin^2(\theta_{13})$. From this figure, it is obvious that the centre of symmetry is only at $\sin^2(\theta_{23}) = 0.5$ for $\sin^2(\theta_{13}) = 0$ and that it moves to higher values of $\sin^2(\theta_{23})$ as $\sin^2(\theta_{13})$ increases, for both mass hierarchies. The centre of symmetry of the $P(\nu_\mu \rightarrow \nu_\mu)$ curve corresponds to its minimum and therefore to the maximal disappearance, so both

terms, centre of symmetry of the $P(\nu_\mu \rightarrow \nu_\mu)$ curve and maximal disappearance are equivalent.

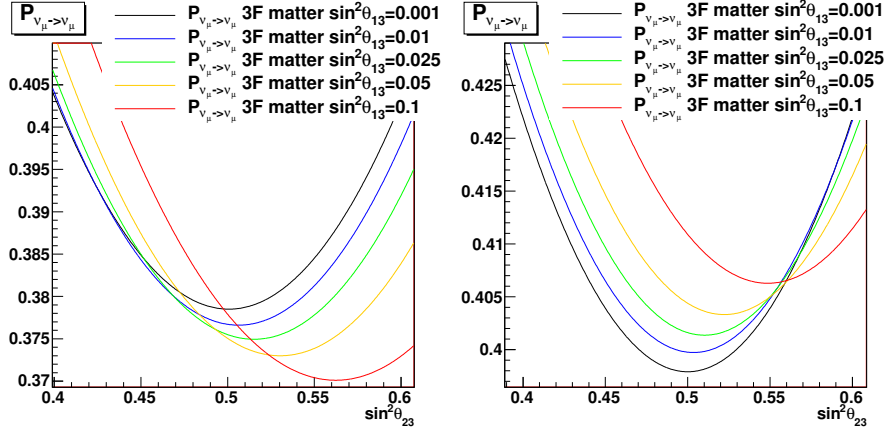


Figure E.1: The 3-flavour $P(\nu_\mu \rightarrow \nu_\mu)$ with matter effects as a function of $\sin^2 \theta_{23}$ for different values of $\sin^2 \theta_{13}$ for the normal mass hierarchy (left) and the inverted mass hierarchy (right); $|\Delta m_{32}^2|$ is fixed to $2.4 \times 10^{-3} \text{ eV}^2/\text{c}^4$ and δ_{CP} is fixed to 0.

The 3-flavour ν_μ -survival probability is:

$$P(\nu_\mu \rightarrow \nu_\mu) = 1 - 4|U_{\mu 2}|^2|U_{\mu 1}|^2 \sin^2 \left(\frac{\Delta m_{21}^2 L}{4E} \right) - 4|U_{\mu 3}|^2|U_{\mu 1}|^2 \sin^2 \left(\frac{\Delta m_{31}^2 L}{4E} \right) - 4|U_{\mu 3}|^2|U_{\mu 2}|^2 \sin^2 \left(\frac{\Delta m_{32}^2 L}{4E} \right) \quad (\text{E.2})$$

where from equation 2.31 the PMNS matrix elements are

$$\begin{aligned} |U_{\mu 1}|^2 &= s_{12}^2 c_{23}^2 + s_{13}^2 s_{23}^2 c_{12}^2 + 2s_{12}s_{13}s_{23}c_{12}c_{23}\cos(\delta) \\ |U_{\mu 2}|^2 &= c_{12}^2 c_{23}^2 + s_{13}^2 s_{23}^2 s_{12}^2 - 2s_{12}s_{13}s_{23}c_{12}c_{23}\cos(\delta) \\ |U_{\mu 3}|^2 &= s_{23}^2 c_{13}^2 \end{aligned} \quad (\text{E.3})$$

The movement of the centre of symmetry can be explained mathematically by making some approximations in equation E.2. Neglecting Δm_{21}^2 , and therefore setting $\Delta m_{32}^2 \approx \Delta m_{31}^2$, the third terms of $|U_{\mu 1}|^2$ and $|U_{\mu 2}|^2$ in Eq. E.3 cancel each other. With this approximation, Eq. E.2 reads:

$$\begin{aligned}
P(\nu_\mu \rightarrow \nu_\mu) &\approx 1 - 4 \sin^2 \left(\frac{\Delta m_{32}^2 L}{4E} \right) c_{13}^2 s_{23}^2 [s_{12}^2 c_{23}^2 + c_{12}^2 s_{13}^2 s_{23}^2 + c_{12}^2 c_{23}^2 + s_{12}^2 s_{13}^2 s_{23}^2] \\
&= 1 - 4 \sin^2 \left(\frac{\Delta m_{32}^2 L}{4E} \right) c_{13}^2 s_{23}^2 (s_{12}^2 + c_{12}^2) [c_{23}^2 + s_{13}^2 s_{23}^2] \\
&= 1 - 4 \sin^2 \left(\frac{\Delta m_{32}^2 L}{4E} \right) c_{13}^2 s_{23}^2 [c_{23}^2 + s_{13}^2 s_{23}^2]
\end{aligned} \tag{E.4}$$

Equation E.4 can be written as

$$y \approx 1 - 4Ax(1-k) [(1-x) + kx] = 1 - 4Ax(1-k) + 4Ax^2(1-k)^2 \tag{E.5}$$

where $A = \sin^2 \left(\frac{\Delta m_{32}^2 L}{4E} \right)$, $x = s_{23}^2 = \sin^2(\theta_{23})$ and $k = s_{13}^2 = \sin^2(\theta_{13})$. The minimum of this equation can be found setting the first derivative to zero:

$$\frac{dy}{dx} = -4A(1-k) + 8Ax(1-k)^2 \tag{E.6}$$

Since $A \neq 0$ and $(1-k) \neq 0$ (for an angle $\theta_{13} < \pi/2$), the value of x at which the oscillation probability is at a minimum is

$$x_{min} = \frac{1}{2(1-k)} \tag{E.7}$$

It is clear from equation E.7 that x_{min} is at $\frac{1}{2}$ when $k = \sin^2(\theta_{13}) = 0$. Also the only physically-allowed values of $\sin^2(\theta_{13})$ are ≥ 0 , and this means that x_{min} is at $\sin^2(\theta_{23}) > \frac{1}{2}$ when $\sin^2(\theta_{13})$ is non-zero. This simple result explains the dependence on $\sin^2(\theta_{13})$ of the centre of symmetry of the $P(\nu_\mu \rightarrow \nu_\mu)$ curve, and therefore the dependence on $\sin^2(\theta_{13})$ of the centre of symmetry between the two minima of the $\Delta\chi^2$ distribution when plotted as a function of $\sin^2(\theta_{23})$.

Several interesting conclusions can be extracted from the result above:

- As the true value of $\sin^2(\theta_{23})$ approaches the centre of symmetry, the two minima become more difficult to separate. If the true value of $\sin^2(\theta_{23})$ is exactly at the centre of symmetry, there is a single minimum in the distribution of $\Delta\chi^2$ vs $\sin^2(\theta_{23})$. For a value of $\sin^2(\theta_{23})$ close to the centre of symmetry, the χ^2 distribution becomes quite flat around the centre of symmetry when statistical fluctuations are added, and the two minima become indistinguishable. This effect produces a bias in the distribution of residuals of $\sin^2(\theta_{23})$ when the true input value is very close to $\sin^2(\theta_{23}) = 0.5$.
- Usually there is one minimum in each one of the two octants. However, when the minima are close to the centre of symmetry, both minima could be in the second octant. For example, the centre of symmetry is at $\sin^2(\theta_{23}) \approx 0.513$ if $\sin^2(\theta_{13}) \approx$

0.025. If one minimum is very close to this centre of symmetry, for instance at $\sin^2(\theta_{23}) = 0.505$, then the second minimum is at $\sin^2(\theta_{23}) = 0.521$, and therefore both are in the second octant.

- The results for the best-fit value for $\sin^2 \theta_{23}$ shown in Tab. 5.8 are almost the same for both mass hierarchies, although the best-fit values for the other oscillation parameters are different. The reason is that the difference between 0.5 and the centre of symmetry of $P(\nu_\mu \rightarrow \nu_\mu)$ as a function of $\sin^2 \theta_{23}$ is different depending on the mass hierarchy selected (being the difference with 0.5 smaller for inverted hierarchy) as observed in Fig.E.1.

List of Figures

2.1	Drawing of the normal and inverted neutrino mass hierarchies, showing the fractions of flavour eigenstates in each mass eigenstate, indicated by colours, that nearly fit the current neutrino data with fixed values of the oscillation parameters. Figure from [64].	18
3.1	Layout of the T2K experiment.	36
3.2	Overview of the T2K neutrino beamline.	39
3.3	Schematic view of the T2K secondary beamline	40
3.4	Effect of an off-axis configuration on the neutrino energy spectrum for different off-axis angles.	42
3.5	Neutrino energy vs parent pion momentum for different off-axis angles. . .	43
3.6	Cross sections per nucleon per energy for CC interactions of ν_μ on Carbon as a function of neutrino energy.	43
3.7	The near detector complex.	44
3.8	The INGRID detector configuration.	45
3.9	Drawings of an INGRID module.	46
3.10	Typical neutrino event in the INGRID detector.	47
3.11	The off-axis ND280 set of detectors.	48
3.12	Slice of the magnetic field mapped in the TPC region.	49
3.13	A schematic view of the PØD design.	51
3.14	Schematic drawing of the TPC structure.	52
3.15	Distribution of energy loss as a function of momentum calculated in the TPCs. .	53
3.16	Example of spatial distortion map in one TPC computed using laser data. .	55
3.17	Deposited energy distribution as a function of the range for particles stopping in FGD1	56
3.18	Example of event display.	57
3.19	Design and location of the Super-Kamiokande detector.	58
3.20	Schematic drawing of the division of Super-Kamiokande into inner and outer detector.	59
3.21	Event display examples for the SK simulation.	62
3.22	Example of the e/ μ separation with the new SK reconstruction algorithm. .	64

3.23	Two dimensional distribution of the ratio of the best-fit likelihood values of the π^0 and electron hypothesis $\ln(L_0/L_e)$ vs m_{π^0}	64
4.1	History of the number of total accumulated protons and the number of protons per pulse.	67
4.2	History of the neutrino beam intensity and neutrino beam centres.	68
4.3	Drawing of the T2K target area.	69
4.4	Time history of the measurement of the muon profile centre at MUMON.	70
4.5	The pions and kaons phase spaces in terms of production angle vs simulated momentum that contribute to the predicted neutrino flux at SK.	73
4.6	The T2K flux prediction for ND280 off-axis and SK detectors.	73
4.7	Example of the total fractional error in muon neutrino flux at ND280 and SK.	76
4.8	The flux correlations for each neutrino flavour, energy and detector.	76
4.9	The ratio between the flux predictions at the far and near detectors of the ν_μ flux and uncertainty on the ratio.	77
4.10	Feynman diagrams for charged current nucleon-neutrino interaction modes.	78
4.11	Fit to MiniBooNE data for single pion production cross sections.	84
4.12	The ND280 2-dimensional distributions in $\cos \theta$ vs momentum of the muon candidate for the ND280 data.	91
4.13	Schematic drawing illustrating the ND280 detector systematics.	93
4.14	Distributions of $\sigma_{\Delta(1/p_T)}$ for the calculation of the TPC momentum resolution.	95
4.15	Input correlations prior to the ND280 fit and correlations after the ND280 fit (right) of the parameters that are propagated to SK in the joint oscillation analysis.	97
4.16	Momentum distribution of the muon candidate for data, MC nominal prediction and MC after the ND28 fit.	98
4.17	SK flux parameters before and after the ND280 fit.	99
4.18	Post-fit values and post-fit fractional errors for each of the flux and correlated cross section systematic parameters after the ND280 fit.	101
4.19	On-timing window ΔT_0	102
4.20	PID parameter and reconstructed momentum distribution for the FCFV single ring events (muon-like events).	104
4.21	PID parameter distribution and visible energy distribution for the FCFV single ring events (electron-like events).	106
4.22	Number of decay electrons and reconstructed neutrino energy distribution (electron-like events).	107
4.23	SK data reduction after each cut of the single ring muon-like and electron-like event selection.	108
4.24	SK detector systematic error correlation matrix.	112
5.1	Examples of the effect of the interdependence between the oscillation parameters in the oscillation probabilities $P(\nu_\mu \rightarrow \nu_\mu)$ and $P(\nu_\mu \rightarrow \nu_e)$	114

5.2	The $P(\nu_\mu \rightarrow \nu_\mu)$ and $P(\nu_\mu \rightarrow \nu_e)$ probabilities expected for different values of $\sin^2 \theta_{23}$ and for δ_{CP} in the interval $[-\pi, \pi]$ for normal (solid) and inverted (dashed) mass hierarchy. The highlighted dot on each ellipse is the point for $\delta_{CP} = 0$ and δ_{CP} increases clockwise (anti-clockwise) for normal (inverted) mass hierarchy. The other oscillation parameter values are fixed to $ \Delta m_{32}^2 = 2.4 \times 10^{-3} \text{ eV}^2/\text{c}^4$ and $\sin^2 \theta_{13} = 0.0243$ (solar parameters fixed to Tab. B.1) and the neutrino energy is fixed to 600 MeV.	115
5.3	The 68% CL regions in the $(\sin^2 2\theta_{13}, \delta_{CP})$ space for the stand-alone appearance analysis on the Run 1+2+3+4 T2K dataset for different values for $\sin^2 \theta_{23}$	115
5.4	Schematic overview of the oscillation analysis flow.	117
5.5	Reconstructed energy spectrum of single μ -like ring events and single e-like ring events with and without the effect of the NA61 flux tuning of the nominal MC templates.	126
5.6	Reconstructed energy spectrum of single μ -like ring events and single e-like ring events with and without the effect of BANFF flux and cross section tuning on the NA61-tuned flux MC templates.	127
5.7	Predicted number of single μ -like ring events and single e-like ring events.	128
5.8	Predicted single μ -like ring and single e-like ring SK reconstructed energy spectra.	129
5.9	Values of the fractional errors for each SK+FSI+PN systematic parameter, defined as listed in Tab. 5.3.	137
5.10	Example of response function (cubic spline).	141
5.11	Total error envelope of the single μ -like ring and single e-like event reconstructed energy spectra.	145
5.12	Distribution of residuals of the four oscillation parameters.	147
5.13	Summary of mean and RMS for the distribution of pulls of the 64 systematic parameters with and without correlations.	148
5.14	Systematic parameter pulls for the 64 systematics allowed to float in the Run 1+2+3+4 joint 3-flavour oscillation fit.	155
5.15	Reconstructed neutrino energy distribution of single μ -like ring and single e-like ring events in the Run 1+2+3+4 dataset along with the best-fit prediction of the joint 3-flavour oscillation analysis and the non-oscillation prediction for NH	156
5.16	Reconstructed neutrino energy distribution of single μ -like ring and single e-like ring events in the Run 1+2+3+4 dataset along with the best-fit prediction of the joint 3-flavour oscillation analysis and the non-oscillation prediction for IH	157
5.17	Comparison of profiled $\Delta\chi^2$ distributions as function of each of $ \Delta m ^2 = \Delta m_{32}^2 (NH)$, $ \Delta m_{13}^2 (IH)$, $\sin^2 \theta_{23}$, $\sin^2 \theta_{13}$ and δ_{CP} for the joint 3-flavour oscillation fit to the Run 1+2+3+4 dataset with normal and inverted hierarchies.	158

5.18	Comparison of 68% and 90% CL regions for the Run1+2+3+4 dataset fit with different mass hierarchy assumptions.	159
5.19	Result of the goodness-of-fit tests.	160
5.20	Comparison of the best-fit spectra of single μ -like ring and single e-like ring events for the Run 1+2+3+4 dataset for normal hierarchy with and without reactor constraint.	162
5.21	Comparison of the best-fit spectra of single μ -like ring and single e-like ring events for the Run 1+2+3+4 dataset for inverted hierarchy with and without reactor constraint.	162
5.22	Comparison of profiled $\Delta\chi^2$ distributions as a function of each of $ \Delta m^2 = \Delta m_{32}^2 (NH)$, $ \Delta m_{32}^2 (IH)$, $\sin^2\theta_{23}$, $\sin^2\theta_{13}$ and δ_{CP} for the joint 3-flavour oscillation fit to the Run 1+2+3+4 dataset with reactor constraint for normal and inverted hierarchies.	163
5.23	Comparison of 68% and 90% CL regions for the Run1+2+3+4 dataset fit with reactor constraint with different mass hierarchy assumptions.	164
5.24	Comparison of 68% and 90% CL regions in the parameter spaces ($\sin^2\theta_{23}$, δ_{CP}) and ($ \Delta m^2 $, δ_{CP}) for the Run1+2+3+4 dataset fit with reactor constraint with different mass hierarchy assumptions.	165
5.25	Confidence regions in the $(\sin^2\theta_{23}, \Delta m_{32}^2)$ parameters space for the Run1+2+3+4 dataset joint fit with and without reactor constraint.	167
5.26	Profiled $\Delta\chi^2$ as a function of δ_{CP} with the results of the critical $\Delta\chi_c^2$ values for normal and inverted hierarchy for the Run1+2+3+4 dataset joint fit with reactor constraint.	168
5.27	Profiled $\Delta\chi^2$ as a function of δ_{CP} with the results of the critical $\Delta\chi_c^2$ values for normal and inverted hierarchy for the Run1+2+3+4 dataset joint fit with reactor constraint, with the excluded regions found overlaid.	169
5.28	Profiled χ^2 as a function of δ_{CP} for the Run1+2+3+4 dataset with reactor constraint (black solid line) and the sensitivity studies performed with 500 toy experiments, showing the averaged profiled χ^2 as a function of δ_{CP} (blue line) and the 1σ band around it for normal hierarchy (left) and inverted hierarchy (right).	170
5.29	Profiled $\Delta\chi^2$ as a function of δ_{CP} for data (black) and for the averaged profiled χ^2 from Fig. 5.28 (blue).	170
5.30	Comparison of confidence regions in the $(\sin^2\theta_{23}, \Delta m_{32}^2)$ parameter space for the Run1+2+3+4 dataset fit for the joint oscillation analysis and the ν_μ -disappearance analysis.	171
5.31	Comparison of confidence regions in the $(\sin^22\theta_{13}, \delta_{CP})$ parameter space for the Run1+2+3+4 dataset fit for the joint oscillation analysis and the latest Run1+2+3+4 ν_e -appearance analysis.	172
5.32	Line of best-fit values in the $(\sin^2\theta_{13}, \delta_{CP})$ space overlaid on the best-fit values of $\sin^2\theta_{23}$ for normal (left) and inverted (right) hierarchy.	173

5.33	Profiled $\Delta\chi^2$ as a function of δ_{CP} with the results of the critical $\Delta\chi_c^2$ values for normal and inverted hierarchy for the Run1+2+3+4 dataset joint fit with reactor constraint, with the excluded regions found overlaid and compared to the excluded regions from the latest stand-alone appearance results in [5].	173
5.34	Confidence regions in the $(\sin^2\theta_{23}, \Delta m_{32}^2)$ parameters space for the T2K joint oscillation analysis with the Run1+2+3+4 dataset including reactor constraint compared to results by MINOS and SK.	175
5.35	Comparison of $\Delta\chi^2$ as a function of δ_{CP} for the T2K and MINOS joint oscillation analyses.	176
6.1	Example of T2K sensitivity study showing the value of the 1σ width for $\sin^2\theta_{23}$ and Δm_{32}^2 vs POT.	179
6.2	Example of T2K sensitivity study for resolving $\sin\delta_{CP} \neq 0$.	180
6.3	Example of sensitivity study for resolving θ_{23} octant.	181
6.4	Example of sensitivity study for T2K alone, NO ν A alone and T2K+NO ν A for resolving $\sin\delta_{CP} \neq 0$ and the mass hierarchy.	181
6.5	Schematic view of the Hyper-Kamiokande detector design. Figure from [193].	182
6.6	Sensitivity studies for the J-PARC to Hyper-K experiment.	183
A.1	Best-fit (p_e, θ_e) distribution result with normal hierarchy for the (p_e, θ_e) analysis.	201
A.2	Best-fit E_ν^{reco} spectrum result with normal hierarchy for the alternative E_ν^{reco} analysis.	201
A.3	The 68% and 90% CL regions in the $(\sin^2 2\theta_{13}, \delta_{CP})$ parameter space.	202
A.4	The $-2\Delta\ln L$ distribution as a function of δ_{CP} .	203
A.5	Best-fit reconstructed energy spectrum for the single ring μ -like events at SK.	205
A.6	The 68% and 90% CL regions in the $(\sin^2\theta_{23}, \Delta m_{32}^2)$ or (Δm_{13}^2) parameter space.	206
A.7	Difference between reconstructed energy and true energy for CCQE events and multinucleon events.	207
B.1	Comparison of confidence regions in the $(\sin^2\theta_{23}, \Delta m_{32}^2)$ and $(\sin^2\theta_{13}, \delta_{CP})$ with and without fitting solar parameters.	209
C.1	Distribution of residuals of the four oscillation parameters.	213
C.2	Pulls of the four oscillation parameters.	213
C.3	Distribution of residuals of the four oscillation parameters in the central peak of $\sin^2\theta_{23}$.	214
C.4	Distribution of residuals of the four oscillation parameters in the peaks of $\sin^2\theta_{23}$ away from the true value.	214
C.5	Distribution of residuals of the four oscillation parameters fixing δ_{CP} .	215

C.6	Distribution of residuals of the four oscillation parameters in the central peak of $\sin^2 \theta_{23}$ fixing δ_{CP}	215
C.7	Distribution of residuals of the four oscillation parameters in the peaks of $\sin^2 \theta_{23}$ away from the true value fixing δ_{CP}	216
C.8	Energy spectrum for the single e-like ring event candidates and oscillation probabilities for those energies.	216
C.9	Lines of equal $P(\nu_\mu \rightarrow \nu_e)$	217
C.10	True $\Delta\chi^2$ distribution for the single e-like ring sample in $(\sin^2 \theta_{13}, \delta_{CP})$ and lines of equal $P(\nu_\mu \rightarrow \nu_e)$	217
C.11	Summary of mean (black circles) and RMS (red squares) for the distribution of pulls of the 64 systematic parameters with (filled) and without (empty) correlations.	219
C.12	Distribution of pulls for the systematic parameters BANFF 0 - 9.	220
C.13	Distribution of pulls for the systematic parameters BANFF 10 - 19.	221
C.14	Distribution of pulls for the systematic parameters BANFF 20 - 29.	222
C.15	Distribution of pulls for the systematic parameters BANFF 30 - 32 and some of the independent cross section systematics.	223
C.16	Distribution of pulls for some of the independent cross section systematics, reconstructed Energy scale and SK+FSI parameters 0-3.	224
C.17	Distribution of pulls for the systematic parameters SK+FSI 4 - 13.	225
C.18	Distribution of pulls for the systematic parameters SK+FSI 14 - 17.	226
D.1	Single μ -like ring (left) and e-like ring (right) reconstructed energy spectra for fake dataset #1. Points with error bars represent the fake data while the solid line corresponds to the best-fit prediction.	228
D.2	Systematic parameter pull means for the oscillation fit to fake dataset #1.	228
D.3	$\Delta\chi^2$ as function of $\sin^2 \theta_{23}, \Delta m_{FL}^2 , \sin^2 \theta_{13}$ and δ_{CP} for fake dataset #1.	231
D.4	$\Delta\chi^2$ surface in the four 2-dimensional parameter spaces for fake dataset #1.	232
D.5	68% and 90% CL regions in the four 2-dimensional parameter spaces for fake dataset #1.	233
E.1	The 3-flavour $P(\nu_\mu \rightarrow \nu_\mu)$ as a function of $\sin^2 \theta_{23}$ for different values of $\sin^2 \theta_{13}$	235

List of Tables

2.1	Standard Model fermions and their quantum numbers indicating the corresponding charges under the gauge group in Eq. 2.4.	15
3.1	Summary table of design and current values of the T2K beam parameters.	38
4.1	Summary of the different T2K data taking periods, showing the horn current, beam power and accumulated POT for each of them. *Run3a was not used for oscillation analyses.	66
4.2	List of neutrino-producing decays considered in JNUBEAM with their branching ratio in percentage.	71
4.3	List of cross section uncertainties indicating type, the interaction they affect, correlation between near and far detector and input value and uncertainties before the ND280 fit (but after the fits to external data).	86
4.4	List of systematic parameters related to the ND280 detector efficiencies and reconstruction models considered in the ND280 fit with their type. *Ubermerging is the systematic caused by two TPC segments from two different particles merged together, producing an incorrect track multiplicity in the event.	92
4.5	List of true neutrino energy bin edges (in GeV) for the flux nuisance parameters included in the ND280 fit depending on the different oscillation analysis.	96
4.6	List of cross section nuisance parameters included in the ND280 fit for each oscillation analysis.	97
4.7	List of flux and correlated cross section systematic parameters included in the ND280 fit, with their values and uncertainties (1σ error) before and after the fit.	100
4.8	Reduction on the observed data and expected MC events (calculated with typical oscillation parameters) after each cut of the single ring muon-like event selection.	107
4.9	Reduction on the observed data and expected MC events (calculated with typical oscillation parameters and $\sin^2 2\theta_{13}=0.1$) after each cut of the single ring electron-like event selection.	108

4.10	Summary on the uncertainties for the selection cuts other than topological cuts.	109
4.11	Binning used for the final output covariance matrix of the SK detector systematic errors, where $1R_\mu$ ($1Re$) represents the single ring muon-like (electron-like) samples.	112
5.1	Predicted number of single muon-like ring and single electron-like ring events for an exposure of 6.57×10^{20} POT after BANFF tuning applied to the MC templates, fixing the systematic parameters to their nominal values, with and without oscillations and with oscillations using the typical parameter values: $\sin^2(\theta_{12}) = 0.306$, $\Delta m_{21}^2 = 7.5 \times 10^{-5}$, $\sin^2(\theta_{23}) = 0.5$, $\Delta m_{FL}^2 = 2.4375 \times 10^{-3}$, $\sin^2(\theta_{13}) = 0.0243$, $\delta_{CP} = 0$ and normal mass hierarchy. The total numbers are broken down into the intrinsic beam and oscillated components. The templates corresponding to $\bar{\nu}_e \rightarrow \bar{\nu}_\mu$ were finally not used in the analysis due to its negligible contribution to both samples.	130
5.2	Numbers of sing μ -like and e-like ring events (see main text).	132
5.3	Summary of systematics included in the joint oscillation analysis.	134
5.4	List of all systematic parameters included in the joint oscillation analysis, indicating whether the systematic parameter is applied on the single μ -like ring and single e-like ring MC templates.	142
5.5	Effect of 1σ systematic parameter variation on the number of single μ -like ring and single e-like ring events using an ensemble of 10^6 toy experiments with oscillations with typical values with all systematic parameters in the given category randomized using their corresponding p.d.f., fixing the rest to their nominal values. The uncertainty is calculated as the one standard deviation of the 10^6 toy experiments.	144
5.6	True input values (shown in bold) and best-fit values for a test ensemble of 6 fake datasets, comparing results with and without including the reactor constraint in $\sin^2 2\theta_{13}$.	149
5.7	Grid limits and spacing used in all confidence regions.	150
5.8	Summary of best-fit values of the oscillation parameters for the joint 3-flavour oscillation fit to the Run 1+2+3+4 dataset.	152
5.9	Best-fit parameters for the joint 3-flavour oscillation fit to the Run 1+2+3+4 dataset comparing with and without reactor constraint.	161
A.1	Expected number of ν_e events for $\sin^2 2\theta_{13} = 0$ and $\sin^2 2\theta_{13} = 0.1$ at 6.57×10^{20} POT with its breakdown according to neutrino flavour.	200
A.2	Uncertainty on the predicted number of ν_e events for each group of systematics under the assumption of $\sin^2 2\theta_{13} = 0$ and $\sin^2 2\theta_{13} = 0.1$, expressed as RMS/mean (%).	200
A.3	Expected number of ν_μ events for $\sin^2 \theta_{23} = 0.5$ and $ \Delta m_{32}^2 = 2.4 \times 10^{-3}$ eV $^2/c^4$ at 6.57×10^{20} POT for different neutrino interaction modes.	204

A.4	Uncertainty on the predicted number of ν_μ events for each systematic errors category, and the 1σ effect of the other oscillation parameters, under the assumption of $\sin^2 \theta_{23} = 0.5$ and $ \Delta m_{32}^2 = 2.4 \times 10^{-3}$ eV $^2/c^4$, expressed in terms of RMS/mean (%).	204
B.1	Values of the solar oscillation parameters used for the results in this appendix.	208
C.1	Values of the oscillation parameters used for the fitter performance validation studies presented in this Appendix.	211
D.1	True input values (shown in bold) and best-fit values for a test ensemble of 6 fake datasets.	229
D.2	True input values (shown in bold) and best-fit values for a test ensemble of 6 fake datasets, comparing results with and without including constraint in $\sin^2 2\theta_{13}$	230